Sheffield Hallam University

Molecular deformation mechanisms in polyethylene

Sandry COUTRY

A thesis submitted in partial fulfilment of the requirements of Sheffield Hallam University for the degree of Doctor of Philosophy

December 2001

Under the sponsorship of BP Chemicals

ABSTRACT

This work is concerned with details of the molecular changes caused by deformation and also establishes any conformational differences between linear and branched polyethylene before, during and after deformation. Four blends of isotopically labelled polymers of different types, rapidly quenched from the melt, have been studied by Mixed Crystal Infra-red Spectroscopy and Small Angle Neutron Scattering (SANS), in order to clarify any differences in the molecular basis of drawing behaviour and in the initial labelled chains conformation.

For all sample types, the neutron scattering results suggest that adjacent folding is not the major type of chain folding here. This point is confirmed by our infrared results where most of the crystal stems contributing to the doublet components are in groups of only 3 to 4 adjacent labelled stems. Differences in initial conformation between the linear and copolymer samples were highlighted by both SANS and FTIR techniques. The evolution of the radius of gyration as a function of molecular weight following the relationship $R_g \propto \overline{M}_W{}^{\alpha}$, determined from the SANS data, is different for linear and copolymer sample types, suggesting a more compact arrangement as the molecular weight of the copolymer DPE guest molecules increases. This was found consistent with the infrared results, where results from both curve fitting and the simulation of the infrared CD_2 bending profiles show that the number of small groups of adjacent labelled stems is significantly larger when the DPE guest is a copolymer molecule.

Our comparative studies on various types of polyethylene lead to the conclusion that their deformation behaviour under drawing has the same basis, with additional effects imputed to the presence of tie-molecules and branches. Three major points were identified in this thesis. The changes produced by drawing imply (1) the crystallisation of some of the amorphous polymer and the subsequent orientation of the newly formed crystals, (2) the re-orientation of the crystalline ribbons and (3) the beginning of crystallite break-up. However, additional effects were observed for the high molecular weight linear sample and the copolymer sample and were attributed, respectively, to the presence of tie- molecules and of branches. It was concluded that both the tie-molecules and the branches are restricting the molecular movement during deformation, and that the branches may be acting as "anchors".

ACKNOWLEDGEMENTS

This work could not have been carried out without the help and guidance of a number of people all of whom I am grateful to.

First of all, I want to thank my supervisor Dr. Steven Spells for his support and patience during this work. I wish to thank BP Chemicals for funding my PhD. I am indebted to Dr. Warren Reed (BP Chemicals) and Dr. Mary Vickers (University of Cambridge) for valuable discussions. I would also like to thank Dr. Steve King (ISIS) and Dr. Bruno Deme (ILL) for assistance with neutron scattering experiments. I also wish to thank all the researchers, students and staff in the MRI for their help and friendship. Finally, I wish to thank my parents and Ascension, my wife, who encouraged me during this work.

à Ascension et à mes parents

merci pour tout

Table of contents:

Introduction

The deformation of polymers is a key process in the commercial production of fibres, film and tapes. While the morphology of polymer fibres has been extensively studied and the effects of deformation are well known, the detailed molecular processes linking the initial and final structures are poorly understood. Also, the influence of branched polymer on the 'drawability' of polyethylene is well known, but the underlying deformation mechanisms have not been clearly established. The aim of this thesis, a collaboration with BP Chemicals, is to provide details of the molecular changes caused by deformation of melt quenched polyethylene in order to investigate how the molecular structure of inter-lamellar tie-chains influences their initial formation and controls subsequent polymer deformation mechanisms. In particular, this work aims to demonstrate any differences in molecular conformation before, during and after deformation between linear and branched polyethylene.

These features are investigated through the use of labelled polymer. We study the molecular mechanism involved in the deformation process by combining two complementary techniques: neutron scattering and FTIR spectroscopy. In previous works, the combination of neutron scattering and infrared spectroscopy of polyethylene, using isotopic labelling, has proved invaluable in the determination of molecular conformation. While the infrared technique is based solely on nearest neighbour interactions, neutron scattering is sensitive to a range of stem correlation distances (where a crystal 'stem' is the part of the molecule corresponding to a single traverse through the crystals). These combined studies were first made on single crystal mats, enabling a detailed molecular model to be determined. This resulted in the determination of a superfolded sheetlike structure, with a high proportion of adjacent re-entry. The details of this model have recently been refined within the framework of a statistical model, which allows the analytical evaluation of various statistical parameters. For melt quenched isotopically labelled PE, neutron scattering data have been interpreted using a subunit model, which envisages small groups of labelled stems

with relatively large separations between groups. Infrared data confirms that groups of neighbouring labelled stems are small, but no statistical analysis has yet been attempted. Branched polyethylene has been of interest, mainly in terms of the possible presence and nature of any phase separation in blends with linear polymer. Extensive neutron scattering studies have accompanied morphological investigations, while deformation behaviour has not been widely explored. A complete literature survey will be found in chapter 1. In moving towards more industrially relevant cases, the same techniques were applied to study the rolling of single crystal mats. This demonstrated the progressive break-up of groups of adjacent labelled crystal stems, through the changing distribution of CD_2 bending doublet splittings in the infrared spectrum. While small angle neutron scattering (SANS) measurements of the radius of gyration showed the developing anisotropy, the infrared technique enabled estimates to be made of the size of crystallite blocks breaking away from the original lamellae, as a function of draw ratio.

This thesis is not only concerned with the mechanisms linking the initial and final stages of deformation, but also establishes any conformational differences between linear and branched polyethylene before, during and after deformation. To do so, we use small angle neutron scattering (SANS) to obtain radii of gyration in both the draw direction and the perpendicular direction. The small angle intensity intercept will be determined, in order to determine the extent of any isotopic fractionation. Infrared measurements of the CD_2 bending region will be used to determine details of local stem arrangements. This will be supported by computer calculation of the CD_2 bending profiles. In addition, infrared measurements of the CH_2 wagging region will be used to monitor the evolution of the number of gauche conformers.

Chapter 2 of this thesis is concerned with the neutron scattering technique. The methods of analysing the neutron data in the small angle (SANS) and intermediate angle (IANS) regions will be summarised, for both isotropic and anisotropic systems. Also, the different available neutron sources will be briefly described.

Chapter 3 is devoted to Fourier transform infrared spectroscopy (FTIR). The effects of isotopic labelling on the infrared spectrum of polyethylene will be presented. The specific analysis of the CD_2 bending region of the infrared spectrum (1070/1100 cm^{-1}), which enables the determination of the local stem arrangement, will be explained. In this chapter the process of computer calculation of the CD_2 bending region is also describe.

Chapter 4 presents the different techniques used to characterised the sample prior deformation. The orthorhombic structure, the deuterated concentration, the long spacing, the presence of isotopic fractionation and the initial isotropy of our samples will also be discussed in this chapter.

The initial radius of gyration (R_g) and local stem arrangement are discussed in chapter 5. The differences between undeformed copolymer and homopolymer systems will be pointed out in term of R_g and of CD_2 bending splittings. Also, the results on the calculation of the infrared CD_2 bending profiles will be presented. These results will serve as baseline results for the study of the molecular mechanism of cold drawing of polyethylene, which are discussed in chapter 6. Neutrons scattering and FTIR results on drawn low molecular weight linear samples will be first considered and analysed, leading to the determination of the different stages involved during cold drawing of linear polyethylene. Using these results as baseline, the effects of increasing the molecular weight of the linear polyethylene and the effects of adding branches on the deformation behaviour will be highlighted. Finally, the conclusion on this work is presented in chapter 7, where our results will be compared and discussed in the light of previous works.

Chapter one:

Polyethylene: a review.

I.1. Structure and Chain conformation in Polyethylene.

I.1.1 Introduction.

It has been known for many years that crystallisation can occur in polymers. But this crystallisation is never perfect: polymers are normally only semi-crystalline.

The most widely studied crystalline polymer is polyethylene $(-CH_2-)_n$. Due to energetic considerations, the most stable molecular conformation in the crystal state involves all bonds in the trans form, i.e. the planar zigzag conformation. These molecules are then packed into an orthorhombic unit cell of dimensions shown in Table I. 1 [1] with the polymer long axis lying parallel to the c-axis.

macromolecule	Crystal System Space group Mol. Helix	Unit Cell dimensions (Å)	Unit cell angles	No. units	ρ_c ($g.cm^{-3}$)
Polyethylene I $—CH_2—$	Orthorhombic Pnam 1*2/1	7.418 4.946 2.546	90° 90° 90°	4	0.9972
Polyethylene II $—CH_2—$	Monoclinic C2/m 1*2/1	8.09 2.53 4.79	90° 107.9° 90°	4	0.998

Table I. 1: *Details of the structures of Polyethylene (from ref. 1).*

Orthorhombic polyethylene (Figure I. 1) is the most stable structure, but mechanical deformation can involve modification of the unit cell to a monoclinic form (Table I. 1).

The width of wide angle X-ray reflections in polyethylene indicates that the size of coherently diffracting crystals is in the range of hundreds of angstroms in the three crystal directions. Indirectly, this implies the presence of straight-chain segments ('stems') of this magnitude within crystallites [2], the segments being nearly perpendicular to the lamellar surface.

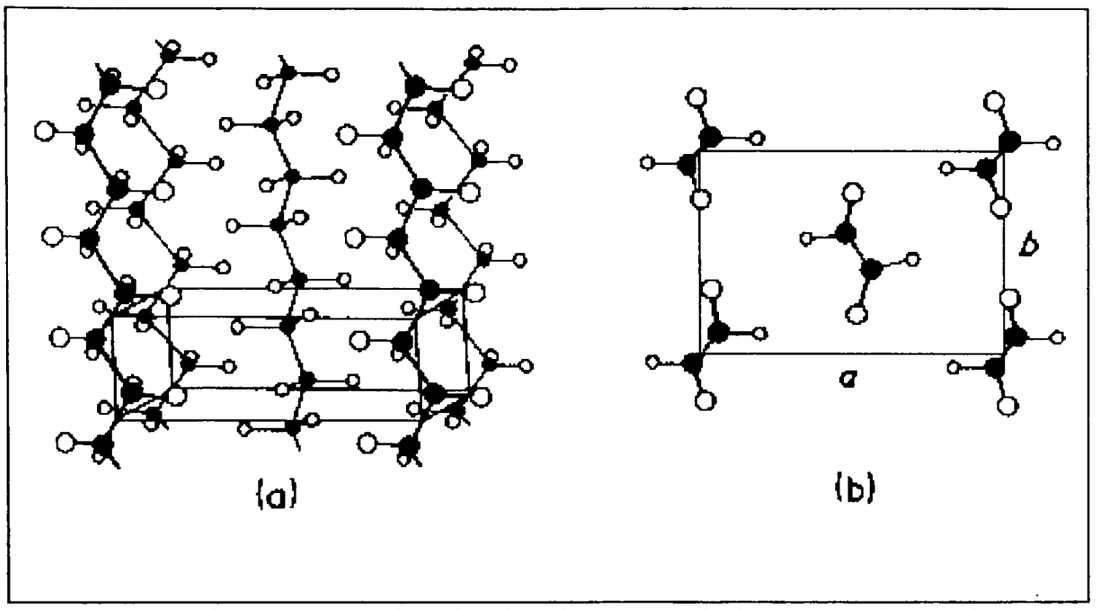

Figure I. 1: *Crystal structure of orthorhombic polyethylene. (a) General view of unit cell. (b) Projection of unit cell parallel to the chain direction (from ref. 1).*

On a molecular level, the chains are usually much longer than the lamellar thickness and, by necessity, this implies folding. Transmission Electron Microscopy with self-decoration provides direct evidence of regular folding parallel to the {110} growth plane of polyethylene single crystals [3]. The fold region forms an interface between the crystal lamellae and the amorphous region. Thus the transition order-disorder is not abrupt. A significant source of disorder in the fold region is the fluctuating height of the fold (Figure I. 2). The high crystallinity and the lamellar morphology of polyethylene suggest that the fold surfaces from neighbouring lamellae are in close contact. This, and the possibility of tie-molecules between them, indicates considerable interactions between lamellae. Thus, the nature of the fold surface is supposed to have considerable effects on the mechanical properties of crystalline polymers.

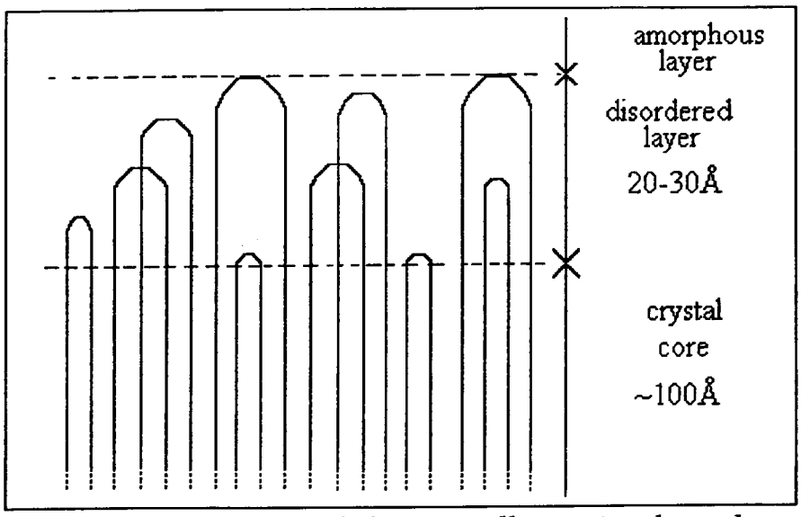

Figure I. 2: *Schematic two-dimensional diagram illustrating how the presence of folds at different depths below the lamellar surface leads to a transition layer (from ref. 4).*

This 'chain path' through the lamellar units has been a matter of considerable interest over the last fifty years (nearly fifty years since the discovery of chain folding). We will summarise the existing knowledge of the chain folding for both solution crystallised and melt crystallised polyethylene.

I.1.2. Solution crystallised polyethylene.

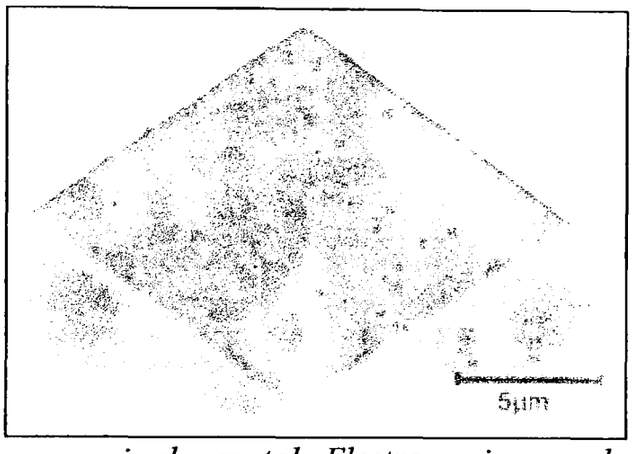

Figure I. 3: *Solution-grown single crystal. Electron micrograph of a lamellar crystal (from ref. 1).*

When formed in dilute solution, the basic morphological units of polyethylene crystals are 'single crystal' lamellae (figure I.3). Because these single crystals have a higher degree of perfection than their melt crystallised counterparts, solution crystallised polyethylene has been extensively studied by both the two complementary techniques, Mixed Crystal Infrared Spectroscopy and Small Angle Neutron Scattering [5, 6, 7, 8], which are both sensitive to the 'trajectory' of an isotopically labelled chain in its unlabelled matrix (or vice-versa). The results indicate that adjacent re-entrant folding along {110} directions is the preferential way of chain folding in single crystals. Neutron scattering showed [9, 10] that polyethylene chains form sheets of stems whose thickness agrees with that expected for rows of stems along {110} planes, while the study of the infrared splitting of the CD_2 bending component of the infrared spectrum of dilute blends of deuterated polymer in unlabelled matrix indicates that this crystalline doublet arises from adjacent stems (and presumably re-entry folding) along a single (110) plane [5, 6].

By showing that radii of gyration are relatively insensitive to molecular weight, Sadler et al [7-9] suggested that chains fold back on themselves (i.e. superfolding) (figure I. 4). This means that on some occasions a non adjacent fold involves a complete departure from a sheet, followed by incorporation in a separate (110) plane.

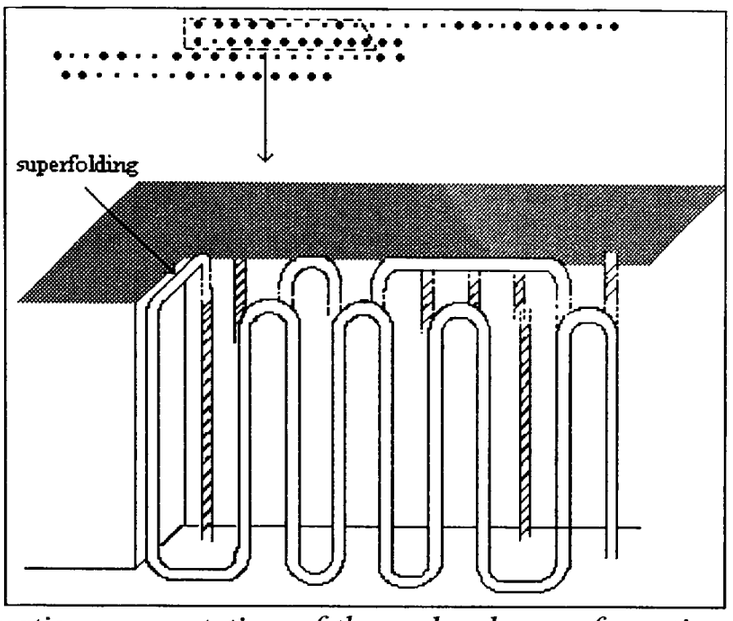

Figure I. 4: *Schematic representation of the molecular conformation of a polyethylene chain within the lamella. The superfolding is defined as a complete departure from a sheet, followed by incorporation in a separate (110) plane. The large spots in the crystal stem projection at the top correspond to the unshaded chain in the perspective sketch. The sketch below includes a possible arrangement of folds (from ref. 10).*

Later, using a combination of both experimental techniques, Spells and others [10, 11] developed a statistical model for the chain folding in polyethylene which shows that the probability of adjacent re-entry in the sheet is 75 % and the dilution (i.e. the proportion of lattice sites in the plane bounded by a labelled molecule which are occupied by that molecule) is 0.5 for crystallisation from xylene solution at 70°C.

This model has recently been updated [12] by adding another parameter which is the probability of having a labelled stem deposited after an unlabelled one. In this updated model, Sonntag et al [12] consider the molecular sheets as one-dimensional sequences of stems, labelled or not, in the {110} direction. A crystal sheet is assumed to contain σ labelled stems. When σ labelled stems are placed down, superfolding occurs and a new sheet is required. Results from this model give good agreement with neutron scattering from solution crystallised polyethylene, using suitable values for these parameters.

I.1.3. Melt crystallised polyethylene.

In dilute solution, the polymer coils are isolated from each other, but as the solution becomes more concentrated the molecules become entangled. In the melt, chain entanglements are of extreme importance and consequently the crystals that form are more irregular than those obtained from dilute solution.

In a polymer crystallised by cooling a melt, the most commonly observed structure is spherical, with chain-folded lamellar ribbons growing outwards from the centre (figure I. 5), twisting regularly as they go. These are named 'spherulites' (figure I. 6). These spherulites are most commonly seen in thin films in the polarising optical microscope.

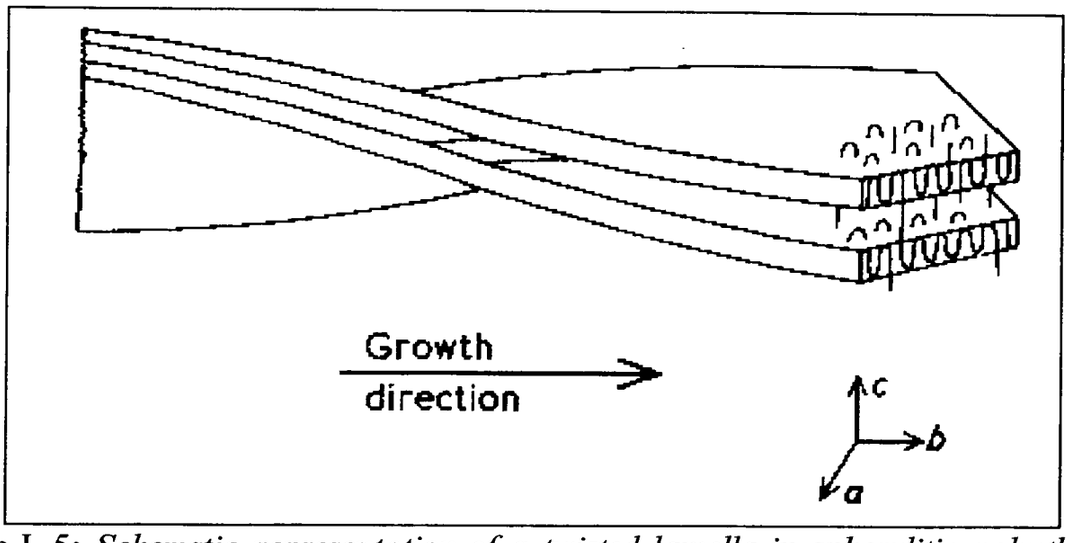

Figure I. 5: *Schematic representation of a twisted lamella in spherulitic polyethylene showing chain-folds and intercrystalline links (from ref. 1).*

As with the solution crystallised polymer, melt crystallised polyethylene has been studied by both Mixed Crystal Infrared Spectroscopy and Small Angle Neutron Scattering, although less extensively.

The infra-red results, as well as the neutron scattering data are interpreted using a statistical distribution of the labelled molecules in the unlabelled matrix. But because of their melting temperature difference, the protonated and deuterated polyethylene are not thermodynamically equivalent. Hence they have different crystallisation rates, and so isotopic fractionation can occur during crystallisation from the melt. This effect of isotopic fractionation has been widely studied by neutron scattering.

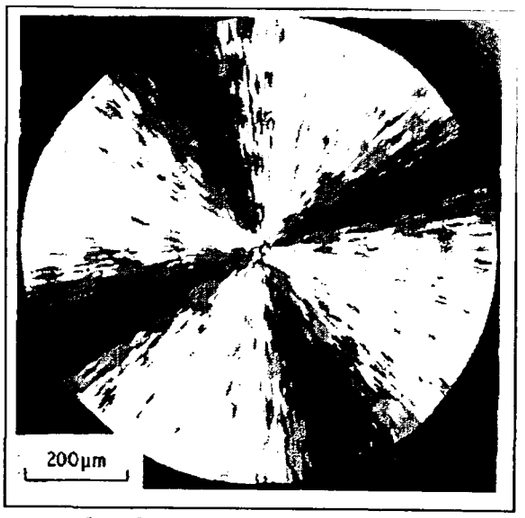

Figure I. 6: *Optical micrograph of a single spherulite growing in isotactic polystyrene (from ref. 1).*

Schelten et al [13] observed a large increase in the scattering at very small angles from melt crystallised polyethylene, by comparison with predicted values. They attributed this to clustering of the isotopic species during crystallisation. Later the same group [14] showed that the cooling rate influenced the degree of fractionation and that the effect of isotopic segregation is minimised for rapid quenching. For this reason, measurements since then have mostly been on quenched samples.

The first study of chain conformation in polyethylene crystallised from slow cooling of the melt was performed with the Mixed-Crystal Infrared technique [5, 15]. By using a dispersive spectrometer and collecting spectra at room temperature, Ching and Krimm [15] have shown that the CD_2 bending mode is a singlet, and that the splitting of the CH_2 rocking modes, which was shown to vary with deuterated polyethylene concentration, is significantly larger than that observed for n-alkane mixtures. They concluded that adjacent {200} folding was responsible for this behaviour. However this was erroneous for two reasons. Firstly their measurements were obtained with a conventional dispersive spectrometer without the capability of adding data from successive scans, and thus, the weak absorption from a small proportion of deuterated polyethylene in the sample may produce a signal/noise ratio which prevents the resolution of doublet component. This problem can be alleviated using FTIR techniques. Secondly their results were obtained at room temperature, which decreases the interactions between crystals stems as compared with low temperature data, thus decreasing the doublet splittings for both the CH_2 rocking and bending vibration. This problem is minimised by cooling the sample to liquid nitrogen temperature, which results in the significant contraction of the orthorhombic unit cell of polyethylene, and therefore increases the

interaction between crystals stems. Ching and Krimm have shown, as well, that the effect of isotopic fractionation is minimised by matching as closely as possible the melting temperatures of the isotopic species.

Later, neutron scattering measurements provided evidence that chain conformations in melt quenched polyethylene are quite different from those in polyethylene single crystals. Sadler and Keller [8] interpreted Intermediate Angle Neutron Scattering results as consistent with scattering from individual stems, rather than from sheets of adjacent stems. This led to the suggestion that adjacent re-entry, was not the major type of folding in melt crystallised polyethylene, and that the data may be consistent with random fold re-entry as claimed earlier [16].

By using Small Angle Neutron Scattering data from samples in the molten state and those quenched from the melt, Schelten et al [13, 14] showed that the radii of gyration in both cases are similar. This correspondence of values indicates that little molecular movement accompanies crystallisation. Based on this concept, a model was developed with crystal stem positions related to the spatial distribution of segments within a Gaussian coil in the melt state (the 'Freezing-in' model shown in figure I. 7) [17].

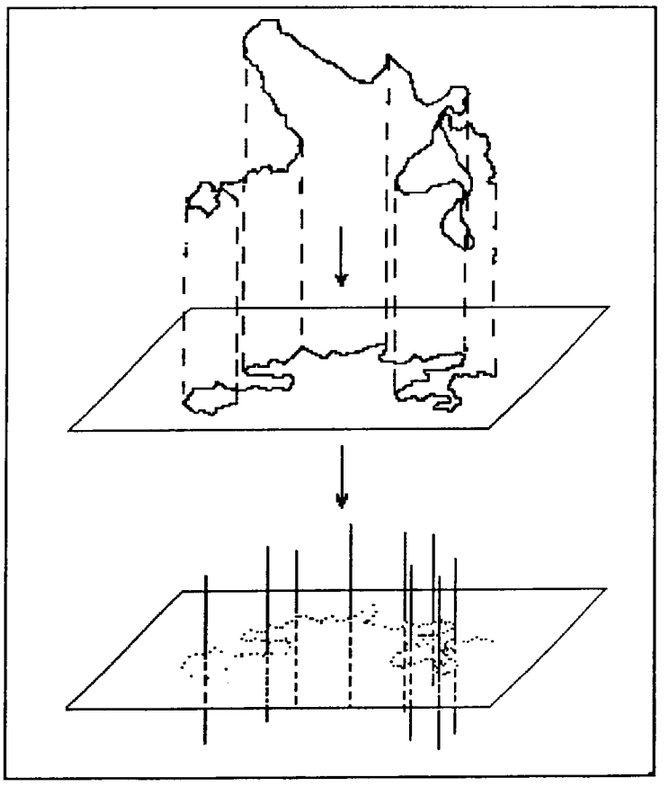

Figure I. 7: *Schematic representation of the 'freezing-in' model: top, a three dimensional random coil; centre, the projection of this on a plane; and below, grouping of adjacent parts of a molecule into stems. For simplicity only one lamella is shown, but if the original coil occupied a space taken up during crystallisation by several lamellae, parts of the molecule would be incorporated in each lamella (from ref. 17).*

This model, although similar to the 'solidification' model of Stamm et al [18], has been shown not to be compatible with the published data. A 'Subunit' model [19] was then proposed which requires a local rearrangement of the chain as it folds during crystallisation, but the distribution of subunits within the whole molecule is imposed by the pre-existing Gaussian chain of the melt. This 'Subunit' model was found to give good agreement with data for a structure of a subunit with around 40% of adjacent folding, but not in any specific crystallographic direction, and with short rows of labelled stems.

In parallel to this work, Guttman et al [20]developed different models in order to calculate the intensity of the Small Angle Neutron Scattering of melt quenched polyethylene. Computations were made on models which allow various amounts and types of chain folding and varying degrees of 'tight' folds. The model that fits the SANS data best for melt quenched polyethylene is their Variable Cluster model (figure I. 8) with fold planes in the {110}, {200} and {310} directions and with an average stem separation larger than 5 Å.

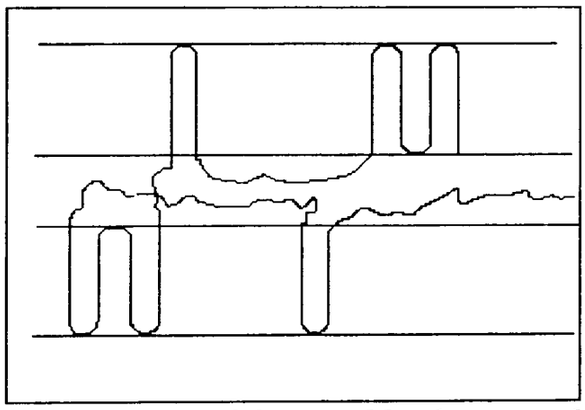

Figure I. 8: *Schematic representation of the variable cluster model (from ref. 20).*

In this model, as each stem finishes its traverse of the crystal phase, it has a probability P_{stem} of making a fold and probability $1-P_{stem}$ of going into the amorphous phase. To characterise the mode of chain folding, they have introduced the probability of tight folding, P_{tf} which is the sum of the probability of adjacent re-entry P_{ar} and the probability of near or next near adjacent re-entry P_{aar} (figure I. 9). They have shown as well that this model fits not only the SANS data, but also the liquid and crystal densities, degree of crystallinity and radius of gyration, and that this model does not show the density anomaly inherent in the random re-entry models.

Taking into account these results, Jing and Krimm [21] repeated their infrared measurements on melt crystallised polyethylene, at liquid nitrogen temperature. As

before, the CD_2 bending vibration was found to be a singlet, but with an asymmetry. Curve fitting was applied to the data, first with a crystalline singlet and a non-crystalline component, but this gives rise to an inadequate fit. Therefore, they introduced in addition doublet components which gave good agreement with the experimental data. They concluded that the crystalline singlet was associated with random re-entry folding and represented 60-70% of the crystal stems. The presence of a doublet, comprising 30-40% of the crystals stems, shows that {110} adjacent re-entry folding exists. The magnitude of the splitting indicates that there are about three adjacent stems in the {110} direction in such structures.

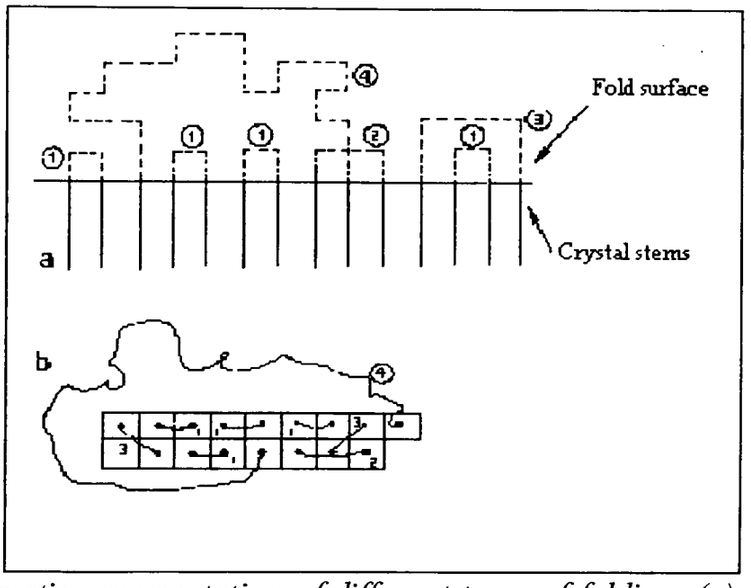

Figure I. 9: *Schematic representation of different types of folding. (a) a variety of tight loops (regular folds) and loose loops are shown in a single given fold plane. Folds marked 1 are adjacent folds. Folds marked 2 and 3 are near adjacent folds. Loops marked 4 are not counted. (b) A variety of regular folds and loose loops are shown on the plane perpendicular to the fold plane (from ref. 20).*

With the aim of improving the infrared spectral resolution, Spells [22] applied the technique of Fourier self deconvolution to melt quenched polyethylene. After deconvolution, two peaks appear on both sides of the singlet component with a splitting of 3.4 cm^{-1}. This corresponds to groups of only three adjacent stems, which is the same as was found by Jing et al [21] using curve fitting. This result confirms the conclusion from neutron scattering that the polymer chains in melt crystallised polyethylene form small clusters of a maximum three adjacent stems in the {110} direction within the crystallite.

I.1.4. Blends of linear and branched polyethylene.

Blends of linear and branched polyethylene have aroused considerable scientific and commercial interest during the last ten years, with the central question being whether or not the components co-crystallise.

Norton and Keller [23] presented electron microscopy findings in favour of segregation of the components in a binary blend of unfractionated commercial grades of linear and ethyl-branched polyethylene (1.4 mole% ethyl groups) crystallised at 397K. They reported that linear polyethylene crystallises at the isothermal temperature in regular shaped sheets (so-called dominant lamellae) whereas the branched polyethylene materials crystallise during the subsequent cooling phase forming finer, S-shaped subsidiary lamellae. On the basis of DSC data, these authors expect the microstructure of the quenched sample to be less segregated, although no conclusive electron microscopy data in favour of such a view was presented in the paper.

Edwards [24] and Hu et al [25] presented data obtained by DSC, WAXS, SAXS and Raman spectroscopy indicating co-crystallisation between linear and ethyl-branched polyethylene. They have associated the co-crystallisation with the presence of a broad single melting peak. Both reports were based on blends of broad molecular weight samples of similar molecular weight.

Rego López and Gedde [26] presented data from the study of crystallisation kinetics and morphology which indicate the existence of two regimes of crystallisation. At high temperatures, the branched polyethylene component crystallises separately in relatively large spherulites. At lower temperatures, both components crystallise and a very fine-textured spherulitic structure is obtained. The transition between the two regimes was found to be very sharp in terms of temperature (of the order of 1K). It was also accompanied by an abrupt change in crystallisation kinetics. In a following paper [27] they presented data obtained by transmission electron microscopy of mixtures of linear and branched polyethylene crystallised at temperatures at which both components crystallise (387-397 K). The absence of white spots in the transmission electron microscopy of thin sections of samples treated with chlorosulphonic acid and stained with uranyl acetate, provides evidence for co-crystallisation of the components.

Hill et al [28] studied the effect of liquid → liquid phase segregation within the melt prior to crystallisation for mixtures of linear and branched polyethylene over a range of

concentrations. Results from several techniques used in combination showed that the miscibility of the polymers in the melt is conditional. The melt segregated region occurs at low linear polyethylene content. This result was deduced from DSC and transmission electron microscopy of quenched melts. Considerable co-crystallisation was observed in the isothermally crystallised sample. The phase diagram they proposed is not a proper equilibrium phase diagram, but a description of the state in which the blend was formed. Also, because the linear polyethylene used had a broad distribution of molecular weights, and the branched polymer had a distribution not only of molecular weight but also of branch content, segregation could occur not only between the two major components but also within each major component itself, leading to a broad and ill-defined boundary in the phase diagram.

In the following paper [29], the effects of varying the molecular weight of the linear component and of varying the branch content and type of the branched polymer on the phase segregation of blends of linear and branched polyethylene was studied. It was found that by lowering the molecular weight of the linear polymer and the branched content and length, phases separation became less probable. The speed of quenching the melt is also a limiting factor to segregation of the two components.

Later, the same group compared blends of linear and lightly branched polyethylene prepared by melt-mixing and by solution blending [30]. The results presented show that the phase behaviour of the melt-mixed material is similar to that for the solution blended sample.

Tashiro et al [31] investigated the crystallisation behaviour for 50/50 wt % blends of deuterated high density polyethylene (DHDPE) with hydrogenous polyethylene with different branch content by DSC and FTIR. It was found that a blend of HDPE with a linear low density polyethylene with a relatively low degree of short chain branching presents signs of co-crystallisation even for the slow cooling process from the melt. On the contrary, for a blend of HDPE with an LLDPE with a high degree of branching, phase segregation was observed. In this paper, it was also shown that the splitting of the crystal phase infrared doublets is affected by the degree of branching.

The morphology of blends of linear and branched polyethylene was also studied by small angle neutron scattering [32, 33]. The first paper confirmed the effect of rapid quenching on the co-crystallisation of the components, while the second one corroborate

that the mixtures are homogeneous for all compositions when the branch content is low (i.e. <4 branches/100 backbone carbon atoms).

Finally, to summarise, co-crystallisation of linear and branched polyethylene is favoured by lowering the molecular weight of the linear component, the branched content and branch size and by rapidly quenching the melt.

I.2. Molecular mechanisms of deformation.

I.2.1. General background.

These days, many polymers are used in structural engineering applications and are subjected to appreciable stresses. With the increasingly widespread use of polymers, an understanding of the mechanism of molecular reorganisation on deforming polymers is becoming essential for the improvement of processing techniques and the design of new polymer grades with superior combinations of properties has resulted in many investigations.

The response of a material to mechanical deformation reflects the microscopic deformation processes which are occurring on a molecular or atomic level. Figure I. 10 presents the idealised stress-strain curve for a ductile polymer. Three stages can be seen. Initially, the stress is proportional to the strain and the Hooke's law is obeyed. The tensile modulus can be obtained from the slope. At this stage, the deformation is said to be elastic. The elastic deformation reflects the displacement of the repeat units out of their low energy positions in the 'potential well' and therefore is recoverable. In the case of a spherulitic polymer, a transition from a spherulitic to an ellipsoidal shape takes place during elastic deformation.

As the strain is increased, the curve decreases in slope until stress reaches a maximum. This is conventionally known as the yield point. It corresponds to the point at which permanent plastic deformation (which occurs by the motion of dislocations through the crystal lattice, and by movement of molecular segments) takes place. At this stage the cross-sectional area of the sample starts to decrease more rapidly at one particular point along the gauge length as a 'neck' start to forms. The nominal stress falls after yield and settles at a constant value as the neck extends along the specimen. This is known as cold drawing. Eventually, when the whole specimen is necked, strain hardening occurs and

the stress rises until fracture intervenes. At high strains the spherulitic microstructure breaks up and a fibre like morphology is obtained.

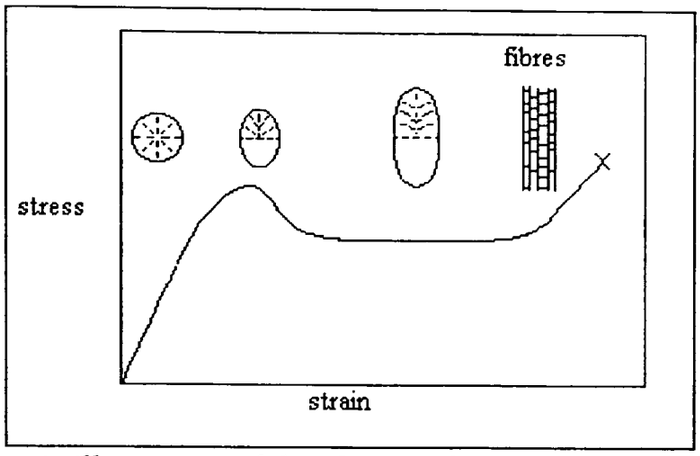

Figure I. 10: *Schematic illustration of the changes from a spherulitic morphology during deformation of a semi-crystalline polymer.*

Our interest is in the plastic deformation, achieved by cold drawing polyethylene.

Several models have been proposed for the type of molecular reorganisation which occur during plastic deformation [34, 35, 36]. All these models suggested molecular chain movement within the crystalline phase during deformation. The simplest, and most commonly quoted, model for the drawing of a polymer through a neck is due to Peterlin [34]. In this model the necking process is envisaged as the breaking away of small blocks of crystals from the lamellar stacks in the undeformed material and their subsequent reorientation and restacking to form microfibrils of oriented material (Figure I. 11). The Peterlin model [34] suggested that the plastic deformation of polyethylene proceeds in three steps:

1) *The continuous plastic deformation of the spherulitic structure before the neck* involving deformation of the crystalline region by a combination of slip, twinning and martensitic deformations. Also, because the amorphous phase is in a rubbery state, deformation by shear of crystals relative to each other is allowed.

2) *The discontinuous transformation in the neck from the spherulitic to the fibre structure.* Micronecks transform each lamella into microfibrils consisting of folded chain blocks broken off the lamella. The chains bridging the crack are partially unfolded during this process and act as interfibrillar tie molecules. The microcracks in every stack of lamellae in a thin destruction zone are concentrated to produce bundles of microfibrils. These fibrils, a few thousand angstroms in width, include the interlamellar ties of the original sample as interfibrillar tie molecules connecting microfibrils. Local

melting is suggested to occur during this step to make possible the movement of the chains.

3) *The plastic deformation of the fibre structure after the neck* involving the stretching of interfibrillar tie molecules and the unfolding of chain sections by which the tie molecules are anchored in the crystal blocks of adjacent microfibrils.

However mechanisms such as this are difficult to verify due to the lack of information concerning changes in the molecular conformation. It has proved easier to study the structures before and after deformation, than to directly observe any intermediate stages.

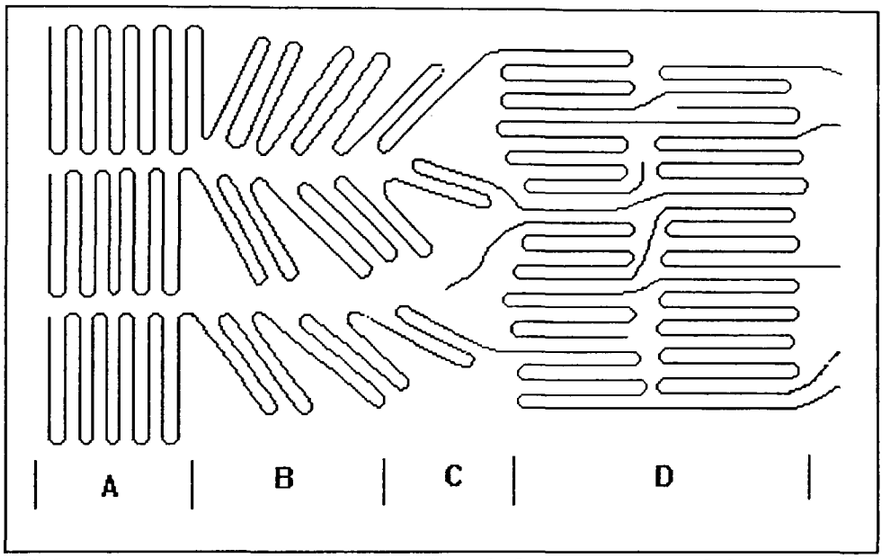

Figure I. 11: *Schematic representation of the deformation model according to Peterlin. The deformation takes place on a molecular level during the formation of a neck in semi-crystalline polymer. (A) Undeformed structure; (B) crystals deforming by slip, twinning and martensitic transformations; (C) crystals break up and molecules pulled out; (D) fibrillar structure forms.*

Sadler and Barham [37] have shown that the Neutron Scattering technique is capable of giving the molecular dimensions on drawing polyethylene, and hence the subsequent change in molecular dimensions during the deformation process. In later papers [38, 39, 40] they have applied this technique to investigate whether or not local melting occurs during deformation. The appearance of an isotopic segregation signal (e.g. see section I.1.3 on melt crystallised polyethylene) has been interpreted as consistent with a local melting and recrystallisation, as suggested in the Peterlin model. This result has been confirmed by Wu et al [41, 42, 43], who have shown that a pure mechanical model is not able to describe the process of deformation, and that local melting and recrystallisation is a major process in the deformation behaviour of polyethylene (probably depending on the conditions, such as the temperature and deformation rate).

Mixed Crystal Infrared spectroscopy has been applied to polyethylene single mats after rolling in order to obtain information on the change of molecular conformation during deformation [44]. By showing a progressive reduction of the outer CD_2 bending splittings, the authors concluded that a reduction in group size occurs during the rolling process. This suggests that the deformation behaviour is characterised by progressively smaller crystalline blocks breaking from the original lamellae and rotating so as to be aligned with the roll direction. In addition, changes in the CH_2 rocking vibrations during the rolling process have been interpreted as due to the creation of monoclinic phase. In a following paper [45], Small Angle Neutron Scattering measurements of the radius of gyration parallel and perpendicular to the roll direction can be interpreted in terms of the progressive break-up of crystallites into smaller crystalline blocks, and with an increase of the separation between blocks. The conclusion drawn is that Mixed Crystal Infrared spectroscopy in combination with Small Angle Neutron Scattering is a powerful technique in order to determine the changes of molecular conformation on deformation.

More recently, Lagarón et al used Raman spectroscopy in conjunction with DSC and WAXS to study the morphological changes occurring upon cold drawing polyethylene [46, 47, 48]. By the fact that the Raman spectrum is mainly sensitive to the conformational state of the polymer chain, they were able to determine the content of extended and non-extended chain segments in different polyethylene samples [46]. They have shown that the proportion of the extended chain segments placed outside the crystalline region increases significantly when the samples are uniaxially stretched. They compared the Raman crystallinity to the one measured from DSC and WAXS, they have shown that after cold drawing, the three techniques supported a disruption of the crystalline morphology towards a highly ill-defined and fractured orthorhombic crystalline phase [47, 48]. It was suggested that this disruption of the crystalline phase results from molecules being pulled through the crystals. Also, WAXS and Raman spectroscopy did not show evidence for large scale phase transformation from orthorhombic to monoclinic or triclinic structures [47].

I.2.2. The effects of branching in Polyethylene deformation.

The mechanical behaviour of polyethylene is markedly affected by the introduction of only a comparatively small concentration of short branches [49] (as small as 1 per 1000 carbons atoms). For example, the creep resistance of polyethylene is improved drastically by only adding a few branches per 1000 carbon atoms [50, 51].

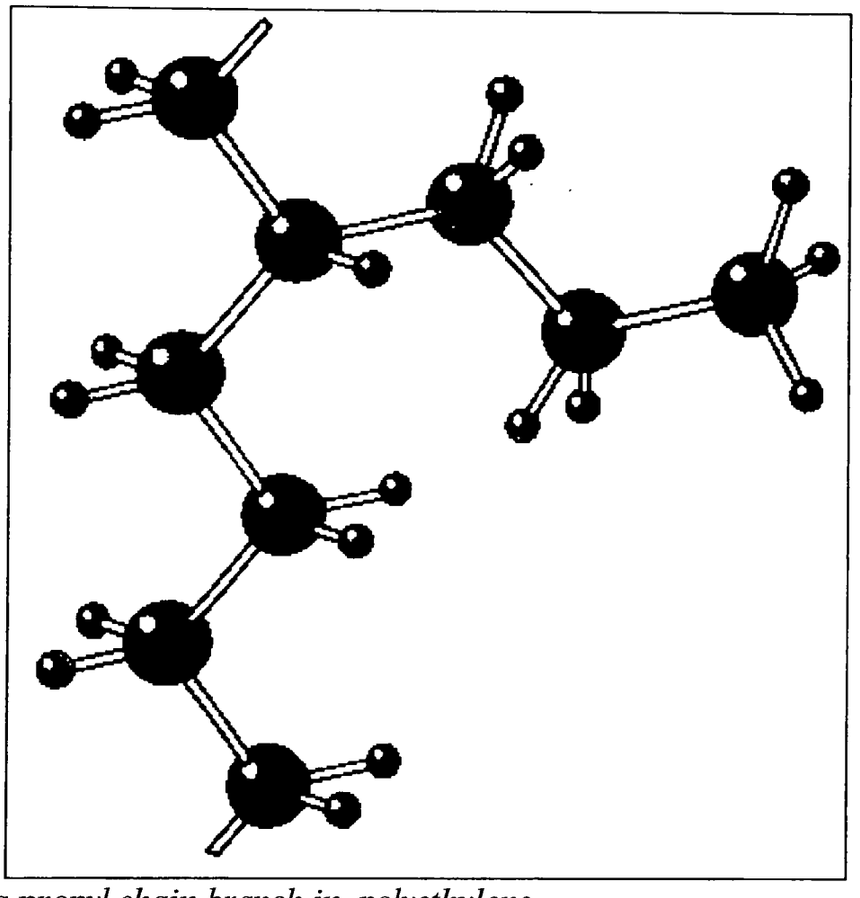

Figure I. 12: *a propyl chain branch in polyethylene.*

The physical properties of branched polyethylene depend on the chemical nature of the branches, their concentration and their distribution along the chain.

It appears that the branch length and the branch concentration (at a fixed molecular weight) determine the spherulite size [52], and consequently, spherulitic boundary area, in which slip, crazing and voiding occurs during deformation. Thus, by increasing the branch length (methyl to hexyl), the equilibrium spherulite size increases, which contributes to smaller spherulite boundary slip and finally to increases in the environmental stress cracking resistance, creep resistance and modulus.

On the other hand, branches longer than a methyl groups [53] are largely excluded from the crystal lamellae into the interfacial and interlamellar regions [54] and even the CH_3 branch appears excluded from the crystalline phase in long chain n-alkanes [55]. This

results in a decrease of the crystallinity, long spacing and lamellar thickness with increasing the number of branches. Assuming that a tie-molecule forms when the end-to-end distance of a molecule in the melt is equal to or greater than the distance between adjoining lamellae produced, it follows that a reduced long spacing results in higher tie-molecule density [52]. It has been shown that increasing tie-molecule density increases the toughness [56]. Furthermore, branches are most effective in improving the mechanical properties when they are placed on longer molecules, i.e. those most likely to act as tie-molecules [57], by increasing the resistance to disentanglement.

Hiss et al [58] compared the deformation mechanism for linear and branched Polyethylene, and shown that their deformation behaviour under applied load has a common basis and is strain controlled. For all the samples they have studied, four characteristic points were found. They suggested that these four characteristic points may be associated with (1) the onset of isolation slip processes, (2) a change into a collective activity of the slips, (3) the beginning of crystallite fragmentation, and (4) chain disentaglement resulting in a finite truly irreversible deformation.

Lagarón et al [48] have shown that for both branched and linear polyethylene the initial orthorhombic phase was disrupted towards a highly ill-defined and fractured orthorhombic structure, and that this disruption was more dramatic for branched molecules because of the branched molecules being pulled through the crystals.

To summarise, by incorporating branching in polyethylene, the crystallinity decreases, the tie-molecule density increases, the toughness increases and in general some mechanical properties of polyethylene, such as environmental stress crack resistance and creep in oriented fibrils, are improved.

Finally, although the effects of branching in polyethylene are quite well known, the way in which the branches act during deformation is not well understood. During the deformation process, the tie-molecules disengage from the crystals. This disengagement process is not known, but it may involve the pulling of a tie-molecule through the crystal, and so the branches may pass through the crystal as well, or alternatively the branches may first act as anchors at the crystal surface under moderate applied stresses, then at higher stress, the crystals disrupt under the pressure exerted by the branch on the crystal surface under the tension of attached chain.

I.2.3. Deformation of spherulites.

Because of the complex structure of spherulites, which includes structural features over a range of length scales and the local orientations of molecules and lamellae in different regions of spherulites, the molecular mechanism of deformation of spherulitic material is very complicated. Several reviews of the existing molecular and lamellar mechanisms of deformation of spherulitic polyethylene were made in the past [59, 60]. We will introduce them briefly, along with new developments.

By considering the re-orientation of the crystallites in terms of the deformation of spherulites, Wilchinsky [61] made a major advance and proposed that affine deformation takes place in the deformation of spherulites. This idea was also developed by Stein et al [62, 63] in their study of polyethylene film by light scattering. When polarised light is scattered by a spherulitic crystalline polymer, the low angle scattering pattern resulting is in the form of 4 "leaves". Upon stretching, this pattern changes to a pattern which is extended perpendicular to the stretching direction. This indicates that the greatest dimension of the scattering object is in the stretching direction. In order to simulate the change of the small angle light scattering pattern with deformation [64, 65], they developed a two stage model of molecular deformation which assumes that affine deformation take place in spherulites, and which involves first the deformation of the spherulite superstructure (deformation of the spherical structure to an ellipsoidal one) followed by rearrangement of the crystallites within a lamella.

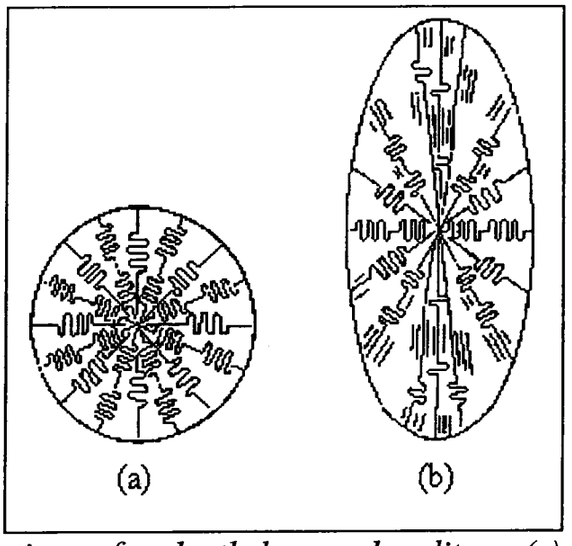

Figure I. 13: *Deformation of polyethylene spherulites. (a) initial spherulite, (b) ellipsoidal structure showing chain unfolding accompanying deformation (from ref. 62).*

Hay and Keller [66] observed the deformation of spherulitic LDPE fine film using optical microscopy and found that the response of the spherulites to deformation (both elastic and plastic) was non uniform and highly recoverable. Deformation was found to take place first of all in the spherulite radii perpendicular to the draw direction. This region usually becomes extensively deformed mainly through chain slip, whereas the regions in which the radii are at a small angle to the deformation axis are fairly undamaged. At higher draw ratios, the whole of the spherulite was found to be deformed and eventually a fibre structure was produced.

Oda et al [67] modified the model proposed by Stein et al [62] for two dimensional spherulites and applied it to the deformation of three dimensional spherulites. By assuming that the c-axis of the chain should reorient towards the stretching direction, owing to strain of tie-chains which connect adjacent lamellae, the authors suggested that this forced reorientation results in tilting of the crystal c-axis within lamellae in the polar zone of spherulite, and untwisting of lamellae in the equatorial zone of the spherulite about the lamellar axis (or the radial direction of the spherulite) (Figure I. 14). In addition, a transition from the folded chain crystals to fringed-micellar crystals due to micronecking of lamellae, crystal twinning and cracking of lamellae may be taken into consideration.

Because the models developed by Stein et al and Oda et al provide only limited information on the crystalline orientation, Nomura et al [68] introduced a mathematical development based on series expansion of the distribution functions in generalised spherical harmonics. Two types of uniaxial deformation model of polyethylene spherulite were proposed. The first one takes account of the unfolding of the chains in the lamellae and untwisting of crystal lamellae (which is the model proposed by Stein et al and modified by Oda et al), while the second one takes into consideration chain tilting and crystal lamellar untwisting. Similarly, as supposed by Stein et al, affine deformation of the lamellae was assumed. Better agreement with experimental data was found in the case of the chain tilting and lamellar untwisting model.

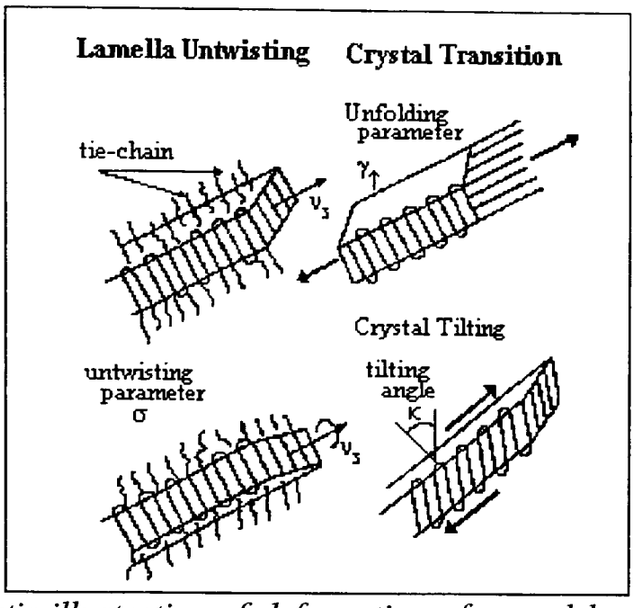

Figure I. 14: *Schematic illustration of deformation of crystal lamellae; (above) model developed by Oda et al [67] taking account of the crystal transition and untwisting of lamella; (lower) model proposed by Nomura et al [68] taking account of the chain tilting and untwisting of lamella (from ref. 68).*

Butler and Donald [69] in their study of deformation of thin spherulitic films of polyethylene by optical and transmission electron microscopy concluded that the spherulite boundaries are the weakest regions of spherulitic polyethylene and that higher strains are generally required to deform the interiors of spherulites.

More recently, Matsuo and Xu [70] studied the deformation mechanism of polyethylene spherulites by X-ray diffraction techniques and small angle light scattering under H_V polarisation conditions. The authors confirmed that a two step model of deformation which includes (1) instantaneous deformation of the spherulite associated with orientation of lamellar axis and rotation of lamella around the lamellar axis (untwisting of the lamellae associated with the deformation from a spherical to an ellipsoid structure) and (2) orientation of crystallites within the oriented lamella is associated with the deformation of spherulites.

In summary, the deformation of spherulitic polyethylene takes place in two steps, with (a) deformation of the spherical structure into a ellipsoid structure which involves untwisting and orientation of the lamellar axis and (b) orientation of the crystallites within the oriented spherulites.

I.3. The tie-molecules.

We have seen in the preceding section that the tie-molecules are a major key to the understanding of the deformation behaviour in polymers. There are two types of effective tie-molecules. The conventional tie-molecule connects two adjacent crystals with the amorphous region in between (figure I. 13.a). If two molecules from adjacent crystals join together in a strong random entanglement (figure I. 13.b-c), then it may also function as a tie-molecule.

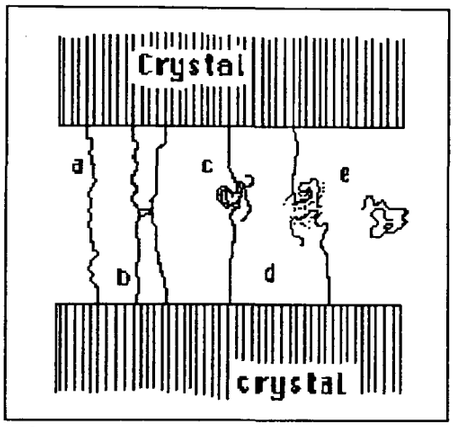

Figure I. 15: *Various molecular arrangements: (a) conventional tie-molecule (taut tie-molecule); (b) effective tie-molecule produced by an interloop; (c) effective tie-molecule produced by a strong entanglement; (d) weakly entangled molecules; (e) molecule with no attachment to a crystal.*

The existence of tie-molecules was demonstrated in a microscopic study by Keith et al [71]. The central role of tie-molecules in the deformation behaviour has been proposed by Backman and De Vries [72], Gibson et al [73], Brown and Ward [74], Lustiger and Markham [56], and Lu et al [75]. Although everyone agrees that the number of tie-molecules plays an important role in the interpretation of mechanical properties of crystalline polymers, no simple and direct methods have been proposed to measure them. This is certainly because tie-molecules are located in the amorphous region of the polymer. In the following section, a brief review of the techniques suitable for this work is given.

Fischer et al [76] showed that neutron scattering data in the small and intermediate angle regions can be used to estimate the average number of tie-molecules. They based their model on the fact that the distances between stems centres within one cluster of stems located in one lamella are much smaller than the distances between stem centres belonging to different lamellae (i.e. stems linked by a tie-molecule). This inhomogeneity

is reflected in the form factor P(q). Thus, in the intermediate q range, the cluster of stems will scatter as independent units, and only at very small q will the interconnection of clusters (tie-molecules) be reflected in the scattering curve. Finally by extrapolation from the intermediate q range, an average number of stems in the clusters can be determined, and therefore, the number of tie-molecules can be evaluated.

By measuring noncrystalline orientation, Lustiger et al [77] have demonstrated that infrared dichroism can be used to determine the relative tie-molecule concentration. They assumed that the principal component in the amorphous region which remains oriented after the end of application of stress are tie-molecules. The main problem is to separate amorphous from crystalline orientation, which is not straightforward. In order to measure amorphous orientation in polyethylene, all the samples used in their study were chlorinated, because the halogen molecules would react preferentially with the amorphous region, and not with the crystalline part, and so would be preferentially localised in the amorphous region. Thus, any dichroism in the region of the C-Cl stretching (611 cm^{-1}) would be due to amorphous orientation (i.e. tie-molecules) and consequently a measure of the tie-molecule concentration is possible.

Huang and Brown [52], in their study of slow crack growth in polyethylene, presented an equation for calculating the number of tie-molecules. This equation is based on the values of the molecular weight and the long spacing which are both easy to obtain. By assuming that a tie-molecule will be formed if the end-to-end distance of the random coil in the melt is greater than the distance between adjoining lamellar crystals, it is possible to calculate the probability for forming a tie-molecule and so to obtain the tie-molecule density.

Because the frequency of a band in a Raman spectrum of a polymer depends on the exact shape of the molecule and its environment, the effect of deformation on the Raman spectrum is a shift in wave number of this band. By using this property, Prasad and Grubb [78] managed to make a direct observation of taut tie-molecules in polyethylene fibres using the C-C asymmetric stretching vibration at 1063 cm^{-1}.

Finally, all the reported methods imply some structural model and the results obtained will depend on the validity of the assumptions made. Thus, in the study of the role of the tie-molecule during deformation, a clear understanding of the structure is necessary.

[1] R.J. Young, P.A. Lovell, *Introduction to Polymers*, Chapman and Hall, 2nd Edition, 1991.
[2] G. Ungar and A. Keller, *J. Pol. Sci. part B, Poly. Phys.*, **25**, 2409 (1987).
[3] A. Keller, *Phil. Mag.* **2**, 1171 (1957).
[4] D.M. Sadler, *Faraday Discuss. Chem. Soc.*, **69**, 91 (1980).
[5] M.I. Bank and S. Krimm, *J.Pol.Sci. part A.2*, **7**, 1785-1809 (1969).
[6] T.C. Cheam and S. Krimm, *J. Poly. Sci: Poly. Phys. Ed*, **19**, 423-447 (1982).
[7] D. M.Sadler and A. Keller, *Polymer*, **17**, 37 (1976).
[8] D.M. Sadler and A. Keller, *Macromolecules*, **10**(5), 1129 (1977).
[9] D.M. Sadler and A. Keller, *Science*, **203**, 263 (1979).
[10] S.J. Spells and D.M. Sadler, *Polymer*, **25**, 739 (1984).
[11] S.J. Spells, A. Keller and D.M. Sadler, *Polymer*, **25**, 749 (1984).
[12] P. Sonntag, C.M. Care, S.J. Spells and I. Halliday, *J. Chem. Soc. Faraday. Trans.*, **91**(16), 2593-2599 (1995).
[13] J. Schelten, G.D. Wignall and D.G.H. Ballard, *Polymer*, **15**, 682 (1974).
[14] J. Schelten, D.G.H. Ballard, G.D. Wignall, G. Longman and W. Schmatz, *Polymer*, **17**, 751 (1976).
[15] J.H.C. Ching and S. Krimm, *J. App. Phy*, **46**(10), 4181 (1975).
[16] D.Y. Yoon and P.J. Flory, *Polymer*, **18**, 509 (1977).
[17] M. Dettenmaier, E.W. Fisher and M. Stamm, *Colloid. Poly. Sci.*, **258**, 343 (1980).
[18] M. Stamm,E.W. Fischer, M. Dettenmaier, P. Convert, (1979), *Disc. Faraday Soc.*, **68**, 263.
[19] D.M. Sadler and R. Harris, *J. Poly. Sci: Poly. Phy. Ed*, **20**, 561-578 (1982).
[20] C.M. Guttman, E.A. DiMarzio and J.D. Hoffman, *Polymer*, **22**, 597 (1981).
[21] X. Jing and S. Krimm, J. Poly. *Sci: Poly. Lett. Ed*, **21**, 123-130 (1983).
[22] S.J. Spells, *Polymer Communications*, **25**, 1921 (1984).
[23] D.R. Norton, A. Keller, *J. Mater. Sci.*, **19**, 447, (1984).
[24] G.H. Edwards, *Brit. Polymer J.*, **18**, 88 (1986).
[25] S.R. Hu, T. Kyu, R.S. Stein, *J. Polym .Sci: Polym. Phys. Ed.*, **25**, 71 (1987).
[26] J.M. Rego López, U.W. Gedde, *Polymer*, **30**, 22 (1989).
[27] M.T. Conde Braña, J.I. Iragorri Sainz, B. Terselius, U.W. Gedde, *Polymer*, **30**, 410 (1989).
[28] M.J. Hill, P.J. Barham, A. Keller, C.C.A. Rosney, *Polymer*, **32**, 8, 1384 (1991).
[29] M.J. Hill, P.J. Barham, A. Keller, *Polymer*, **33**, 12, 2530 (1992).
[30] C.C. Puig, J.A. Odell, M.J. Hill, P.J. Barham, M.J. Folkes, *Polymer*, **35**, 11, 2452 (1994).
[31] K. Tashiro, R.S. Stein, S. L. Hsu, *Macromolecules*, **25**, 1801 (1992).
[32] G.D. Wignall, J.D. Londono, J.S. Lin, R.G. Alamo, M.J. Galante, L. Mandelkern, *Macromolecules*, **28**, 3156 (1995).
[33] R.G. Alamo, W.W. Graessley, R. Krishnamoorti, D.J. Lohse, J.D. Londono, L. Mandelkern, F.C Stehling, G.D. Wignall, *Macromulecules*, **30**, 561 (1997).
[34] A. Peterlin, *Journal of Materials Science*, **6**, 409-508 (1971).
[35] P.B. Bowden and R.J. Young, *Journal of Materials Science*, **9**, 2034 (1976).
[36] J. Petermann, W. Kluge, H. Gleiter, *J. Polym .Sci: Polym. Phys. Ed*, **17**, 1043 (1979).
[37] D.M. Sadler and P.J. Barham, *J. Poly. Sci: Poly. Phys. Ed*, **21**, 309 (1983).
[38] D.M. Sadler and P.J. Barham, *Polymer*, **31**, 36 (1990).
[39] D.M. Sadler and P.J. Barham, *Polymer*, **31**, 43 (1990).

[40] D.M. Sadler and P.J. Barham, *Polymer*, **31**, 46 (1990).
[41] G.D. Wignall and W. Wu, *Polymer Communications*, **24**, 354 (1983).
[42] W. Wu and G.D. Wignall, *Polymer*, **26**, 661 (1985).
[43] W. Wu, G.D. Wignall and L. Mandelkern, *Polymer*, **26**, 661 (1985).
[44] E.U. Okoroafor and S.J. Spells, *Polymer*, **35**, 4578 (1994).
[45] S.J. Spells and E.U. Okoroafor, *Polymer*, **35**, 4590 (1994).
[46] J.C. Rodríguez-Cabello, J. Martín-Monge, J.M. Lagarón, J.M. Pastor, *Macromol. Chem. Phys.*, **199**, 2767 (1998).
[47] J. Lagarón, N.M. Dixon, W. Reed, J.M. Pastor, B.J. Kip, *Polymer*, **40**, 2569 (1999).
[48] J. Lagarón, S. López-Quintana, J.C. Rodríguez-Cabello, J.C. Merino, J.M. Pastor, *Polymer*, **41**, 2999 (2000).
[49] G. Capaccio and I.M. Ward, *J. Polym. Phy. Sci.:Polym. Phy. Ed*, **22,** 475 (1984).
[50] X. Lu, X. Wang and N. Brown, *J. Polym. Sci.: Polym. Phys. Ed*, **29**,129 (1991).
[51] Y.-L. Huang and N. Brown, *J. Polym. Sci.: Polym. Phys. Ed*, **29**, 129 (1991).
[52] R.A. Bubeck and H.M. Baker, *Polymer*, **23**, 1680 (1982).
[53] R.G. Alamo, B.D. Viers, and L. Mandelkern, *Macromolecules*, **26**, 5740 (1993).
[54] C. France, P.J. Hendra, W.F. Maddams and H.A. Willis, *Polymer*, **28**, 710 (1987).
[55] J.P. Gorce, *PhD thesis*, Sheffield Hallam University, Sheffield, 2000.
[56] A. Lustiger and R.L. Markham, *Polymer*, **24**, 1647 (1983).
[57] Z. Zhou, N. Brown, *Polymer*, **35**, 3619 (1994).
[58] R. Hiss, S. Hobeika, C. Lynn, G. Strobl, *Macromolecules*, **32**, 4390 (1999).
[59] P.B. Bowden, R.J. Young, *J. Mater. Sci.*, **9**, 2034 (1974).
[60] L. Lin, A.S. Aragon, *J. Mater. Sci.*, **29**, 3619 (1994).
[61] Z.W. Wilchinsky, *Polymer*, **5**, 271 (1964).
[62] K. Sasagury, S. Hoshino, R. S. Stein, *J. Appl. Phys.*, **35**, 47 (1964).
[63] K. Sasagury, R. Yamada, R.S. Stein, *J. Appl. Phys.*, **35**, 3188 (1964).
[64] S. Clough, J.J. Van Aartsen, R.S. Stein, *J. Appl. Phys.*, **36**, 10, 3072 (1965).
[65] J.J. Van Aartsen, R.S. Stein, *J. Polymer Sci.: A-2*, **9**, 295 (1971).
[66] I.L. Hay, A. Keller, *J. Matter. Sci.*, **2**, 538 (1967).
[67] T. Oda, S. Nomura, H. Hawai, *J. Polymer Sci: A*, **3**, 1993 (1965).
[68] S. Nomura, A. Asanuma, S. Suehiro, H. Kawai, *J. Polymer Sci: A-2*, **9**, 1991 (1971).
[69] M.F. Butler, A.M. Donald, *J. Mater. Sci.*, **32**, 3675 (1997).
[70] M. Matsuo, C. Xu, *Polymer*, **38**, 17, 4311 (1997).
[71] H.D. Keith, F.J. Padden, Jr., and R.G. Vadimsky, *J. Mater. Sci*, **4**, 267 (1966).
[72] D.K. Backman and K.L .De Vries, *J. Polym. Sci*, A1, **7**, 2125 (1969).
[73] A.G. Gibson, S.A. Jaward, G.R. Davies, and I.M. Ward, *Polymer*, **23**, 349 (1982).
[74] N. Brown and I.M. Ward, *J. Mater. Sci.*, **18**, 1405 (1983).
[75] X. Lu, X. Wang, and N. Brown, *J. Mater. Sci*, **23**, 643 (1988).
[76] E.W. Fischer, K. Kahn, J. Kugler, U. Strutk and R. Ban, *J. Polym. Sci, Phys. Ed.*, **22**, 1491, (1984).
[77] A. Lustiger and N.Ishikawa, *J. Polym.Sci, B, Polym. Phys.*, **29**, 1047 (1991).
[78] K. Prasad and D.T. Grubb, *J. Polym. Sci, B, Polym. Phys.*, **27**, 381 (1989).

Chapter two:

Neutron Scattering Technique.

II.1. Introduction.

Neutron Scattering in the study of polymers presents two main advantages in comparison to other techniques, such as light and X-ray scattering.

Neutrons used to study condensed matter are obtained by moderating the very highly energetic neutrons produced by nuclear reactions. The kinetic energy of these thermal neutrons is of the order of k_BT, where k_B is the Boltzmann constant and T the moderator temperature (typically about 300K). Taking account the wave nature of the neutron , one can determine the wavelength λ to be of the order of several Ångstroms. This distance is appropriate to explore the distance scale from a few repeat segments to the dimension of whole polymeric molecules.

Also, because neutrons are scattered by nuclei and not by electrons (as in the case of X-rays), there is a large difference in the neutron scattering from hydrogen atoms (^1H) and deuterium atoms (^2H). Thus, the use of the neutron technique for studying polymers has relied on this difference in order to highlight molecules. Labelled molecules can be studied in a neutron experiment surrounded by other molecules, within the characteristic structure of a particular sample (i.e. almost in their 'natural' state).

In this chapter, we only give a general background on the Neutron Scattering technique. Detailed description can be found elsewhere [1,2,3].

II.2. Theory of Neutron Scattering.

II.2.1. Principles: Interactions between neutrons and matter.

We consider a simple scattering experiment schematically shown in figure II.1. The incident beam of neutrons, characterised by a wave vector $\mathbf{k_0}$ ($\mathbf{k_0} = \frac{2\pi}{\lambda}\mathbf{u_0}$, where $\mathbf{u_0}$ is a unit vector in the direction of propagation) and a uniform flux ϕ (neutrons crossing unit area per unit time) falls on a sample of transmission T having N identical atoms in the beam. Some neutrons will be scattered with a wave vector $\mathbf{k}$ and can be measured by a detector which subtends a solid angle $\Delta\Omega$ and has efficiency η.

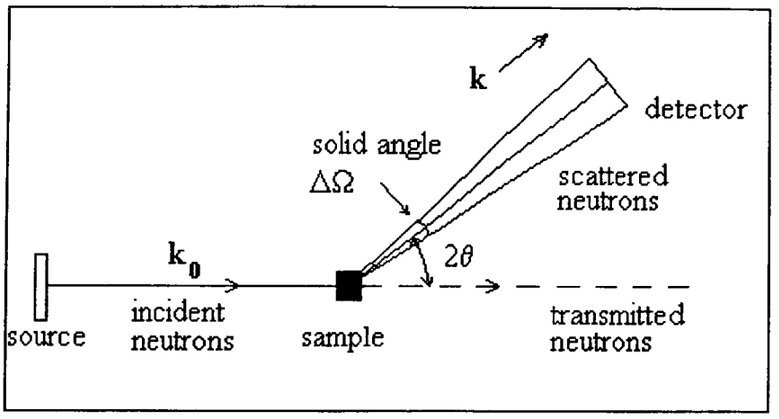

Figure II.1: *Schematic diagram of a neutron scattering experiment.*

The coherent scattering from neighbouring nuclei will give interference effects, and this is how, in principle, structural information is available. There will be a phase difference of $(\mathbf{k}-\mathbf{k_0}).\mathbf{r_{ij}}$ for the scattering between two nuclei separated in space by $\mathbf{r_{ij}}$. If we consider only elastic scattering, as we will do in this thesis, $\mathbf{k_0}$ and $\mathbf{k}$ are equal in magnitude (where $k = 2\pi/\lambda$). The scattering angle 2θ is commonly expressed in terms of the momentum transfer $\mathbf{q} = \mathbf{k}-\mathbf{k_0}$ and hence $q = (4\pi/\lambda)\sin\theta$.

The measured scattered intensity is then proportional to the quantities defined above, and the constant of proportionality is called the differential scattering cross section. The intensity is defined by:

$$I(\mathbf{q}) = \Phi(\Delta\Omega)TN\eta\frac{d\sigma}{d\Omega} \qquad (II.1)$$

The quantity $\Phi(\Delta\Omega)N\eta\frac{d\sigma}{d\Omega}$ corresponds to the total number of neutrons scattered per second into the solid angle $\Delta\Omega$, regardless of their energies. In the case where the atoms

in the sample are both non-interacting and identical, the differential cross section is just a constant:

$$\frac{d\sigma}{d\Omega} = b^2 \tag{II.2}$$

The quantity b is defined as the coherent scattering length and is a property only of the nucleus of the scattering atom (its atomic number Z and atomic weight A). Since the scattering length b is the amplitude of the scattered wave relative to that of the incident wave, b^2 is then the probability that a neutron will be scattered per nucleus, per incident neutron, per unit solid angle (solid angle is expressed in steradians).

II.2.2. Scattering by a system of N nuclei.

In the case of a system of N nuclei, equation II.2 can be generalised as:

$$\frac{\partial\sigma}{\partial\Omega} = \sum_{j,k}^{N}\left\langle b_j b_k \exp[i\mathbf{q}\cdot(\mathbf{r_k}-\mathbf{r_j})]\right\rangle$$

$$= \sum_{k=1}^{N}\left\langle b_k{}^2\right\rangle + \sum_{j\neq k}^{N}\left\langle b_j b_k \exp[i\mathbf{q}\cdot(\mathbf{r_k}-\mathbf{r_j})]\right\rangle \tag{II.3}$$

The first part of equation II.3 correspond to N times the average value $\overline{b^2}$. Because b_j and b_k are not correlated with the positions of the atoms, $b_j b_k$ can be written as $\overline{b_j b_k} = \bar{b}_j \bar{b}_k = \bar{b}^2$.

Thus equation II.3 becomes:

$$\frac{\partial\sigma}{\partial\Omega} = N\overline{b^2} + \bar{b}^2 \sum_{j\neq k}^{N}\left\langle \exp[i\mathbf{q}\cdot(\mathbf{r_k}-\mathbf{r_j})]\right\rangle \tag{II.4}$$

by introducing the value $\overline{\Delta b^2} = \overline{b^2} - \bar{b}^2$,

$$\frac{\partial\sigma}{\partial\Omega} = N\overline{\Delta b^2} + \bar{b}^2 \sum_{j,k}^{N}\left\langle \exp[i\mathbf{q}\cdot(\mathbf{r_k}-\mathbf{r_j})]\right\rangle \tag{II.5}$$

$\overline{b^2}$ is the average of the square of the scattering lengths made over the N scattering units. The first term in equation II.5 is the incoherent scattering which depends only on the fluctuations of the length b, and therefore no structural information on the scattering species can be obtained. The second term contains information about the relative positions of the scattering units in the sample. This term is named the coherent scattering and can be written as:

$$\left.\frac{\partial\sigma}{\partial\Omega}\right|_{coh} = \bar{b}^2 \sum_{j,k}^{N} \left\langle \exp[i\mathbf{q}\cdot(\mathbf{r}_k - \mathbf{r}_j)] \right\rangle \qquad \text{(II.6)}$$

The coherent scattering is in fact the Fourier Transform of the scattering length correlation in the sample, and describes the interference effect between waves scattered from different nuclei in the sample.

II.2.3. Scattering by a mixture of two different nuclei.

If we consider a mixture of two components with N_1 molecules of scattering length b_1 and N_2 of scattering length b_2 [3], the coherent scattering is:

$$\left.\frac{\partial\sigma}{\partial\Omega}\right|_{coh} = b_1^2 S_{11}(\mathbf{q}) + b_2^2 S_{22}(\mathbf{q}) + b_1 b_2 S_{12}(\mathbf{q}) + b_2 b_1 S_{21}(\mathbf{q}) \qquad \text{(II. 7)}$$

where

$$S_{km}(\mathbf{q}) = \sum_{i=1}^{N_k}\sum_{j=1}^{N_m} \left\langle \exp[-i\mathbf{q}\cdot(\mathbf{r}_i - \mathbf{r}_j)] \right\rangle, \; k, m = 1, 2 \qquad \text{(II. 8)}$$

In the case of polymeric systems, the density fluctuations are negligible, the system is incompressible [1] and:

$$S_{11}(\mathbf{q}) + S_{21}(\mathbf{q}) = 0 \qquad \text{(II. 9a)}$$

$$S_{12}(\mathbf{q}) + S_{22}(\mathbf{q}) = 0 \qquad \text{(II. 9b)}$$

Since $S_{12} = S_{21}$, equation II.7 can be simplified to give,

$$\left.\frac{\partial\sigma}{\partial\Omega}\right|_{coh} = (b_1 - b_2)^2 S_{11}(\mathbf{q}) = (b_2 - b_1)^2 S_{22}(\mathbf{q}) = -(b_1 - b_2) S_{12}(\mathbf{q}) \qquad \text{(II. 10)}$$

II.2.4. Generalisation to a mixture of p+1 species.

These results can be generalised to a system consisting of p+1 different species i ($0 \leq i \leq p$) of number density of segments $n_i(\mathbf{r})$. By assuming that the segments all have the same volume v_0 [1], we can generalise:

$$\left.\frac{\partial\sigma}{\partial\Omega}\right|_{coh} = \sum_{i=1}^{p} (b_1 - b_0)^2 S_{ii}(\mathbf{q}) + 2\sum_{i<j} (b_i - b_0)(b_j - b_0) S_{ij}(\mathbf{q}) \qquad \text{(II. 11)}$$

with the hypothesis of incompressibility, i.e.:

$$\sum_{i=0}^{p} S_{ki}(q) = 0 \qquad \text{(II. 12)}$$

II.2.5. Decomposition of S(**q**) into intra- and intermolecular interference.

If we define a scattering unit with 2 indices, one of which is characteristic of the chain p or q and ranges from 1 to N_k, the second is characteristic of the position of the monomer on the chain, j and m, and goes from 1 to z_k, we can write equation II.8 as:

$$S_{kk}(\mathbf{q}) = \sum_{p=1}^{N_k}\sum_{q=1}^{N_k}\sum_{j=1}^{z_k}\sum_{m=1}^{z_k}\left\langle \exp[-i\mathbf{q}\cdot(\mathbf{r}_{p,j} - \mathbf{r}_{q,m})]\right\rangle \qquad \text{(II. 13)}$$

We extract the terms corresponding to the same molecules (p = q) and the terms corresponding to two different molecules (p ≠ q).

$$S_{kk}(q) = N_k \sum_{j_1=1}^{z_k}\sum_{m_1=1}^{z_k}\left\langle \exp[-i\mathbf{q}\cdot(\mathbf{r}_{j_1} - \mathbf{r}_{m_1})]\right\rangle + N_k^2 \sum_{j_1=1}^{z_k}\sum_{m_2=1}^{z_k}\left\langle \exp[-i\mathbf{q}\cdot(\mathbf{r}_{j_1} - \mathbf{r}_{m_2})]\right\rangle \qquad \text{(II. 14)}$$

or

$$S_{kk}(q) = N_k z_k^2 P_k(q) + N_k^2 z_k^2 Q_{kk}(q) \qquad \text{(II. 15)}$$

and similarly, we can define

$$S_{nk}(q) = N_n N_k z_n z_k Q_{nk}(q) \qquad \text{(II. 16)}$$

where

$$P_k(q) = \frac{1}{z_k^2}\sum_{j_1=1}^{z_k}\sum_{m_1=1}^{z_k}\left\langle \exp[-i\mathbf{q}\cdot(\mathbf{r}_{j_1} - \mathbf{r}_{m_1})]\right\rangle \qquad \text{(II. 17)}$$

$$Q_{nk}(q) = \frac{1}{z_n z_k}\sum_{j_1}^{z_n}\sum_{m_2}^{z_k}\left\langle \exp[-i\mathbf{q}\cdot(\mathbf{r}_{j_1} - \mathbf{r}_{m_2})]\right\rangle \qquad \text{(II. 18)}$$

$P_k(\mathbf{q})$ and $Q_{nk}(\mathbf{q})$ are normalised so as to go to unity at q=0. The term $P_k(\mathbf{q})$ depends only on the size and shape of the polymer, and is named the form factor of the molecule.

I.3. Application: Scattering from isotopic mixtures of polymer systems.

We consider a mixture of N chains of which xN are deuterated and (1-x)N are protonated (x is the volume fraction of deuterated chains) and z is the degree of polymerisation. If we assume that the two polymers are identical and differ only by their coherent scattering length b_H and b_D and also that the volumes of the scattering units are identical, we can write

$$\left.\frac{\partial\sigma}{\partial\Omega}\right|_{coh} = (b_D - b_H)^2 S_{DD}(\mathbf{q}) = (b_H - b_D)^2 S_{HH}(\mathbf{q}) = -(b_H - b_D) S_{HD}(\mathbf{q}) \quad \text{(II. 19)}$$

Remembering that $z_D=z_H=z$ and thus $P_D=P_H=P$ and $Q_{DD}=Q_{HD}=Q$, we can express S_{DD}, S_{HH} and S_{HD} in terms of P(q) and Q(q) to obtain:

$$\begin{aligned} xNz^2P(q) + x^2N^2z^2Q(q) &= (1-x)Nz^2P(q) + (1-x)^2N^2z^2Q(q) \\ &= -x(1-x)N^2z^2Q(q) \end{aligned} \quad \text{(II. 20)}$$

Using these equalities it can be shown [1] that

$$Nz^2P(q) + N^2z^2Q(q) = 0 \quad \text{(II. 21)}$$

or

$$NQ(q) = -P(q) \quad \text{(II. 22)}$$

Using this value of Q(q) in any of the three relationships (II.20) gives

$$\left.\frac{\partial\sigma}{\partial\Omega}\right|_{coh} = (b_D - b_H)^2 x(1-x)Nz^2P(\mathbf{q}) \quad \text{(II. 23)}$$

The quantity $zP(\mathbf{q})$ is known as the normalised intensity $I(\mathbf{q})$.

II.4. Data processing.

II.4.1. Data reduction.

In order to obtain the derived information from the neutron experiments, the raw data must be reduced in the way reported below:

- Background subtraction: during the measurements, the detector records neutrons not originating in the incident beam and not having passed through the sample. A run with a cadmium (neutron absorber) sample allows us to determine this unwanted noise and also the contribution of the electronic background. The first step of the

data processing is to subtract both of them from the sample runs and background runs. This being done, subtraction must be done of the background (the empty cell from the run sample).

- Correction for detector efficiency: the terms ϕ, $\Delta\Omega$, η and N in equation II.1 are constant for a series of measurements. In order to be able to correct for detector efficiency, it is necessary to use a substance that scatters entirely incoherently in the q range of the experiment (i.e. there must be no angular dependence of the scattering from such a substance). Common standards that are used are water or vanadium. The standard we used was a pure protonated polyethylene (the H-blank).
- Blank subtractions: all the equations derived in the previous sections assumed that the incoherent scattering has been subtracted. For a dilute mixture of a deuterated polymer in a hydrogenous matrix, the incoherent scattering is almost entirely due to that from the protonated matrix. In this case, the scattering from a 100% hydrogenous sample can be subtracted with virtually no error because of the very small amount of incoherent scattering from the deuterium.

If there are no specific interactions between protonated and the deuterated species the reduced scattering intensity can be split into two terms (equation II.15). The first of these terms is proportional to the scattering contrast and contains the information on the single chain form factor P(**q**), which is the term of interest. The other term is related to the Fourier transform of the density fluctuations, which can be determined from the completely deuterated sample.

Thus, for isotopic labelling of molecules, a measurement of I(**q**) requires the recording of count rate versus scattering angle for:

- the isotope mixture,
- equivalent polymer samples of one pure isotope (the H- and D-blanks),
- the empty specimen container,
- the container with a neutron absorbing piece of cadmium in place of the specimen,
- an isotropic scatterer (we used the H-blank).

II.4.2. Normalisation of the scattering intensity.

After subtraction of the incoherent scattering (as explained above from equation II.1), the scattering intensity can be written as:

$$I(\mathbf{q}) = \Phi_0(\Delta\Omega)TN_D\eta\left.\frac{d\sigma}{d\Omega}\right|_{coh} \qquad \text{(II. 24)}$$

where Φ_0 is the incident neutron intensity on the sample (i.e. the incident flux), T the transmission, η the detector efficiency, $\Delta\Omega$ the solid angle subtended by the detector elements at the sample, N_D the number of deuterated monomers and $\left.\frac{d\sigma}{d\Omega}\right|_{coh}$ the coherent differential scattering cross section for one deuterated monomer.

As we have seen in the above section, in order to be able to correct for the detector efficiency, it is necessary to use a substance that scatters entirely incoherently in the q range of the experiment. It is a good approximation to say that this can be achieved by using a purely protonated sample, for example the H-blank.

The scattering from the blank can be written as:

$$I_H(\mathbf{q}) = \Phi_0(\Delta\Omega)T_H N_H \eta\frac{\sigma_H}{4\pi} \qquad \text{(II. 25)}$$

where N_H is the number of protonated monomers and σ_H the total cross section of the protonated monomer.

The ratio of the two intensities gives the coherent differential cross section for the deuterated monomer:

$$\left.\frac{d\sigma}{d\Omega}\right|_{coh} = \frac{\sigma_H}{4\pi}\frac{N_H}{N_D}\frac{T_H}{T}\frac{I(\mathbf{q})}{I_H(\mathbf{q})} \qquad \text{(II. 26)}$$

Assuming the volume fraction of the deuterated chain is less than 1, we have seen in section II.3 that for a mixture of isotopic polymer, the differential cross section (equation II.23) is given by:

$$\left.\frac{\partial\sigma}{\partial\Omega}\right|_{coh} = \left(b_D - b_H\right)^2 xNz^2P(\mathbf{q}) \qquad \text{(II. 27)}$$

Thus by combining equations II.26 and II.27 and noticing that $xN = N_D$, the normalised intensity $zP(\mathbf{q})$ is:

$$zP(q) = \frac{\sigma_H}{4\pi}\frac{N_H}{zN_D}\frac{T_H}{T}\frac{1}{(b_D - b_H)^2}\frac{I(q)}{I_H(q)} \qquad \text{(II. 28)}$$

where:

$$N_H = \frac{m_H}{M_H}N_A$$
$$zN_D = nx\frac{m}{M_D}N_A \qquad \text{(II. 29)}$$

m and m_H are the masses of the sample and H-blank, N_A is Avogadro's number, M_D and M_H the molar masses of the deuterated and protonated monomers respectively and n is the number of hydrogen or deuterium atoms per monomer. zN_D is the number of deuterium atoms in the whole sample.

An interesting point is that the molecular weight of the deuterated chain is given by:

$$M_{W_D} = \frac{zM_D}{n} \qquad \text{(II. 30)}$$

and finally, the normalised intensity for an isotopic mixture is:

$$zP(q) = \frac{\sigma_H}{4\pi}\frac{M_D}{M_H}\frac{T_H}{T}\frac{1}{nx(b_D - b_H)^2}\frac{m_H}{m}\frac{I(q)}{I_H(q)} \qquad \text{(II. 31)}$$

II.5. Data analysis.

II.5.1. The different types of neutron scattering experiment.

- Small-angle (SANS), $q < 0.1$ Å^{-1}: this is the region over which the radius of gyration (R_g) can be determined. The zero angle extrapolated intensity, I_0, provides a check on the molecular weight.
- Intermediate-angle (IANS), $0.1 < q < 0.4$ Å^{-1}: this region gives information about the statistical arrangement of labelled stems.
- Wide-angle (WANS), $q > 0.4$ Å^{-1}: this region includes the different crystallographic peaks which start for polyethylene with the (110) peak at:

$$q = \frac{4\pi}{\lambda}\sin\theta = \frac{2\pi}{d_{110}} = 1.52 \text{ Å}^{-1}.$$

II.5.2. The behaviour at small q values.

In section II.2.5 the form factor for a system of N chains, each having z monomers, has been defined as:

$$P(q) = \frac{1}{z^2}\sum_{i=1}^{z}\sum_{j=1}^{z}\left\langle \exp\left[-i\mathbf{q}\cdot\mathbf{r}_{ij}\right]\right\rangle \qquad \text{(II. 32)}$$

where $\mathbf{r}_{ij}$ is the vector joining two scattering points of a molecule and the sum extends to its z^2 scattering vectors. The $\langle\ \rangle$ indicate that an average value has to be taken over all conformations and orientations. If we do the averaging over the orientation, we find:

$$P(q) = \frac{1}{z^2}\sum_{i=1}^{z}\sum_{j=1}^{z}\left\langle \frac{\sin qr_{ij}}{qr_{ij}}\right\rangle \qquad \text{(II. 33)}$$

where the average has to be taken over the r_{ij} distances only. This relation was first derived by Debye.

For small q, we can expand P(q) in powers of q [1]

$$P(q) = 1 - \frac{q^2}{3!z^2}\sum_{i=1}^{z}\sum_{j=1}^{z}\left\langle r_{ij}^2\right\rangle + \frac{q^4}{5!z^2}\sum_{i=1}^{z}\sum_{j=1}^{z}\left\langle r_{ij}^4\right\rangle - \ldots \qquad \text{(II. 34)}$$

One of the most important properties of small angle neutron scattering results from the fact that the second term in equation II.34 is independent of the scattering properties of the sample, and depends only on the geometry of the chain. It is named the radius of gyration [4]. The radius of gyration of a particle made of z identical elements is given by

$$\overline{R_G^2} = \frac{1}{z}\sum_{i=1}^{z}\left\langle r_i^2\right\rangle = \frac{1}{2z^2}\sum_{i=1}^{z}\sum_{j=1}^{z}\left\langle r_{ij}^2\right\rangle \qquad \text{(II. 35)}$$

where $\mathbf{r}_i$ is the vector joining the scattering point i to the centre of gravity of the molecule. Equation II.34 can be rewritten for small vector **q** as

$$P(q) \approx 1 - \frac{q^2}{3}\overline{R_G^2} \qquad \text{(II. 36)}$$

In addition, if the absolute intensity has been calculated, the molecular weight can be obtained at the limit q = 0.

By combining equations II.36 and II.31 and II.30, the behaviour of the normalised intensity at small q is given by

$$\frac{1}{I(q)} = \frac{M_D}{nM_{W_D}}\left(1 + \frac{q^2}{3}\overline{R_G^2}\right) \qquad \text{(II. 37)}$$

which is true only in the q-range defined by $q^2\overline{R_G^2} \leq 1$

The usual way of plotting the intensity in the Guinier region (i.e. $q \rightarrow 0$) is to plot the inverse of the intensity versus q^2 (A Zimm plot). As we have seen earlier, in this region the inverse of the intensity yields a straight line when plotted versus q^2. A very convenient way to obtain the radius of gyration and the molecular weight is to do a linear fit on the small angle data and so:

$$\frac{1}{I(q)} = \alpha + \beta q^2 \qquad \text{(II. 38)}$$

Thus, by combining II.37 and II.38,

$$\overline{R_G^2} = \frac{3\beta}{\alpha}$$
$$\overline{M}_w = \frac{M_D}{n\alpha} \qquad \text{(II. 39)}$$

where α is the intercept of the linear fit, β the slope, M_D the molecular weight of the deuterated monomer and n the number of deuterium atoms per monomer.

II.5.3. The case of anisotropic scattering (detector masking).

In the case where the scattering from sample is isotropic, then the intensity is radially averaged and is output as I(r) versus r, where r is the position on the detector measured from the centre of the incoming neutron beam. But, if the scattering is anisotropic, then it can no longer be radially averaged. Instead it must be analysed on a cell-by-cell basis. For deformed polymer systems, it is possible to obtain the radius of gyration parallel and/or perpendicular to the deformation by analysing only those sectors of the detector that are approximately parallel and/or perpendicular to the deformation axis (figure II.2). Thus two radii are obtained, the radius parallel (R_{Par}) and perpendicular to the deformation axis (R_{Per}). They are given by [5]:

$$\frac{I_{Par}(0)}{I_{Par}(q)} = 1 + R_{Par}{}^2 q^2$$
$$\frac{I_{Per}(0)}{I_{Per}(q)} = 1 + R_{Per}{}^2 q^2 \qquad \text{(II. 40)}$$

Other methods involving rectangular strips [6], or indeed the whole detector [7] have been developed in order to analyse small angle scattering from anisotropic system.

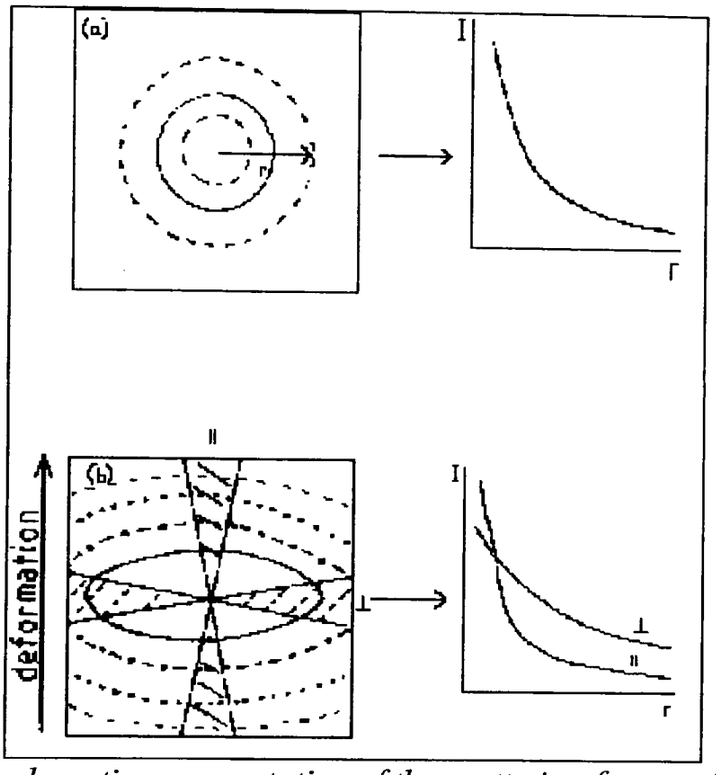

Figure II. 2: *(a) A schematic representation of the scattering from an isotropic scatterer as seen by the detector. The scattering is represented by contours of equal intensity, which are then averaged to give I(r) versus r. (b) A similar representation but for an anisotropic scatterer. The deformation axis is marked on the figure . The data are analysed from sectors of the detector, as shown by the hatched areas. The scattering can be averaged parallel and perpendicular to the deformation axis to give* $I(r)^{//}$ *and* $I(r)^{\perp}$*, respectively.*

II.5.4. Data analysis in the intermediate q region.

In the intermediate q region, the interpretations of neutron scattering are made by calculating intensities from models and comparing with measurements. There are several methods of calculation of I(q) in this region, one using the fact that for polymers of high crystallinity, calculation can be made using the 'stem' sequence in the crystals [5, 8]. Within one crystallite, the structure is in fact a convolution of a single stem with a two-dimensional structure describing the position of the stems, which is our interest (This is for a perfectly oriented mat. In melt-crystallised polyethylene, the stem orientations are fairly random but not their positions).

The normalised intensity (for q>>(stem length)$^{-1}$) for a pair of stems separated by a distance R can be written as [8]:

$$I(q) = \frac{\pi n_L}{2q}\left(1 + J_0(qR)\right)C_2(q) \qquad \text{(II. 41)}$$

where n_L is the number of hydrogen atoms per length of stem, $J_0(q, R)$ is the zeroth order Bessel function and $C_2(q)$ is the ratio of calculated intensities for a stem structure of finite diameter to that for infinitely thin stems, approximated by (for $q > R_0^{-1}$, and q>> (stem length)$^{-1}$):

$$C_2(q) = \exp(-\frac{1}{2}R_0^2 q^2) \qquad \text{(II. 42)}$$

where R_0 is the root mean square of the distance of the hydrogen atoms from the axis of the molecule. For polyethylene, $R_0 = 1.46$Å.

We can generalise equation II.41 for a group of n stems:

$$I(q) = \frac{n_L \pi}{q}\left\{\int \Gamma(R) J_0(qR)\right\}C_2(q) \qquad \text{(II. 43)}$$

where $\Gamma(R)$ is a correlation function for the stems.

Thus I(q) can be rewritten as:

$$I(q) = I_C(q)C_2(q) \qquad \text{(II. 44)}$$

where I(q) is our experimental normalised intensity, and $I_C(q)$ is the normalised intensity for the two dimensional structure (only if the array of stems is oriented; if not we have to consider a three dimensional structure) describing the position of the stems.

II.6. Instruments and neutron sources.

The neutron results presented in this thesis have been obtained on instruments at two different neutron sources.

The experiments at low draw ratio (DR<1.5) have been carried out at the ISIS pulsed neutron source (Rutherford Appleton Laboratory, Didcot) on the LOQ instrument, while for higher draw ratio (DR up to 5.0) the measurements were made at the Institute Laue - Langevin (ILL Grenoble) on the D11 instrument.

ILL uses a reactor neutron source, where the neutrons are obtained by fission of enriched ^{235}U. They are produced continuously and, after thermalisation in the surrounding moderator (H_2O), beams are emitted with a broad band of wavelengths. The

beam is then monochromated by a helical slot which selects neutrons according to velocity (normally $\Delta\lambda/\lambda$ is around 10%). In our case , the wavelength distribution was centred at $\lambda = 8.5$Å.

The detector D11 is composed of 64×64 pixels, each of which is 10 mm^2. Each array of elements contains boron in gaseous form (BF_3) so that the neutrons initiate nuclear reactions producing α particles which are then detected. The count rate (intensity) is given in arbitrary units by the total number of neutrons counted divided by the counts recorded during the measurement by a beam monitor. The specimen to detector distance can be chosen from 1.1 and 35.7 m giving an accessible q range of 5.10^{-4} to $0.3Å^{-1}$. For our experiment, the detector was set at 8m from the sample.

Instrument	LOQ (HAB)	D11
Source	Spallation	Reactor
Incident Wavelength (Å)	2.2-10.0 at 25Hz	8.5
Flux at sample (n cm^{-2} s^{-1})	2×10^5	10^6
q_{min} ($Å^{-1}$)	0.008 (0.15)	2.5×10^{-3}
q_{max} ($Å^{-1}$)	0.24 (1.4)	0.05
Detector type	^{3}He (^{6}Li and P)	BF_3
Sensitive area of the detector (cm^2)	64×64 (1500)	64×64
Pixel size (mm^2)	5.3×5.3 (6.0×6.0)	10×10
Sample/detector distance (m)	4.05 (0.50)	available: 1.1 to 35.7 used: 8

Table II.1: *Comparison of the characteristic and performances of LOQ and D11 instruments.*

On the contrary to ILL, ISIS is a spallation source, where high energy protons remove neutrons from a heavy metal target, such as depleted tantalum. They are produced by a combination of a linear accelerator followed by a proton synchrotron. This generates intense bursts of high energy protons, which are directed at the target. The process is then repeated 50 times a second. When hitting the target, each high energy proton produces many neutrons by chipping nuclear fragments from the heavy metal nucleus. The neutrons produced in this process generally have very high energies and must be slowed down to be used in condensed matter studies. This is achieved by an array of

small hydrogenous moderators around the target, where the neutrons passing through are slowed down by many collisions with the hydrogen nuclei.

LOQ is a fixed geometry detector, which covers a broad q-range (table II.1) obtained by time sorting different wavelength neutrons as they arrive on the detector (using a velocity selecting chopper and by timing the neutrons over a measured distance, usually between two monitors). LOQ uses , as does D11, a gas detector (^{3}He in this case) composed of a 64×64 arrays of elements.

At ISIS, we have used as well the LOQ high-angle bank (HAB), a scintillator detector. With this instrument, neutrons of momentum transfer up to 1.4Å^{-1} can be detected.

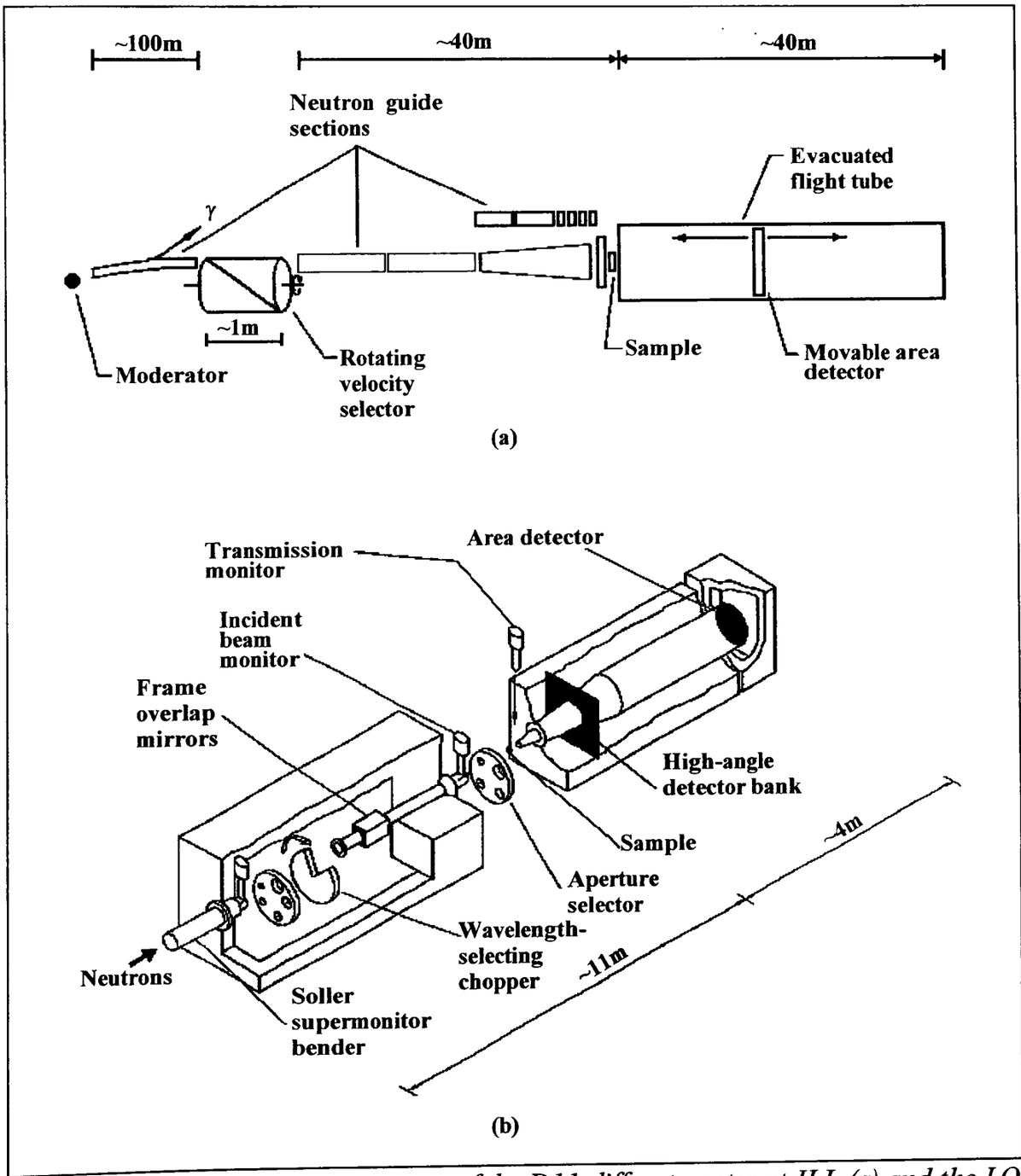

Figure II. 3: *Schematic representation of the D11 diffractometer at ILL (a) and the LOQ diffractometer at ISIS(b).*

[1] J. S. Higgins and H. C. Benoit, *Polymers and Neutron Scattering*; Clarendon Press, Oxford (1994).
[2] K. Sköld and D.L. Price, *Methods of Experimental Physics, Neutron Scattering*, Vol. 23-Part A, Chap. 1, Academic Press Inc (1986).
[3] K. Sköld and D.L. Price, *Methods of Experimental Physics, Neutron Scattering*, Vol. 23-Part C, Chap. 22, Academic Press Inc (1987).
[4] A. Guinier, *Théorie et Technique de la radiocristallographie*, Dunod, Paris(1956).
[5] D.M. Sadler, *Crystalline Polymers* , Chap 4, Ed. I. Hall, Applied Science, London (1984).
[6] D.M. Sadler and P.J. Barham, *J. Polym. Sci. Poly. Phys. Ed.*, **21**, 309 (1983).
[7] R. F. Saraf, *Macromolecule*, **22**, 675 (1989).
[8] D.M. Sadler and S.J. Spells, *Polymer*, **25**, 739 (1984).

Chapter three:

Infrared spectroscopy.

Infrared Spectroscopy is a powerful tool for the study of polymeric systems. It is not only useful for identifying the chemical structure of the polymer, but also enables the determination of molecular structure, including the structural defects present.

Certainly the most widespread use of infrared spectroscopy is for characterisation of organic compounds. This is based on the fact that vibrational frequency of particular groups of atoms in a molecule, such as C–H or C=O, may, under suitable conditions, be largely independent of the nature of adjacent groups of atoms. These typical vibrational frequencies are named group frequencies. The examination of a very wide range of low molecular weight organic compounds has led to extensive frequency/structure correlations. Therefore, by noting the presence of peaks at these typical frequencies in the infrared spectrum of an unknown compound, it is possible to identify it.

Our main goal in this thesis is to look at conformational effects, rather than this simple structural use. Therefore a secondary property of the infrared spectroscopy will be used, the fact that some infrared bands are configurationally sensitive.

In this chapter we will introduce infrared spectroscopy applied to polymers, in particular to polyethylene and describe in more detail the Mixed Crystal Infrared technique we used to monitor the molecular rearrangement of the polyethylene chains during deformation.

III.1. Origin of the infrared spectrum.

Polyatomic molecules consist of atoms bound together by chemical bonds. These bonds and the angles between them are not rigid. Thus the molecule can be considered as a set of coupled harmonic oscillators. When disturbed from its equilibrium state, each atom will vibrate at the same frequency with a superposition of a number of simple harmonic vibrations, named the normal modes. The typical frequency of these vibrations is within the infrared region of the electromagnetic spectrum (0.3 to 250 THz).

For example, let the masses of the atoms in a diatomic molecule to be m_1 and m_2 and let their separation be r. In the harmonic approximation, the potential energy V(r) of the molecule is given by

$$V(r) = V_0 + \frac{1}{2}k(r - r_0)^2 \qquad \text{(III. 1)}$$

where V_0 is a constant, k is the force constant and r_0 is the equilibrium separation of the atoms. It is easy to show that when the molecule is disturbed from equilibrium it will vibrate with simple harmonic motion of frequency ν, where:

$$\nu = \frac{1}{2\pi}\sqrt{\frac{k(m_1 + m_2)}{m_1 m_2}} \qquad \text{(III. 2)}$$

Because the energy of each normal mode is quantized, infrared radiation can be absorbed if its frequency ν is defined by:

$$\nu = \Delta E/h, \qquad \text{(III. 3)}$$

where ΔE is the energy difference between the upper and lower vibrational energy levels for a particular vibration and h is Planck's constant.

For polyatomic molecules constituted of N atoms, there are 3N-6 possible vibrations (3N-5 for linear molecules). Luckily, not all these modes of vibration can absorb infrared radiation. For a vibrational mode to be infrared active, there has to be a change in the dipole moment $\Delta\mu$ of the molecule during the vibration, i.e.:

$$\Delta\mu = q\Delta r \neq 0 \qquad \text{(III. 4)}$$

where q is the charge and Δr is the displacement of the charge.

In general the infrared activity of a normal mode is predicted using symmetry concepts (see reference [1] for more details).

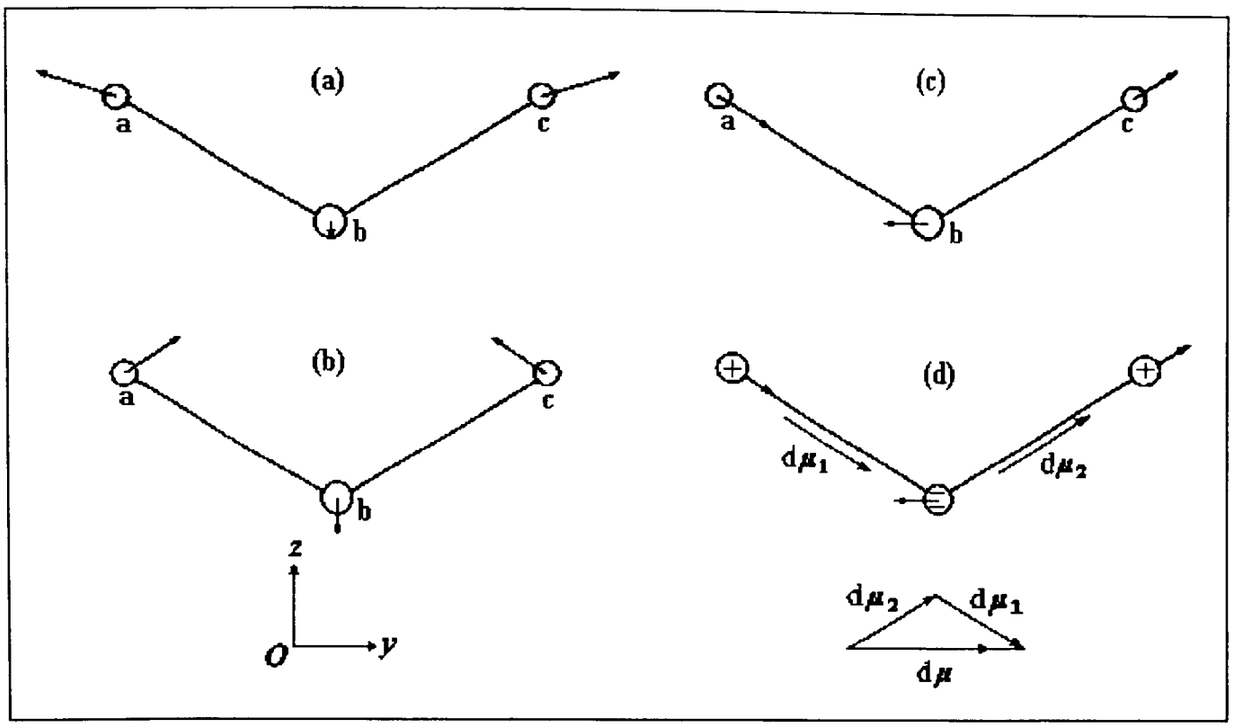

Figure III.1: *Symmetry modes of a bend triatomic molecule: (a) A_1 symmetric stretch; (b) A_1 bend; (c) B_2 antisymmetric stretch; (d) resultant change in dipole moment produced by vibration in the antisymmetric mode. The + and - represent fractional charges, not displacements.*

Figure III.1 shows the vibrational modes present in a bent triatomic molecule. The total number of modes is 3N-6 = 3. Both the symmetric stretch and bending (a, b) give rise to a change of dipole moment in the Oz direction, while for the antisymmetric stretch (c), the change occurs in the Oy direction. In the case of carbon dioxide, which is also a triatomic molecule but linear in this case, there are 3N-5 modes of vibration, namely symmetric, antisymmetric stretching and two bending as presented in figure III.2.

Because no change in the dipole moment occurs during the symmetric stretching, this mode is not infrared active; only the antisymmetric stretch will be seen in the infrared spectrum. For the bending vibrations, both give rise to a change in the dipole moment. But, because of the symmetry of the molecule, these two vibrations are identical, and therefore are degenerate. Thus only one band corresponding to the bending will be seen in the infrared spectrum. Finally, from four normal modes possible in CO_2 only two are seen in the infrared spectrum.

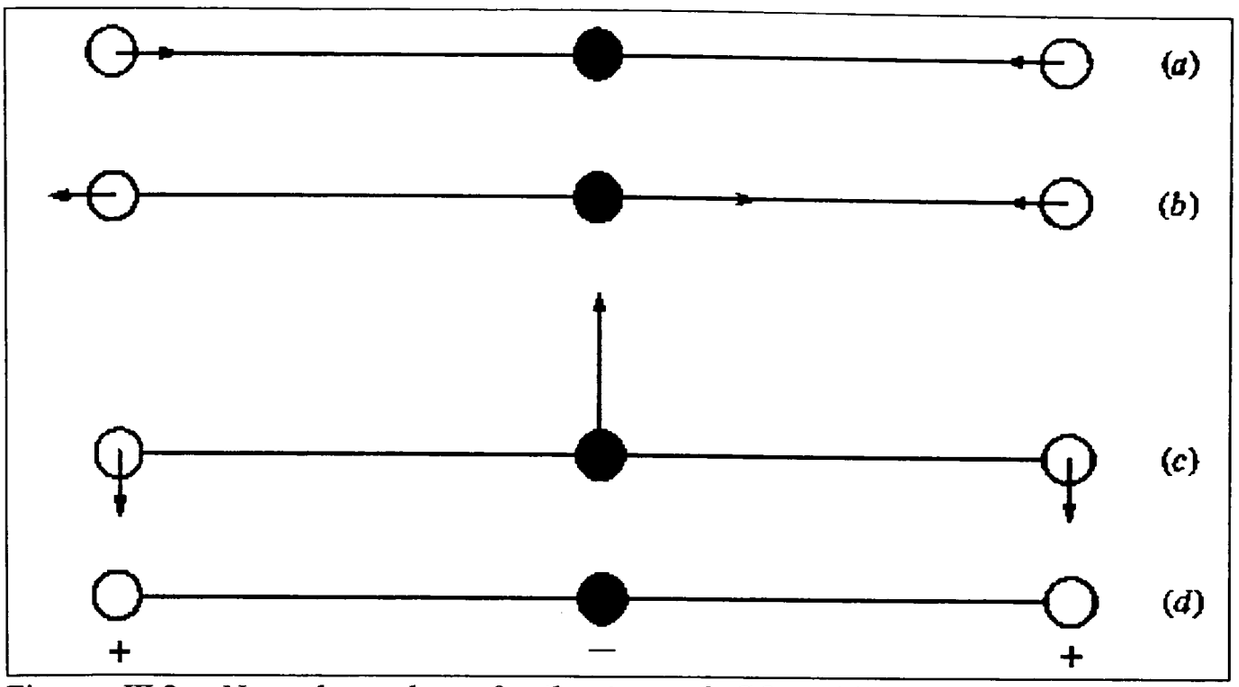

Figure III.2: *Normal modes of vibration of CO_2. (a) symmetric stretch; (b) antisymmetric stretch; (c) and (d) bend.*

III.2. Fourier Transform Infrared Spectroscopy [2].

III.2.1. Introduction.

The development of FTIR spectrometry started almost a century ago with the invention of the two-beam interferometer by Michelson and the recognition that the spectrum is in fact the Fourier Transform of the interferogram [3, 4]. But it is only with the development of the micro-computer and small gas laser in the 1970s that FTIR became the technique for measuring high quality infrared spectra and so supplanted the traditional dispersive instruments (based on a grating to disperse the infrared radiation).

FTIR spectrometers have two main advantages over dispersive instruments. Firstly there is the multiplex advantage, with the recognition by Fellgett that the interferometer allows the continuous detection of all transmitted energy simultaneously, so that the intensity falling on the detector is much greater than that for a dispersive instrument of the same optical aperture. Secondly, Jacquinot showed that a higher optical aperture can be used for a given resolution than with a dispersive spectrometer, again increasing the intensity falling on the detector. These two advantages result in a very much higher signal-to-noise ratio for a given time taken to record a spectrum. In combination with the development of the Fast Fourier Transform (FFT) algorithm by Cooley and Tuckey

in 1964 [5], these features enable us to obtain spectra of high-quality much more rapidly than with dispersive instruments.

III.2.2. The Michelson Interferometer.

As we said before, a Fourier Transform spectrometer is based on a Michelson interferometer, which divides a beam of radiation into two paths and recombines the two beams after a path difference has been introduced. Thus the detection of a signal will depend on the interference between the two beams, and so the intensity variation of the resultant beam is measured as a function of path difference by the detector.

A Michelson interferometer, as schematically represented in figure III.3 consists of 2 mutually perpendicular plane mirrors, one of which (M) can moved as described in the figure with a constant velocity v. Between the two mirrors is a beamsplitter, where a beam of radiation from an external source can be partially transmitted to the movable mirror (M) and partially reflected to the fixed one (F). Afterwards, the beams interfere and are again partially reflected and transmitted.

When the path difference, x, between the two beams is an odd integer multiple of half the wavelength λ, i.e. if $x = (n+1)\lambda/2$ with n an integer , destructive interference will occur and the measured intensity will be zero. When, however, the path difference is an integer multiple of λ, i.e. if $x = n\lambda$ with n an integer, the two beams constructively interfere to give a maximum measured intensity.

For a monochromatic source of wavenumber $\tilde{\nu}$ ($\tilde{\nu} = 1/\lambda$), the intensity measured by the detector as a function of the path difference, x, is determined by:

$$I(x) = 0.5I_0(\tilde{\nu})T(\tilde{\nu})(1+\cos 2\pi\tilde{\nu}x) \qquad \text{(III. 5)}$$

where $T(\tilde{\nu})$ is the transmittance of the sample at $\tilde{\nu}$ and $I_0(\tilde{\nu})$ is the incident intensity. The path difference x is equal to twice the mirror displacement, measured from the position where the two paths are equal, and the factor 0.5 arises from the assumption that on average, half the radiation is reflected back to the source by the beamsplitter.

We can rewrite I(x) as:

$$I(x) = 0.5I(\tilde{\nu}) + 0.5I(\tilde{\nu})\cos 2\pi\tilde{\nu}x \qquad \text{(III. 6)}$$

where the first term in equation III.6 is a constant and of no interest in spectroscopic measurement. The second term is a modulated component and is named the interferogram.

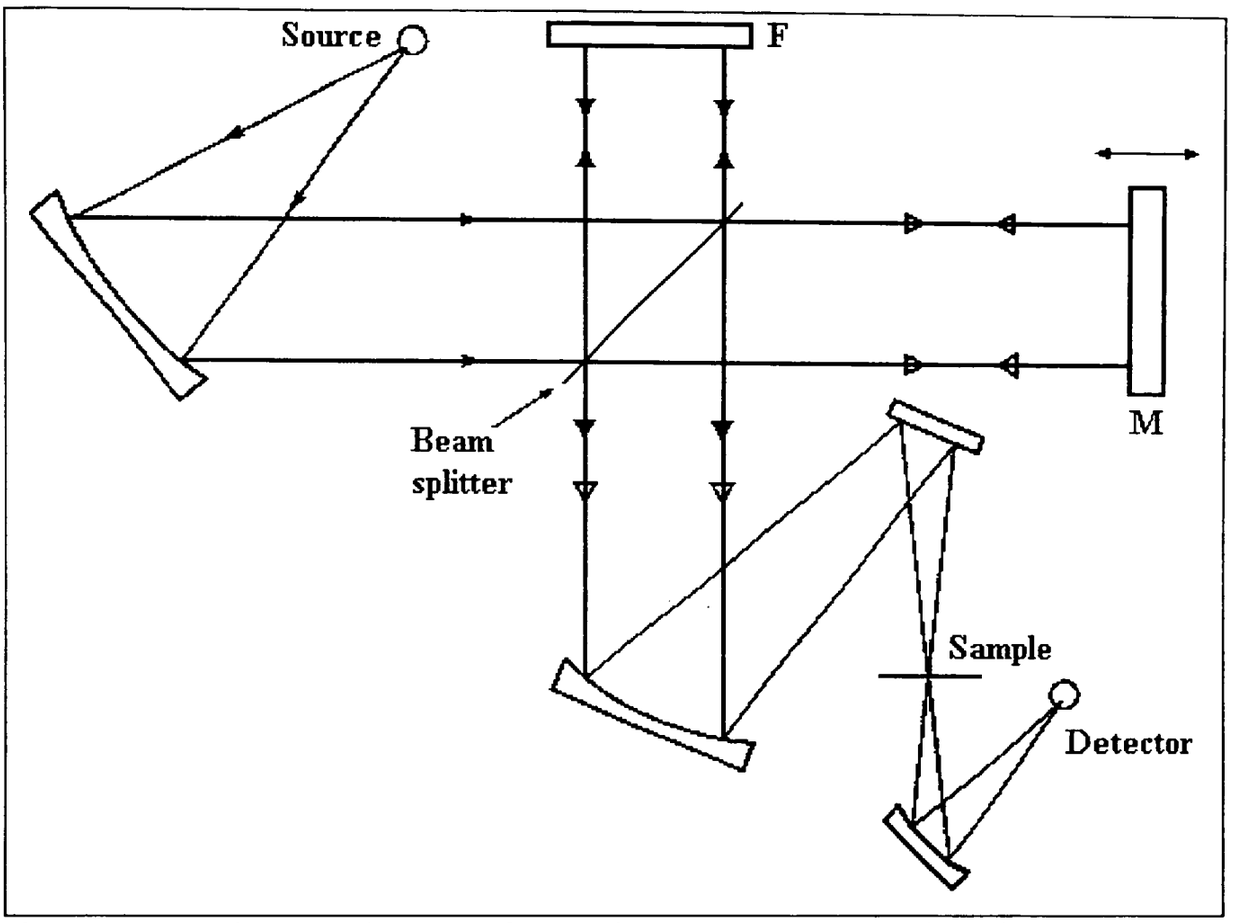

Figure III. 3: *Schematic diagram of a simple FTIR spectrometer based on a Michelson interferometer.*

In a real infrared experiment, polychromatic radiation is used, and the interferogram is the integral of the contribution from all wavenumbers in the spectrum:

$$I(x) = 0.5\int_{-\infty}^{+\infty} I(\tilde{\nu})\cos(2\pi x\tilde{\nu})d\tilde{\nu} \qquad \text{(III. 7)}$$

In practice, the amplitude of the interferogram measured is not only proportional to the intensity of the source, but also to the instrument characteristics (detector response, beamsplitter efficiency....). These factors remain constant for a given spectrometer configuration and equation III.7 can be expressed as:

$$I(x) = \int_{-\infty}^{+\infty} B(\tilde{\nu})\cos(2\pi x\tilde{\nu})d\tilde{\nu} \qquad \text{(III. 8)}$$

where $B(\tilde{\nu})$ is the intensity of the source at a wavenumber $\tilde{\nu}$ as modified by the instrumental characteristics. The spectrum is calculated from the interferogram by computing the inverse Fourier Transform of I(x), which is:

$$B(\tilde{\nu}) = \int_{-\infty}^{+\infty} I(x)\cos(2\pi\tilde{\nu}x)dx \qquad \text{(III. 9)}$$

In practice, data acquisition involves signal averaging of interferograms and requires that all the signals are added coherently. For this purpose, a reference interferogram of a monochromatic source (He-Ne laser) is measured along with the main interferogram

(from the polychromatic infrared source). The different interferograms can be digitised at exactly the same position during each scan by sampling at each zero value of the sinusoidal reference interferogram. It is however necessary for the first data point to be sampled at an identical retardation for every scan. This is achieved using a third interferogram from a white light source. The very sharp interferogram produced by the source gives a reproducible marker at the same retardation and whenever the interferograms exceed a certain threshold voltage, data collection begins at the next zero crossing of the laser reference interferogram.

III.2.3. Mathematical Techniques for processing spectra.

Usually infrared spectra consist of peaks of absorption which vary in width from 5 (or even smaller in the case of gas) to 30cm^{-1}. Study of the shapes and widths of such peaks should give a lot of information on the microstructure of the polymer. But generally, overlapping of peaks due to different modes of vibration and unresolved peaks components makes this almost impossible, even when the spectra are taken at low temperature. Mathematical treatments, such as curve fitting and Fourier-Self deconvolution of the infrared spectra become necessary to resolve these problems.

Because isolated infrared peak can be described using a combination of Gaussian and Lorenztian shapes, a complex region of a known number of overlapping peaks can be computer fitted to find the values of the centres, half-widths and height of these peaks. Since real peaks are not a perfect combination of Gaussian and Lorenztian shapes and are noisy, the fit obtained may not be unique, especially if there is any doubt about the number of peak components. For these reasons, curve fitting is never applied on its own but needs to be used in conjunction with a peak-narrowing method such as Fourier Self deconvolution.

Fourier self-deconvolution involves the deconvolution of an intrinsic line-shape function from the experimental spectrum. Convolution is essentially the smearing of one line shape by another. It is assumed that the spectral resolution obtained is limited by the natural line-shape rather than by instrumental factors. A spectrum E(ν) is derived from an interferogram I(x) as $\Im\{I(x)\}$, where $\Im$ symbolises a Fourier transformation. The self-deconvoluted interferogram, I′(x) is then expressed as:

$$I'(x) = \frac{D_g(x)}{\Im^{-1}\{E_0(\nu)\}} I(x) \qquad \text{(III. 10)}$$

where $E_0(\nu)$ is the intrinsic line-shape function and $D_g(x)$ is an apodization function. $\Im^{-1}$ denotes an inverse Fourier transformation. The denominator represents the deconvolution, with $D_g(x)$ determining the final line-shape. Fourier transformation then simply yields a spectrum $E'(\nu)$. In practise, a Lorenztian was used for the intrinsic line-shape $E_0(\nu)$, and a Bessel function for apodization ($D_g(x)$).

In this thesis, we use Fourier Self-deconvolution provided by the software 'FIRST' in order to improve the spectral resolution of CD_2 bending profiles.

Experimentally, we have used a Mattson Instrument 6020 FTIR spectrometer based on a Michelson interferometer, with corner cube reflectors (instead of the classical mirror), and Mercury Cadmium Telluride (MCT) detector. The source is a heated ceramic material (T~1200 ° C) which provides a useful spectrum range from 400 to 4000 cm^{-1}. The pyroelectric detector has to be cooled to liquid nitrogen temperature and allows a detection range from 700 to 4000 cm^{-1}.

All the infrared measurements presented in this thesis were made at liquid nitrogen temperature. This was achieved using a cryostat (P/N 21500 by Graseby/Specac) equipped with a temperature controlled cell (P/N 20120) under vacuum.

In order to remove any trace of water vapour and carbon dioxide, the sample environment was under a dry air purge during the recording of the spectra.

The 'in-situ' measurements on the stretched samples were possible with the use of a home-made clamp which fits in the heating cell of the cryostat.

III.3. The infrared Spectrum of Polyethylene.

Because of its relatively simple chemical structure, polyethylene was one of the first polymers to be studied using infrared spectroscopy, but it was only in the 1970s that band assignments of its infrared spectrum could be regarded as complete and more or less accepted by the scientific community. A full description of the spectrum of polyethylene can be found for example in reference 6, page 105. A typical infrared spectrum of a linear polyethylene (M_w=385000, M_n=48000, M_w/M_n=8) is presented in figure III. 4. The assignments of the most important bands in the crystalline phase of polyethylene are presented in table III.1.

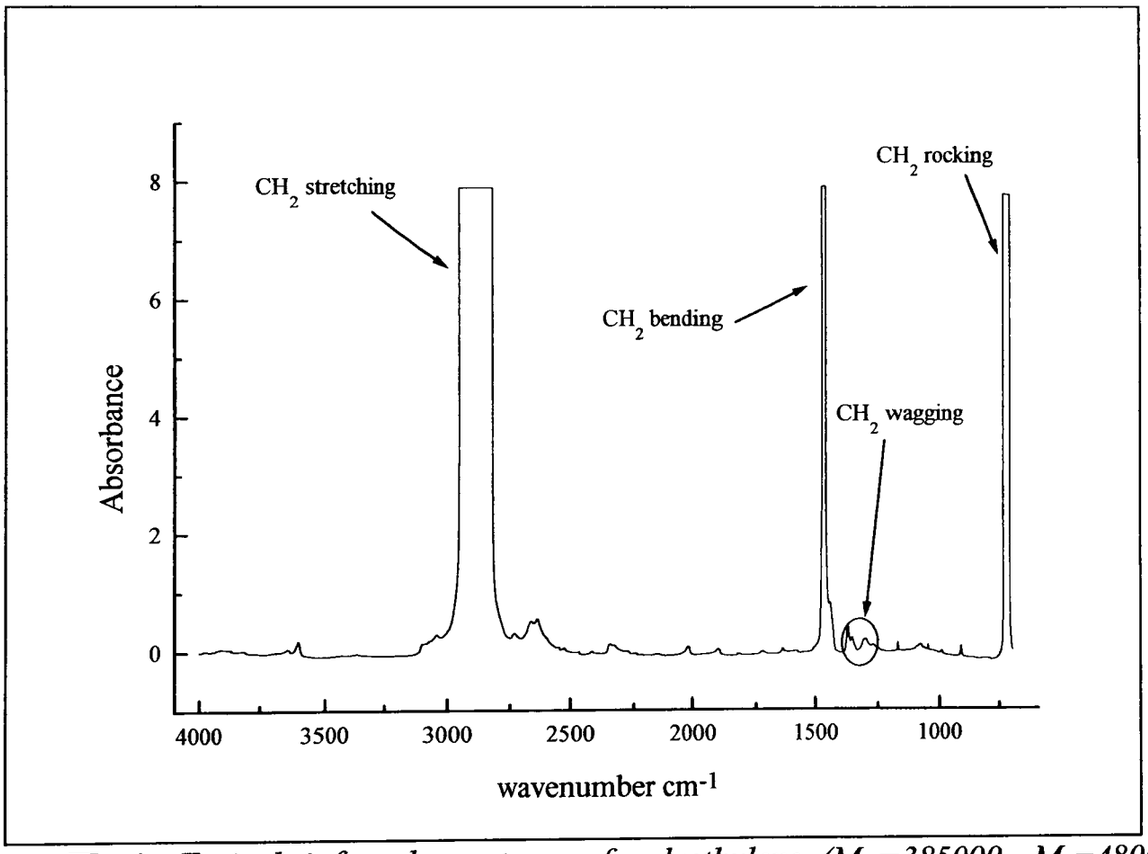

Figure III. 4: *Typical infrared spectrum of polyethylene (M_w=385000, M_n=48000, M_w/M_n=8)*

In this paragraph, we will focus our attention on the effect of isotopic substitution on the infrared spectrum of polyethylene, on the CX_2 bending region (where X can be H or D, which occurs at respectively 1473/1463 cm^{-1} and 1092/1085 cm^{-1}) and on the CH_2 wagging region of the spectrum (1400-1200 cm^{-1}).

Description	Sym. Sp.	Polarisation	Observed peak, cm^{-1}
$\gamma_r(CH_2)$	B_{2u}	b	721
	B_{1u}	a	734
$\gamma_t(CH_2)$	B_{3u}	c	1050
$\gamma_w(CH_2)$	B_{3u}	c	1175
$\delta(CH_2)$	B_{2u}	b	1463
	B_{1u}	a	1473
$\nu_s(CH_2)$	B_{1u}	a	2851
	B_{2u}	b	2857
$\nu_a(CH_2)$	B_{2u}	b	2899
	B_{1u}	a	2919

Table III.1: *Assignment of fundamental factor group vibrations of polyethylene. γ_r, γ_t, γ_w, δ, ν_s, ν_a are respectively rocking, twisting , wagging , bending, antisymmetric and symmetric stretching modes. a, b or c indicates polarisation parallel to crystal a, b or c axis.*

III.3.1. The effect of isotopic substitution on the infrared spectrum.

The frequency of a vibrational mode depends on the masses of the atoms as well as on the geometry of the molecule and the force constants. If the mass of one type of atom can be changed by substituting a different isotope from the normally predominant one and the other factors which determine the frequencies of the modes remain constant, then certain simple predictions can be made about the changes in frequency which will be observed. Clearly, if the type of atom for which the substitution is made does not move in a particular mode, the frequency of that mode will be unchanged, whereas if the mode involves predominantly the movement of this type of atom the change of frequency may be quite large. Isotope substitution may thus be a useful aid in making vibrational assignments.

Consider, for instance, the totally symmetric 'breathing mode' of the methane molecule, in which all four hydrogen atoms move radially in and out of phase with each other. In the simplest model the frequency of this mode can be calculated using equation III.2, and is given by

$$\nu = \frac{1}{2\pi}\sqrt{\frac{k}{m_H}} \qquad \text{(III. 11)}$$

where m_H is the mass of the hydrogen atom and k is the force constant for C-H stretching, since in this mode the carbon atom does not move and the vibration has the same frequency as that of a diatomic molecule consisting of a hydrogen atom bonded to

an atom of infinite mass by a bond with force constant k. Since the frequency of this mode is independent of the mass of the carbon atom, it would not change if the mass of the carbon atom was changed from the usual 12 to 13 amu (atomic mass unit) by isotopic substitution, whereas if the masses of all the hydrogen atoms were changed from 1 to 2 amu by the substitution of deuterium the frequency would, in the harmonic approximation, be reduced by a factor $\nu_{CH}/\nu_{CD} = \sqrt{\frac{m_D}{m_H}} \approx \sqrt{2}$.

The effect of isotope substitution on the frequency of any particular normal mode could only be predicted accurately if the precise molecular geometry and force constants were known, and only approximate shifts can be calculated. There is a simple approximate rule derived by Krimm [6] which seems to apply quite well to the case of hydrogen-deuterium substitution. If ν is the frequency of a vibration of the molecule before isotopic substitution, and ν' is the frequency of the same vibration after isotopic substitution, the ratio of these two frequencies is

$$\frac{\nu'}{\nu} = \sqrt{1 - \frac{\Delta T}{\rho T}} \qquad \text{(III. 12)}$$

where T is the total kinetic energy associated with the vibration and ΔT is the change in kinetic energy which results from isotopic substitution. ρ is the ratio of the mass of the isotopic substituent to the normal mass (ρ=2 in the present case).

III.3.2. Origin of the CX_2 bending doublet.

The usual unit cell of polyethylene is orthorhombic, and contains two molecules, one molecule passing through the centre of the cell and one molecule at each corner of the cell, shared with three other unit cells, as presented in figure I.1. Considering the CX_2 bending vibration (figure III.5 (a)), the symmetry of the factor group allows only two different phase relationships between the two chains in the unit cell: in and out of phase with each other as presented in figure III.5 (b). Thus, by resolving the change of dipole moment for each chain and adding them together, the overall dipole moment is seen to lie parallel to the b-axis in the upper diagram in figure III.5(b) and parallel to the a-axis in the lower one.

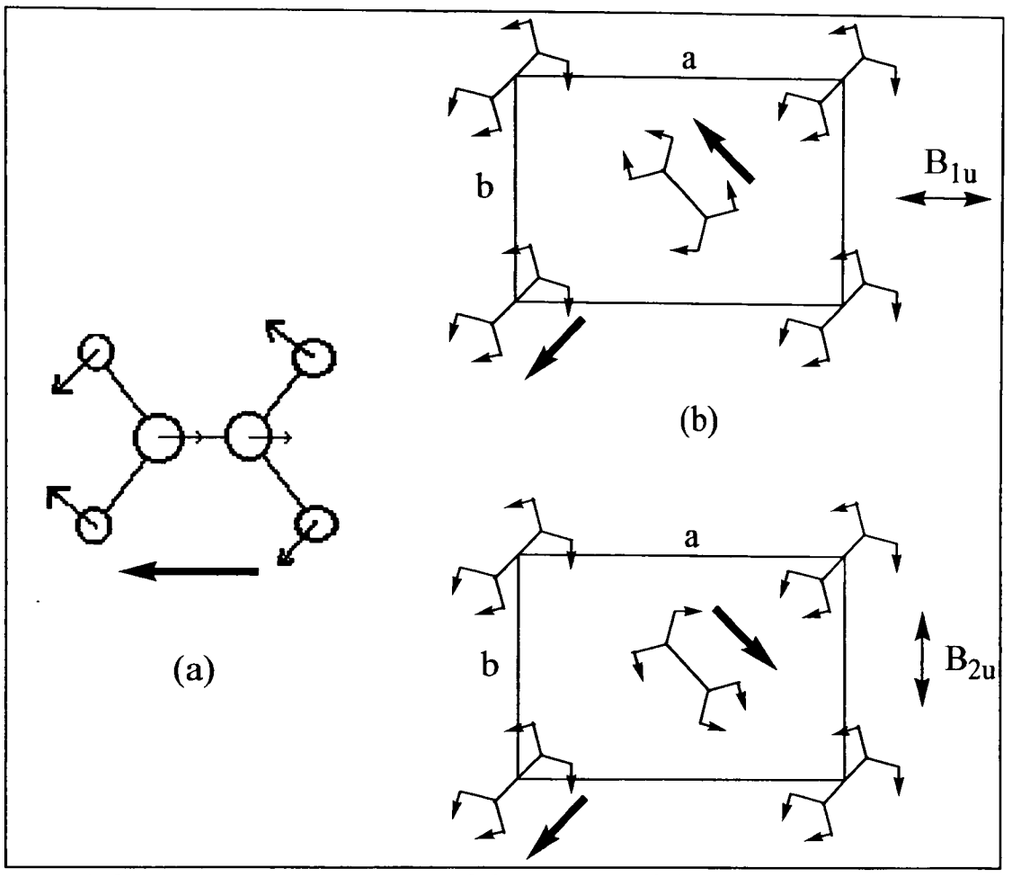

Figure III. 5: *Schematic representation of the nature of the CX_2 bending (where X can be H or D) doublet modes in polyethylene: (a) the bending vibration of a single chain viewed along the chain axis. The broad arrow indicates the direction of the instantaneous dipole moment, which is the vector sum of those due to the four C-H bonds, (b) the two allowed phase relationships of the vibration of the two chains in the unit cell and the corresponding net dipole change.*

This simple application of the group theory analysis of crystalline polyethylene was verified by measurements [7] on the 1463/1473 cm^{-1} infrared CH_2 bending mode doublet, using polarised radiation. This study showed that the peak at 1463 cm^{-1} is b-polarised (B_{2u}) and the one at 1473 cm^{-1} is a-polarised (B_{1u}).

III.3.3. The CH_2 wagging region.

A certain number of absorption bands in the infrared spectrum of polyethylene cannot be assigned to the vibrational modes of an infinitely long and fully extended chain. Also, the absorbance of these bands increases greatly with increasing temperature, suggesting that they are associated with vibrations of non planar chains. The CH_2 wagging region (1380-1300 cm^{-1}) in the infrared spectrum of polyethylene is one such region.

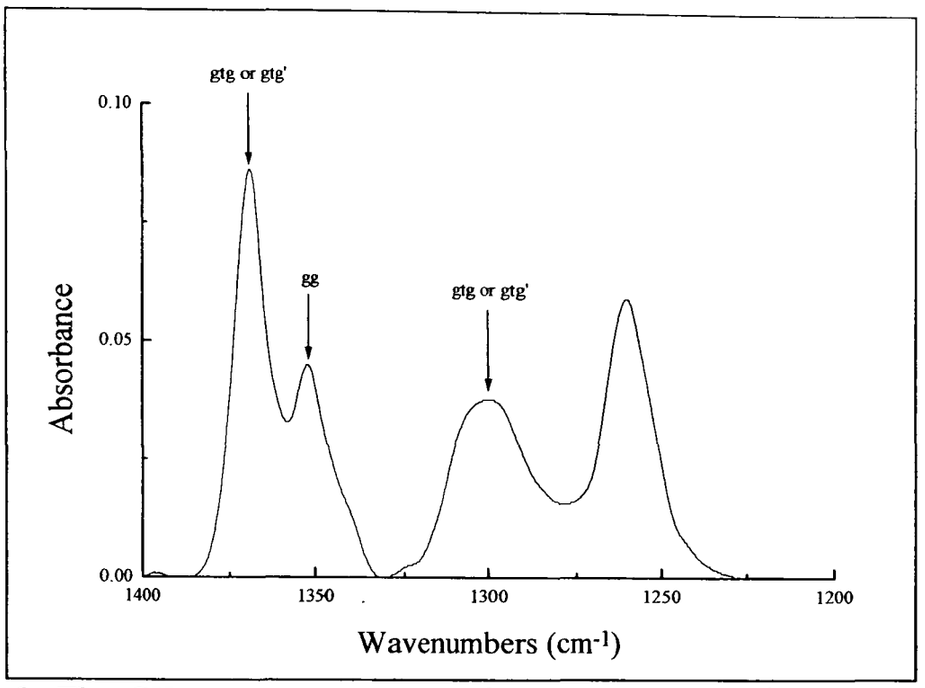

Figure III. 6: *The CH_2 wagging region in low temperature infrared spectrum for a linear polyethylene. The bands arise from departure from an all-trans polymer chain, as indicated here.*

By comparing the frequencies of absorption bands measured and calculated for n-alkanes using a Valence Force Field, Snyder [8] gave the following band assignments in this region (which are now widely accepted for polyethylene), where g and g' represent the two gauche conformations, which denote conformations which differ from an all-trans chain (as explained in figure III. 7) and t the trans one:

1365 cm^{-1}	gtg and g'tg'
1350 cm^{-1}	gg
1306 cm^{-1}	gtg and g'tg'

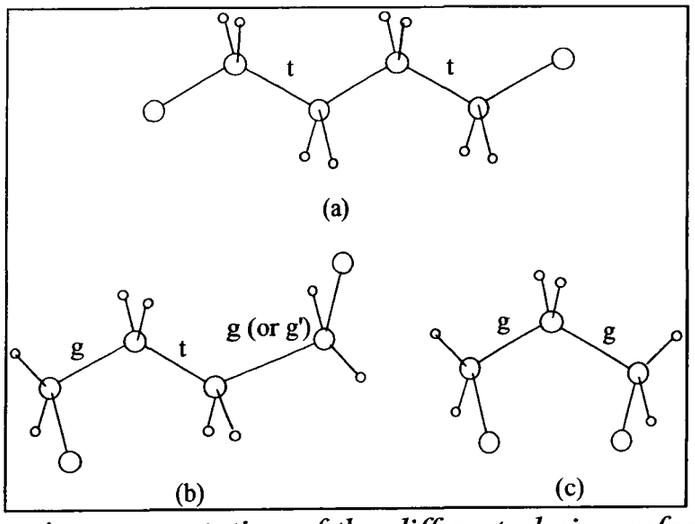

Figure III. 7: *Schematic representation of the different chain conformations present in the CH_2 wagging region of the infrared spectrum of polyethylene. (a) all-trans conformation; (b) gtg or gtg' conformation; (c) gg conformation. The small circles represent hydrogen atoms, while the large one carbon atoms.*

III.4. Mixed Crystal Infrared Spectroscopy.

III.4.1. Introduction.

As we said before, polyethylene usually crystallises with an orthorhombic structure. In this case, the unit cell contains two symmetrically non-equivalent chains giving rise to both in-phase and out-phase components to certain modes in the infrared spectrum. For this reason, some vibrations appear as doublets in the infrared spectrum.

In the mixed crystal technique a mixture containing (usually) mostly protonated (PEH) and a small amount of deuterated (PED) polyethylene is crystallised, and the characteristic doublet splittings in the infrared spectrum are analysed to determine the relative locations of chain stems of the PED in the crystal lattice. By assuming there are no significant interactions between PEH and PED stems, and the interactions between like stems are limited to the nearest neighbour stems [9, 10], this splitting results primarily from interactions between labelled stems that are adjacent to one another in a <110> direction. The magnitude of the splitting is related to both the size and shape of a group of such adjacent labelled stems.

For example, on an orthorhombic lattice, there are four possible sites for nearest neighbours around a labelled stem. If all these four sites are occupied by labelled stems, the doublet splitting will be maximised. If the labelled stem is isolated (i.e. the labelled stem is surrounded by unlabelled stems), the vibration will appear as a singlet in the spectrum. The amorphous chains also contribute to the singlet.

Thus, during deformation, the original arrangement of stems is expected to be modified. The original distribution of splittings would be modified to an extent dependent on the level of deformation. In fact, it is this evolution of the distribution of splittings with deformation, that we use. In order to understand the mechanism involved during the deformation of the initial arrangement of stems within the crystallites, the infrared experimental data are compared with a model calculation simulating deformation of the crystalline lamellae.

Experimentally, we monitor the response of the CD_2 bending vibration (1094/1084cm^{-1}) to strain to analyse first, the change of local arrangement of labelled stems within crystallites, and second the progressive destruction of the initial spherulitic morphology

with strain. In addition, the CH_2 vibrations are used to follow the development of molecular orientation and changes in the populations of various gauche conformers.

III.4.2. The Theory of the Mixed Crystal Infrared technique.

As we said earlier, various arrangements of labelled crystals stems within a predominantly unlabelled crystal lattice can give rise to splittings in infrared vibrations of the labelled species. These splittings result from labelled stems that are adjacent to one another in {110} directions and depend on the size and shape of a group of such adjacent labelled stems. Thus, knowing the size of the splitting from the infrared spectrum, it is possible to determine the local arrangement of labelled crystal stems.
The first calculation of the doublet splitting of the CD_2 bending infrared peak was done for finite chains of coupled oscillators, where a pair of such oscillators comprises the two non equivalent labelled stems in the unit cell [11]. Cheam and Krimm developed this simple coupled oscillator theory in a semi-empirical manner.

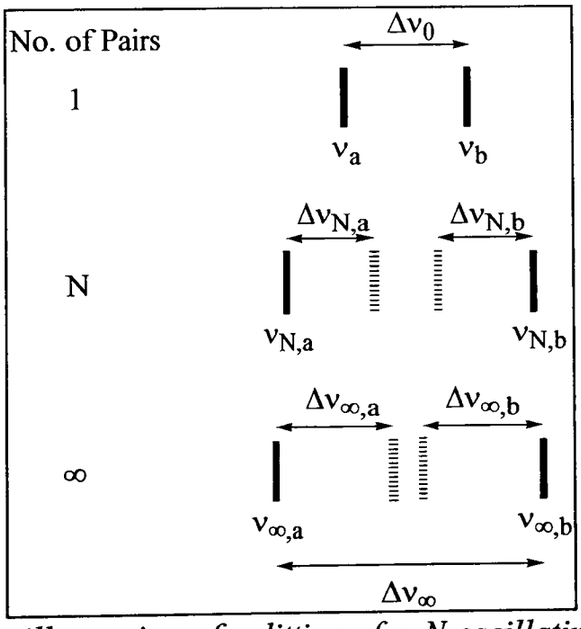

Figure III. 8: *Schematic illustration of splittings for N oscillating pairs in terms of the infrared splittings for one and an infinite number of pairs. The black line represents the Infrared active mode; the dash line the Raman active mode (from ref. 11).*

The frequencies of the normal modes for a row of M equivalent oscillators, each with an uncoupled frequency ν_0, can be written as [12]:

$$\nu_{M,s}^2 = \nu_0^2 + 4\nu'^2 \sin^2 \frac{(M-s)\pi}{2M}, \quad s = 1, 2, \ldots M \qquad \text{(III. 13)}$$

with

$$\nu_0^2 = \frac{K}{4\pi^2 m}$$
$$\nu'^2 = \frac{K'}{4\pi^2 m} \qquad \text{(III. 14)}$$

where K is the internal force constant of each oscillator with reduced mass m and K′ is the coupling force constant between adjacent oscillators. By reference to an infinite sequence of oscillators, equation III.13 can be rewritten as:

$$\nu_{M,s}^2 = \nu_{\infty,\infty}^2 + (\nu_{\infty,1}{}^2 - \nu_{\infty,\infty}{}^2)\sin^2\frac{(M-s)\pi}{2M} \qquad \text{(III. 15)}$$

The maximum splitting occurs for the frequencies of the s=1 and s=M modes. The s=M mode has greatest infrared intensity whereas the mode s=1 has the greatest Raman intensity. Thus, this maximum splitting, $\Delta\nu_M$, is then obtained from:

$$\nu_{M,1}^2 - \nu_{M,M}^2 = (\nu_{\infty,1}^2 - \nu_{\infty,\infty}^2)\sin^2\frac{(M-1)\pi}{2M} \qquad \text{(III. 16)}$$

If we suppose that M is large, then $(\nu_{M,1} + \nu_{M,M}) = (\nu_{\infty,1} + \nu_{\infty,\infty})$ and we can write the splitting $\nu_{M,1} - \nu_{M,M}$ as:

$$\Delta\nu_M = \Delta\nu_\infty \sin^2\frac{(M-1)\pi}{2M} \qquad \text{(III. 17)}$$

where $\Delta\nu_M = \nu_{M,1} - \nu_{M,M}$ and $\Delta\nu_\infty$ is the corresponding frequency separation for an infinite sequence. This splitting is in fact the difference between an Infrared active and a Raman active frequency of a chain of simple oscillators (see Figure III. 8).

As we said earlier, the unit cell in polyethylene contains two non equivalent stems in the {110} direction, which give rise to the doublet splitting in the infrared spectrum. If we assume that the frequencies of the two infrared bands of a pair of such oscillators are given by ν_a and ν_b, for N pairs, these frequencies will split into an infrared active mode (one of lower frequency than ν_a and one of higher frequency than ν_b) and a Raman active mode (of reverse order). The difference in frequency between these bands, $\Delta\nu_{N,a}$ and $\Delta\nu_{N,b}$ is given by equation III.17 and is schematically represented in Figure III. 8. Thus the infrared splitting for N pairs is then given by:

$$\Delta\nu_N = \left[\nu_b + \frac{1}{2}\left(\Delta\nu_{\infty,b}\sin^2\frac{(N-1)\pi}{2N}\right)\right] - \left[\nu_a - \frac{1}{2}\left(\Delta\nu_{\infty,a}\sin^2\frac{(N-1)\pi}{2N}\right)\right]$$
$$= \Delta\nu_0 + \left(\Delta\nu_\infty - \Delta\nu_0\right)\sin^2\frac{(N-1)\pi}{2N} \qquad \text{(III. 18)}$$

where $\Delta\nu_0 = \nu_b - \nu_a$.

Now we extend the analysis to crystal stems arranged on adjacent {110} planes. We consider j adjacent deuterated stems on a {110} planes, and k such adjacent planes along the corresponding [110] direction as represented in Figure III. 9. Our goal is then to calculate the splitting $\Delta\nu\{(110)_j(110)_k\}$ associated with such a structure. If we consider the j stems as an oscillator with an infrared splitting $\Delta\nu\{(110)_j[110]_1\}$ [13], we can calculate the splitting for the whole stem arrangement from equation III.18:

$$\Delta\nu\left\{(110)_j(110)_k\right\} = \Delta\nu\left\{(110)_j(110)_1\right\} + \left[\Delta\nu\left\{(110)_j(110)_\infty\right\} - \Delta\nu\left\{(110)_j(110)_1\right\}\right]\sin^2\frac{(k-1)\pi}{2k} \qquad \text{(III. 19)}$$

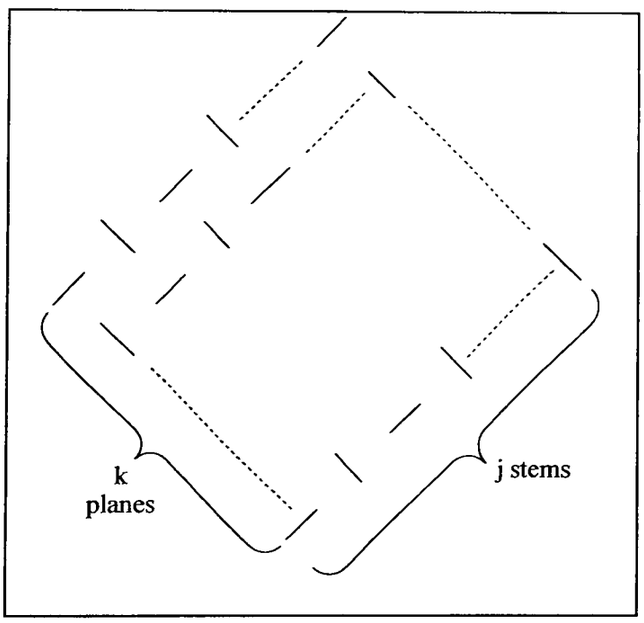

Figure III. 9: *Schematic view of a $\{(110)_j\,[110]_k$ arrangement of crystals stems.*

Experimental data for PED and simple symmetry relations enable the determination of several terms in equation III.19. Low temperature infrared measurements on pure PED [11] give a CD_2 bending splitting of 10.2 cm^{-1}, corresponding to $\Delta\nu\left\{(110)_\infty(110)_\infty\right\}$. Hence for a single infinite sheet of PED surrounded by PEH, the number of interactions of the two non-equivalent stems in the unit cell is half that for pure PED, so that

$$\Delta\nu\left\{(110)_\infty(110)_1\right\} = 5.1\ cm^{-1} \qquad \text{(III. 20)}$$

The infrared splitting of an isolated pair of PED stems adjacent to each other along a (110) plane, $\Delta\nu_0$, was taken as the value from a normal vibration calculation (2.25 cm^{-1}),

scaled to the experimental splitting obtained in pure PED (10.2 cm^{-1}) by comparison with the normal vibration calculation (8.76 cm^{-1}), i.e.[11]:

$$\Delta\nu_0 = 2.25 \times (10.2 / 8.76) = 2.62\ cm^{-1} \qquad \text{(III. 21)}$$

Results of the above calculation of the CD_2 bending splitting are given in table III.1.

$\Delta\nu$ (cm^{-1})									
j\k	1	2	3	4	5	6	8	10	∞
2	2.6	5.1	6.4	6.9	7.2	7.3	7.5	7.5	7.7
3	3.3	6.1	7.7	8.1	8.4	8.6	8.7	8.8	8.9
4	3.9	6.7	8.1	8.6	8.9	9.1	9.2	9.3	9.5
5	4.2	7.0	8.3	8.9	9.2	9.4	9.5	9.6	9.7
6	4.5	7.2	8.5	9.1	9.3	9.5	9.7	9.7	9.9
7	4.6	7.3	8.6	9.2	9.4	9.6	9.7	9.8	9.9
8	4.7	7.4	8.7	9.2	9.5	9.7	9.8	9.9	10.0
9	4.8	7.4	8.7	9.3	9.6	9.7	9.9	9.9	10.0
10	4.9	7.5	8.8	93	9.6	9.7	9.9	10.0	10.1
12	4.9	7.5	8.8	9.4	9.6	9.8	9.9	10.0	10.1
14	5.0	7.6	8.8	9.4	9.6	9.8	9.9	10.0	10.1
16	5.0	7.6	8.8	9.4	9.7	9.8	10.0	10.0	10.2
∞	5.1	7.7	8.9	9.5	9.7	9.9	10.0	10.1	10.2

Table III. 1: *Predicted splittings, in cm^{-1}, of CD_2 bending modes for $\{(110)_j[110]_k\}$.*

But, when Cheam and Krimm used this method to analyse experimental splittings for polyethylene single crystals [11, 14], it appeared that the dimensions of the labelled groups obtained were much smaller than that expected for a complete molecule. Also with the use of low temperature measurements (which minimise the variation in lattice dimensions with sample morphology, increasing the splitting and reducing the band width) and Fourier Transform Interferometers, the splitting appears as a complex multiplet band structure, where different bands tend to overlap each other. Therefore, curve fitting, as used by Krimm et al [11], can only provide a limited interpretation in terms of stem arrangements.

As an alternative, Spells and al [15, 16] used stem arrangement models to calculate infrared band profiles and to compare them with experimental results. This way, they were able to use the detailed stem arrangements [15] developed to fit the neutron scattering data to calculate infrared spectra. Also, instead of using the model of regularly arranged groups of labelled stems, they used a statistical model to generate a set of molecular conformations. These arrangements were divided into groups of labelled stems adjacent in {110} directions. Each group was then transformed into an equivalent

group of simpler shape but of the same number of stems and same distribution of nearest neighbour interactions. The splitting of equivalent groups was then calculated using an interpolation based on calculated splittings [16] (Table III. 1) for groups with equal numbers of labelled stems in each sheet, named a closed-group. A singlet component, resulting from isolated labelled stems in <110> directions and from non-crystalline chain segments, was included in the calculation. Finally, a Lorentzian line-shape was used for each (singlet and doublet) contribution to the multiplet band profile with a bandwidth equal to the experimental resolution used (usually $1cm^{-1}$). Then all components were added together and the result was compared with the self-deconvoluted data.

Using this model, Spells et al showed, from both infrared and neutron data, that polyethylene chain in single crystals formed a sheet like structure, mainly constituted of adjacently re-entrant folding along {110} directions, with superfolding (i.e. a complete departure from a sheet) and the dilution of fold planes with unlabelled chain stems.

This method has also been applied to the monitoring of the conformational changes in rolled polyethylene single crystal [17]. It was shown that rolling the single crystal mat at room temperature resulted in the reduction of the outer CD_2 bending doublet splitting, consistent with a reduction in group size. The use of model calculations to simulate the infrared spectra obtained on rolled polyethylene, indicates that the block size, i.e. the maximum extent of groups of adjacent stems, is reduced to about 3.6 nm for a roll ratio of 6. The conclusion was that the behaviour is characterised by progressively smaller blocks breaking from the original lamellae and rotating so that the molecular axis ultimately aligns in the roll direction.

This model has recently been updated [18] by adding another parameter which is the probability of having a labelled stem after an unlabelled one. In this updated model, Sonntag et al [18] consider the molecular sheets as one-dimensional sequences of stems, labelled or not, in the {110} direction. A crystal sheet is assumed to contain σ labelled stems and is generated by the following procedure:

a) An initial labelled stem is placed down.

b) Subsequent labelled stems are placed down with probability P_A, the probability of adjacency, if the previous stem was a labelled one or probability P_U if the previous one was unlabelled.

c) Step 2 is repeated σ times.

When σ labelled stems are placed down, superfolding occurs and a new sheet is required. Results from this model give good agreement with neutron scattering from solution crystallised polyethylene, using suitable values for these parameters.

III.5. Simulation of Infrared Spectrum of Polyethylene.

In order to understand the mechanism involved during the deformation of the initial arrangement of stems within the crystallites, the infrared experimental data are compared with a model calculation simulating deformation of the crystalline lamellae. Based on current statistical models for chain conformation in solution crystallised polymers [18], a general statistical model for melt-crystallised structures has been developed, which follows the ideas of the subunit model [19], namely that crystal "stems" are arranged in small groups, with large separations between these groups.

This 'subunit' model was introduced and fully described in chapter I.1.1.3. Here we will briefly reconsider it in order to derive an algorithm which will simulate infrared spectra.

Unlike the case of single crystals, in melt crystallised polyethylene, adjacent re-entry is not the major type of folding. In view of the similarity of the radius of gyration, from neutron scattering measurements, in both the melt and in polyethylene quenched from the melt [20, 21], a 'subunit' model [19] was proposed which requires a local rearrangement of the chain as it folds during crystallisation, but the distribution of groups (note that these groups are not necessarily the same as infrared groups) of adjacent stems, i.e. 'subunits', within the whole molecule is imposed by the pre-existing Gaussian chain in the melt. This 'subunit model' was found to give good agreement with neutron data for a structure with around 40% of adjacent folding, but not in any specific crystallographic direction, and for subunits consisting of short rows of labelled stems.

Taking account of that, our model must contain different types of fold direction as well as the possibility to make 'long jump' to start new subunits. The basis of our model is a development of the rolled single crystal model [17]. Hence it includes the probability of adjacent folding (P_A), the probability of having a deuterated stem after a undeuterated one (P_U), but it also includes the probabilities of adjacent folding in several directions, (<110>, <020> and <200> directions), and also probability for a "jump" to a distant lattice point (P_J). This jump is considered sufficiently long as to create a new group of

labelled stems, from the point of view of the infrared technique. Instead of considering the eight possible directions of adjacent folding, only four (directions [110], [1-10], [020] and [200]) were chosen. This was to avoid having a site occupied more than once (i.e. the chain can not come back on itself). This assumption is possible because in the case of the 'subunit model', groups of adjacent stems are expected to be small.

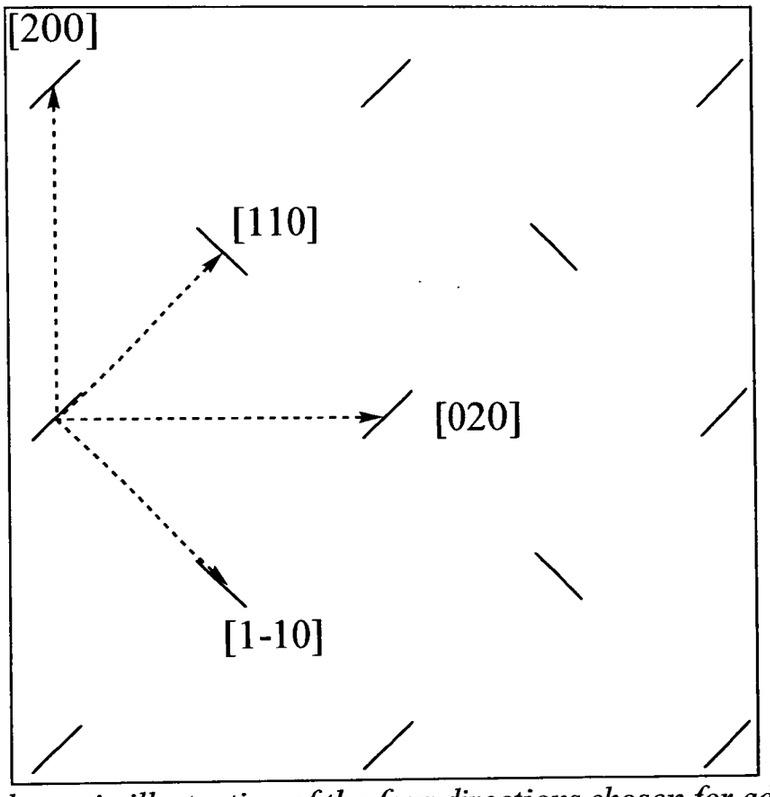

Figure III. 10: *Schematic illustration of the four directions chosen for adjacent folding.*

The crystal arrangement of stems is generated by the following procedure:

a) An initial labelled stem is placed down.

b) The direction of the next labelled stem is chosen with the probabilities $P_{[110]}$, $P_{[-110]}$, $P_{[020]}$, $P_{[200]}$ for the four different directions.

c) Subsequent labelled stems are placed down with probability P_A, if the previous one was labelled or probability P_U if the previous one was unlabelled.

d) If the probability P_A is not achieved, a long jump may occur with the probability P_J

e) Step b is repeated n times.

When the required number of crystal stems have been deposited, the resulting distribution can be plotted to visualise the trajectory. The arrangement is then analysed in terms of stems with <110> nearest neighbours. This is because the infrared CD_2 bending splitting is related to the group size of labelled stems with <110> nearest neighbours. Similarly, the number of isolated stems is counted.

During the next step, the infrared splittings of groups of nearest neighbour labelled stems are calculated, as explained in section III.4.2. Finally, a simulated infrared spectrum is drawn based on the calculated splitting and on the number of groups having the same splitting [15,16]. This simulated spectrum is then compared to the experimental spectrum.

---

[1] D.I. Bower, W.F. Maddams, *The Vibrational Spectroscopy of Polymers*, Chap 2 and 3, Cambridge Solid State Science Series, Cambridge University Press (1989).
[2] P.R. Griffiths and J.A. de Haseth, *Fourier Transform Infrared Spectrometry*, Chemical Analysis vol. 83, Wiley-Interscience Publication.
[3] A.A. Michelson, *Phil. Mag (5)*, **31**, 256 (1891).
[4] A.A Michelson, *Light Waves and Their Uses*, University of Chicago Press, Chicago (1902); reissued in the paperback Phoenix Edition (1961).
[5] J.W. Cooley and J.W. Tuckey, *Math. Comput.*, **19**, 297 (1965).
[6] S. Krimm, *Advance in Polymer Science*, **2**, 51 (1960).
[7] S. Krimm, *J. Chem. Phys.*, **22**, 567 (1954).
[8] R. G. Snyder, J. Chem. Phys., **47**, 4, 1316 (1967.
[9] M. Tasumi, S. Krimm, *J. Chem. Phys.*, **46**, 755 (1967).
[10] M. Tasumi, S. Krimm, *J. Pol. Sci., A_2,* **6**, 995 (1968).
[11] T.C. Cheam, S. Krimm, *J. Polym. Sci., Poly. Phys. Ed.*, **19**, 423 (1981).
[12] R. Zbinden, *Infrared Spectroscopy of High Polymers*, Academic New York, 1964, p. 134.
[13] L. Gribov, *Opt. Spectrosc.*, **29**, 465 (1970).
[14] X. Jing and S. Krimm, *J. Polym. Sci., Polym. Letters Edn*, **21**, 123 (1983).
[15] S.J. Spells and D.M. Sadler, *Polymer*, **25**, 739 (1984).
[16] S.J. Spells, A. Keller and D.M. Sadler, *Polymer*, **25**, 749 (1984).
[17] E. U. Okoroafor and S. J. Spells, *Polymer*, **35**, 4578 (1994)
[18] P. Sonntag, C.M. Care, S.J. Spells and I. Halliday, *J.Chem.Soc.Faraday.Trans.*, **91**(16), 2593 (1995)
[19] D. M. Sadler and R. Harris, *J. Poly. Sci: Poly. Phy. Ed*, **20**, 561 (1982)
[20] J.Schelten, G.D.Wignall and D.G.H.Ballard, *Polymer*, **15**, 682 (1974)
[21] J.Schelten, D.G.H.Ballard, G.D.Wignall, G.Longman and W.Schmatz, *Polymer*, **17**, 751 (1976).

Chapter four:

Sample Preparation and Characterisation.

IV.1. Introduction.

In order to understand the molecular changes occurring when deforming a polymer, a perfect knowledge of the initial characteristics, such as the crystalline structure, degree of crystallinity, lamellar thickness, long spacing, molecular weight of the sample are ideally required. The purpose of this chapter is to describe the production of our samples, the different techniques used to characterise them and the characterisation results obtained.

The technique of Gel Permeation Chromatography (GPC) is a powerful method for determining the complete molar mass distribution of a polymer. Studying the thermal behaviour of the sample with Differential Scanning Calorimetry (DSC) enables us to determine its degree of crystallinity and, indirectly, the lamellar thickness.

Wide angle X-ray scattering allows us to determine the crystalline structure, while small angle X-ray scattering provides a means of measuring the long spacing of the sample. Because we are using a blend of a normal polyethylene with its isotopically labelled counterpart, the real isotopic concentrations need to be known. This is achieved by using the Fourier Transform Infrared (FTIR) spectroscopy. FTIR also provides a means to check the homogeneity of the blend.

IV.2. Sample preparation and nomenclature.

After discussion with BP Chemicals, it appeared that the way in which the samples are made plays an important role in their drawing behaviour. There are two possibilities of mixing the isotopic material. One way is to blend the two isotopes in the melt state. By doing this, the chains become well entangled with each other, which is known to improve the drawing behaviour. For this purpose we used a torque rheometer. When the temperature in the mixing chamber had reached 150°C, the mixer was started. The H- and D-polymers were placed in the mixing chamber using a hydraulic ram. The blending continued for fifteen minutes after the viscosity had reached a constant value. Finally, the blend was removed from the chamber. The major problem of this technique is the large amount of material needed (around 40 g) with the mixer available in the University. For this reason only one sample was made by melt mixing.

A less expensive way is to do the mixing in solution, since smaller quantities can be prepared in this way. Firstly, the H- and D-polymers (respectively 95 and 5 % in w/w for the first samples and 97 and 3 % for the latest) were dissolved together at 1% total w/w in boiling xylene (≈134°C) and mixed. The mixing took place for around thirty minutes, after which the mixture was precipitated in excess of methanol, filtered and finally dried under vacuum at 70°C for 8 hours.

In order to obtain a thin film with smooth surfaces, the blended material was placed between two sheets of a polymeric material with a high melting temperature. The sandwich was then wrapped in aluminium foil. The packet obtained was placed in a hot press heated to a temperature of 160°C, and pressed for 10 minutes at low pressure ($\approx 0.5.10^5$ Pa), followed by five minutes at high pressure ($\approx 5.10^5$ Pa). Finally the sample was quenched in cold water. As a result, films of approximately 0.3 mm in thickness were made.

The nomenclature used to identify our sample is, for example, CL/95/385/1.0. The first letter is the type of D-polyethylene used, which is L in the case of an linear one or C for a copolymer one. The second is the type of hydrogenated host. The first number is the molecular weight of the D-guest divided by 1000 and the second one the same quantity for the H-host. The last number is the draw ratio. Thus, the example denotes a

copolymer D-guest with a molecular weight of 95000 mixed with a linear H-host of molecular weight 385000. Finally, the sample has not been drawn.

For samples made by blending the two isotopic counterpart in the melt, the letters MM (melt mixed) are added to their nomenclature, as for example LL/413/385/MM/1.0.

Purely hydrogenated or deuterated samples are denoted, respectively as H-Bl/X/XX or D-Bl/X/XX, where X is the type of the molecule (L for homopolymer and C for copolymer) and XX the molecular weight divided by 1000.

Also it is important to note that, in this thesis, all the D-polymer used (linear and copolymer) were fully deuterated (with a degree of deuteration larger than 99%).

IV.3. Sample characterisation.

IV.3.1. Gel Permeation Chromatography (GPC).

The method of GPC was developed during the mid-1960s, and is an extremely powerful method for determining the complete molecular mass distribution of a polymer. The physical basis is the separation of macromolecules, with respect to molecular mass, when a solution is pumped through certain gels.

In GPC a dilute polymer solution is injected into a solvent stream which flows through a column packed with gels containing well-defined pore sizes (of typical sizes from 50 to 10^6 Å). The separation with respect to molecular size is due to the selective permeation of polymer molecules into the gel. The smallest polymer molecules are able to pass through most of the pores and so have a relatively long flow-path through the column. However, the largest molecules are excluded from all but the largest of the pores, and so have a much shorter flow-path. The concentration of polymer in the eluent is monitored continuously, using for example spectroscopic methods such as ultraviolet or infrared absorption spectroscopy. The chromatograph obtained is a plot of concentration against elution volume, which provides a qualitative indication of the molecular mass distribution. However, in order to obtain quantitative results, the GPC column has to be calibrated. Calibration is usually performed with standard samples with narrow molecular mass distribution and known average molecular mass. By plotting the molecular mass of these standard samples versus the measured GPC elution volume, the

relationship between elution volume and molecular mass for a polymer of given chemical constitution can be established.

The GPC results obtained were kindly made at the University of Bristol and by BP Chemicals. The different GPC values are listed below in Table IV. 1:

Sample	Type	$\overline{M}_W$ ($x10^{-3}$)	$\overline{M}_N$ ($x10^{-3}$)	$\overline{M}_W/\overline{M}_N$	*SCB/1000 C
E	L DPE	76	55	1.39	/
AY1	"	95	48	1.97	/
AD1	"	136	77	1.76	/
R6403 **	"	413	157	2.6	/
R6412#1 **	C DPE	95	11	8.6	6.3 C_6
R6401 75° **	"	378	181	2.1	8 C_4
NR1	L HPE	86	24	3.58	/
NR(A3N)	"	90.3	30	3	/
A	"	134	18	7.5	/
B	"	385	48	8	/
C	C HPE	181	14.9	12.1	6 C_4

Table IV. 1: *GPC characterisation of the different raw materials used. L and C denotes respectively linear and copolymer polyethylene, while HPE and DPE stand for, respectively, hydrogenated and deuterated polyethylene. *SCB/1000C = amount of short chain branches per thousand carbon atoms on backbone molecule. ** material polymerised by a metallocene catalysis process.*

IV.3.2. Differential Scanning Calorimetry.

IV.3.2.1. Theory.

When a material undergoes a change of state, such as melting, heat is either absorbed or given out. Differential Scanning Calorimetry (DSC) provides a means of measuring the enthalpies, ΔH, of these processes from which both the crystallinity and lamellar thickness will be derived.

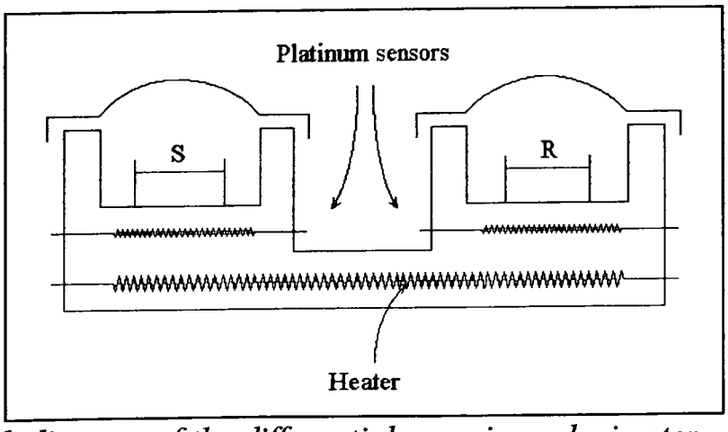

Figure IV. 1: *Block diagram of the differential scanning calorimeter.*

Two pans, one containing the sample, the other empty used as a reference are placed on two positions equipped with sensors (Figure IV. 1).

A temperature scanning consists of heating or cooling the sample at a given rate (°C/min). The temperature difference between the sample and the reference is constantly monitored and sent to a control module. The heating power of the reference is adjusted so as to reduce the temperature difference with the sample. In case a thermal event occurs during the temperature scanning, i.e. an endothermic or an exothermic transformation, this will require more or less heat to be sent to the reference. A DSC measurement will consist of plotting the rate of heat applied to the reference against the temperature. Endotherms or exotherms will then appear as peaks. If the sample undergoes no phase transformation, no temperature difference develops between the specimen and the reference, and the experiment is isothermal. If any temperature difference does appear between them, because of phase transformation for example, the instrument compensates by changing the heat flux $\frac{dQ}{dt}$. The heat flux difference, in other word, the thermal energy difference per unit time is measured:

$$\Delta H = \int \frac{dQ}{dt} dT \qquad \text{(IV. 1)}$$

In this method the glass transition, T_g, appears as a shift in the baseline, and melting and crystallisation processes are exothermic and endothermic peaks respectively. Thus the heat exchange involved in the transition is determined by measuring the area under the peaks by:

$$\Delta H = \frac{KRA}{m} \qquad \text{(IV. 2)}$$

where K is a constant characteristic of the equipment, m the mass of the sample, R the sensitivity used, and A the area under the peak. ΔH is defined here as enthalpy change per unit of mass.

Since thermal analysis is not an absolute measuring technique, calibration is of prime importance. Calibration is necessary for the measurement of the temperature, T (in K); and the amplitude, expressed as heat flux, $\frac{dQ}{dt}$ (in Js^{-1}). In this thesis, the melting temperature and heat flux of Indium (respectively 430 K and 28.45 Js^{-1}) were used for both calibration.

If the heat of crystallisation is known for the totally crystalline polymer, the degree of crystallinity can be determined from the heat absorbed during melting and the mass of the sample:

$$x\% = \frac{\Delta H_{meas}}{\Delta H_{cryst}} \cdot 100 \qquad \text{(IV. 3)}$$

In the case of polyethylene, the heat of crystallisation for totally crystalline polymer, ΔH_{cryst}, is equal to 293 Jg^{-1} [1].

Another important application of the DSC melting curves is the determination of the lamellar thickness. If we rewrite the Gibbs-Thompson equation as:

$$\ell = \frac{T_m^0}{T_m^0 - T_m} \frac{2\sigma_e}{\Delta H_m} \rho \qquad \text{(IV. 4)}$$

where T_m (in K) is the melting point related to a lamellar thickness, ℓ. T_m^0 is the melting point for an infinite crystal (418.95 K [2]), σ_e the surface energy of the base plane involving chain folding (93×10^{-7} Jcm^{-2} [2]), ΔH_m the melting enthalpy per unit volume (280 Jcm^{-3} [2]) and ρ is the density of a perfect crystal (1.0 gcm^{-3}). Thus, by knowing the melting temperature of the sample, its lamellar thickness is obtained by equation IV.4.

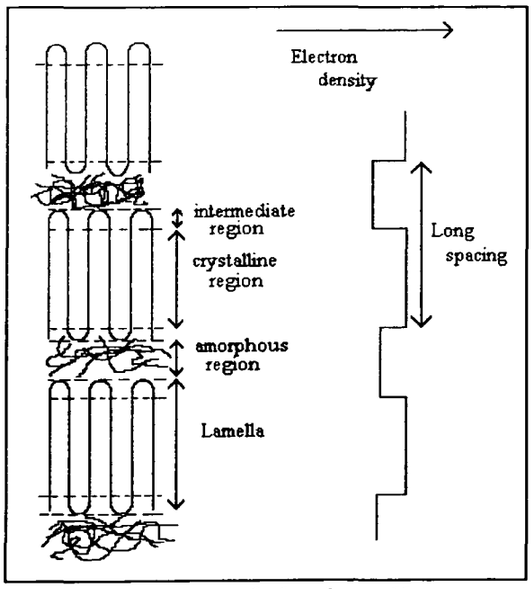

Figure IV. 2: *Schematic representation of the lamellar structure in polyethylene. The long spacing is defined as the periodicity of the variation in electron density due to the regular alternation of crystalline regions and amorphous regions. The long spacing is equal to the crystal thickness plus the intermediate region thickness plus the amorphous thickness. The lamella is the crystalline region plus the two nearest intermediate regions. The intermediate region is where the fold takes place.*

Also, the long period, L_{DSC}, can now be calculated using the assumption of linear crystallinity as shown in Figure IV. 2:

$$L_{DSC} = \frac{1}{x}\ell \qquad \text{(IV. 5)}$$

where x is the degree of crystallinity. This value can then be compared with the one measured with small angle X-rays scattering, L_{SAXS}.

VI.3.2.2. DSC results.

Experimentally, we have used a Mettler DSC 30 system with a typical heating rate of 10°C min^{-1} and a sample weight of 10 mg. The reference was an empty aluminium pan. Indium was used to calibrate the temperature and heat flux. The crystallinity was calculated using the Constructor software with the different constants listed above and are presented in Table IV. 2, along with the melting temperature T_m, lamellar thickness ℓ, the long spacing, L_{DSC}, derived form crystallinity.

Sample Name	x (%)	T_m (°C)	ℓ (Å)	L_{DSC} (Å)
H-Bl/L/385	50	132.3	206	421
LL/95/385/1.0	53	134.1	238	449
LL/413/385/1.0	49	134.1	238	485
LL/413/385/MM/1.0	59	132.9	216	367
CL/95/385/1.0	52	132.3	206	396
CL/378/385/1.0	50	132.5	209	418
H-Bl/L/90	54	132.5	209	387
LL/413/90/1.0	44	131.8	199	452
CL/378/90/1.0	48	131.8	199	414
LL/95/134/1.0	54	132.7	212	393
CL/95/134/1.0	57	132.7	212	372
H-Bl/C/181	39	124.3	129	332
LC/95/181/1.0	42	123.7	126	300
LC/413/181/1.0	41	123.9	127	310
CC/95/181/1.0	38	125.2	135	355
CC/378/181/1.0	38	124.7	132	347

Table IV. 2: *DSC results for the different samples used in this thesis. The crystallinity (x) is calculated with equation IV.3. T_m is the position of the melting peak. The lamellar thickness, ℓ is derived from equation IV.4 using the different values listed in the text. The long spacing, L_{DSC} is obtained through equation IV.5, assuming linear crystallinity. The experimental errors are estimated to be around 10%.*

All the copolymer samples have smaller crystallinity, lamellar thickness and long spacing than their linear counterparts. This is expected since branches are suspected to be excluded into the interfacial and interlamellar regions [3] leading to a reduction of lamellar thickness and long spacing. The values listed in Table IV. 2 are comparable to

the ones found in the literature for similar types of sample [2, 4, 5]. But it is important to note that a significantly smaller lamellar thickness is found for our linear samples (206 Å for H-Bl/385) than the one listed in reference 2 (320 Å for sample U). This is expected since the lamellar thickness is dependent on the cooling regime, with rapid cooling (quenching in our case, and slow cooled in reference 2) producing smaller lamellae. In the case of the copolymer, the difference in lamellar thickness between the two modes of crystallisation, quenching and slow cooling (129 Å for H-Bl/C/181 and 138.5 Å for sample C in reference 2), is comparable to the experimental error and therefore the lamellar thickness appears to be independent of the crystallisation mode. Similar observations were previously made [5]. This is explained by the fact that the length between branches is seen as a major factor in determining the lamellar thickness because the branches can be incorporated in the lamellae only to a certain extent.

The similarity between the DSC characteristics of the samples and their corresponding hydrogenated matrix confirms the fact that the addition of a small amount of deuterated polyethylene to the hydrogenated matrix has a very small effect on the crystallisation process. It is the hydrogenated matrix which dictates the crystallisation processes, the deuterated guest acting only as an impurity.

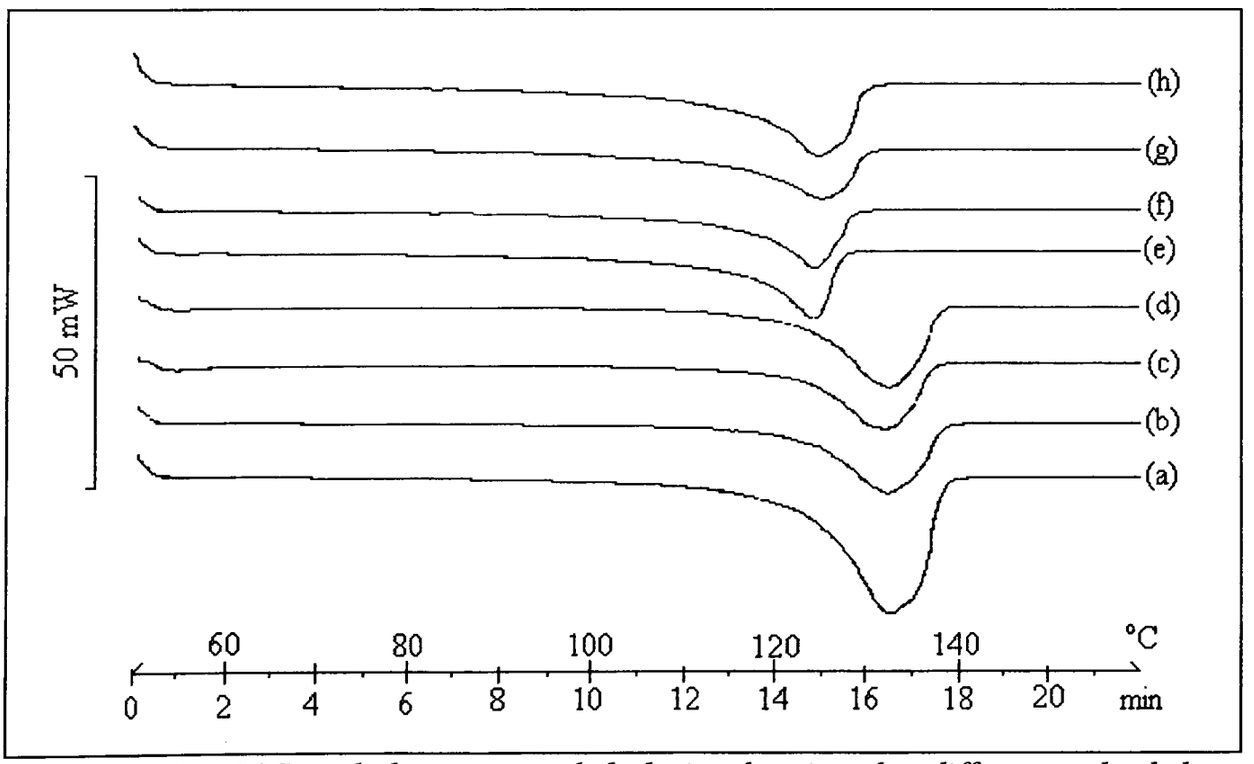

Figure IV. 3: *DSC endotherms recorded during heating the different polyethylene samples at 10 °C / min. (a) LL/413/385/MM/1.0, T_m = 132.9 °C; (b) LL/95/385/1.0, T_m = 134.1 °C; (c) CL/95/385/1.0, T_m = 132.3 °C; (d) CL/378/385/1.0, T_m = 132.5 °C; (e) LC/95/181, T_m = 132.9 °C; (f) LC/413/181/1.0, T_m = 123.9 °C; (g) CC/95/181/1.0, T_m = 125.2 °C; (h) CC/378/385/1.0, T_m = 124.7 °C.*

IV.3.3. X-Ray scattering.

We have used the technique of wide angle X-ray scattering (WAXS) in order to confirm the orthorhombic structure and the absence of orientation in samples prior to deformation. The small angle technique (SAXS) was used in order to determine the long spacing. In this paragraph, we will briefly introduce the WAXS, and SAXS techniques and will present the different characterisation results.

IV.3.3.1. Wide angle X-ray scattering (WAXS).

If a monochromatic X-ray beam falls on a crystalline structure, the beam will be diffracted by a set of crystallographic planes. As we have already mentioned in chapter two, constructive interference between the scattered beams is only possible when the Bragg law is verified, i.e.:

$$2d\sin\theta = n\lambda \qquad \text{(IV. 6)}$$

where n is the order of reflection, λ is the X-ray wavelength, d the distance between atomic planes and θ the Bragg angle, that is half the scattering angle. Atomic planes are usually characterised by Miller indices. These indices describe the intercepts of the given plane with the crystallographic axes and are related to the unit cell dimension (the smallest repeating volume unit).

If the unit cell of the space lattice is represented by the vectors **a**, **b** and **c**, then the reciprocal lattice is defined by vectors **a***, **b*** and **c*** in reciprocal space where:

$$\mathbf{a}^* = \frac{\mathbf{b}\times\mathbf{c}}{V} \qquad \mathbf{b}^* = \frac{\mathbf{c}\times\mathbf{a}}{V} \qquad \mathbf{c}^* = \frac{\mathbf{a}\times\mathbf{b}}{V} \qquad \text{(IV. 7)}$$

V is the volume of the unit cell. A general property of the reciprocal lattice is that the vector s(h,k,l) from the origin to any lattice point (h,k,l) is perpendicular to a set of parallel planes in the real lattice which intersect **a**, **b** and **c** axes at intervals of a/h, b/k and c/l respectively. The spacing between subsequent planes is d = 1/s. These planes are called Miller planes and (h,k,l) are the Miller indices. In the reciprocal lattice, all planes with the same indices refer to a single point only.

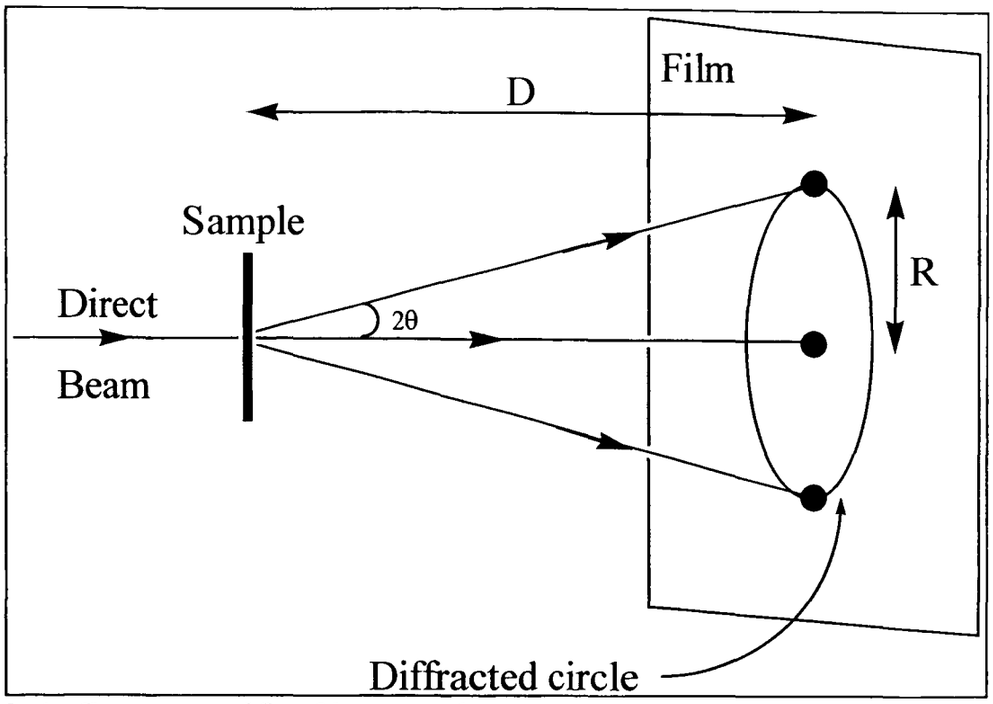

Figure IV. 4: *Geometry of flat film recording.*

In this WAXS study, we used a Worhus flat film camera where a photographic film was placed a few centimetres away from the sample and perpendicular to the unscattered beam, whereupon most of the diffraction cones are intercepted, giving a pattern based on concentric circles (Figure IV. 4) since no orientation is considered. But, because of the semi-crystalline nature of polymers, a monochromatic X-ray beam scattered by a polymer will generate a diffraction pattern consisting of a number of relatively sharp concentric circles (from randomly oriented crystallites) superposed on a background of diffuse X-ray scatter (from the amorphous phase).

In this case, the diameter 2R of each circle is measured and the Bragg angle is calculated using:

$$\tan 2\theta = \frac{R}{D} \qquad \text{(IV. 8)}$$

where D is the specimen to film distance.

Finally the d-spacing of a reflection is given by:

$$d = \frac{\lambda}{2\sin\left[\frac{1}{2}\tan^{-1}\frac{R}{D}\right]} \qquad \text{(IV. 9)}$$

The measured d-spacings are compared with those calculated for various sets of hkl planes of unit cells with different structures and dimensions. In the case of the orthorhombic structure ($a \neq b \neq c$, $\alpha=\gamma=\beta=90°$), the interplanar spacing is:

$$d_{hkl} = \left(\frac{h^2}{a^2} + \frac{k^2}{b^2} + \frac{l^2}{c^2} \right)^{-\frac{1}{2}} \qquad \text{(IV. 10)}$$

For the (110) and (200) planes, the interplanar spacing are, respectively:

$$\begin{aligned} d_{110} &= 4.11\text{Å}, \\ d_{200} &= 3.70\text{Å} \end{aligned} \qquad \text{(IV. 11)}$$

Thus, by comparing the interplanar spacing measured with the one calculated using equation IV.5 and by noting the absence of any additional (e.g. monoclinic) peaks, the orthorhombic structure of the different sample can be verified.

As we said earlier, for the wide angle diffraction pattern of an unoriented sample, each interplanar distance yields a circular diffraction ring. The effect of the presence of any preferred orientation is to transform these circles into an arc or sickle-shape. Thus, a quick orientation check of our samples is to determine the absence or presence of any intensity variation within the diffraction ring in the diffraction pattern.

IV.3.3.2. Small angle X-ray scattering.

Because polymers consist of an alternation of crystallites and amorphous regions, the electron density distribution is heterogeneous. These inhomogeneities take place over distances which are large in comparison with the wavelength of the X-rays and therefore the resulting interference is only visible at small angles.

As we said earlier, X-rays diffraction is ruled by the Bragg equation (IV.1). But, in this case, the term d denotes the periodicity of the alternation of crystalline and amorphous regions as presented in figure IV.2. It is named the long spacing, L.

VI.3.3.3. Experimental results.

Experimentally, we have used, for both WAXS and SAXS a CuK_α X-ray source which gives a monochromatic beam with a wavelength of 1.542 Å. In the case of the WAXS experiments, we used a Worhus flat plate camera with three different film positions. We have employed the second film position. In order to determine with accuracy the sample to film distance (D), we had to calibrate the camera using the diffraction pattern of a reference with a known interplanar spacing. A powder of $CaCO_3$ with a d-spacing of 3.035 Å was used for this purpose. The sample to film distance (D) was measured to be 72.8 mm.

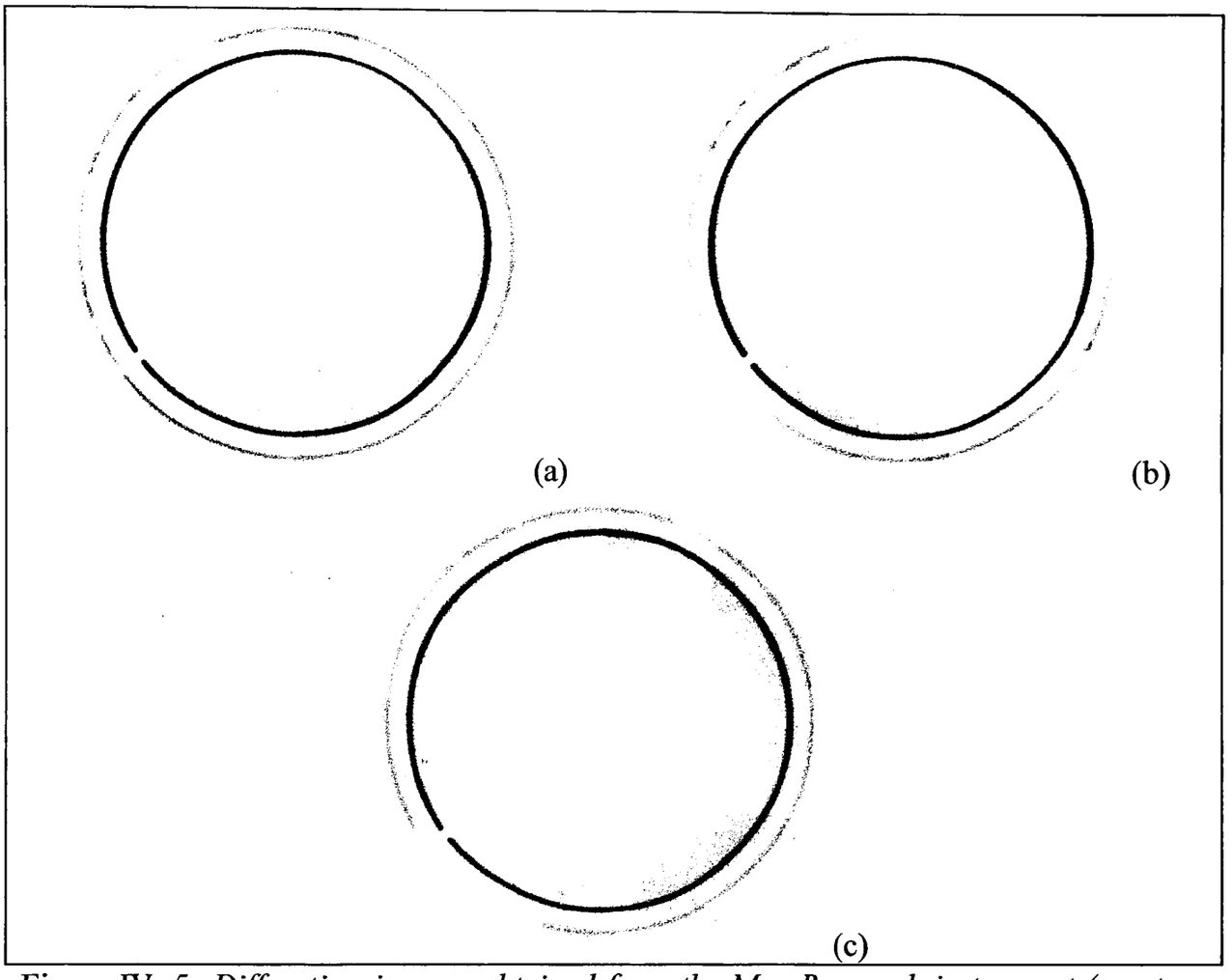

Figure IV. 5: *Diffraction images obtained from the Mar Research instrument (courtesy of Dr. G. Ungar, Sheffield University) for samples (a) LL/95/385/1.0; (b) LC/95/181/1.0; and (c) CC/95/181/1.0. The exposure time was 5 minutes. In all cases, no sign of a preferred orientation was found. The centre spot corresponds to the beam stop.*

Also for the WAXS measurements, we have used a Mar Research instrument with an image plate detector, courtesy of Dr. G. Ungar from the University of Sheffield. The sample to detector distance was 186.85 mm.

Figure IV. 5 is an example of the picture obtained using the Mar Research instrument. The samples are (a) LL/95/385/1.0; (b) LC/95/181/1.0; and (c) CC/95/181/1.0. As can be seen, only two circles are visible. No intensity variation along the scattering circles is visible, and thus no preferred orientation is present in all three samples. Similarly, no sign of preferred orientation was found in the other samples.

By plotting the intensity of the scattered beam as a function of the magnitude of the scattering vector **q** ($q = \frac{4\pi}{\lambda}\sin\theta$ as defined in chapter II.2.1), the d-spacing defined by equation IV.6 is then:

$$d = \frac{2\pi}{q} \qquad \text{(IV.12)}$$

Figure IV. 6 is a such plot for samples (a) LL/95/385/1.0; (b) LC/95/181/1.0; and (c) CC/95/181/1.0. The d-spacings measured for peaks 1 and 2 are respectively:

(a) $d_1 = 4.154$ Å

$d_2 = 3.743$ Å

(b) $d_1 = 4.221$ Å

$d_2 = 3.759$ Å

(c) $d_1 = 4.179$ Å

$d_2 = 3.779$ Å

By comparing these values with the orthorhombic interplanar spacings from equation IV.11, good agreement is found between d_1 and d_{110} and d_2 and d_{200}. Thus the first diffraction peak in picture IV.4 corresponds to diffraction from orthorhombic (110) planes, while the second arise from diffraction from orthorhombic (200) planes. Because no additional peaks (monoclinic) are present, the structure of all three samples is orthorhombic. Similarly all the other samples used in this thesis have an orthorhombic structure prior too deformation.

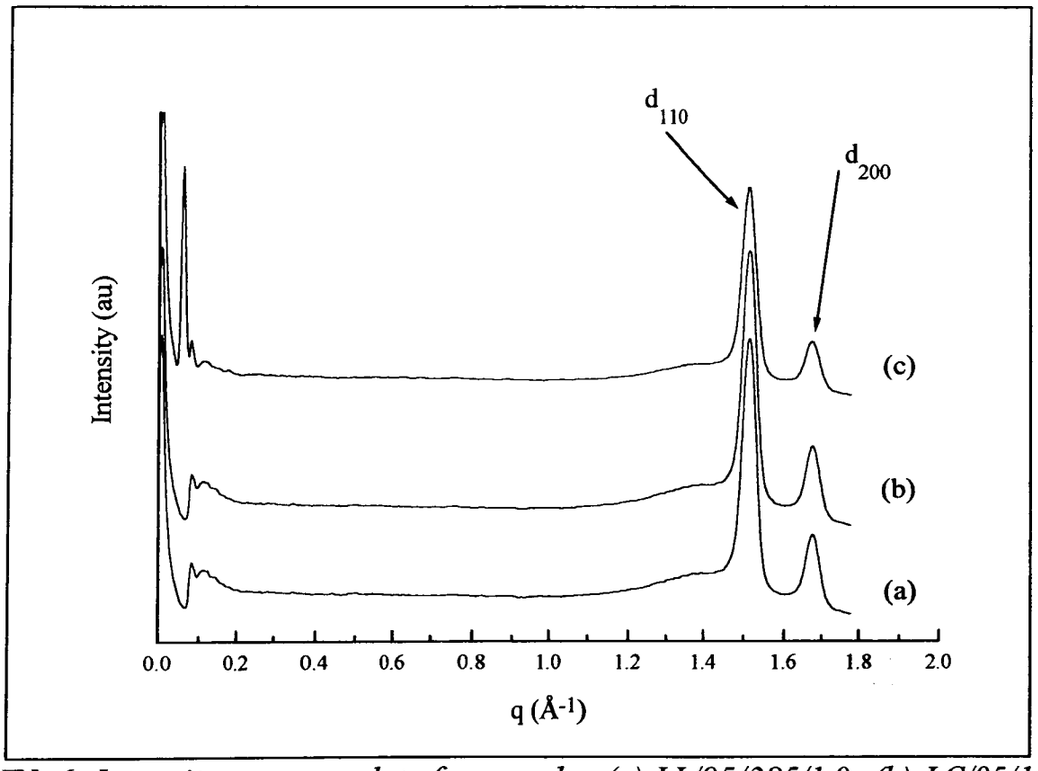

Figure IV. 6: *Intensity versus q plots for samples (a) LL/95/385/1.0; (b) LC/95/181/1.0; and (c) CC/95/181/1.0. The d-spacing is calculated with equation IV.12. The more intense peaks correspond to diffraction from orthorhombic (110) planes, while the smaller ones refer to orthorhombic (200) planes. No monoclinic peaks are present.*

The long spacings of some of the samples were measured with a small-angle X-rays Rigaku-Denki camera (courtesy of Dr. G. Ungar from the University of Sheffield). The sample to film distance (D) was of 264 mm. The long spacings measured, L_{SAXS} are listed in Table IV. 3 along with the long spacing derived from the DSC measurements, L_{DSC}.

Sample	L_{SAXS} (Å)	L_{DSC} (Å)
LL/95/385/1.0	254±13	449±39
LL/413/385/1.0	269±7	485±42
CL/95/385/1.0	259±14	396±34
LC/95/181/1.0	203±13	300±26
CC/95/181/1.0	185±15	355±31

Table IV. 3: *Comparison of the long spacing measured with SAXS, L_{SAXS}, with the long spacing derived from the DSC measurements, L_{DSC}.*

The difference between the DSC and SAXS values of long spacing results from the way the two techniques sample the polymer structure. Application of the Gibbs-Thompson equation to the peak melting temperatures implies measurement of the crystals at the top end of the thickness range. SAXS, on the other hand, responds to the weight average crystal thickness. Thus good agreement between the two techniques is, therefore, not expected with the SAXS values bound to be smaller [5].

IV.3.4. FTIR spectroscopy.

In order to carry out the hydrogenous polyethylene matrix subtractions in the neutron scattering analysis (see chapter II), the true isotopic concentrations in our samples need to be known. As stated at the beginning of this chapter, our samples consist of 95 or 97% of hydrogenated polyethylene mixed with 5 or 3% of deuterated polyethylene. But because some material may be lost during the different stages of the sample preparation, it is necessary to verify the isotopic concentration of the final product. For this purpose, we used infrared spectroscopy. FTIR also gives a means of verifying the homogeneity of the sample blend.

As we said in the chapter III, the intensity of an infrared absorption peak is, according to the Lambert-Beer law, proportional to the concentration of the absorbing units and the sample thickness. In our case we have two different absorbing units in the sample, the

hydrogenated polyethylene and the deuterated polymer. Thus the ratio, r, of the intensity of the infrared CH_2 bending and CD_2 bending bands is:

$$r = \frac{I_{\nu_{CD_2}}}{I_{\nu_{CH_2}}} \propto \frac{c(D)}{c(H)} \qquad \text{(IV. 13)}$$

where c(D) is the concentration of deuterated polyethylene and c(H) of hydrogenated polyethylene. Because c(H)=1-c(D), the concentration of deuterated polyethylene is:

$$c(D) \propto \frac{r}{1+r} \qquad \text{(IV. 14)}$$

The proportionality constant was then obtained through calibration samples of known deuterated polyethylene concentration.

The calibration samples have been prepared by mixing the isotopic species in boiling xylene, in the same way as for the other samples. Then a drop of the hot mixture was cast onto one KBr disc. The resulting gel was dried in order to remove all traces of solvent. Finally, an infrared spectrum was taken and the intensities of the different bands measured. A linear fit to the plot of the D-concentration as a function of r/(1+r) gives the proportionality constant. Thus, equation IV.14 becomes:

$$c(D) = 169.7\frac{r}{1+r} \qquad \text{(IV. 15)}$$

For all the samples studied in this thesis, the composition of the blends was around 5% of deuterated polymer and 95% of hydrogenated polymer.

Because of the difference in melting temperature between deuterated and hydrogenated polyethylene, fractionation can occur during crystallisation from the melt, leading to a concentration gradient in the crystals. As both the techniques of Mixed Crystal Infrared Red and Neutron Scattering rely on a statistical distribution of the labelled polymer within the unlabelled matrix, the homogeneity of the sample must therefore be checked. This is done by checking the splitting of the CD_2 bending mode in the infrared spectrum of each sample.

As explained in chapter III, the size of the CD_2 bending splitting is related to the number of nearest labelled neighbours. When fractionation occurs, larger clusters of deuterated polyethylene are present, leading to an abnormally large CD_2 bending splitting ($\Delta\nu\{(110)_\infty(110)_\infty\} = 10.2\ cm^{-1}$ for PED itself, see Table III. 2).

In order to check the homogeneity of our samples, a fractionated sample (LL/76/86) was made by slow cooling a melt (0.5°C min^{-1}). As expected , the infrared CD_2 bending splitting from the slow cooled sample was very large ($\Delta\nu$ = 9.8 cm^{-1}) in comparison with the different quenched samples as shown in Figure IV. 7.

All the samples used in this thesis show no sign of isotopically fractionation on the basis of our infrared results.

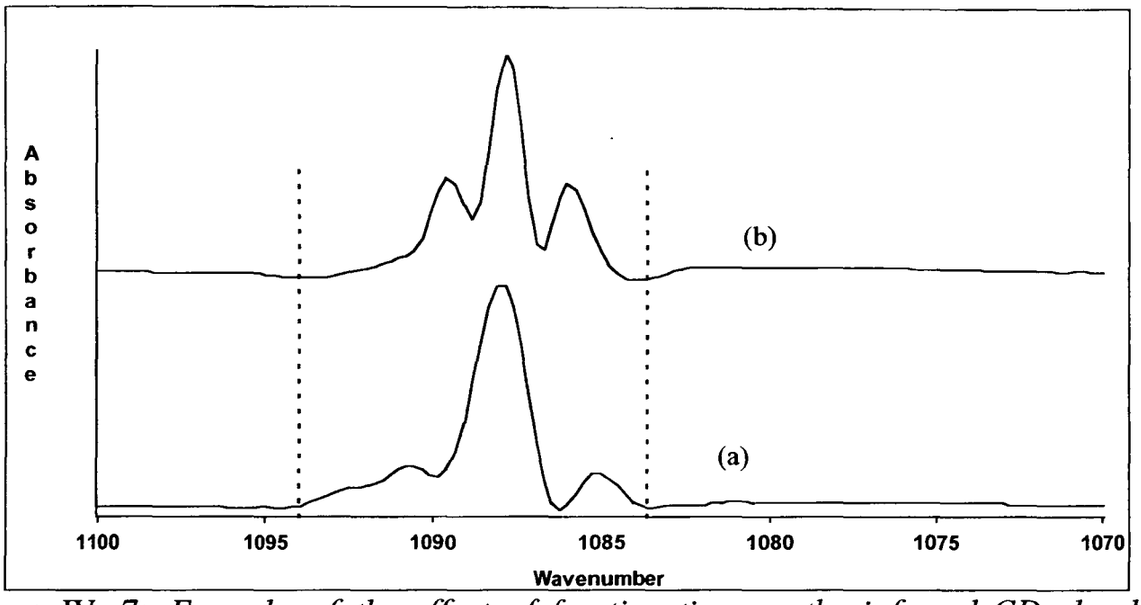

Figure IV. 7: *Example of the effect of fractionation on the infrared CD_2 bending splitting. (a) a fractionated sample (LL/76/86) obtained by slow cooling (0.5°C min^{-1}) the melt, and (b) the same sample obtained by quenching the melt. As it can be seen, the outermost splitting is far larger ($\Delta\nu$ = 9.8 cm^{-1}) in the case of the fractionated sample (a) than in the case of the melt quenched sample (b).*

IV.4. Conclusion.

In this chapter we have presented the characterisation results for the different samples prior to drawing.

All the samples have an orthorhombic structure, with no sign of monoclinic structure present (WAXS). No preferred orientation prior to drawing was found (WAXS). The different characteristics, such as crystallinity, long spacing (DSC and SAXS) are similar to those found in the literature, taking into account that our samples are crystallised by quenching a melt.

The statistical distribution of the labelled polymer within the hydrogenated matrix has also been demonstrated (FTIR).

---

[1] B. Wunderlich, *Thermal Analysis*, Academic Press, New York, 1990.
[2] M.F. Butler, A.M. Donald, and A.J. Ryan, *Polymer*, **38**, 5521 (1997).
[3] FC. France, P.J. Hendra, W.F. Maddams and H.A. Willis, *Polymer*, **28**, 710 (1987).
[4] J.M. Lagarón, S. López-Quintana, J.C. Rodriguez-Cabello, J.C. Merino and J.M. Pastor, *Polymer*, **41**, 2999 (2000).
[5] R. G. Matthews, A.P. Unwin, I.M. Ward and G. Cappacio, *J. Macromol. Sci. Phys.*, B38(1&2), 123 (1999).

Chapter five:

Experimental results on undeformed samples.

In this chapter, we will present the neutron scattering and infrared spectroscopy results obtained prior to deformation of the sample. These results will be used as a reference for the study of the molecular rearrangement during the cold drawing of thin films of polyethylene.

In this study four different combinations of deuterated guest in hydrogenated host were used:

(a) Linear D-guest in Linear H-host (LL sample).

(b) Copolymer D-guest in Linear H-host (CL sample).

(c) Linear D-guest in Copolymer H-host (LC sample).

(d) Copolymer D-guest in Copolymer H-host (CC sample).

The different molecular weights of the different raw materials are listed in the previous chapter table IV.1.

Several linear H-matrices were used: two with a low molecular weight (NR1, M_w = 86000, and NR(A3N), M_w = 90300, both courtesy of Dr. Barham, University of Bristol), and one with a high molecular weight (HM5420, M_w = 385000 from BP Chemicals). Because of availability, only one copolymer H-matrix was used (002.40NAT, M_w = 181000, with 6 C_4 branches per 1000 carbons from BP Chemicals). In order to study the effect of chain branching and molecular weight on the molecular rearrangement with cold drawing, sample LL/95/385 was used as a "baseline".

Here, we will show that while the neutron scattering radii of gyration prior to deformation for the different linear and copolymer samples of the same molecular weight are similar, their local stem arrangements, as determined by infrared splittings, are different.

V.1. Neutron scattering results.

For the neutron scattering experiments, at both ILL and ISIS, samples of typically 100mg were placed in the beam. This was achieved by stacking approximately ten pieces of the sample (cut from the original thin film, as seen in chapter IV) and wrapping them in aluminium foil. The small aluminium parcel was then placed in the neutron beam for approximately 20 minutes in the case of the ILL experiments and 2 hours in the case of the ones carried out on the pulsed source of ISIS.

The scattering signal from the isotopic blend was considered to be a simple superposition of (i) a signal from the empty aperture and from the aluminium foil, (ii) incoherent scattering, (iii) a coherent scattering signal $I_\rho(q)$ due to density differences between crystals and the disordered regions, cracks, voids, and, possibly, impurity, and (iv) the desired molecular scattering , I(q) arising from the isotope difference. The additivity of $I_\rho(q)$ and I(q) depends on the corresponding scattering length fluctuation being uncorrelated in space. In practice, the collected data were cell subtracted and radially averaged, using respectively, the program COLETTE for ISIS experiments and RNILS and XPOLY for the ILL ones. Simple subtraction procedures were used to remove the dependence of (ii) and (iii) of I(q) by subtracting the scattering of a 100% hydrogenous sample. Finally the coherent scattering was normalised as explained in chapter II section 4.

The thickness of the samples in the beam, t, was calculated from the average transmission, T, of a given sample by:

$$t = \frac{\ln 1/T}{N\sigma_T} \qquad \text{(V. 1)}$$

where N is the number of scatterers per volume and σ_T the total cross section. Because the concentration of deuterated polyethylene and the total cross section of the deuterated monomer are very small in comparison to the ones of the hydrogenated component, we can make the following approximations: $N \approx N_{CH_2}$ and $\sigma_T \approx \sigma_T^{CH_2}$, where N_{CH_2} and $\sigma_T^{CH_2}$ are respectively the number of CH_2 groups per unit volume and the total cross section of the protonated monomers. They are respectively equal to (d is the density of polyethylene):

$$N_{CH_2} = \frac{N_A}{M_{CH_2}} d = 4.3 \times 10^{22} \text{ groups.cm}^{-3}$$
$$\sigma_T^{CH_2} = 170.2 \times 10^{-24} \text{ cm}^2 \qquad \text{(V. 2)}$$

V.1.1. Radius of gyration and Molecular weight measured by SANS.

Figures V. 1 and V. 2 include Zimm plots of undrawn quenched films for the four different combinations of DPE guest in HPE matrix. The low molecular weight DPE guest is represented in Figure V. 1 and the high molecular weight guest is shown in Figure V. 2.

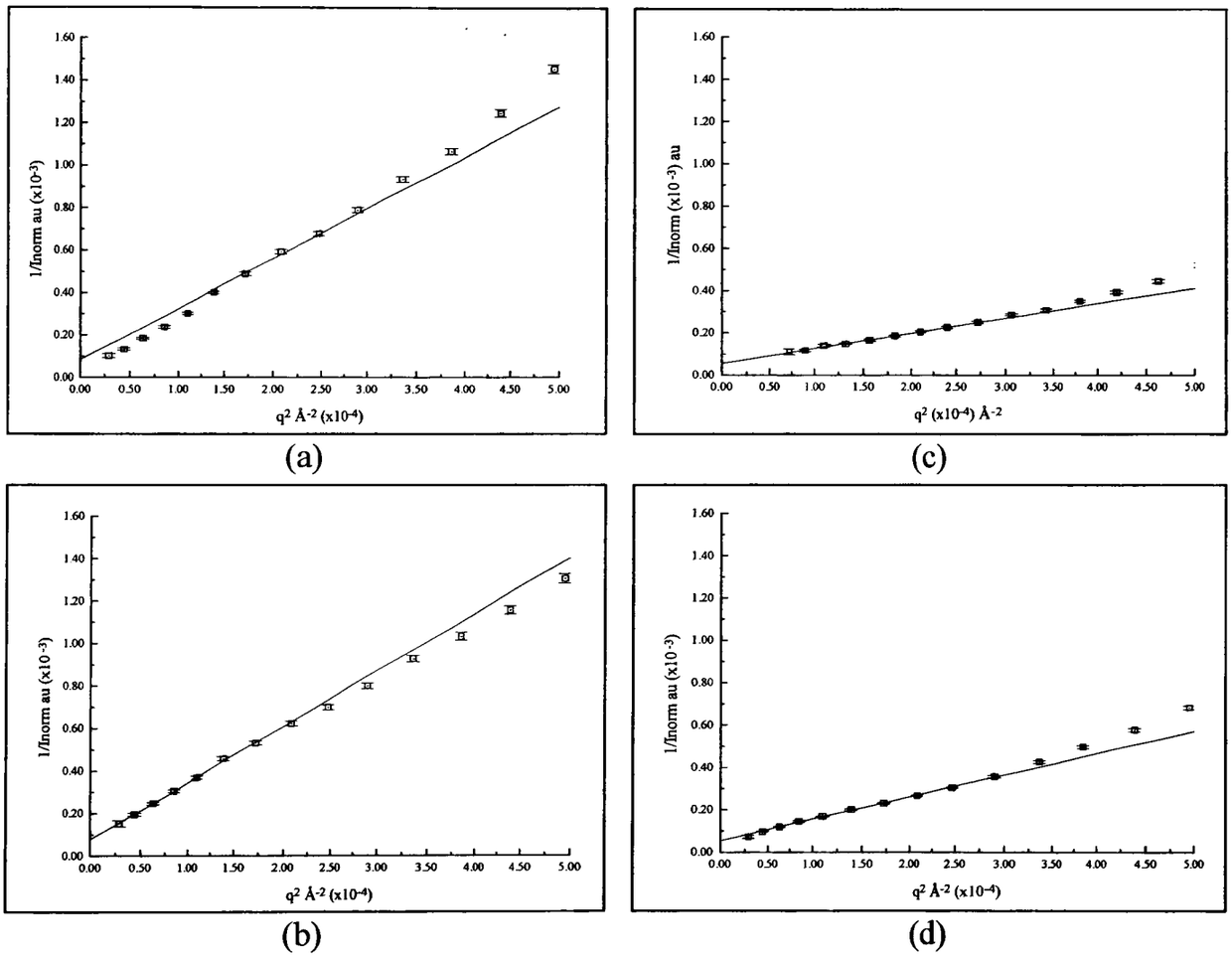

Figure V. 1: *Zimm plots for the different combination of low molecular weight DPE in HPE matrix. (a) Sample LL/95/385 (ILL);(b) sample LC/95/181(ILL); (c) sample CL/95/385 (ISIS); and (d) sample CC/95/181 (ILL). The straight lines are least squares weighted fits of the linear regions of the Zimm plots.*

Most of the Zimm plots presented were obtained with data collected with D11 at ILL; only the Zimm plot of CL/95/385 (Figure V. 1c) was obtained from data measured at ISIS. It can be seen that this plot does not reach as low q values as for the measurements made at ILL.

In the case of the low molecular weight DPE guest, the plots are highly linear, even to relatively large value of q^2. For sample LL/95/385 (Figure V. 1a), there is a departure of 1/I(q) below the line of the best fit for the few measurement points at the smallest q values. This could result from two different factors. The first one is an inadequate H-Blank subtraction which may result from a wrong estimation of the DPE concentration. As shown in Chapter 4, the DPE concentration was calculated from the FTIR spectra. Since the DPE concentration was checked several times, it is not believed that the departure observed at low q values results from an inadequate H-Blank subtraction. The second reason is the presence in the quenched blend of isotopic fractionation, which would result in a higher I(q) at the very low q values than is expected (see chapter I.1.3 and reference 1). In the case of sample LL/95/385, the departure from the expected Zimm plot is very small in comparison with previous fractionated data [1], particularly for the q=0 intercept. This suggests that, if isotopic fractionation was present, it is not a dominant effect. Therefore it is unlikely to affect the analysis here. In this case, the intercept of the linear fit was fixed to obtain the molecular weight value measured by GPC, and the linear fit was taken as tangent to the concave plots, a similar procedure to that used by Sadler et al [1].

For the high molecular weight linear DPE guest, the linear regions of the Zimm plots (Figure V. 2a and b), where the Zimm approximation is valid, are very small, including at most only two experimental points. As with sample LL/95/385 (Figure V. 1a), the intercept of the least squares fit was fixed to obtain the value of the molecular weight measured by GPC. Why this curvature occurs is not fully understood. It may be due to inadequate blank subtraction or to the presence of impurities. Indeed, catalyst residue were detected by XRF in the high molecular weight linear DPE guest (around 3 % of silicate residue were found). For the copolymer DPE, the Zimm plots are highly linear (Figure V. 2c and d).

From both Figure V. 1 and V. 2, the Zimm plots for the same type of DPE guest are very similar to each other, whichever the HPE matrix used. When comparing the linear DPE guest with the copolymer one, the Zimm plots appear very different, with the scattered intensity from copolymer DPE guest being greater than in the case of the linear guest. Another feature comes when comparing the two different types of DPE guest is that the Zimm plots for copolymer DPE guests are highly linear, even for the high molecular weight. However, these differences are not reflected in the R_g values obtained from the

least squares fits, which are very similar for the different types of DPE guest (Table V. 1).

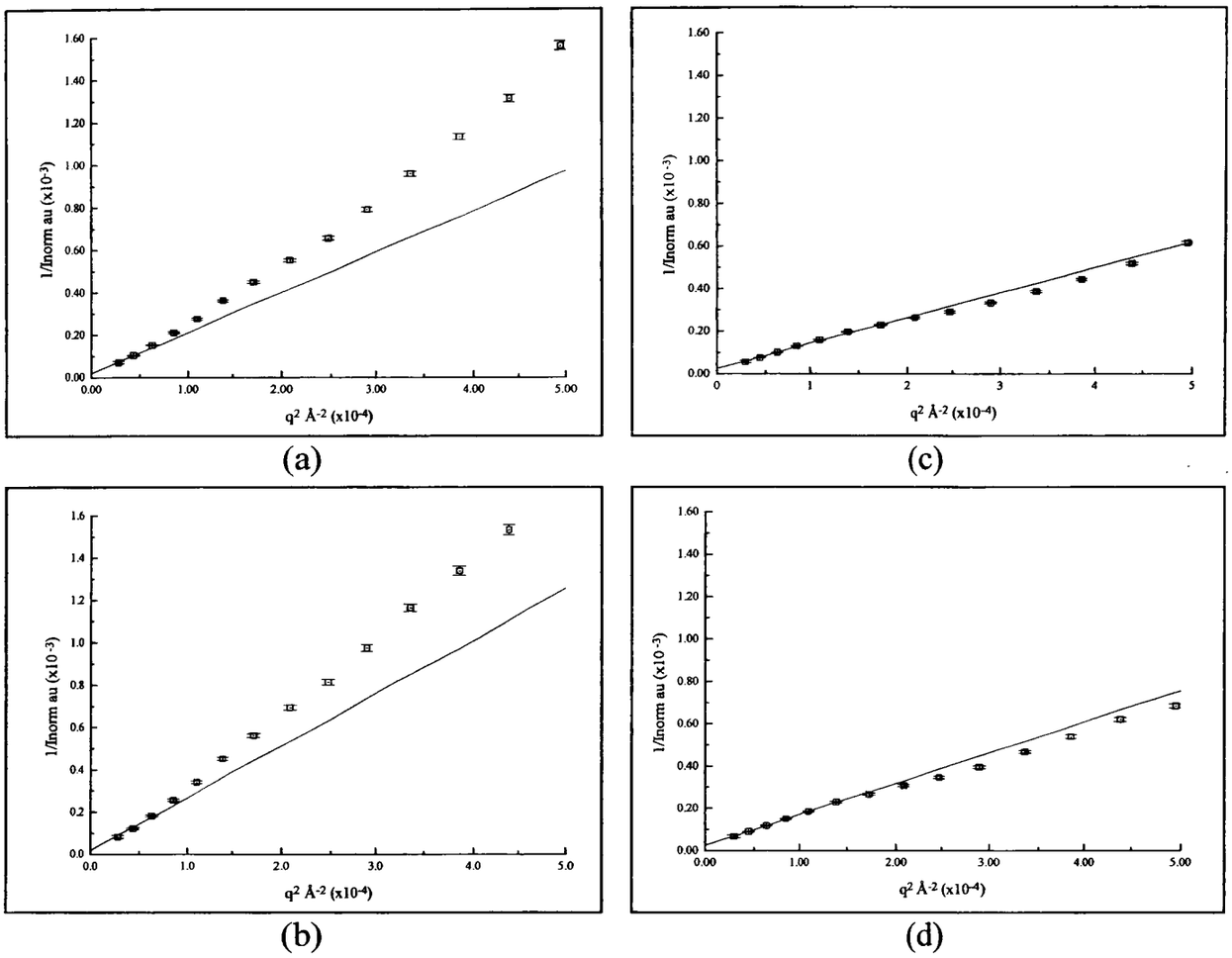

Figure V. 2: *Zimm plots for the different combination of high molecular weight DPE in HPE matrix. (a) Sample LL/413/385 (ILL);(b) sample LC/413/181(ILL); (c) sample CL/378/385 (ILL); and (d) sample CC/378/181 (ILL). The straight lines are least squares weighted fits of the linear regions of the Zimm plots.*

The R_g and molecular weight values derived from the least square fits of the small angle data are reported in Table V.1 for the different combinations of deuterated guest in hydrogenated host (LL, LC, CL and CC), obtained from the instruments LOQ (ISIS) and D11 (ILL).

Concerning the LOQ measurements, these were performed during 5 different experimental periods. The ILL measurements were carried out later in order to reach much higher deformations, leading to R_g values which were not measurable at ISIS, and also to validate the values of R_g measured at ISIS.

R_g and the $\overline{M}_W$ values were calculated respectively from the slope and intercept of the linear fits as explained in chapter II.5.2. We will briefly recall the relationship between the intercept, a, and the slope, b, of the least square weighted fit:

$$\overline{R_g^2} = \frac{3b}{a}$$
$$\overline{M}_w = \frac{8.0175}{a} \qquad (V.3)$$

Practically, less then five experimental points were usually present in the linear region of the Zimm plot; therefore, only these points were used in the linear fitting procedures. This fitting process involved using the experimental intensity errors as weighting factors.

It is important to note that the uncertainty in R_g, as listed in Table V. 1, results from least squares weighted fits on a very small number of points, and therefore may be underestimated. This suggests that the uncertainties on R_g are bigger than the reported ones in Table V. 1. A good estimation of the error would be around 20%.

	ISIS		ILL	
	R_g (Å)	$\overline{M}_w$ ($\times 10^{-3}$)	R_g (Å)	$\overline{M}_w$ ($\times 10^{-3}$)
LL/136/86	233±42	160±19	/	/
LL/95/86	236±31	150±13	/	/
LL/76/86	155±15	63±2	/	/
LL413/90**	260±18	413*	/	/
LL/95/385	269±14	95*	291±15	95*
LL/413/385**	509±40	413*	543±45	413*
LL/413/385/MM**	408±33	413*	376±43	413*
LC/95/181	319±34	175±25	318±21	102±4
LC/413/181**	/	/	618±33	413*
CL/378/385**	363±41	570±42	371±35	310±20
CL/95/385**	209±14	144±6	/	/
CL/378/90**	234±41	1458±170	210±24	367±27
CC/95/181**	/	/	237±18	146±7
CC/378/181**	/	/	410±27	308±14

Table V. 1: *Radius of gyration (R_g) and molecular weight ($\overline{M}_w$) for the different combinations of deuterated (DPE) guest in hydrogenated (HPE) host measured using the LOQ instrument at ISIS (Didcot, England) and the D11 instrument at ILL (Grenoble, France). The * is for samples where the intercept was fixed during the process of the linear fitting of the SANS data to make use of the molecular weight value measured by GPC. ** Metallocene catalysed DPE guest molecules.*

As can be seen, both the radii of gyration calculated using ISIS and ILL data are in good agreement. Consequently, in the following parts of this thesis, only the weighted average values of the two measurements will be quoted.

The values of R_g from LL samples tabulated are of the same order as the ones listed by Sadler and Barham [2] for melt quenched polyethylene of equivalent molecular weight and (in ref. 2, the R_g values are listed as $R_x^2=1/3\ R_g^2$), although they are generally a little larger here. These values are all higher than previously published data for melt quenched linear polyethylene film [3, 4, 5, 6]. However, as in reference 2, an unfractionated HPE matrix was used here, which may explain the higher R_g values measured in both cases. Such effects of matrix type are discussed later.

From Table V. 1, eleven samples gave linear Zimm plots over a range of q similar to that shown in Figures V. 1 and V. 2. For those cases, where the plots were demonstrated to be linear, a molecular weight was calculated from the intercept intensity determined by the least squares fits. As shown, the agreement between the $\overline{M}_w$ measured by GPC and calculated from the neutron scattering data are well within a factor of 2 (except for the CL/95/90 which will be explained in the next paragraph).

Only the plots from samples containing the linear high molecular weight HPE matrix ($\overline{M}_w$=385000), or containing the linear high molecular weight DPE ($\overline{M}_w$=413000) guest were not linear. In those cases, the least square fits were made as tangents to the curvature and the intensity intercepts were fixed in order to obtain the $\overline{M}_w$ values measured by GPC as shown in Figure V. 1a and V. 2a, b. The high molecular weight linear DPE guest host gave a large curvature, with a linear region containing only two experimental points. This abnormal curvature may result from the presence of impurity in the deuterated polyethylene. After discussion with BP Chemicals, catalyst residues were discovered in the high molecular weight DPE guest by XRF. Also, the small linear region means that, in order to measure correctly the R_g for this guest, a lower q range must be reached. This suggests that the molecular weight is too high for satisfactory measurements with these instrument parameters.

The low molecular weight linear DPE ($\overline{M}_w$=95000, Figure V. 1a for example) presented a very small fractionation signal, too small to have much physical significance, as mentioned earlier.

	α
LL/X/385	0.48±0.04
CL/X/385	0.45±0.06
LC/X/181	0.48±0.03
CC/X/181	0.40±0.05

Table V. 2: *Results of the least squares fits on the evolution of R_g as a function of the molecular weight of the DPE guest ($R_g \propto \overline{M}_w^{\alpha}$) presented in* Figure V. 1.

Figure V. 3 shows the dependence of R_g on $\overline{M}_w$ for (a) the measurements made by Sadler and Barham [2] on linear DPE guest in a linear HPE matrix and (b)-(f) our measurements. All the plots are shown in a logarithmic form. The value of the exponent, α, for the dependence of R_g on $\overline{M}_w$ ($R_g \propto \overline{M}_w^{\alpha}$) is obtained from the slope of a least squares fit on such data. The results of the least squares fits are listed in Table V. 2.

The evolution of R_g as a function of $\overline{M}_w$ for the linear samples (Figure V. 3b, c) is similar to the published data, with an exponent value around 0.45. In the case of the LC and CL types, the exponent in the dependence of R_g in $\overline{M}_w$ is similar, within the experimental errors, to that for the LL type samples. Only for CC type samples, is a lower value of α found (α=0.40±0.05) but this is still in agreement to within the experimental errors. This may suggest that the guest copolymer molecules in this case crystallise in a less dispersed way than for the others types of samples. But, because only two different molecular weight copolymer DPE samples were at our disposal, this difference may not be significant.

Finally, these results show that all the different types of samples have similar dependence of R_g on the $\overline{M}_w$ of the guest molecule and are consistently slightly lower than 0.5 (0.5 is the exponent value expected for a random coil system).

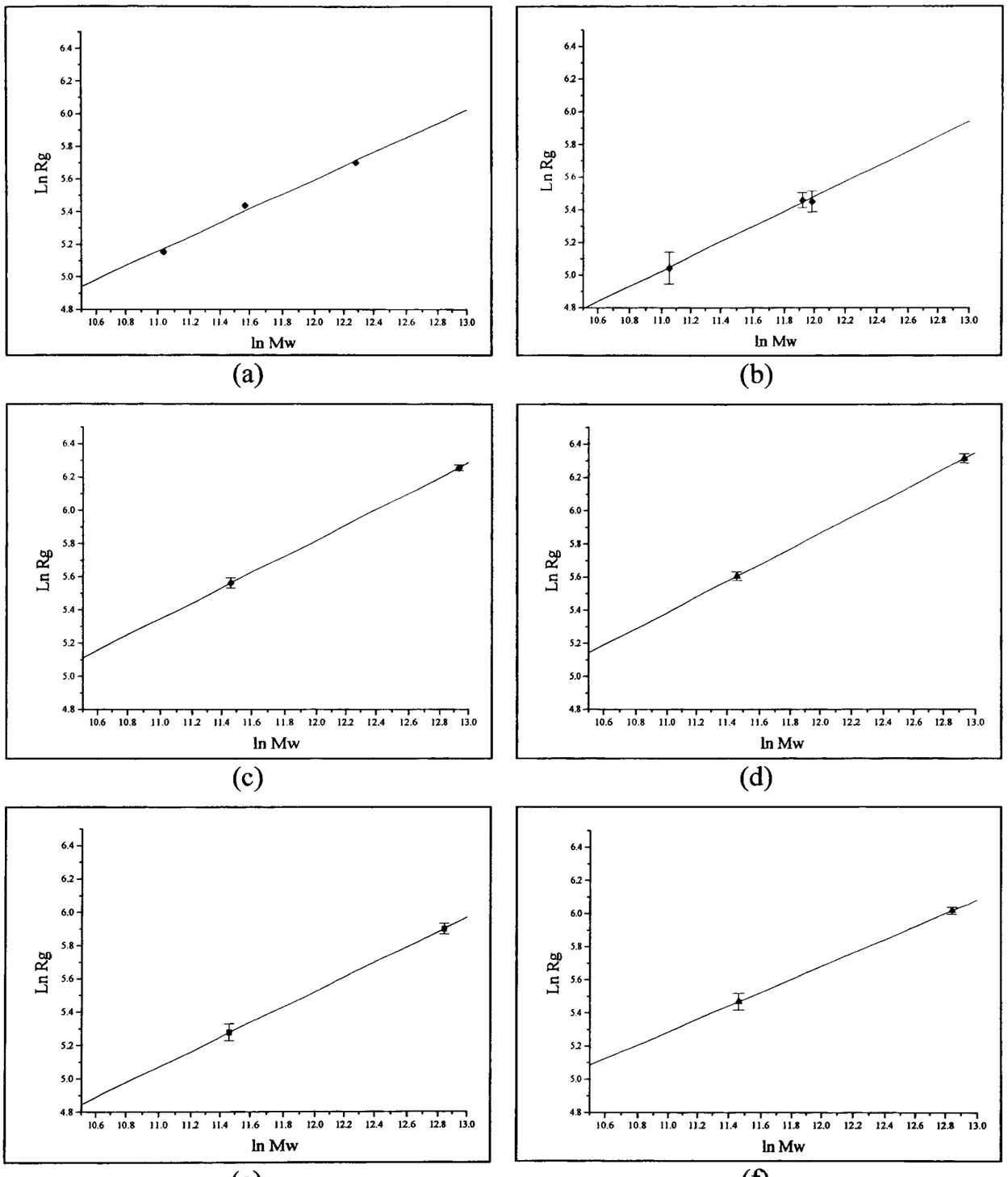

Figure V. 3: *Behaviour of the radius of gyration as a function of the molecular weight plotted in logarithmic from. The lines are linear fits where the slope give the exponent of the relationship* $R_g \propto \overline{M}_W^{\alpha}$ *for (a) Measurements from Sadler and Barham* [2] *on linear samples,* $\alpha=0.44\pm0.05$*; (b) LL/X/86,* $\alpha=0.46\pm0.06$*; (c) LL/X/385,* $\alpha=0.47\pm0.04$*; (d) LC/X/181,* $\alpha=0.48\pm0.03$*, (e) CL/X/385,* $\alpha=0.45\pm0.06$*; and (f) CC/X/181,* $\alpha=0.40\pm0.05$*.*

V.1.1.1. Effect of the molecular weight of the linear matrix on R_g.

In this part we will look at the change in R_g for the same DPE guest when varying the molecular weight of the linear matrix, as shown in Table V. 1. The average R_g values are recalled in Table V. 3:

ID	$<R_g>$ (Å)
LL/95/86	236±31
LL/95/385	279±10
LL/413/90	260±18
LL/413/385	524±30
CL/378/90	216±20
CL/378/385	367±27

Table V. 3: *Evolution of the average radius of gyration for the same DPE guest when changing the molecular weight of the linear HPE matrix.*

For the low molecular weight DPE molecules ($\overline{M}_W$ = 95000), almost no changes have resulted from increasing the molecular weight of the linear HPE matrix, which is as expected. This is not the case for the high molecular weight linear and copolymer guests ($\overline{M}_W$ = 413000 and $\overline{M}_W$ = 378000 respectively), where the R_g have almost doubled when increasing the molecular weight of the matrix (from 90000 to 413000). We should also note the dependence of R_g on $\overline{M}_W$ for samples LL/95/86 and LL/413/90, which have almost the same R_g. It appears that the guest molecules has not expanded as would be expected. This suggests that some kind of fractionation between the guest and host has occurred during the crystallisation process. The molecular weight distributions of both the DPE and HPE materials are very narrow ($\overline{M}_W/\overline{M}_N$ = 2.6 and $\overline{M}_W/\overline{M}_N$ = 3 respectively). The big difference in molecular weight between the components and their narrow molecular weight distributions may have induced isotopic fractionation, where, in the extreme case, the DPE material forms clusters during quenching, within the HPE matrix. This phenomenon of isotopic fractionation leads to an abnormally small R_g and an excess of scattered intensity at very low q values. Both were observed for sample LL/413/90. The same explanation can be applied to sample CL/378/90, where the molecular weight distribution of the copolymer material is very narrow ($\overline{M}_W/\overline{M}_N$=

2.1): a low R_g value and very high molecular weight were obtained from the SANS experiment.

This effect of isotopic fractionation does not occur in samples with high molecular weight linear matrix ($\overline{M}_W$ = 385000, $\overline{M}_W/\overline{M}_N$ = 8) because its molecular weight distribution is wide and the molecular weight of the two components are closely matched.

As said earlier, signs of fractionation were present in sample LL/95/385, in measurements made at both ISIS and ILL. But because only a small fractionation signal was seen (Figure V. 1a) and because no signs of separate crystallisation were detected either by DSC and infrared measurements, it is not believed that isotopic fraction has occurred for this sample. It is suggested that because of the wide molecular weight distribution of the matrix, the guest molecules are "sampling" the matrix. In other words, the guest molecules may co-crystallise with the lowest molecular weight molecules (those with similar melting temperature) of the matrix and form zones enriched in DPE within the spherulites. This way, isotopic fractionation may be avoided because the distribution of the isotopic species is still random within the enriched DPE zones (if the local concentration in DPE is still sufficiently low). This would be consistent with the very small deviation from Zimm behaviour at very low q values (Figure V. 1a).

V.1.1.2. Effect of the type of the guest and host molecules on R_g.

In this part, we will look at the effect of the type of the molecules (guest or host) on R_g. The average values of R_g are recalled in Table V. 4 for the low molecular weight DPE and in Table V. 5 for the high molecular weight DPE.

ID	$\langle R_g \rangle$ (Å)	R_{gL} (Å)
LL/95/385	279±10	
CL/95/385	209±14	242 (M_W=91000)
LC/95/181	318±12	
CC/95/181	237±18	262 (M_W=91000)

Table V. 4: *Average values of R_g for the low molecular weight DPE. R_{gL} is the radius of gyration of a linear DPE of equivalent $\overline{M}_W$ to the copolymer guest.*

V.1.1.2.1. Replacing linear DPE by its copolymer counterpart.

When the linear DPE was replaced by its copolymer counterpart (in the same matrix, i.e. changing from LL to CL samples), the values of R_g have decreased by around 22% for the low molecular weight samples and by around 32% for the high molecular weight samples.

Remembering that the molecular weight measured by GPC for the copolymer materials took into account the molecular weight of the branches, the real molecular weight of the "linear chains" of the copolymer (without the contribution from the side chains) would be smaller than the one measured by GPC. From the characteristics of the raw materials listed in Table IV.1, the low molecular weight copolymer ($\overline{M}_W$=95000) has 6.3 hexyl (C_6) side chains per thousand carbon atoms and the high molecular weight copolymer ($\overline{M}_W$=378000) has 8 butyl (C_4) side chains per thousand carbon atoms. It is possible to estimate the true molecular weight of the main chain, $\overline{M}_{WL}$, and to calculate an equivalent linear radius of gyration, R_{gL} using the dependence of R_g on molecular weight for the different types of samples (the results of the linear fits are listed in Table V. 3).

The low and high molecular weight copolymer DPE would be equivalent to a linear DPE with a molecular weight, respectively, around 4% and 3% smaller. The estimated linear radius of gyration, R_{gL} values are listed in Table V. 4 and Table V. 5 for, respectively, the low and high molecular weight DPE according to the different dependence of R_g on $\overline{M}_W$ measured for the different sample types (Table V. 3).

ID	$\langle R_g \rangle$ (Å)	R_{gL} (Å)
LL/413/385	524±30	
CL/378/385	367±26	473 ($\overline{M}_{WL}$=367000)
LC/413/181	618±33	
CC/378/181	410±27	513 ($\overline{M}_{WL}$=367000)

Table V. 5: *Average values of R_g for the high molecular weight DPE. R_{gL} is the radius of gyration of a linear DPE of equivalent $\overline{M}_{WL}$ to the copolymer guest.*

Taking this into account, the R_g values measured for the copolymer guest are still smaller than the estimated R_{gL} values, by around 13% and 22% for respectively the low

and high molecular weight DPE for the linear matrix samples and by around 10% and 20% for the copolymer matrix blends.

As said earlier, the uncertainties in R_g are larger than the ones listed in the different tables, because very few points of the Zimm plots were used in the fitting process, and a reasonable estimation of the uncertainty in R_g would be around 20%. Consequently, the differences between the R_g measured and the R_{gL} estimated are within the experimental errors, and therefore may not be significant. However, it is notable that R_g values for copolymer DPE guest are consistently lower than predictions. A more compact molecular conformation may be thus indicated for the copolymer guest blends.

V.1.1.2.2 Replacing the linear matrix by a copolymer one.

When the linear matrix was replaced by a copolymer one, as for example samples LL/95/385 and LC/95/181, a slight increase in R_g was observed, in both the low and high molecular weight DPE guest (Tables V. 3 and V. 4), of around 13% for LL to LC low molecular weight samples, of around 13% for CL to CC low and high molecular weight samples and of around 17% for LL to LC high molecular weight samples.

These differences are smaller than the estimated uncertainties in R_g (which were estimated to be around 20%) and may not be significant, but they are consistently in the same direction. Also, because the proportionate increase seems to be independent of the molecular weight of the DPE guest, changing the linear matrix to a copolymer one may have resulted in a genuine increase in the R_g of the DPE guest.

It is known that short side chains tend to be excluded from the crystals [7, 8, 9] (see chapter I.2.2), leading to a decrease in crystallinity, to an increase of the number of tie-molecules [10], and to a decrease of the lamellar thickness. We have observed in chapter 4 Table VI.2, that the lamellar thickness decreased from 238 Å for LL/95/385 to 126 Å for LC/95/181. This reduction of lamellar thickness may be responsible for the apparent increase of R_g. However, as the radius of gyration depends on the other molecular dimensions, as well as on the c-axis one, it is not clear (without a specific model) whether R_g should increase with decreasing lamellar thickness. Also, this increase in R_g seems contradictory to the small alpha exponent determined from the evolution of R_g with increasing molecular weight. In view of these different points, and since the increase of R_g is of the order of the estimated uncertainties on R_g, this effect may not be significant.

V.1.2. The intermediate angle region.

In the intermediate q region ($q>0.1Å^{-1}$), the scattered intensities are related to the scattering of the basic "subunit" of the molecule. In the case of melt quenched polyethylene, the "subunits" are individual stems, for which the scattered intensity can be approximated by:

$$I(q) = I_C(q)C_2(q) \qquad (V.4)$$

where $I_C(q)$ is the normalised intensity for the 2 dimensional structure (see chapter II.4.2), $C_2(q) \approx \exp(1/2\,q^2R_0^2)$ is the intensity ratio for the actual polyethylene chain to an infinitely thin rod and R_0 is the root mean square of the distance of the hydrogen atoms from the axis of the molecule. For a single stem as subunit, $I_C(q)$ is given by:

$$I_C(q) = \frac{\pi n_L}{q} \qquad (V.5)$$

where n_L is the number of hydrogen atoms per unit length of stem. For a polyethylene molecule, $R_0 = 1.46Å$ and $n_L = 1.57Å^{-1}$.

The experimental data are presented in term of $I_C(q)$, where $I_C(q) = {}^{I(q)}\!/_{C_2(q)}$. A convenient way of representing the data involves plotting $I_C(q)q^2$ against q (a Kratky plot). In this format, an arrangement of isolated stems would produce a straight line plot passing through the origin. This provide a convenient way of illustrating departures from isolated stem scattering. Also, this representation allow comparisons with published data, especially with the Sadler and Harris "subunit model"[11].

Often, in the intermediate q region, the scattering from the crystal lattice (Bragg scattering), may add a contribution to the scattering from the subunit. In powder diffraction patterns, the Bragg scattering is proportional to the square of the structure factor, F_{hkl} which is defined by the following relation [12, 13]:

$$F_{hkl} = \sum_j b_j \exp(-i\tau_{hkl}.\mathbf{r}_j) \qquad (V.6)$$

where τ_{hkl} is a reciprocal lattice vector, $\mathbf{r}_j$ is the position vector of the j^{th} atom within a unit cell, and b_j is the coherent scattering length of the j^{th} atom. In order to remove the contribution of the "wings" of Bragg peaks from the scattered intensity at intermediate angles, this scattering (which starts with the {110} peak at $q=1.52Å^{-1}$ for polyethylene) can be fitted with a combination of exponential functions and subtracted from the

scattering intensity. Figure V. 4 shows experimental data replotted in this way. For clarity, the error bars are only shown in Figure V. 4a.

All the intermediate angle measurements were made using the high angle detector of the LOQ instrument at ISIS.

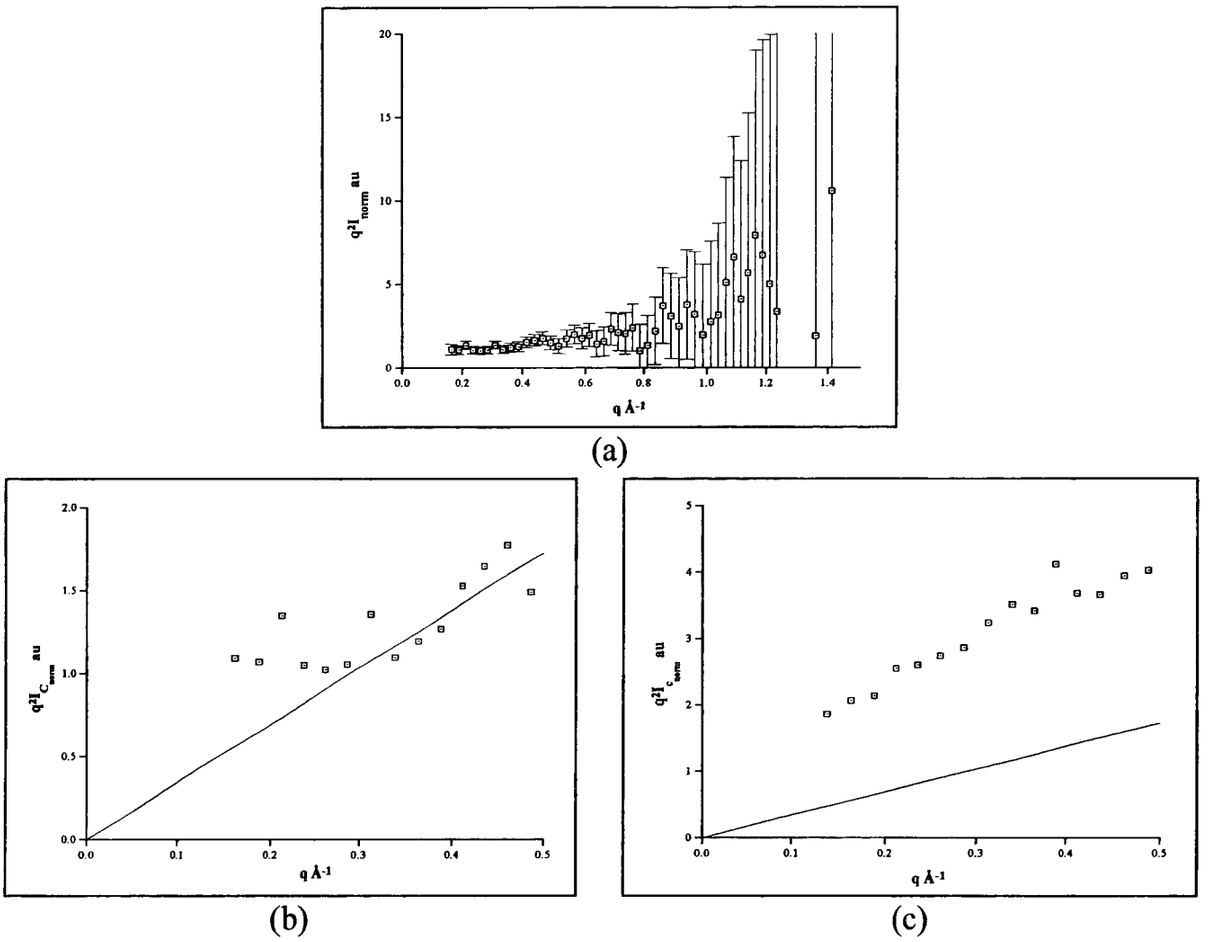

Figure V. 4: *IANS data plotted in a Kratky format, in which the single stem scattering gives a straight line. The line is that expected for single stem scattering, and corresponds to about 70% of the labelled chains being in the form the isolated stems. (a) LL/413/90 first showing the whole range and the error bars and (b)LL/413/90 for q<0.5Å, (c) for sample CL/95/385 showing excess scattering.*

Unfortunately, several problems made this analysis very difficult. The first one was the disagreement between the intensities measured from the SANS area detector and the HAB detector of LOQ. No physical reasons were found to explain this phenomenon. The second one arises from the Bragg scattering, which affected the intermediate region over an unexpectedly large q range. Thus, even after subtraction, some unwanted contributions were still present in the range studied, resulting in excess intensity as seen in Figure V. 4c. Another problem was the high degree of uncertainty in the intensity in this region, which was around 30% in the best case, and this even after 2 hours of data collection.

Finally, only one sample gave satisfactory results, sample LL/413/90 as presented in Figure V. 4b. It can be seen that the asymptotic behaviour is the straight line corresponding to isolated stems as the scattering units. The slope of this line is approximately 70% of that predicted if all the chains present are in form of straight stems. This result is very similar to what was observed by Sadler and Harris [11]. They have analysed their data in term of a "subunit" model, where the polyethylene molecule is described as composed of subunits (groups of a small number of stems) separated by a distance which is large in comparison to the stem separation within the subunit.

V.2. FTIR results on undeformed samples.

Because the intensity of an infrared absorption peak is dependent on the sample thickness, in order to compare different samples, the infrared intensities require normalisation. Usually, this normalisation is achieved by using the area of a non conformationally dependent band as reference, such as the CH_3 deformation (1378 cm^{-1}). However, this band appears only as a shoulder of the CH_2 wagging band (1365 cm^{-1}) in most of our samples, and also, a recent study [9] has shown that variation in intensity and frequency of the CH_3 deformation can occur as a function of the methyl group molecular envirronment. Therefore, this band may not be independent of the molecular rearrangement introduced by cold drawing and so cannot be used with confidence as a reference for the normalisation of the infrared spectrum.

As been observed by Okoroafor and Spells [14], the largest groups of labelled stems are broken down upon deformation into smaller groups and ultimately to single labelled stems. Therefore, the decrease in the area of the outermost doublets of the CD_2 bending region is compensated by an increase in the area of the singlet component, as a result of the conservation of area under the whole CD_2 bending region of the infrared spectrum. Hence we have used this area of the whole CD_2 bending region as our reference for the normalisation of the infrared spectra. In order to remove the dependence of the absorption on sample thickness, all the infrared spectra reported here were normalised using the area (calculated between 1080 cm^{-1} and 1095 cm^{-1} by integration) under the whole CD_2 bending region. In order to increase the splitting and to reduce the band width of individual components (as explained in chapter 3), all the infrared spectra were recorded at liquid nitrogen temperature.

The CD_2 bending profiles obtained experimentally and by calculation can be compared, but because the infrared spectra did not provide sufficient spectral resolution to distinguish all the different components of the CD_2 bending profiles, even for measurements made at low temperature, such comparisons are very limited. The infrared spectra benefit from improved spectral resolution, which was achieved by applying the technique of Fourier self-deconvolution to the raw data. For similar reasons, the technique of curve fitting was applied on the deconvoluted data (see chapter 3.2.3 for more details).

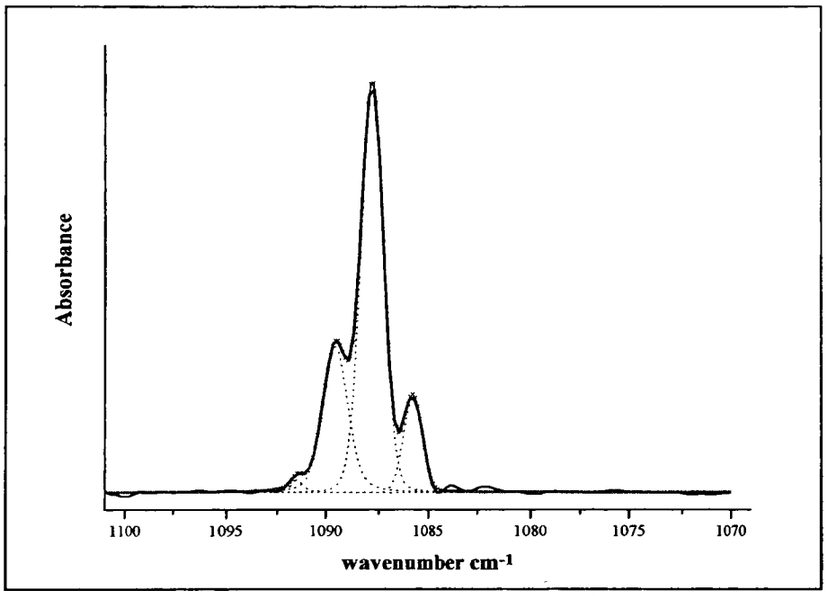

Figure V. 5: *Example of the use of curve fitting on the infrared spectrum of LL/95/385. 4 Voigt shape functions (combination of Gaussian and Lorentzian functions) were used (in dots) and added to fit (line and cross) the deconvoluted data (plain line).*

At this stage an important distinction must be made between the calculation of infrared profiles and the curve fitting process. Calculations of the infrared CD_2 bending profiles were made by combining 34 Lorentzian line shapes, the centre frequencies of which were determined from the splittings calculated using a coupled oscillator model (see table III.1). The weightings of the Lorentzian functions were adjusted manually to obtain optimum agreement with experimental data. Hence, the number of stems contributing to groups of adjacent labelled stems (adjacent in [110] directions) of different sizes can be determined. This process does not, strictly, constitute curve fitting, but probably provides the best estimates of the numbers of different groups present. On the other hand, curve fitting of the deconvoluted CD_2 bending data was carried out using four to five Voigt functions (combination of Lorentzian and Gaussian functions), with positions determined from the deconvoluted data such as those presented in Figure V. 5. Here we have used the minimum number of doublets necessary for a reasonable fit. However the

frequencies should not be interpreted as corresponding to the only groups present in the structure. Normally the best approximation to an infrared absorption peak is expected to be a Lorentzian lineshape, however because of the noise in the spectrum, a Voigt lineshape (combination of Gaussian and Lorentzian functions) gives more flexibility.
In this part of the chapter we will present the results from both the curve fitting and the calculation of the infrared CD_2 bending profiles. Also, comparisons between the different types of samples will be made in order to determine if there are differences between the sample types.
All the data presented in this thesis were obtained using a Mattson FTIR spectrometer with a nominal resolution of 1 cm^{-1}. During the experiments, the sample was mounted in a cell cooled at -170°C. Both the background run and sample run involved typically 200 scans. Deconvolution of the raw data were made using the Mattson deconvolution software from FIRST with representative values of the deconvolution parameters α (full width at half maximum absorbance of the intrinsic lineshape) and K (enhancement factor) of 2.5 cm^{-1} and 3, respectively. A Lorentzian lineshape was always used for the deconvolution of the infrared data.

V.2.1. The CD_2 bending profiles.

Data obtained from the undeformed samples are presented in Figure V. 6, along with the deconvoluted data. It can be seen that the CD_2 bending profiles are very similar. From the raw data, one can infer the presence of several different peaks. Five to six peaks are resolved after deconvolution. The central one, of highest absorbance, is the singlet component. It arises from contributions from the isolated stems (isolated in terms of [110] directions) and from amorphous chains. The side peaks result from interactions with [110] neighbouring stems, and are a consequence of the orthorhombic structure of polyethylene (see chapter III.3 section 2). The high wavenumber side of the singlet corresponds to bending vibrations with a polarisation parallel to the a-axis of the polyethylene unit cell. On the other hand, the low wavenumber side corresponds to b-polarised vibrations. The splittings between conjugate a- and b-polarised bands are related to the number of adjacent labelled stems in [110] directions. The intensity of a given doublet (the a- and b-polarised components) is related to the number of stems forming the corresponding group of adjacent labelled stems. Within a doublet, both the a- and b- polarised components should have the same intensity. However, their

coefficients of absorption are not equal, leading to the difference in intensity between the a- and b-polarised bands.

The "ripple" effect in the tails of the deconvoluted CD_2 bending profiles is due to the deconvolution process and is related to the noise in the original spectrum and therefore has no physical significance.

V.2.1.1. Curve fitting results.

V.2.1.1.1. Low molecular weight samples.

The data for the low molecular weight samples are shown in Figure V. 6. Results of the curve fitting on the deconvoluted data for the low molecular weight samples are presented in Table V. 6 along with the crystallinity measured by DSC.

The general shape of the CD_2 bending profile before deconvolution for samples LL/95/385, CL/95/385 and CC/95/181 appears very similar, although the components seem better resolved for both CL/95/385 and CC/95/181 than for LL/95/385. These profiles are composed of a central peak at a frequency of 1087.8cm^{-1} and 3 to 4 shoulders on each side. The width at half height of the whole CD_2 bending peak for the 3 samples is also similar.

After deconvolution, for sample LL/95/385, four peaks were resolved (Figure V. 6a). Four Voigt shape functions were used in the curve fitting process. The splitting between the outermost peaks, as determined by curve fitting, is around 5.6 cm^{-1}. This splitting corresponds to 4 adjacent labelled stems distributed in 2 planes (groups named 2×2. See chapter III section 4.2 for the complete definition of the terminology used here). For sample CL/95/385, five peaks were well resolved by deconvolution (Figure V. 6b). The splitting between the outermost doublet components is around 6.5 cm^{-1}. This maximum splitting corresponds to groups of 2×3 to 4×2 adjacent labelled stems. Another peak at a frequency of around 1084cm^{-1} can be distinguished, but its intensity is similar to that of the noise. Therefore this band was not included in the curve fitting of the deconvoluted data. For sample CC/95/181 (Figure V. 6c), 6 peaks were well resolved after deconvolution, with a splitting between the outermost bands of almost 8.5 cm^{-1}. This corresponds to groups of 3×4 adjacent labelled stems. However, only a small fraction of the crystal stems contribute to this doublet. Thus, the splitting appears to increase when changing the DPE linear guest to its copolymer counterpart. This increase is even larger when the copolymer guest is mixed with a copolymer matrix.

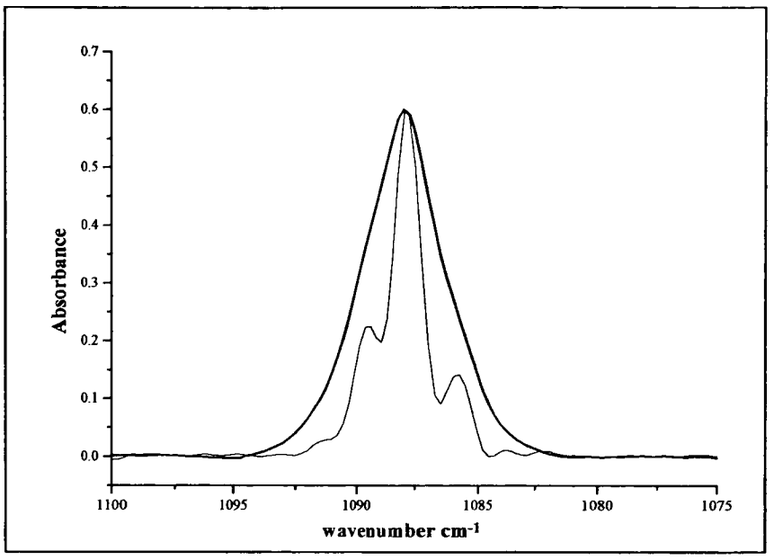

(a)

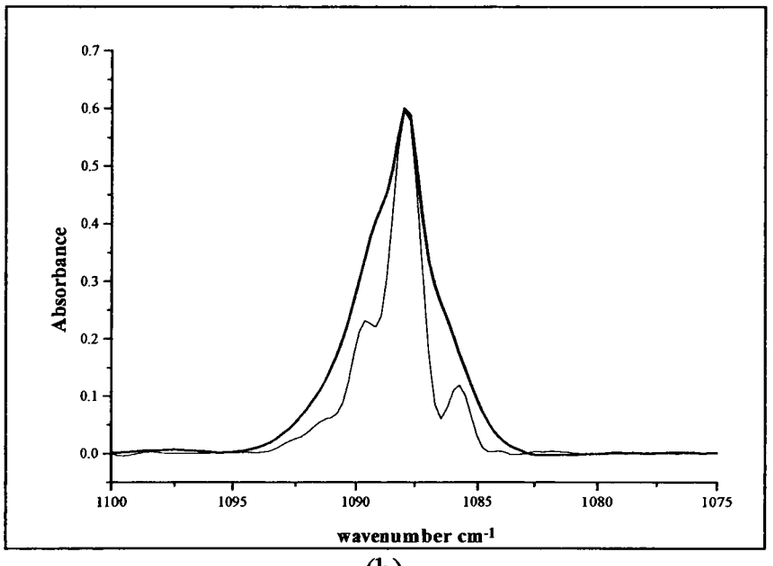

(b)

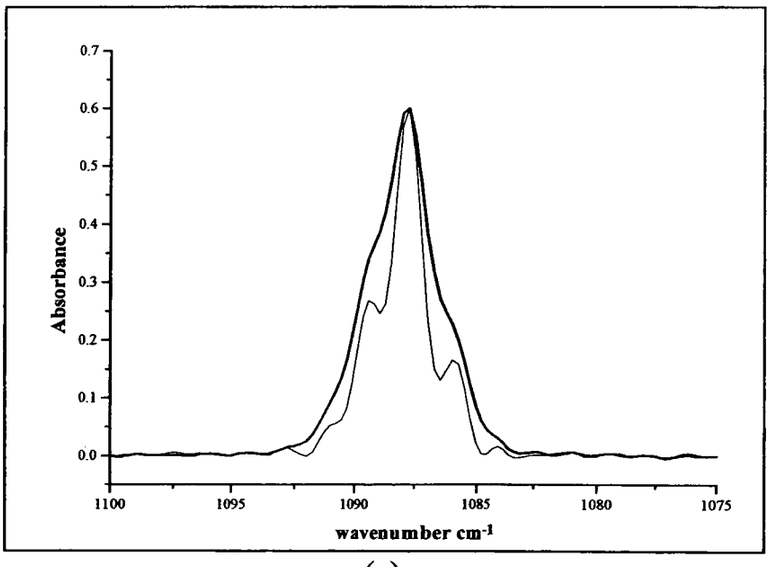

(c)

Figure V. 6: *The CD_2 bending region of the different samples: (a) LL/95/385; (b) CL/95/385; (c) CC/95/181. The thick line represents the raw data while the fine line shows the deconvoluted data. All the measurement were made at -170°C. The deconvolution was performed using the deconvolution software of FIRST with α = 2.5 cm^{-1} and K = 3.*

	χ_c (%)	outermost splitting (cm^{-1})	singlet (%)	doublet (%)	s_c (%)	d_c (%)
LL/95/385	53	5.6	60	40	44	56
CL/95/385	52	6.5	58	42	42	58
CC/95/181	38	8.5	62	38	38	62

Table V. 6: *Curve fitting results on the deconvoluted data for the low molecular weight samples. The DSC crystallinity (in %) of the samples are listed in column χ_c; the separation of the outermost peaks are listed in column "splitting"; the normalised area of the singlet component (in %) is in column "singlet"; the total normalised area of the doublets components (normalised area of the a- and b-polarised bands, in %) is in column "doublet"; the normalised area of the singlet and doublet components without the contribution of the amorphous region (as explained later in the text, in %) are, respectively, in column s_c and d_c.*

The proportion of the singlet component listed in Table V. 6 includes both the contribution from the isolated labelled stems in the crystals (with no neighbour labelled stems in any [110] directions) and from the chains in the amorphous region. Our interest is the contribution of the "crystal" stems (as opposed to the amorphous region). In order to remove the contribution from the amorphous polymer to the singlet component, the normalised area of the singlet component is multiplied by the crystallinity of the sample. The contributions of the "crystal" stems to the area of the singlet are listed in Table V. 6 column s_c and in column d_c is listed the proportion of the doublet components.

From the curve fitting results, it can be seen that the majority of the crystal stems are in groups larger than a single stem. The proportion of crystal stems contributing to the doublets increased when the linear DPE guest was replaced by its copolymer counterpart. When the copolymer DPE is mixed within a copolymer matrix, even more crystals stems contributes to the doublets. This means that groups of adjacent stems are favoured in the copolymer DPE chains. This is likely to involve more adjacent folding than for the linear DPE. Also, the matrix type appears to influence the local arrangement of the DPE chains. The local arrangement of the DPE chains shows dependence on the type of guest molecules and also on the type of matrix. It seems that the presence of branches in the guest molecules increases the proportion of adjacent folding, favouring the formation of groups of adjacent stems in [110] directions. This effect is even further amplified when the copolymer DPE is co-crystallised with a copolymer matrix. Also, the size of the largest groups is dependant on the type of the guest and host molecules.

Largest groups are obtained with a copolymer DPE guest co-crystallised with a copolymer matrix.

For all the low molecular weight samples, the majority of the stems are in small groups from 2 to 4 stems distributed in 1 plane. This is a significant difference by comparison with solution crystallised polyethylene [15, 16, 17, 18], where most of the stems were in the largest groups. In our cases only a very small proportion of the crystals stems are in the largest groups.

V.2.1.1.2. High molecular weight samples.

The CD_2 bending region of the infrared spectra for sample LL/413/385, CL/378/385 and CC/378/181 is presented in Figure V. 7 along with the deconvoluted data. From these curves, it can be seen that the CD_2 bending profiles appear wider than for the low molecular weight samples, especially for CL/378/385. Otherwise, their shapes are generally very similar to the profiles of the low molecular weight samples described in the preceding section.

The results of the curve fitting on the deconvoluted data are presented in Table V. 7. As for the low molecular weight analysis, the contributions of the crystal stems to the singlet for the four samples are listed in column s_c in this table.

From the raw data of LL/413/385, one peak can be seen with one shoulder on each side. Five components were resolved by deconvolution. The principal one was again the central peak at around 1087.8 cm^{-1}, corresponding to the contribution from isolated stems and chains in the amorphous region. Two doublets can also be seen, one with a splitting of around 3.3 cm^{-1} and one of very low absorbance with a splitting of around 7.8 cm^{-1}. Therefore, five bands were used in the curve fitting process.

As for LL/95/385, the contribution of the crystal stems to the singlet is of 45%. This means that 45% of the stems are [110] isolated, i.e. they have no labelled neighbouring stems in any [110] direction. This is again different the conclusions of Jing and Krimm [19]. Using a dispersive infrared instrument at low temperature, they have found that 60 to 70% of the crystal stems were contributing to the singlet component.

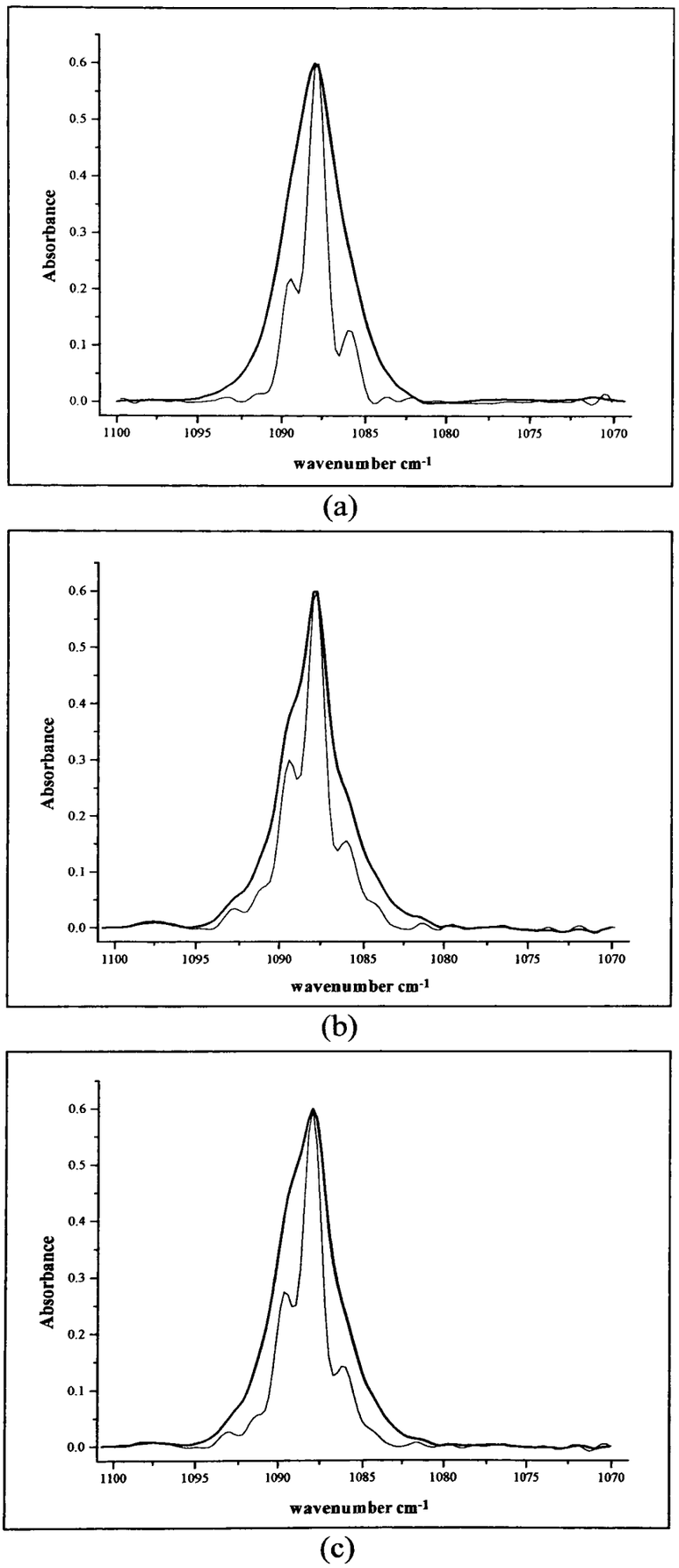

Figure V. 7: *The CD_2 bending region of the different samples: (a) LL/413/385; (b) CL/378/385; (c) CC/378/181. The thick line represents the raw data while the thin line shows the deconvoluted data. All the measurement were made at -170°C. The deconvolution was performed using the deconvolution software of FIRST.*

As for LL/95/385, most of the stems contributing to the doublets, and therefore associated with [110] adjacent folding, are distributed in small groups, no bigger than 4×1 adjacent stems. Only a very few of them are distributed in the largest groups of up to 3×3 adjacent labelled stems giving rise to a maximum splitting of 7.8cm^{-1}. As can be noted, this maximum splitting is not much bigger than that observed for LL/95/385, although the molecular weight of the guest molecule is four times bigger. Since in melt crystallised polyethylene adjacent folding is not the main mode of chain folding, the size of the groups is expected to be more or less independent of the molecular weight of the guest molecules.

	χ_c (%)	maximum splitting	singlet (%)	doublet (%)	s_c (%)	d_c (%)
LL/413/385	49	7.8 cm^{-1}	62	38	45	55
CL/378/385	50	8.5 cm^{-1}	53	47	36	64
CC/378/181	38	8.5 cm^{-1}	54	46	21	79

Table V. 7: *Curve fitting results on the deconvoluted data for the high molecular weight samples. The DSC crystallinity (in %) of the samples is listed in column χ_c; the separation of the outermost peaks are listed in column "splitting"; the normalised area of the singlet component (in %) is in column "singlet"; the total normalised area of the doublets components (normalised area of the a- and b-polarised bands, in %) is in column "doublet"; the normalised area of the singlet and doublet components without the contribution of the amorphous region (as explained in the text, in %) are, respectively, in column s_c and d_c.*

The infrared and deconvoluted profiles of samples CL/378/385 and CC/378/181 are very similar. In both cases, four peaks can almost be distinguished in the raw data. Again, the central peak is the one of highest intensity. After deconvolution, five peaks were well resolved with intensities significantly higher than the noise, giving rise to doublet splittings of 3.5, 6.9 and 8.5cm^{-1}. Also, on the low frequency side of the CD_2 bending region, another peak can be distinguished, but its intensity is of the order of the noise and therefore will not be taken into account in the curve fitting analysis. Finally, six Voigt shape functions were used in the curve fitting of the deconvoluted data for both CL/378/385 and CC/378/181.

From the curve fitting results on samples CL/378/385 and CC/378/181 listed in Table V. 7, it can be seen that fewer crystal stems were contributing to the singlet component of the CD_2 bending region than in sample LL/413/385. Also the maximum splitting for

this sample was larger than for LL/413/385. This was a similar observation to that for the low molecular weight samples. This suggests that the high molecular weight copolymer guest, as with its low molecular weight counterpart, tends to form groups of adjacent stems. Although, most of the stems are in small groups, only a very small number of them are in the largest groups. As for the LL samples, the maximum splitting of CL/378/385 and CC/378/181 is not much wider than in the case of, respectively CL/95/385 and CC/95/181. In fact, from Figure V. 6b, c and Figure V. 7b, c, it can be seen that exactly the same number of peaks at the same frequencies can be distinguished after deconvolution. For the low molecular weight CL, the peak at 1084 cm^{-1} has a very low intensity, of the order of the noise, and therefore could not be used in the curve fitting process, whereas for the high molecular weight CL, this peak is well resolved. This explains why a larger splitting is quoted for CL/378/385. Thus, in both the low and high molecular weight CL, the maximum groups size are equivalent, but only a negligible number of stems are in these largest groups in the low molecular CL samples. This is again a proof that adjacent folding is not the main mode of folding in melt crystallised polyethylene.

Finally the curve fitting results on the high molecular weight samples lead to a similar conclusion as for the low molecular weight results. It appears that the copolymer chains slightly favour the formation of groups of adjacent stems, but, contrary to the case of solution crystallised polyethylene, most of the stems are in the smallest groups. This may be understood by the fact that the branches of the copolymer materials are not expected to be included in the crystalline layers. This may force the copolymer chains to undergo more folding than their linear counterparts, leading to a decrease in the number of isolated crystal stems. This explanation may account for the increase of the group size from the linear guest molecules to the copolymer ones.

Because only a qualitative study of the CD_2 bending profile is accessible with the curve fitting analysis, we will now present the complementary results obtained from the calculated spectra.

V.2.1.2. Calculated CD_2 bending profiles.

Because the technique of curve fitting is not absolute (i.e. a solution may not be unique and may not accurately reflect the true distribution of group sizes), this method may be combined with another analysis technique in order to validate the results obtained. To

do so, the CD_2 bending profiles were calculated using a computer program. The process of calculation is the same as the one used by Spells et al [15, 16, 17, 18]. These calculations of the profiles were done by summing together the contributions of up to 34 Lorentzian shape functions (NB: in the curve fitting analysis, already discussed, only 4 to 5 Voigt shape functions were used to simulate the profile). The position of each conjugate Lorentzian (the high and low frequency doublet components, ν_{high} and ν_{low}) was determined by the theoretical splitting, $\Delta\nu$, calculated from the interaction between adjacent stems in a group of given size and shape (see chapter III section 4.2 and Table III. 1) and are given by [18]:

$$\begin{aligned} \nu_{high} &= 1087.4 + 0.56(\Delta\nu)\text{cm}^{-1} \\ \nu_{low} &= 1087.4 - 0.44(\Delta\nu)\text{cm}^{-1} \end{aligned} \qquad \text{(V. 7)}$$

These equations were the results of a linear fit on a range of doublet splittings obtained from a set of solution crystallised samples and similar samples subjected to heat annealing [16]. When our first calculations were made with the coefficient values used by Spells et al, the calculated positions of the high and low frequency components did not agree with the deconvoluted experimental ones. The coefficient values for respectively ν_{high} and ν_{low} were than corrected and their corrected values are shown in equation V. 7. Their original values were 0.64 for ν_{high} and -0.36 for ν_{low}.

In some early calculations of the CD_2 bending profiles, the central singlet component was excluded [15, 16]. As said earlier, the singlet includes contribution from non-crystalline chains, isolated labelled stems within the crystal lattice and rows of crystals stems with fold directions other than [110]. This component was omitted because of the apparent sensitivity of frequency position of the singlet band with the type of fold arrangement [16]. However, the central peaks show constant position in the deconvoluted spectra presented in this work, and therefore the singlet components were included in our calculations. For the purpose of the singlet intensity calculation, the proportion of non-crystalline material must be taken into account. As said earlier, non-crystalline chains contribute to the singlet intensity, and therefore all the other contributions (such as single stems) are weighted in proportion to the numbers of monomer units involved.

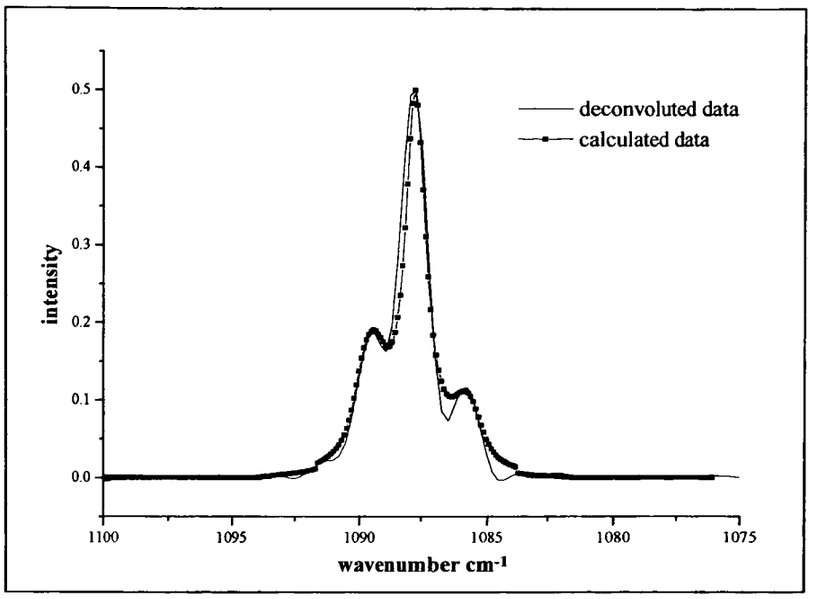

(a)

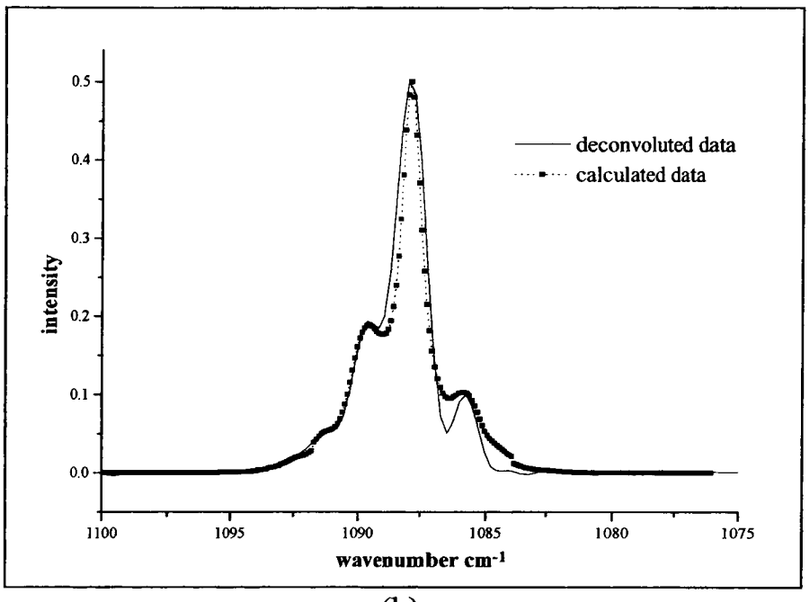

(b)

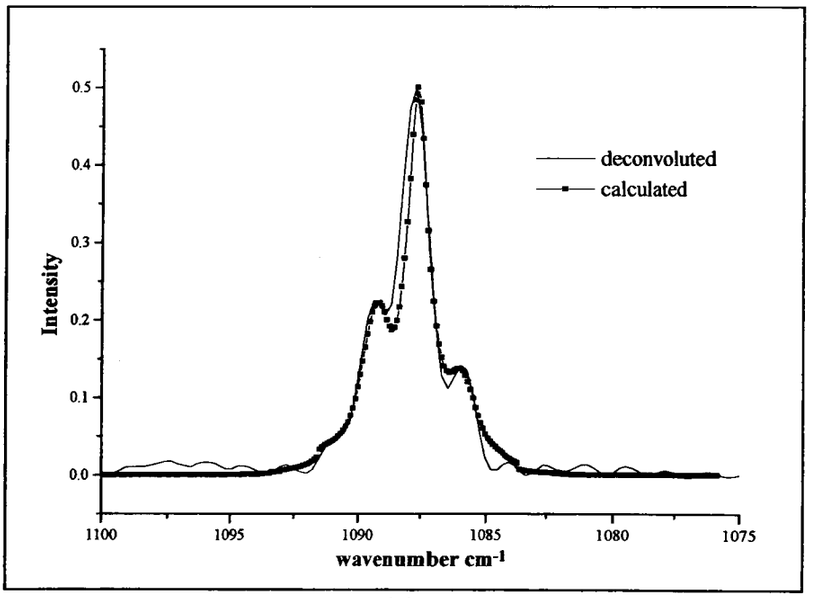

(c)

Figure V. 8: *CD_2 bending profile for the undeformed samples. Continuous line for the deconvoluted data, and in line and squares, the calculated data. (a) for sample LL/95/385; (b) sample CL/95/385; and (c) sample CC/95/181.*

The difference in absorbance between the a- and b-polarised components was compensated by introducing a scaling factor on the b-polarised side of the spectrum. The intensity of each Lorentzian was adjusted so as to match, as closely as possible, the calculated and the experimental profiles.

Because these intensities are related to the numbers of stems contributing to each group, the stem distribution can than be checked and compared with the curve fitting results.

In a similar way to the curve fitting analysis, the contribution of the chains in the amorphous regions was removed from the singlet components. For clarity the "crystal" stem distributions, used to calculate the CD_2 bending profiles, were divided into 4 categories: isolated stems (which contribute to the singlet); small groups of 2 to 4 adjacent stems in one plane (2×1 to 4×1 groups, which contribute to the inner doublets); medium groups of 5 to 7 adjacent stems in one or two planes (5×1, 2×2 and 3×2 groups); and large groups with 8 to 12 adjacent stems in two or three planes (4×2, 5×2, 3×3, and 4×3 groups, which contribute to the outermost doublets).

V.2.1.2.1. Low molecular weight samples.

The calculated CD_2 bending profiles for the low molecular weight samples are shown in Figure V. 8, while the crystal stem distributions, as determined by this calculation, are listed in Table V. 8.

	LL/95/385 (χ_c= 53%)	CL/95/385 (χ_c= 52%)	CC/95/181 (χ_c= 38%)
isolated stems	50%	42%	32%
small groups	46%	42%	58%
medium groups	4%	12%	6%
large groups	0%	4%	4%
max. splitting	4.2 cm^{-1}	8.1 cm^{-1}	8.1 cm^{-1}

Table V. 8: *Stem distributions used to calculate the CD_2 bending profile for the low molecular weight samples. χ_c is the crystallinity measured by DSC. The maximum splitting used in the calculation of the CD_2 bending profile is also listed.*

The general agreement between deconvoluted experimental spectra (Tables V. 6 and 7) and the calculated profile can be considered as good. The positions and intensities of the inner doublets are in very good agreement with the deconvoluted spectra. So are the intensities of the singlet peaks (the central peak at a frequency of around 1087.8 cm^{-1}).

In general, however, the calculated singlet width is narrower than the deconvoluted one. This is because a Lorentzian function was used to calculate the shape of the singlet peak here, and better agreement can be obtained with a Voigt shape function (a combination of Lorentzian and Gaussian shape functions) which has a greater bandwidth than a Lorentzian function. Narrower bandwidths are therefore expected in the calculated spectrum. Difficulties were encountered in calculating the outermost doublet (corresponding to the components with highest and lowest frequencies), especially on the low frequency side of the spectrum, where the calculated bands are more intense than the deconvoluted data. This is due to the tails of the inner doublets (corresponding to the smaller splittings), which still have a non-zero contribution at these frequencies. These tail contributions are larger than the actual intensity of the deconvoluted outermost bands, leading to the disagreement between the calculated and deconvoluted outermost bands. This is also the reason why the calculated band at around 1091.5 cm^{-1} is more intense than the deconvoluted one for sample LL/95/385. The discontinuity in the calculated profiles occurs where these contributions from the inner peaks stop (at around 1084 cm^{-1} and 1092 cm^{-1}).

For the low molecular weight samples, the bigger groups contain up to 4 adjacent stems distributed in 3 planes (groups named 4×3), and only a very small number of stems are in these largest groups. This is significantly different from the results of the calculations of the CD_2 bending profile performed on solution crystallised polyethylene, where most of the crystal stems were found in the largest groups. The outermost splitting measured and calculated for single crystal polyethylene was around 8.4 cm^{-1} [16, 18] for similar DPE molecular weight. This approximately corresponds to groups of 6×3 adjacent stems in [110] directions.

For sample LL/95/385, half the number of crystal stems have no neighbouring labelled stems in any [110] directions. Most of the stems which are contributing to the doublets are in small groups, groups no bigger than 4 adjacent stems. This suggest that adjacent folding is not the principal way of folding in melt quenched polyethylene. Also, when adjacent folding does occur, only very small groups are formed.

Similar, though less comprehensive, results were obtained in earlier infrared measurements on melt quenched polyethylene. From early dispersive infrared and FTIR results [17, 19], it was suggested that around 60-70% of the crystal stems were associated with random re-entry folding. The remaining 30-40% were distributed in adjacent

arrangements giving rise to a CD_2 bending vibration with a maximum splitting of 3.4cm^{-1}.

For sample CL/95/385, the crystal stem distribution appears different from what was seen for sample LL/95/385. The calculation of the CD_2 bending region was done with a crystal stem distribution where 56% of the stems were contributing to the doublets, giving rise to a maximum splitting of 8.1 cm^{-1}. This splitting corresponds to groups of 3×4 adjacent stems, but only a very small number of the crystal stems are in the largest groups (<2%). As in the case of LL/95/385, most of the crystal stems which contribute to the doublets are distributed in small groups of 2×1 to 4×1 adjacent stems (42%). Also, more stems (12%) are in medium size groups (from 5×1 to 3×2) than in LL/95/385, as can be seen in Figure V. 8b where the outermost well resolved peaks are of higher intensity and the CD_2 bending profile appears wider than for LL/95/385.

Finally, the number of isolated stems has decreased. From these results, groups of adjacent stems are favoured when the guest molecule is a copolymer. This could be explain by the fact that branches are preferably excluded from the crystalline layers. This exclusion of the branches may force the copolymer chains to undergo more frequent folding. This is even more accentuated when the matrix is a copolymer one, as for sample CC/95/181. For this sample, a crystal stem distribution where 66% of the crystal stems were contributing to the doublets and only 34% were isolated has been used to calculate the CD_2 bending profile. These results confirm that groups of adjacent stems are favoured with copolymer chains. A very high proportion of the crystal stems are distributed in small groups (60%). Only 6% are in medium groups, giving rise to a maximum splitting of 6.4cm^{-1}. This splitting corresponds to groups of 3×2 adjacent stems.

These results from the two copolymer samples are very different to that was seen for the linear sample and from early infrared measurements on linear polyethylene [17, 19]. Only a small proportion of the crystal stems are actually associated with random folding, whereas the majority of stems are in adjacent arrangements giving rise to a relatively small doublet splitting and corresponding to groups of 2×1 to 4×1 adjacent stems.

As for the curve fitting results, the calculated data show that the copolymer DPE guest mixed in a copolymer HPE matrix has a greater tendency to form groups of adjacent stems. This may be the effect of the branches, although it may only be an indirect effect of the crystallinity difference between the linear and copolymer samples. As said above,

the branches are preferentially excluded from the crystalline layer, which may force the copolymer to undergo more folding and in consequence to exhibit a local arrangement where most of the stems are in groups of 2 to 4 stems.

V.2.1.2.2 High molecular weight samples.

The high molecular weight calculated spectra are presented in Figure V. 9, along with the deconvoluted data. The stem distributions are listed in Table V. 9

As for the low molecular weight samples the general agreement between the deconvoluted data and the calculated profile is good. Both the intensity and position of the singlet component agree very well with the deconvoluted spectra. As noted for the low molecular weight sample, the width of the calculated singlet is somewhat narrower than the deconvoluted data. As explain earlier, this is because a Lorentzian shape function was used to calculate the singlet component, and this has a narrower bandwidth than the actual infrared peak. In both curves, the inner doublets are well reproduced by the calculated spectra.

For LL/413/385, as for its low molecular weight counterpart, difficulties were encountered in the calculation of the outermost doublet. The calculated bands are more intense than the deconvoluted ones. This is explained by the non-zero contribution of the Lorentzian functions used to calculate the inner bands which is of higher intensity than the bands of highest and lowest frequencies. Thus, because these bands are clearly resolved in the deconvolution spectrum, they were taken into account in the calculated spectra, even if after adding together all the contribution from the Lorentzian the resulting intensity at these frequencies is larger than the experimental one.

For both samples CL/378/385 and CC/378/181, very good agreement was found between the calculated and deconvoluted outermost bands both in position and in intensity, although small differences can be seen on the low wavenumber side of the spectra.

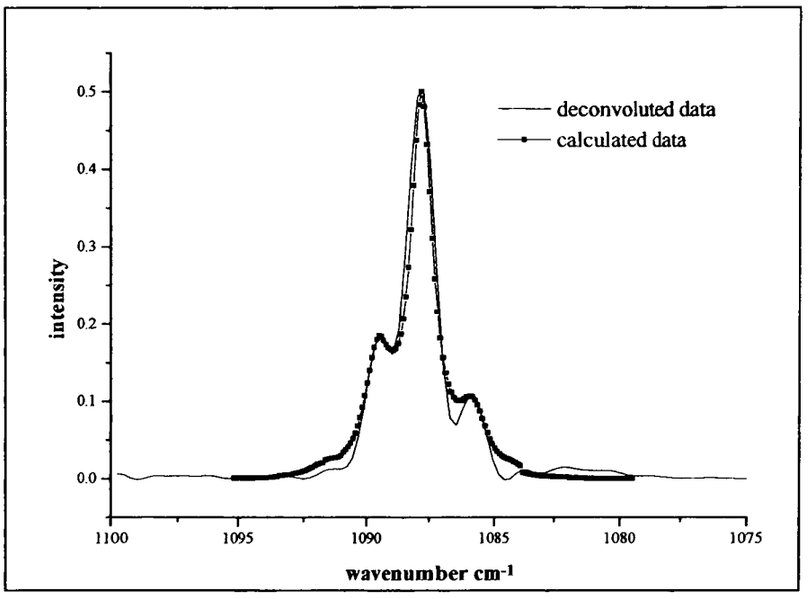

(a)

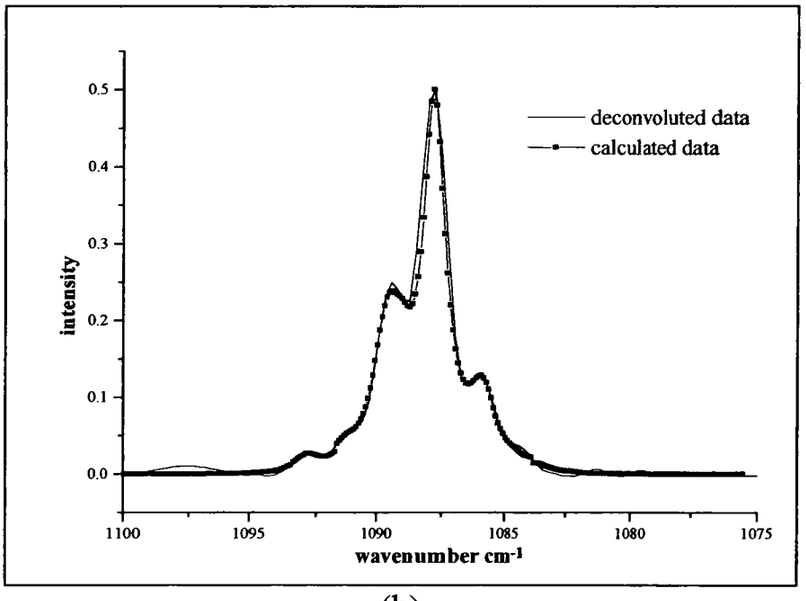

(b)

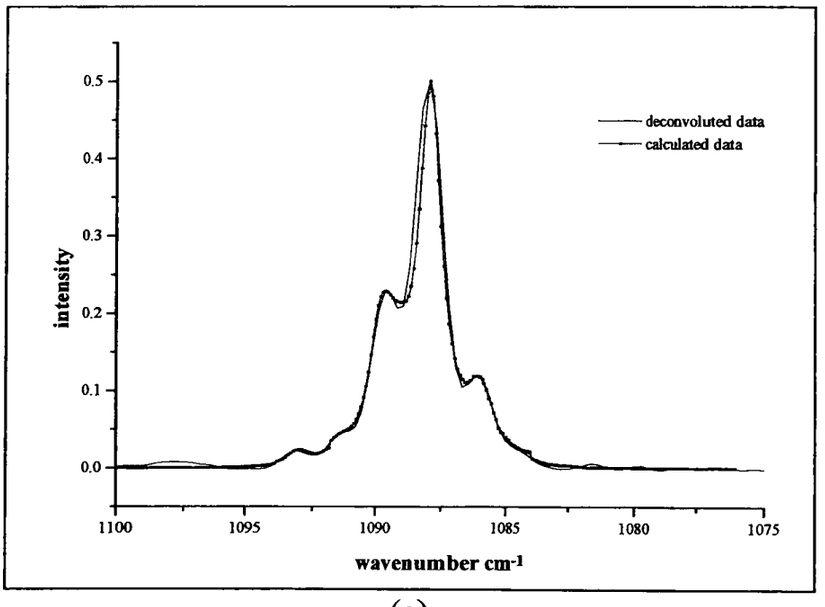

(c)

Figure V. 9: *CD_2 bending profile for the undeformed samples. Continuous line for the deconvoluted data, and in line and squares, the calculated data. (a) for sample LL/413/385; (b) sample CL/378/385 and (c) sample CC/378/181.*

	LL/413/385 (χ_c= 49%)	CL/378/385 (χ_c= 50%)	CC/378/181 (χ_c= 38%)
isolated stems	50%	34%	29%
small groups	43%	56%	63%
medium groups	4%	6%	4%
large groups	3%	4%	4%
max splitting	7.2cm^{-1}	8.5cm^{-1}	8.5cm^{-1}

Table V. 9: *Stem distributions used to calculate the CD_2 bending profile for the high molecular weight samples. χ_c is the crystallinity measured by DSC. The maximum splitting used to calculate the CD_2 bending profile of these samples is also listed.*

From the stem distributions listed in Table V. 9 for sample LL/413/385, 50% of the crystal stems contribute to the singlet component, and therefore have no neighbouring labelled stems in any [110] directions. The majority of the stems which contribute to the doublets are in small groups (43%). These small groups contains no more than 4 stems distributed in one plane (groups named 4×1). Only a very small proportion of the total number of crystal stems are in the largest groups, giving rise to a maximum splitting of 7.2 cm^{-1}. This corresponds to groups of 6×2 adjacent labelled stems. As was noted in the curve fitting analysis, the size of the largest groups is not much bigger than for LL/95/385, although the molecular weight of the guest molecule has quadrupled. This is explained because adjacent folding is not the main mode of folding in melt crystallised polyethylene, and therefore the maximum doublet splitting should be independent of the molecular weight of the guest molecules.

For both samples CL/378/385 and CC/378/181, the calculation of the CD_2 bending region was done using a crystal stem distribution where respectively only 34% and 29% of the total number of crystal stems contribute to the singlet. Most of the crystals stems are in small groups, and a very small number of them are in the largest groups, giving rise to a maximum splitting of 8.5 cm^{-1}. This splitting corresponds to groups of 4×4 adjacent stems. Again not much difference between the maximum splitting of the high and low copolymer samples is observed.

As for the low molecular weight copolymer samples, groups of adjacent stems are favoured in samples CL/378/385 and CC/378/181, and most of the crystal stems are distributed in small groups of up to 4 adjacent stems. Also, bigger groups are formed in both CL/378/385 and CC/378/181 than in LL/413/385. This is consistent with the fact

that the branches tend to be excluded from the crystal layer. This exclusion may force the copolymer chain to undergo more folding than the linear chain, leading to a decrease of the number of isolated stems and an increase of the number of stems in groups.
Finally, the calculation results lead to similar conclusions as do the curve fitting results. For the linear samples, around half the number of the crystal stems are isolated. Most of the crystal stems which are contributing to the doublets are in small groups of up to 4 adjacent stems. Only a very small number of stems are in the largest groups. This is very different from the situation in solution crystallised linear polyethylene, where most of the stems were contributing to the doublet, and most of them were in the largest groups [16, 17, 18]. For the copolymer samples, the crystal stems distributions are significantly different from the linear samples. Around 60% of the crystals stems are associated with the doublets, most of them in small groups of up to 4 adjacent stems. It is suggested that this difference can be attributed to the presence of the branches which force the copolymer chain to show more folding, leading to the creation of small groups of adjacent stems.

V.2.2 The CH_2 wagging region.

In this part, we will present the CH_2 wagging region of the undeformed samples. The bands in this region are associated with the departure from the all-trans polymer chain.
The wagging regions of the different samples are presented in Figure V. 10. All the spectra presented were measured at -170°C. This results in a decrease in the number of gauche conformations arising from thermal activation.
It is important to note that, in this paragraph, we are looking at the wagging region of the HPE chains, and no longer at the guest molecules as above.
In Table V. 10 are recall the bands assignment in the wagging region.

Position	Assignment
1378 cm^{-1}	methyl deformation
1365 cm^{-1}	gtg and gtg'
1350 cm^{-1}	gg
1342 cm^{-1}	g(t) (end-gauche)
1306 cm^{-1}	gtg and gtg'

Table V. 10: *Band assignments in the CH_2 wagging region.*

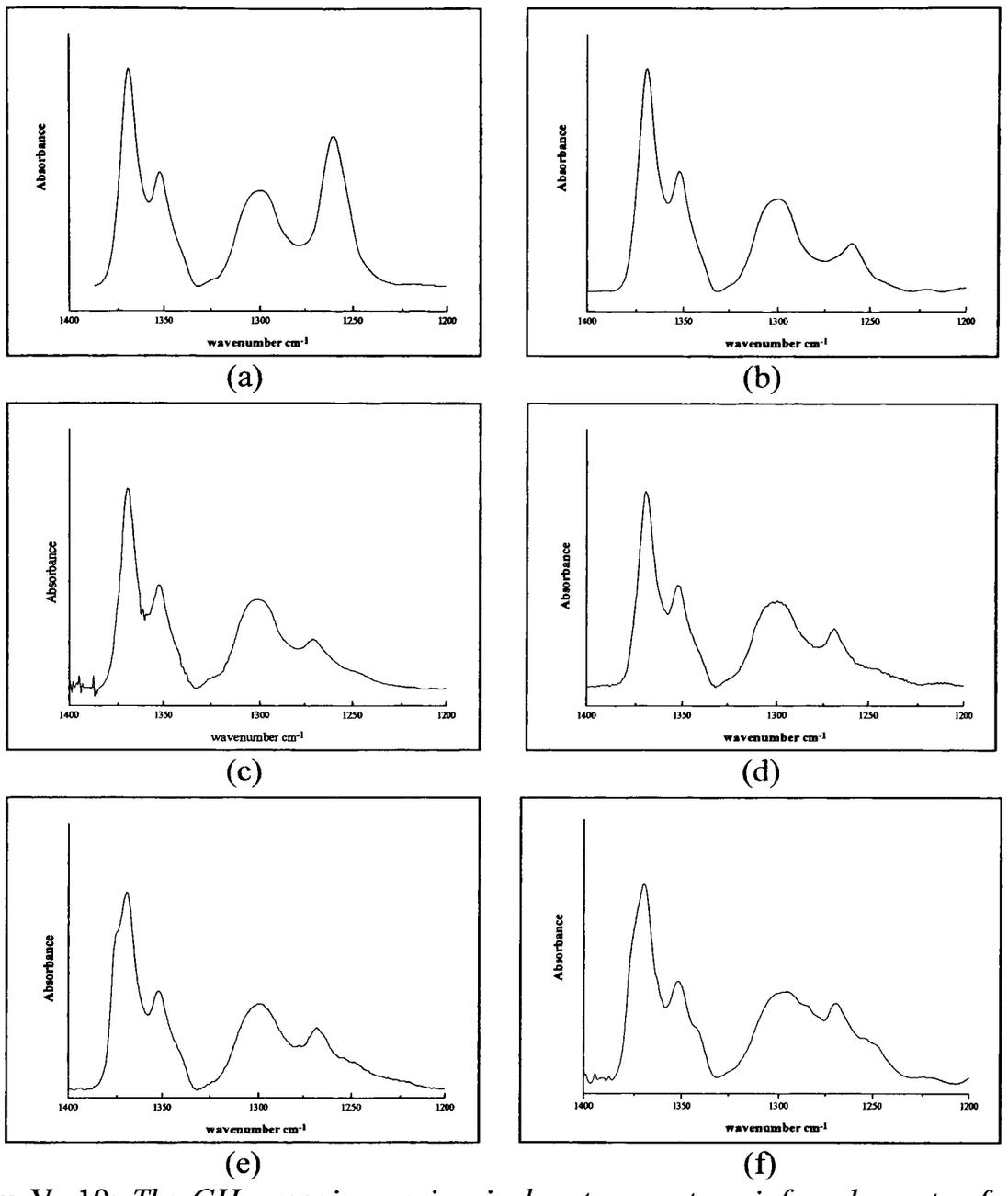

Figure V. 10: *The CH_2 wagging region in low temperature infrared spectra for (a) LL/95/385; (b) LL/413/385; (c) CL/95/385; (d) CL/378/385; (e) CC/95/181 and (f) CC/378/181.*

From Figure V. 10, in addition to the non all-trans conformation bands, another peak at around 1260 cm^{-1} appears in all samples. The assignment of this band is not known, but is not related to any wagging type vibrations. It is supposed that this band is related to vibration of the deuterated chains. Therefore this band will not be included in our analysis of the wagging mode.

For all samples with the linear matrix, the wagging region is similar, although the type of guest molecules has changed. This is expected since the DPE molecules can be considered as impurities in the HPE matrix and therefore are not supposed to affect the host molecules. Also, it can be seen that the proportion of non all-trans conformations is

similar for the low molecular weight samples and the high molecular weight samples. This is expected since we are looking at the HPE matrix, and not at the DPE guest.

A shoulder at 1378 cm^{-1} appears in the wagging region of both samples CC/95/181 and CC/378/181. This shoulder corresponds to the methyl group deformation. This shoulder does not appear in the spectrum of the linear matrix samples. This is expected since the methyl groups are only found at the ends of linear chains. Consequently, in comparison to the number of CH_2 units, there is only a small number of methyl groups, and hence the band does not appear in the spectrum. With the copolymer matrix, the methyl groups are also found at the ends of the molecule, but also at the end of each branch. Thus the proportion of methyl groups is larger with the copolymer matrix than with the linear matrix, and we expect to see the CH_3 methyl deformation in the spectrum of CC/95/181. Apart from this shoulder at 1378 cm^{-1}, no major differences in the amount of non all-trans conformations were found between the linear and the copolymer matrix.

V.3. Summary and discussion.

In this chapter we have presented some aspects of chain conformation prior to the deformation of isotopic blends of polyethylene, both on the scale of crystal stems (by means of mixed crystal infrared spectroscopy) and on the overall molecular scale (by means of neutron scattering). This investigation has revealed small but significant differences in the guest molecular conformation in isotopic blends of homopolymer and copolymer. First of all, we have studied the effect of changing the type of the matrix molecules, i.e. changing from a linear to a copolymer host molecule. Infrared results have shown that the guest molecules exhibit a higher degree of adjacency. Such a phenomenon is certainly related to the reduction of degree of crystallinity and thus, of lamellar thickness observed when crystallising a copolymer sample (chapter 4). Indeed, larger number of groups of adjacent labelled stems, and therefore higher degree of adjacency is expected for the same probability of adjacent folding when a guest molecule is incorporated in thinner lamellae compared to the same molecule incorporated in thicker lamellae. This decrease of the lamellar thickness may also be responsible for the slight increase in the radius of gyration observed when the matrix is a copolymer. However, as the radius of gyration does not only depend on the c-axis dimension but also on the other molecular dimensions, it is not clear whether the radius of gyration should increase with decreasing lamellar thickness. Also, an increase of R_g in a copolymer matrix appears to be in contradiction with the observation of a smaller alpha exponent in the evolution of R_g with molecular weight for copolymer matrix samples. Finally, for all these reasons and for the fact that the increase is slightly smaller than the uncertainties in R_g, this effect may not be significant.

Secondly, changing from a linear guest to a copolymer one results in an increase of the proportion of crystal stems included in groups, while the radius of gyration decreases slightly for the copolymer DPE guest. It appears that the copolymer guest molecules tend to have a more compact molecular conformation than their linear counterparts and that the copolymer molecules give rise to more adjacent folding and to a higher degree of adjacency than the linear DPE guest. The only difference between the two guests is the presence of branches for the copolymer since both guests, co-crystallised in the same matrix, exhibit the same lamellar thickness and crystallinity (see chapter 4). The

presence of branches may be responsible for the observed increase of adjacent folding. The reasons for such a phenomenon are not clear. However, studies on n-alkanes [9] have shown that C_{192}-alkanes with a methyl group near the middle ($C_{96}H_{193}CH(CH_3)C_{94}H_{189}$) always form folded chains, so the branch is "forcing" the molecule to fold, and may also determine the type of fold and influence adjacency. This cannot always be true for polyethylene, as some branches are certainly inside the crystals, but the branches could still affect the adjacency. Finally, since more adjacent folding is observed when the guest is a copolymer and since the lamellar thickness is unchanged, the resulting radius of gyration of the copolymer guest would be slightly reduced.

From the infrared CD_2 bending region of all type of samples, it was shown that, contrary to previous results for solution crystallised polyethylene, most of the crystal stems were in small groups with a maximum of 4 adjacent stems in [110] directions. This, in addition to the intermediate angle and small angle neutron scattering analysis, shows that our results are broadly consistent with the subunit model developed by Sadler and Harris. In this subunit model, it is suggested that a large local rearrangement of the chain occurs in order for chain-folded crystallisation to be accomplished (the subunit), but the distribution of the subunits themselves is determined by the Gaussian chain in the melt state [11]. Also, the neutron scattering results showed that the exponent of the relationship $R_g \propto \overline{M}_W{}^{\alpha}$ for the CC samples types is different, suggesting a more compact arrangement as the molecular weight of the DPE guest molecules increases. This was found consistent with the infrared results, where both results from curve fitting and from the simulation of the infrared CD_2 bending profiles show that the number of small groups of adjacent labelled stems is significantly larger when the DPE guest is a copolymer molecules. Finally, by contrast to previous results on solution crystallised polyethylene, our results support the general absence of a significant degree of adjacency in the local stem arrangements.

[1] D.M. Sadler, A. Keller, *Macromolecules*, **10**, 5, 1128 (1977).
[2] D.M. Sadler, P.J. Barham, *J. Polym. Sci. Polym. Phys. Ed.*, **21**, 309 (1983).
[3] G.G. Summerfield, J.S. King, *J. Appl. Cryst.*, **11**, 548 (1975).
[4] J. Shelten, D.G.H. Ballard, G.D. Wignall, G. Longman and W. Schmatz, *Polymer*, **17**, 751 (1976).
[5] D.M. Sadler, A. Keller, *Science*, **203**, 263 (1979).
[6] D.G.H. Ballard, A.N. Burgess, A. Nevin, P. Cheshire and G.W. Longman, *Macromolecules*, **13**, 667 (1980).
[7] C. France, P.J. Hendra, W.F. Maddams and H.A. Willis, *Polymer*, **28**, 710 (1987).
[8] R.G. Alamo, B.D. Viers, and L. Mandelkern, *Macromolecules*, **26**, 5740 (1993).
[9] J.P. Gorce, *Thesis for the degree of Doctor of Philosophy*, Sheffield Hallam University, Sheffield, 2000.
[10] Z. Zhou, N. Brown, *Polymer*, **35**, 3619 (1994).
[11] D.M. Sadler, R. Harris, *J. Polym. Sci. Polym. Phys. Ed.*, **20**, 561 (1982).
[12] M. Stamm,, E.W. Fisher, M. Dettenmaier, , P. Convert, *Discuss. Faraday Soc.*, **68**, 263 (1979).
[13] G.D. Wignall, L. Mandelkern, C. Edwards, M. Glotin, *J. Polym. Sci. Polym. Phys. Ed.*, **20**, 224 (1982).
[14] E. U. Okoroafor and S. J. Spells, *Polymer*, **35**, 4578 (1994).
[15] S.J. Spells, D.M. Sadler, *Polymer*, **25**, 739 (1984).
[16] S.J. Spells, A. Keller, D.M. Sadler, *Polymer*, **25**, 749 (1984).
[17] S.J. Spells, *Polymer Communications,* **25**, 162 (1984).
[18] S.J. Spells, *Polymer,* **26**, 1921 (1985).
[19] X. Jing, S. Krimm, *J. Polym. Sci. Polym. Phys. Ed.*, **21**, 123 (1983).

Chapter six:

Experimental Results on Deformed Samples.

This chapter contains the Neutron scattering and FTIR results obtained 'in situ' on deformed samples and obtained from the samples relaxing following deformation.

First of all, we will concentrate on the evolution of the radii of gyration taken parallel and perpendicular to the draw direction with deformation and as a function of the elapsed time after unclamping the samples. Secondly, the evolution of the CD_2 bending region with deformation will be monitored, and the local stem rearrangement will be characterised. Finally the evolution of the amount of non all-trans conformations will be described.

In order to observe the effects of mechanical deformation, largely without the complication of thermal effects, we present here results obtained with samples deformed at room temperature (see chapter 1).

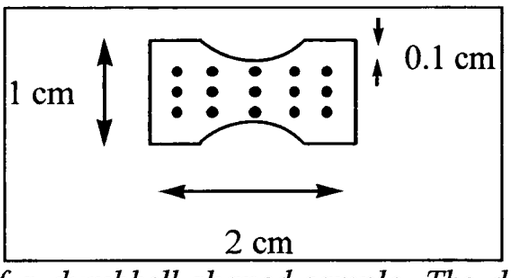

Figure VI. 1: *Example of a dumbbell-shaped sample. The dots drawn on the sample have a spacing of 0.2 cm. This enables the measurement of the exact draw ratio of the region in the beam after deformation of the sample by using a travelling microscope.*

The drawing of the sample was performed on small pieces of 2×1 cm cut from the sample sheet. Also, in order to concentrate the deformation, the samples were cut with a dumbbell-shape as shown in Figure VI. 1. The samples were drawn to the required draw ratio with a Minimat tester at a rate of 1 mm per minute. The exact draw ratio of the region in the beam was determined by measuring the distance between small dots painted on the sample prior deformation as described in Figure VI. 1. The initial spacing between the dots was 2 mm. The draw ratio measurements were made using a travelling microscope. The values of the deformed spacing in the region exposed to the beam were averaged over the beam area in order to obtain the exact draw ratio of this area.

VI.1. Neutron scattering results.

In the case of the neutron scattering experiments, the Minimat with the drawn sample was mounted on the LOQ or D11 sample table. Its position was then adjusted so that the neutron beam passed through the neck region of the sample, where the draw ratio was measured. Within this arrangement the sample was kept stretched at the required draw ratio during the whole neutron experiment with the draw direction horizontal.

For the ISIS experiments, the beam aperture was circular with a diameter of 6 mm. For the ILL experiments, a circular aperture of 5 mm were used. For the very highest deformation (for a draw ratio, DR, of 5.6 with sample LC/95/181) the beam area was larger than the width of the sample, and therefore a smaller aperture with a diameter of 4 mm was used.

As for the undeformed sample, the scattering signal from the isotopic blend was considered to be a simple superposition of (i) a signal from the empty aperture, (ii) incoherent scattering, (iii) a coherent scattering signal $I_\rho(q)$ analogous to that which was observed in small angle X-ray scattering, and (iv) the desired molecular scattering I(q) arising from the isotope difference. $I_\rho(q)$ is due to density differences between crystal and disordered regions, cracks, voids, and impurities. In order to remove the dependence on $I_\rho(q)$, the scattering resulting from a purely hydrogenated blank, deformed to the same draw ratio as the sample, was subtracted from the scattering of the deformed sample.

The sample thickness was calculated from the average neutron transmission using the same process as for the undeformed sample. It is important to note that the amount of material in the beam after deformation was almost 10 times smaller than in the case of the undeformed sample. In order to obtain reasonable statistics, the exposure time was increased to 2 hours for the ISIS experiments and to 1 hour for the ILL ones. Also, to verify if stress relaxation occurs in the clamped samples, some measurements were carried out over a period of time of 6 hours. In these cases, the evolution of the radii parallel and perpendicular was characterised at a fixed draw ratio with varying time.

Because the scattering is anisotropic, it is not possible to azimuthally average the count rate of each detector cell. In our case the averaging was carried out on sectors which were horizontal (parallel to the draw direction) and vertical (perpendicular to the draw direction). For all the measurements made at ISIS and at ILL, 30° sector angles were

used. Thus the radii of gyration parallel and perpendicular were calculated from the scattering intensities parallel and perpendicular to the draw direction. The complete anisotropic analysis is described in Chapter 2 section 5.3.

In our last neutron experiment carried out at ISIS, problems with the cell subtraction process were encountered. After doing the H-Blank subtraction, the values of the radius perpendicular, R_{Per} were found to be larger than the radius parallel to the draw direction, R_{Par} in the case of the low deformation samples (DR<1.2). It was suggested that because of the very weak scattering intensity measured, the empty cell subtraction may introduce large errors. Therefore, no cell subtraction was performed in our last ISIS sets of data. This removed the problem described above.

The values of the radius parallel (R_{Par}) and perpendicular (R_{Per}) were derived from least squares fits of the Zimm plots (Figure VI. 2) for the intensities measured parallel and perpendicular to the draw direction, using the following relationships:

$$R_{Par} = \sqrt{\frac{\beta_{Par}}{\alpha}} \qquad R_{Per} = \sqrt{\frac{\beta_{Per}}{\alpha}} \tag{VI 1}$$

where β_{Par} and β_{Per} are respectively the slopes of the linear fits of the data in the parallel and perpendicular directions. The intercept for both directions, α, was determined from the intercept values of the data taken perpendicular to the draw direction. This allows better estimation of the intercept since the region where the Zimm approximation is valid is larger in the perpendicular direction, and therefore, more experimental points can be used for the fitting process. The errors on the radii were calculated by:

$$\delta R_{Par} = \frac{R_{Par}}{2}\sqrt{\left(\frac{\delta\beta_{Par}}{\beta}\right)^2 + \left(\frac{\delta\alpha}{\alpha}\right)^2} \qquad \delta R_{Par} = \frac{R_{Per}}{2}\sqrt{\left(\frac{\delta\beta_{Per}}{\beta}\right)^2 + \left(\frac{\delta\alpha}{\alpha}\right)^2} \tag{VI. 2}$$

where $\delta\beta_{Par}$, $\delta\beta_{Per}$ and δa are respectively the errors in β_{Par}, β_{Per} and α obtained with the fitting software. The molecular weight is defined by equation V. 3, as shown in Chapter five.

VI.1.1. In situ deformed samples.

In this section we will compare the behaviour of the radii of gyration measured in directions parallel and perpendicular to the deformation axis for the different types of sample. The experiments presented in this section were done with the samples kept stretched in the Minimat for the whole time of the measurement. Because some of the neutron measurements presented here lasted for several hours, it is important to verify if relaxation phenomena occur with time. Therefore, first of all we will present in this section the evolution of the radii with time for the stretched and clamped samples. This will be followed by the evolution of the radii with deformation.

Figure VI. 2 includes example of Zimm plots in the parallel and perpendicular directions and their respective least squares fits at different draw ratios. From these plots, the increase of the anisotropy with draw ratio can be observed. Also, the intercepts of the observed Zimm plots appear smaller after deformation. This may suggest that the actual molecular weight of the sample measured by the SANS is larger after deformation. In Chapter 5, this abnormally large molecular weight was shown to result from isotopic segregation. It was seen in the introductory chapter that the appearance of an isotopic segregation signal after deformation can be interpreted as consistent with local melting and recrystallisation [1, 2, 3] introduced by deformation. However, these effects were observed for deformation taking place at high temperature, and not for cold drawing. More recently, Lagarón et al [4] showed DSC traces with evidence of fractionation on cold drawing. This could be the reason for the apparent change in molecular weight determined from SANS. But in our case, the "segregated molecular weight" is not larger than two times the value of the undeformed molecular weight and was only observed for sample LL/95/385, presented in Figure VI. 2 and for sample LC/95/181. In the other samples no such phenomena were observed. As explained in the preceding chapter, this apparent difference in the molecular weight before and after deformation may be due to a mismatch in I_p between the sample blend and the HPE blank sample. Therefore no definite conclusion on the phenomena of melting and crystallisation induced by deformation can be drawn from our SANS results.

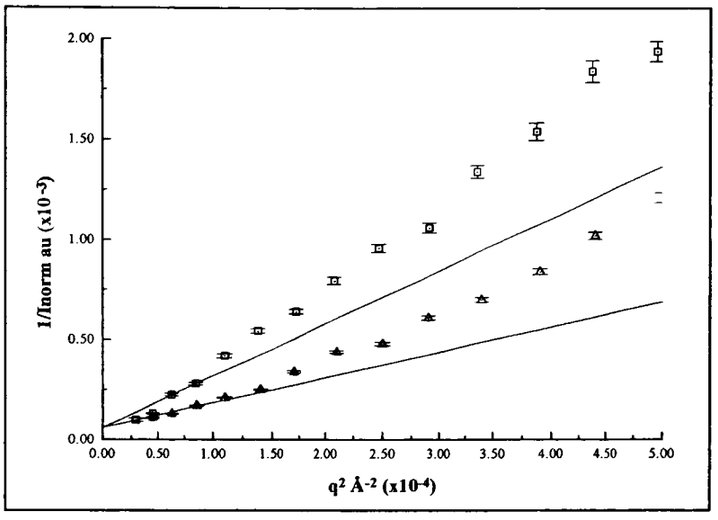

(a)

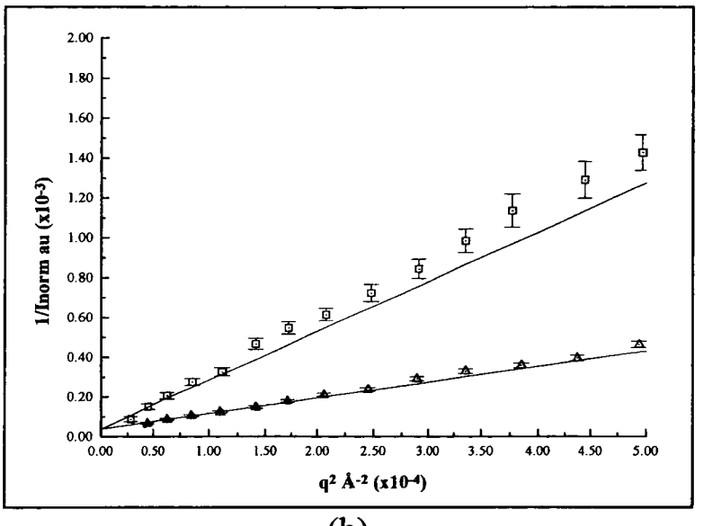

(b)

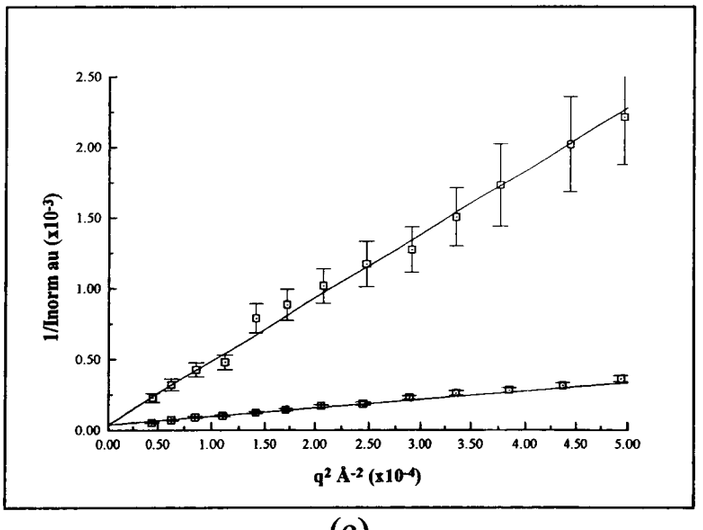

(c)

Figure VI. 2: *Examples of Zimm plots for LL/95/385 deformed with (a) DR=1.2; (b) DR=1.5; and (c) DR=2.6. The measurements were made at ILL. The squares are for the intensity measured in the direction parallel to the deformation. The up triangles are for the intensity perpendicular to the draw direction. The lines represent least squares fits to the data.*

VI.1.1.1. Time dependence results on the clamped samples.

Because some experiments took several hours, it was important to determine if stress relaxation occurs. Therefore, a scattering pattern was collected for each 30 minute interval during the whole experiment. The evolution of the radii parallel and perpendicular with time, at a fixed draw ratio are presented in Figure VI. 3, obtained with the LOQ instrument at ISIS.

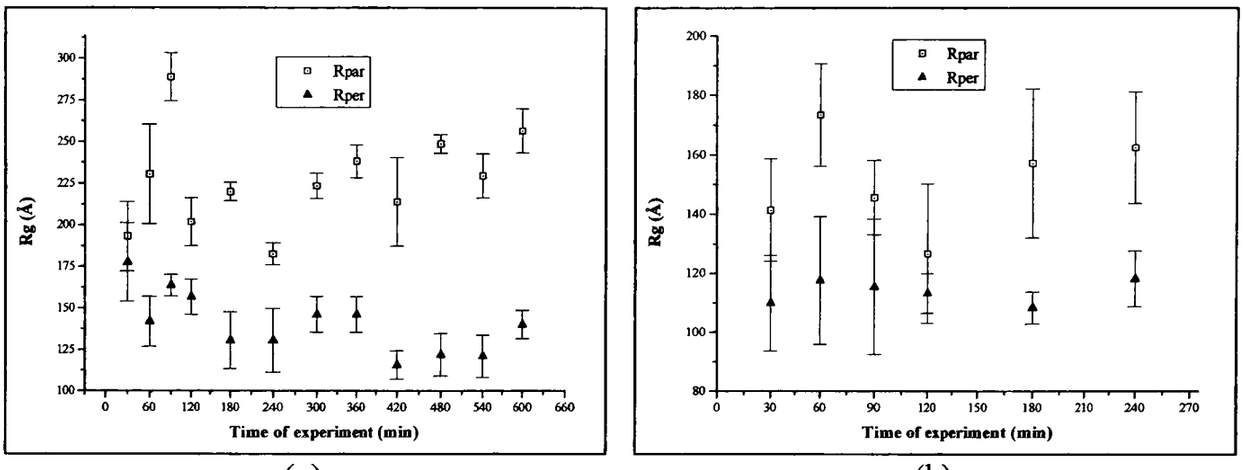

Figure VI. 3: *Evolution of the radii parallel and perpendicular to the draw direction with time for the sample kept stretched during the whole experiment. (a) sample LL/95/385/1.5; (b) sample CL/95/385/1.5. These measurements were made with LOQ at ISIS. The errors bars were determined using equation VI. 2. As in the case of the undeformed sample, the experimental errors are almost certainly underestimated.*

From these preliminary results, different behaviour can be seen for the linear sample and the copolymer one. For sample LL/95/385/1.5, presented in figure VI. 3a, R_{Par} seems to increase in general with time, while R_{Per} is decreasing. There appears to be a development of the molecular deformation within the sample with time. However, the small samples involved and short data acquisition times led to large experimental errors, possibly obscuring any significant trends. In the case of sample CL/95/385, the values of the radii stay constant to within experimental errors during the whole run.

Repeating the measurements on D11, for samples stretched and then left clamped for the duration of the experiment, showed negligible variation of R_{Par} or R_{Per} as a function of time, with the possible exception, at least in some cases, of the shortest times after stretching. The results on stretched and clamped samples measured with D11 at ILL are presented in figure VI. 4.

This tends to confirm that the ISIS results should be viewed with caution. In view of the ILL results, both R_{Par} and R_{Per} can be considered constant during the whole time of the

experiments, and therefore it is possible to calculate a weighted average of the data for each draw ratio.

The evolution of the weighted averaged radii with draw ratio for the different types of samples are presented in the following sections.

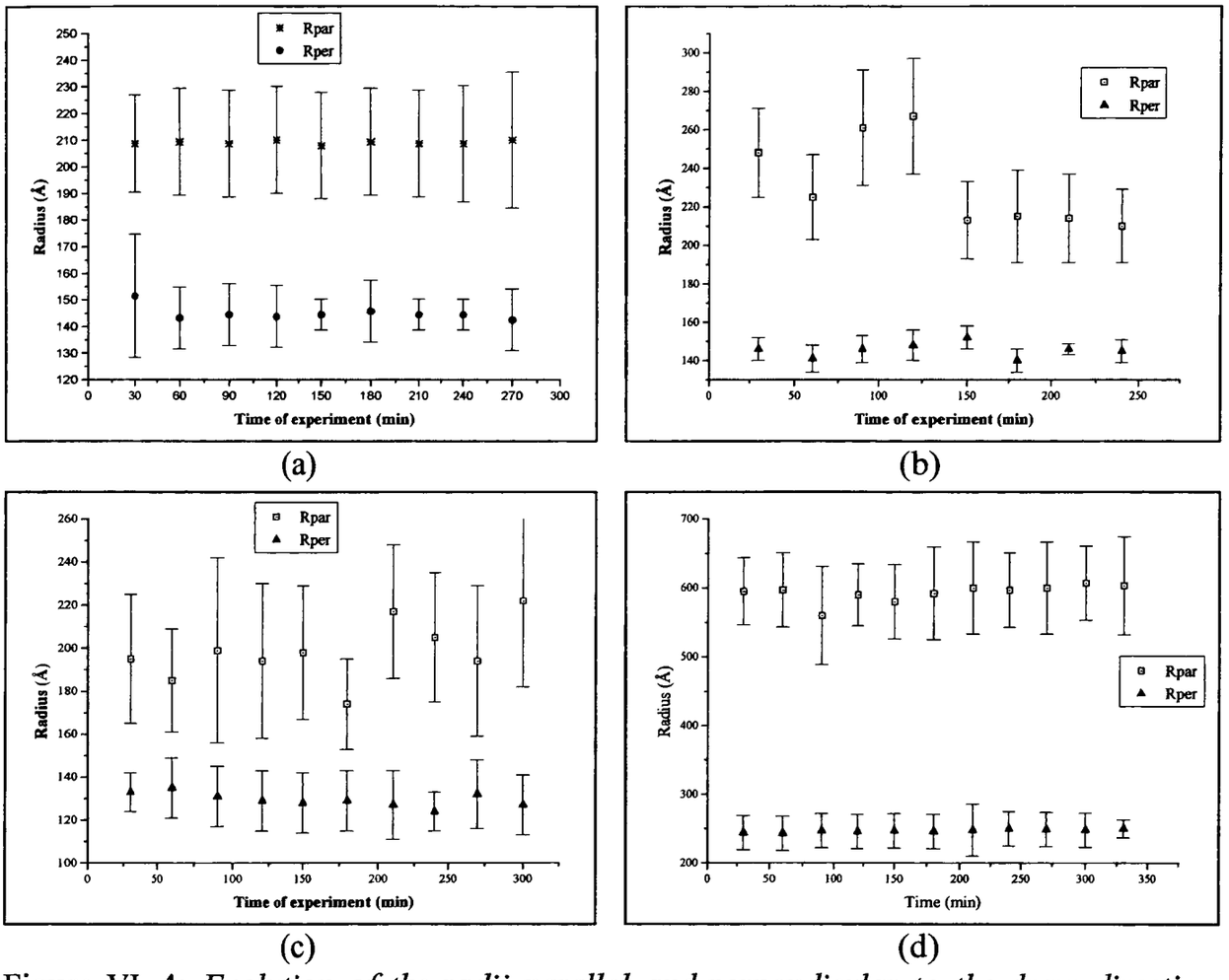

Figure VI. 4: *Evolution of the radii parallel and perpendicular to the draw direction with time for the sample kept stretched during the whole experiment. (a) sample LL/95/385/1.2; (b) sample LC/95/181/1.44; (c) CC/95/181/1.5; and (d) LC/413/181/2.33. These measurements were made with D11 at ILL.*

VI.1.1.2. Evolution of the R_{Par} and R_{Per} with draw ratio.

Examples of the evolution of the R_{Par} and R_{Per} with draw ratio for the samples are presented in figure VI. 5.

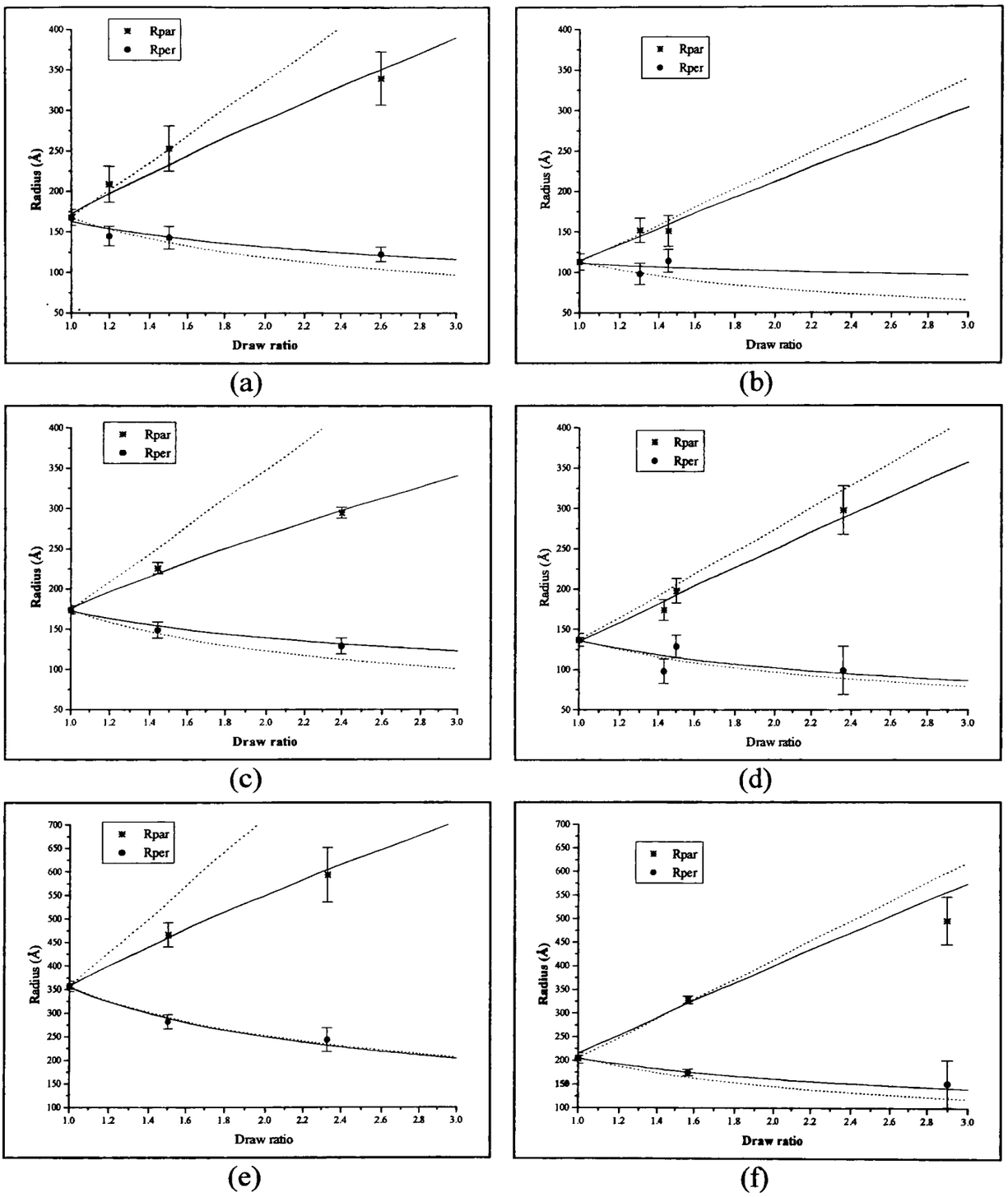

Figure VI. 5: *Evolution of the radius of gyration parallel and perpendicular to the draw direction with draw ratio for samples (a) LL/95/385; (b) CL/95/385; (c) LC/95/181; (d) CC/95/181; (e) LC/413/181; and (f) CC/378/181. The dotted lines represent the expected evolution of R_{Par} and R_{Per} if the deformation is affine. The lines represent the least squares weighted power law fits, $y = ax^b$, on the radii parallel and perpendicular.*

In order to compare the evolution of the radii with the theoretical affine deformation, the data were fitted using the power law function $y = ax^b$. For affine deformation, where the

changes in microscopic dimensions follow the corresponding changes in macroscopic dimensions, the radii parallel and perpendicular, R_{Paraff} and R_{Peraff}, are determined by:

$$R_{Paraff} = \lambda R_x$$
$$R_{Peraff} = \lambda^{-1/2} R_x \qquad \text{(V.I. 3)}$$

where λ is the sample draw ratio. Therefore for an affine deformation the expected values of the exponent b are respectively 1 in the direction parallel and -0.5 in the direction perpendicular to the draw direction.

The first noticeable point observed from Figure VI. 5 is the difference between the evolution of R_{Par} and R_{Per}. The dimension measured perpendicular to the draw direction corresponds approximately to affine deformation in all the cases and in the whole deformation range studied, while deviations from the affine prediction are observed in some cases for the radius parallel to the deformation direction. The actual onset and the degree of departure of R_{Par} from affine predictions are different for the different sample types. For sample LL/95/385 (Figure VI. 5a), the evolution of R_{Par} is in very good agreement with the affine predictions for DR $\leq$ 1.5. For DR > 1.5, departures from affine behaviour are observed, and at DR of 2.6, the end of our data set, a ratio of 1.3 is measured between the experimental and predicted values of R_{Par} values (respectively, 340 Å and 440 Å). When changing the matrix type, as in the case of sample LC/95/385 (Figure VI. 5c), a small deviation from affine behaviour is already observed at a DR = 1.4, and for a DR = 2.4 a ratio of 1.5 is measured between experimental and predicted R_{Par} values (respectively, 295 Å and 417Å). When increasing the molecular weight of the linear DPE guest molecules, for sample LC/413/385 (Figure VI. 5e), the behaviour observed is very similar to LC/95/181. Departure from affine behaviour is already observed at a draw ratio of 1.4 and the difference between prediction and measurement increases as the draw ratio is increasing and a ratio of 1.4 is measured between experimental and predicted R_{Par} values (respectively, 593 Å and 832 Å). In the case of a copolymer DPE guest mixed with a linear HPE matrix, as for sample CL/95/385 (Figure VI. 5b) good agreement is found between experimental and predicted R_{Par} values in the limited deformation range studied. In a similar way for both CC/95/181 and CC/378/181, the experimental R_{Par} agree with affine predictions to well within the error bars throughout the whole deformation range studied. This is in sharp contrast to the linear DPE guest samples, where differences between affine predictions and measured R_{Par} are observed and increase with increasing draw ratio. This difference in the

evolution of R_{Par} should be reflected in the value of the exponent b_{Par} listed in Table VI. 1.

	a_{Par}	b_{Par}	a_{Per}	b_{Per}
LL/95/385	167±3 Å	0.70±0.06	165±3 Å	-0.34±0.06
CL/95/385	114±8 Å	0.89±0.3	111±8 Å	-0.13±0.32
LC/95/181	176±4 Å	0.60±0.04	173±4 Å	-0.31±0.05
CC/95/181	135±7 Å	0.89±0.13	136±8 Å	-0.42±0.22
LL/413/385*	253 Å	0.57	253 Å	-0.59
LC/413/181	358±6 Å	0.62±0.05	355±6 Å	-0.51±0.06
CC/378/181	215±11 Å	0.89±0.11	205±13 Å	-0.34±0.05

Table VI. 1: *Values of the weighted average least squares power law fits on the radii parallel and perpendicular to the draw direction for the different samples. The listed data are the weighted average values of power law fits made on the radii measured at ILL and at ISIS.* a_{Par} *and* b_{Par} *are the value of the fits obtained on* R_{Par}. a_{Per} *and* b_{Per} *are the fit results obtained from* R_{Per}. *For an affine deformation, it is expected that* $b_{Par} = 1$ *and* $b_{Per} = -0.5$. * *No error bars are given for sample LL/413/385 because only one data point was measured (at a DR = 1.39).*

It can be seen that the values of b_{Par} obtained from the power law fits of the linear DPE guest samples (samples LL/95/385, LC/95/181 and LC/413/181) are significantly smaller than the values expected for an affine deformation ($b_{Paraff} = 1$) and agree with each other to within experimental errors. It appears that LL and LC samples have similar behaviour in the evolution of the chain dimension measured in the direction parallel, which shows significant departure from affine behaviour at draw ratios larger than 1.5. On the other hand, the exponent b_{Par} obtained for the copolymer DPE guest samples (samples CL/95/385, CC/95/181 and CC/378/181) agree within errors with the predicted affine exponent, although experimental values are slightly smaller. The later values are also identical to each other ($b_{Par} = 0.89$ in all three samples). Therefore, it appears that the affine behaviour is preserved to substantially larger deformations in the case of the copolymer DPE guest samples.

On the other hand, it appears difficult using b_{Per} values to see this distinction between affine and non-affine behaviour. This is probably because the fractional errors for b_{Per} values are generally larger for b_{Par}, so conclusions are less reliable. Such a difference between the behaviour in the parallel and perpendicular directions may be connected with the constraint imposed by the clamps.

VI.1.1.3. Discussion on the evolution of the R_{Par} and R_{Per}.

Before commenting on the evolution of R_{Par} and R_{Per} with draw ratio, one needs to recall the definition of an affine deformation. In an affine deformation, the changes in molecular dimensions are proportional to the corresponding dimensional changes in the bulk material. In other words a single chain elongates exactly as the sample as a whole. Such behaviour is expected to occur in Gaussian coils. On the other hand, it is most unlikely that crystalline lamellae can be deformed affinely over a wide range of draw ratio. This is simply because various processes are involved during the deformation of crystalline material (e.g. slip, re-orientation and crystal break-up). In semi-crystalline materials under stress, the amorphous regions will be aligned first in general. When the stress is high enough, the lamellae themselves will be affected by the deformation. Hence, departure from affine behaviour observed in the evolution of the radius parallel to the draw direction may suggest that the lamellae start to be deformed.

When stretching of the sample has begun, we have seen that both the radii parallel and perpendicular follow affine behaviour, up to a draw ratio of 1.5 for the linear DPE samples and up to around 2.4 for the copolymer DPE samples. This suggests that initially, the stress may be concentrated in the intercrystalline regions. When the deformation is large enough, the lamellae themselves undergo deformation. This would result in departure from affine behaviour, which is observed at draw ratios in excess of the figures quoted above. However, this process of lamellar deformation must have started at much lower draw ratios than observed here, since plastic yielding, which is generally agreed to be a lamellar deformation process [5], has already begun. It is believed that the plastic yielding process has first a minor effect and that at low draw ratios it is the deformation of the amorphous regions which is dominant. At higher draw ratios, deformation of the crystalline regions becomes major, and departure from affine behaviour is observed. But how can this delay in departure from affine behaviour for the copolymer DPE guest samples relative to their linear guest counterparts be explained?

One reason may be related to the difference in the degree of crystallinity between the copolymer and linear DPE guest samples. But this is not the case since LL and CL sample types have almost the same degree of crystallinity (53% and 52% respectively for LL/95/385 and CL/95/385, see chapter 4 section 3.2.2), as have LC and CC sample types (42% and 38%, respectively for LC/95/181 and CC/95/181): indeed, we would expect sample crystallinity, for identical crystallisation conditions, to be controlled by

the majority matrix species. We have seen that departure from affine behaviour occurs at larger deformations for both CL and CC samples relative to LL and LC samples, so this difference in behaviour is not related to the difference of crystallinity between the copolymer and linear guest samples.

A second reason may be related to the fact for the copolymer guest molecules, the branches are preferentially excluded from the lamellae [6, 7, 8]. The branches may act as "anchors" on the crystallite surface and may be "locking up" the lamellae, delaying the onset of their deformation (and maybe of their break-up).

VI.1.2. Time dependent results on the relaxing samples.

In this section we will present the results on the relaxation behaviour following unclamping. As for the in situ deformed sample, the thin film samples were drawn using a Minimat Tensile Tester at 1 mm min^{-1} and at ambient temperatures. After stretching, the Tester was mounted in the neutron beam and the sample unclamped. Values were obtained for R_{Par} (the component of Rg in the drawing direction) and R_{Per} (the perpendicular component of Rg), as a function of time after unclamping. The results are presented in Figure VI. 6 as plots of the ratio R_{Par}/ R_{Per}.

Since this problem may be treated as the relaxation of a labelled chain within an unlabelled matrix after removal of the constraints, an analogy with the dynamics of a polymer in a fixed network can be easily made. The problem of the motion of a chain moving through a fixed network has been widely treated in the past (see for example reference 9). A key concept to solve it was the reptation model proposed by de Gennes [10]. However, the de Gennes reptation model refers to amorphous systems and therefore may not be directly related to our problem. Since, as stated above, we are mainly concerned with amorphous alignment at low draw ratios, using this theory is probably a good assumption in this region. In a situation where a chain is surrounded by a fixed network of obstacles, it was suggested that the motion of the chain is almost confined in a tube-like region. As time passes, the polymer is able to twist out of the tube in which it initially found itself and create a new part of the tube. This new part of the tube then becomes a constraint for the rest of the chain, while the part of the tube vacated by the polymer disappears. In other words, the chain uses the degrees of freedom at its ends to change shape gradually during its motion along itself. From the reptation theory, it was shown [9] and later verified by computer simulation [11, 12] and by measurement of the

diffusion constant of a melt of a deuterated polyethylene in a polyethylene matrix [13, 14] that the self diffusion constant for a polymer should be inversely proportional to the square of the molecular weight [9]. Therefore, it is expected that the relaxation time increases as the polymer molecular weight increases. Also, it was shown using the same theory that the self diffusion constant decreases exponentially with the branch length [9]. Again, it is expected that the relaxation time for a copolymer will be larger than for a linear polymer.

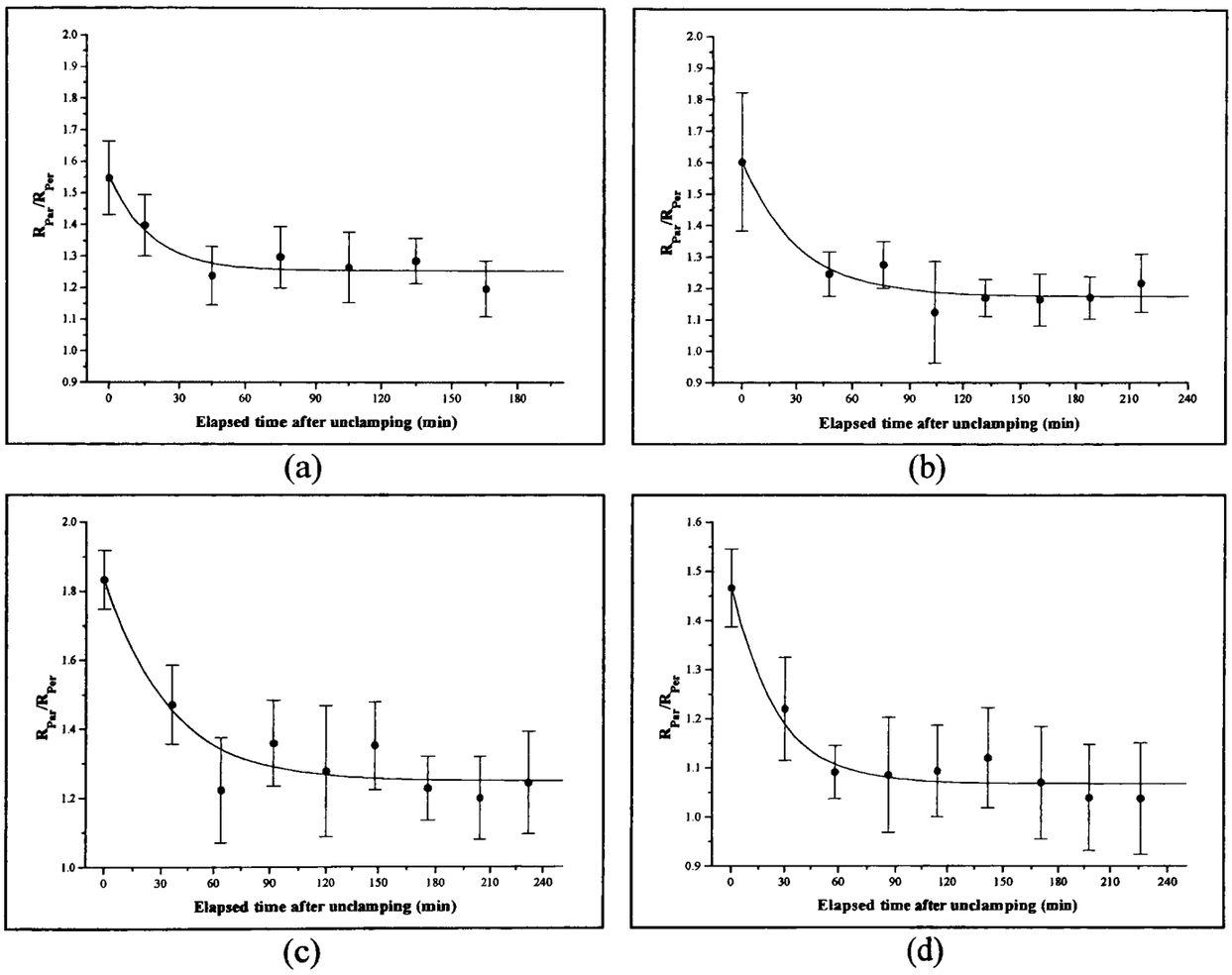

Figure VI. 6: *Evolution of the ratio R_{Par}/R_{Per} in function of the elapsed time after unclamping the sample for samples (a) LL/95/385/1.3; (b) CL/95/385/1.3; (c) CC/95/181/1.4; and (d) LL/413/385/1.3. The black lines represent exponential decay fits of the data.*

As can be seen in Figure VI. 6, the plots of the ratio R_{Par}/ R_{Per} could generally be adequately fitted to a single exponential decay defined by:

$$R_{Par}/R_{Per} = \alpha_{unreco} + \alpha_{reco} e^{-t/\tau} \qquad \text{(VI. 4)}$$

where, τ is the characteristic relaxation time, t the elapsed time after unclamping, α_{reco} the recoverable degree of deformation and α_{unreco} the permanent molecular deformation.

The characteristic relaxation times, τ, for each sample are listed in Table VI. 2 along with the recoverable degree of deformation, α_{reco}, and the permanent molecular deformation, α_{unreco}.

	DR	α_{reco}	α_{unreco}	τ (min)
LL/95/385	1.25	0.30 ± 0.06	1.25 ± 0.1	17.5 ± 8
LL/413/385	1.28	0.40 ± 0.03	1.07 ± 0.02	25 ± 5
CL/95/385	1.29	0.43 ± 0.05	1.17 ± 0.02	30.5 ± 11
CC/95/181	1.38	0.53 ± 0.05	1.25 ± 0.03	35 ± 10

Table VI. 2: *Results of the single exponential delay fits on the evolution of the ratio R_{Par}/ R_{Per} with elapsed time after unclamping the samples. α_{unreco} is the degree of permanent molecular deformation, α_{reco} is the recoverable degree of deformation, and τ the characteristic relaxation time.*

The initial degree of deformation was chosen to be roughly the same for all samples. This allows the comparison of the different characteristics listed in Table VI. 2.

From this table it can be seen that the relaxation time seems to vary with sample type. As expected from the discussion above, sample CC/95/385 has taken the longest time to relax, while sample LL/95/385 is the fastest. Also, it appears from these results that increasing the molecular weight of the guest molecule increases the relaxation time, which is in qualitative agreement with the reptation predictions, although the relaxation time clearly does not increase as the cube of the molecular weight. A similar trend is observed for the amount of recoverable deformation. The copolymer guest samples appear to be more 'elastic' than their linear counterparts.

Unfortunately, due to the way the experiments were carried out, most of the rapid early stages of relaxation could not be assessed. Also because short data collection times and small samples were used, the uncertainties in the time constants are very large. This makes it difficult to draw any firm conclusion from these results. The experiment is clearly on the limit of practicality with current SANS instrumentation.

VI.2. FTIR results on in-situ deformed samples.

In the case of the FTIR experiments, it was not possible to mount the Minimat tester with the drawn sample in the FTIR sample holder because of space limitations. In order to do in situ deformation experiments, a clamping system was constructed. This clamping system was positioned on the stretched sample, held in the Minimat at the required draw ratio. The clamps were tightened to hold the stretched sample without any relaxation. The sample was than removed from the Minimat, and kept within the clamp. The clamp and sample were than installed in the spectrometer cryostat sample holder, and cooled to -170°C under vacuum. When this temperature was reached, a measurement was taken. The whole process took on average 15 minutes between the completion of the stretching and the start of the FTIR measurement. In order to make a measurement in the region where the draw ratio was measured (in the necked region), a 2 mm diameter circular aperture was installed on top of the clamping system.

In order to increase the spectral resolution, Fourier-self deconvolution was performed on the FTIR data as explained in chapter III section 2.3. The acquisition and deconvolution of data were made using the FIRST software.

As in the case of the undeformed analysis, curve fittings of the deconvoluted data were carried out in order to obtain the areas of the different contributions to the CD_2 bending region. Firstly, we will characterise the orientation development using the evolution of the areas of the a- and b- polarised parts of the CD_2 bending peak. Secondly we will compare the total area of the doublet components with the area of the singlet component and we will look at the evolution of the splitting with deformation. This will give us information on the local rearrangement of stems occurring with deformation. Finally, more information on the evolution of the local stem arrangement will be obtained by a computer calculation of the CD_2 bending profiles using the same process as described in the preceding chapter.

It is important to note the difference between the two analyses. In the curve fitting process, four to five Voigt shape functions (combinations of Lorentzian and Gaussian shape functions) were used to fit the data. On the other hand, to calculate the CD_2 bending profile, 36 Lorentzian shape functions, corresponding to the small groups of stems expected, were added together. The position of each Lorentzian was determined

using the theoretical splittings of given sizes of group of adjacent labelled stems. While not strictly a curve fitting process, the end result is similar to a highly constrained fit. Because the sample thickness changes during the deformation process, it was important to normalise the infrared spectra obtained. This was done by using the whole area under the CD_2 bending profile as reference (see the previous chapter for more information). Therefore, all the results obtained by both analysis methods were normalised.

VI.2.1. General remarks: Crystallographic re-orientation effects.

Before analysing our infrared data, one should recall the crystallographic re-orientation processes expected for spherulitic polyethylene material.

For an undeformed polyethylene spherulite, we have seen in the first chapter that the crystalline ribbons grow outwards from the centre of the spherulite and are twisting regularly as they go, the b-axis being radial to the spherulite as shown in Figure VI. 7a (this last point is a characteristic of polyethylene, and is not the case for many other polymers). Therefore, initially all three axes are equivalent in their projections in the plane of the sample. When the spherulites become deformed, their spherical structure changes to an ellipsoidal one as shown in Figure VI. 7b. Ultimately, in highly drawn material the fibre morphology is characterised by the chains being parallel, aligned in the draw direction (i.e. c-axis is parallel to the draw direction). In different regions of the undeformed spherulite, the c-axis has different initial orientations with respect to the draw direction, and hence the reorientation process involving the ultimate alignment of the c-axis parallel to the draw direction must vary from one locality to the other.

For radii perpendicular to the draw direction, ($1_\perp$ and $2_\perp$ in Figure VI. 7a), the c axis orientation is varying periodically with respect to the direction of deformation. In a particular region (region $1_\perp$), the c-axis is along the draw direction to begin with, and therefore does not require any reorientation. For the other extreme case, corresponding to the situation $2_\perp$ where the c-axis is perpendicular to the plane of the sample, and for the intermediate situations, the unit cell needs rotating about b so as to achieve fibre orientation. Thus, the a-axis will leave the plane of the sample while the c-axis is moving into the plane (Figure VI. 7b, region $2_\perp$). This rotation about the b-axis leads to the untwisting of the crystalline ribbons close to the minor axis of the deformed spherulite. This untwisting phenomenon was previously incorporated in the different

models describing the evolution of the light scattering pattern of deformed polyethylene [15, 16, 17, 18, 19, 20, 21] and observed by optical microscopy [22]. From the point of view of the infrared experiment, this would result in a decrease of the a-polarised component of absorbance of the CD_2 bending vibration, while the absorbance of the b-polarised component would remain constant.

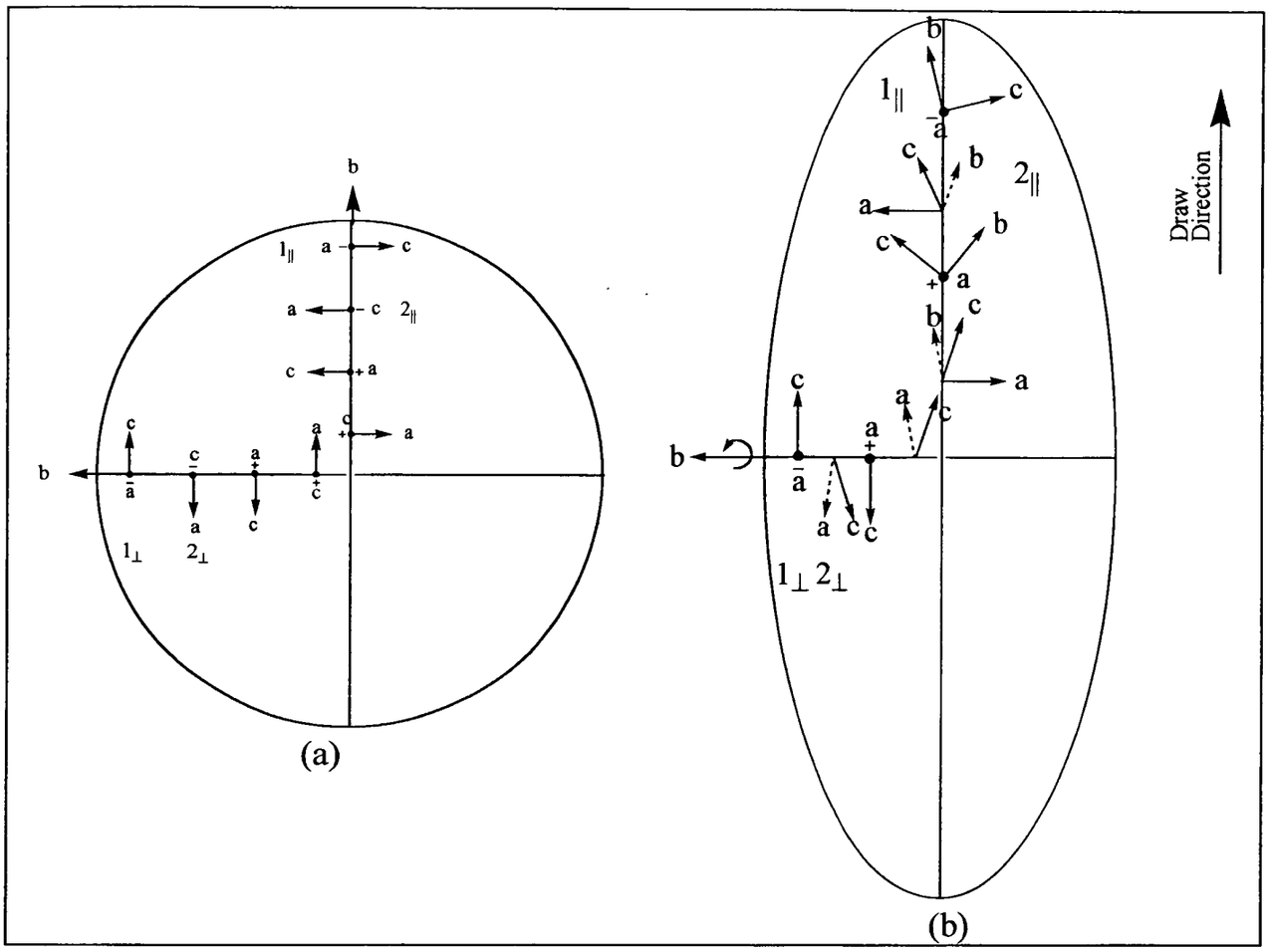

Figure VI. 7: *(a) illustration of an homogeneous spherulite showing the periodicity of the orientation of the unit cell and (b) for a deformed spherulite showing the processes of reorientation (from ref. 12). The dashed arrows are for axes leaving the plane of the sample. The plain arrows are for axes in the plane or coming into the plane of the sample.*

For radii parallel to the draw direction, ($1_{||}$ and $2_{||}$ in Figure VI. 7a) c is always perpendicular to the draw direction, while b is along it. Therefore, alignment of c must involve rotation of the unit cell about a for all crystals along this radius. In the region $1_{||}$, both b and c-axes are in the plane of the sample, while a is normal to it. Both b and c will stay in the plane of the sample during the reorientation process (Figure VI. 7b, region $1_{||}$). As a result, in region $1_{||}$ the infrared absorbance of the a and b-polarised components stays constant during this process. In the region $2_{||}$, it is now c which is normal to the plane of the sample, while both a and b are in this plane. The rotation

about a involves the departure of the b-axis from the plane of the sample, while the c-axis is moving into the plane. This behaviour suggests that break-up must occur for the ribbon parallel to the draw direction. This results in a decrease of the infrared absorbance of the b-polarised component of the CD_2 bending profile, the a-polarised absorbance staying constant.

For radius perpendicular to the plane of the sample and perpendicular to the draw direction, the c-axis is varying periodically with respect to the draw direction but is always in the plane of the sample, while the b-axis is normal to it. The unit cell requires rotation about the b-axis so as to achieve c-axis alignment with the direction of the deformation. In this case, both the infrared absorbance of the b- and a-polarised components would stay constant.

Hay and Keller [21], in their study of the deformation of polyethylene spherulites, have observed evidence of rotation of the unit cell about the b-axis to begin with (up to a draw ratio of 7), while signs of rotation about the a-axis were only found at the largest draw ratio studied (draw ratios of 10 and more). They suggested that radii parallel to the draw direction appear more resistant to deformation to begin with and they concluded therefore that rotation of the crystals axes about b occurs more readily than about a. More recently, wide angle X-ray patterns obtained by Hiss et al [23] on different types of polyethylene stretched up to a draw ratio of around 5 suggest also that the reorientation of the chain axis about the b-axis occurs more readily than about the a-axis. This would mean that there should be a larger component of rotation about the b-axis than about the a-axis in our samples and for all draw ratios.

Radius	Axis of unit cell rotation	Effect on components absorbance
$\|\|$ to draw direction	a	a •, b ↓
$\perp$ to draw and in sample plane	b	a ↓, b •
$\perp$ to draw and $\perp$ to plane	b	a •, b •

Table VI. 3: *Summary of the expected axis of unit cell rotation and the effects on the a- and b-polarised absorbance components induced by stretching. a • means that the a-polarised absorbance stays constant, b ↓ means that the b-polarised absorbance decreases.*

In conclusion the crystallographic re-orientation induced by stretching should result in a decrease in the infrared absorbance of the a-polarised component with increasing the degree of deformation while the absorbance of the b-polarised component should stay

constant to begin with and then perhaps decrease at higher draw ratios, if re-orientation of lamellae parallel to the draw direction becomes significant.

It is important to remark that the deformation processes occurring in the amorphous regions are not taken into account in this analysis. Only the overall effect of the crystallographic re-orientation has been considered here.

VI.2.2. Sample LL/95/385.

First of all, before being able to study the effect of branching on the molecular rearrangement occurring upon deformation, a clear understanding of the behaviour of a linear sample is necessary. As we have said in chapter 5.1.1, sample LL/95/385 is used as a baseline in our study of the molecular deformation of polyethylene and the behaviour of the different samples with stretching will be compared to that of LL/95/385.

VI.2.2.1. The CD_2 bending region.

Figure VI. 8 shows the evolution of the CD_2 bending region with draw ratio. For all draw ratios, both the raw and deconvoluted data are shown. Deconvolutions of the raw data were made using the Mattson deconvolution FIRST software with representative values of the deconvolution parameters α (full width at half maximum absorbance of the intrinsic lineshape) and K (enhancement factor) of 1.5 cm^{-1} and 2, respectively. A Lorentzian lineshape was always used for the deconvolution of the infrared data.

The first thing to notice is that the CD_2 bending profile has changed little through the deformation. The spectrum for a DR = 6.7 shows no major differences by comparison with the one measured for the undeformed sample. This was a surprising result, especially since in early FTIR measurements on single crystal polyethylene the CD_2 bending profile obtained on a sample deformed to a roll ratio of 6 was almost reduced to the singlet component [24].

Four major steps can be identified from the data (Figures VI. 8 and VI. 9a). Up to a draw ratio of 1.4, the a-polarised component almost doubles in area while the b-polarised component stays more or less constant. From a DR of 1.4 to 3.1, a big increase in the intensity on the high wavenumber side of the band occurs, which corresponds to vibrations polarised parallel to the crystal a-axis (see chapter III.3.2), while on the low wavenumber side, corresponding to vibrations with polarisation parallel to the crystal b-axis, the absorbance decreases. From a draw ratio between 3.1 and 4.5, little change is observed in either of the a and b-polarised components. Finally from a DR of 4.5 up to 6.7 (the end of our data set), a decrease of the intensity of the a-polarised side was observed. The intensity of the b-polarised side initially increases and then stays constant.

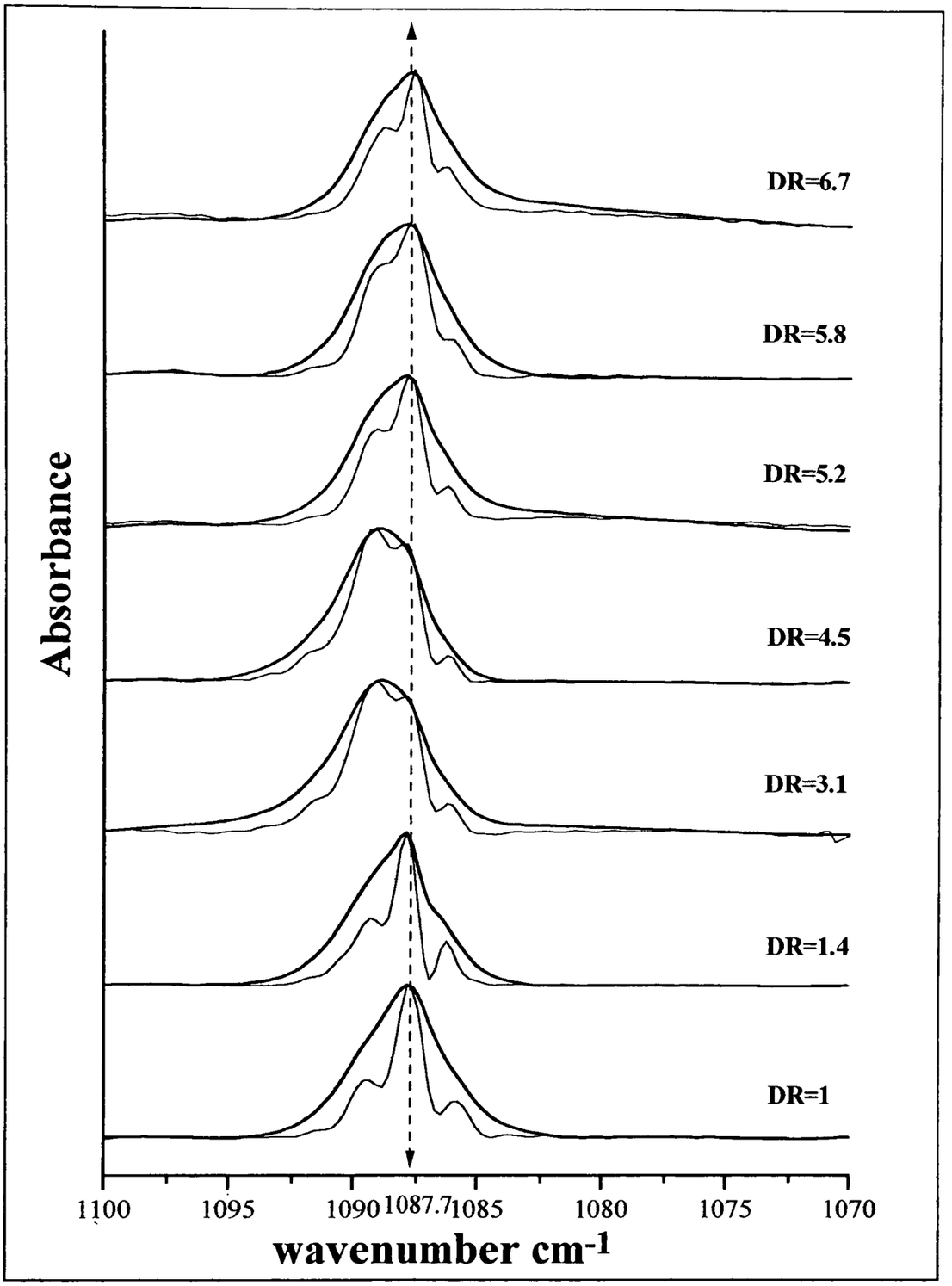

Figure VI. 8: *Evolution of the infrared CD_2 bending region for sample LL/95/385 with draw ratio. The different draw ratios are indicated. The thick line represents the raw data and the fine line, the deconvoluted data. The vertical dashed line indicates the position of the singlet component.*

By looking more closely at the spectra presented in Figure VI. 8, 4 to 5 infrared peaks can be distinguished. The most prominent is the central one, which is identified as the singlet component and includes contributions from [110] isolated labelled stems, and from amorphous chains (as explained in chapter III.). The other peaks result from the orthorhombic structure of polyethylene and the splitting between them is related to the

size and shape of groups of labelled stems which are adjacent in the [110] direction. The different peak positions and areas were determined by curve fitting the normalised deconvoluted data with 4 to 5 bands. Because individual components are not always resolved on deconvolution, we do not always use an odd number of peaks. Each of these peaks was taken as a combination of Lorentzian and Gaussian components, in a similar way to the analysis used in the preceding chapter on the undeformed samples

VI.2.2.1.1. Evolution of the a- and b-polarised sides of the CD_2 bending region.

In this section we will characterise the behaviour of the a- and b- polarised bands of the CD_2 bending mode with the deformation of LL/95/385. The areas of the a- and b-polarised parts of the profile were determined by adding the areas of each Voigt shape function used for fitting the CD_2 bending doublets. The evolution of the areas of the a- and b- polarised bands is presented in Figure VI. 9a. Also, the ratio of the areas of the b- and a-polarised bands was determined and is shown in Figure VI. 9b.

In Figure VI. 9a, two stages of deformation were determined. In the first stage of deformation, the area of the a-polarised component of the CD_2 bending region increases and reaches a maximum at a draw ratio of 4.5, where the area of the b-polarised part of the profile reaches a minimum. This may be related to the progressive alignment of the a-axis in the plane of the sample, while the b-axis appears to leave the plane of the sample. The second phase of the deformation sees a rapid decrease in the a-polarised area while the b-polarised area increases and reaches a plateau value (almost its starting value) up to the end of the drawing range studied. This is attributable to the a-axis leaving the plane of the sample. We have seen in section VI.2.1 that the final c-axis alignment with the draw direction involves a decrease of the absorbance of the a-polarised side while the absorbance of the b-polarised component of the CD_2 bending mode should stay constant. Therefore, the second stage of the deformation appears to be consistent with the progressive alignment of the c-axis with the draw direction. As shown in section VI.2.1, this c-axis orientation involves the untwisting of the crystalline ribbons close to the spherulite axes perpendicular to the draw direction.

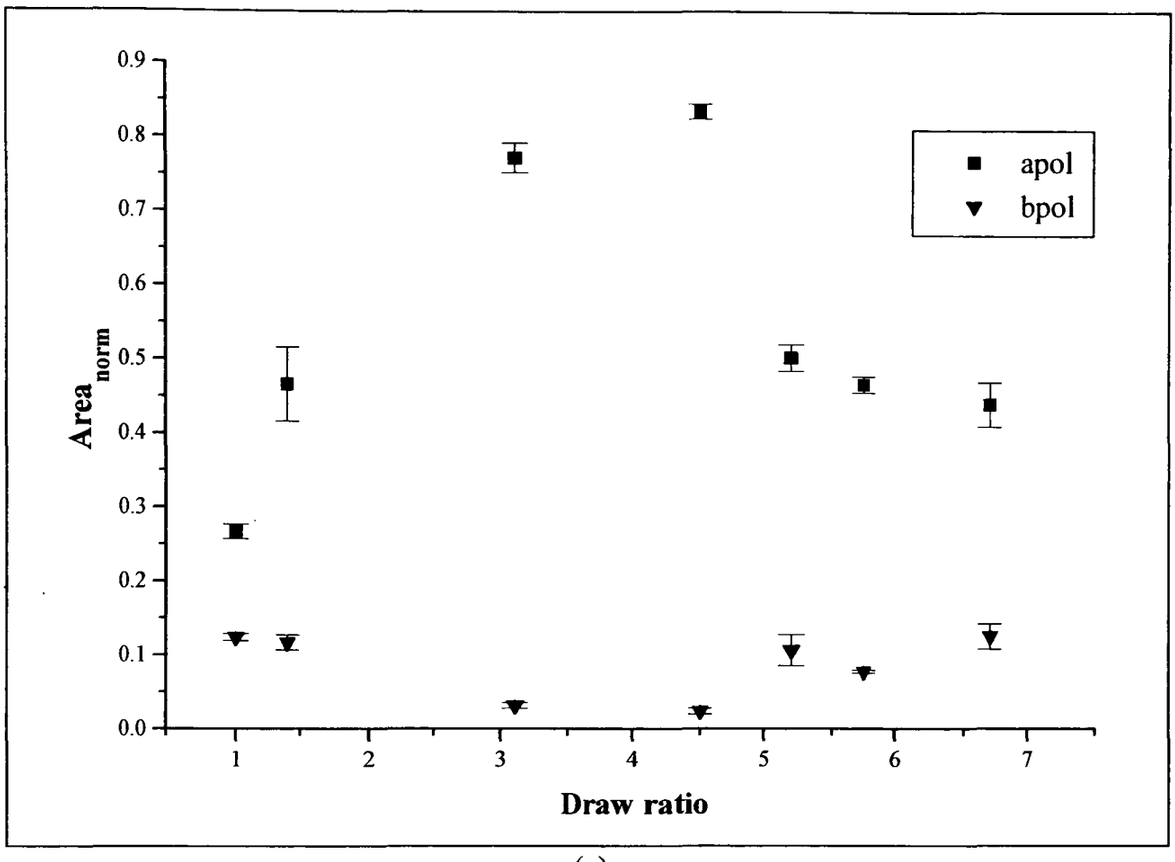

(a)

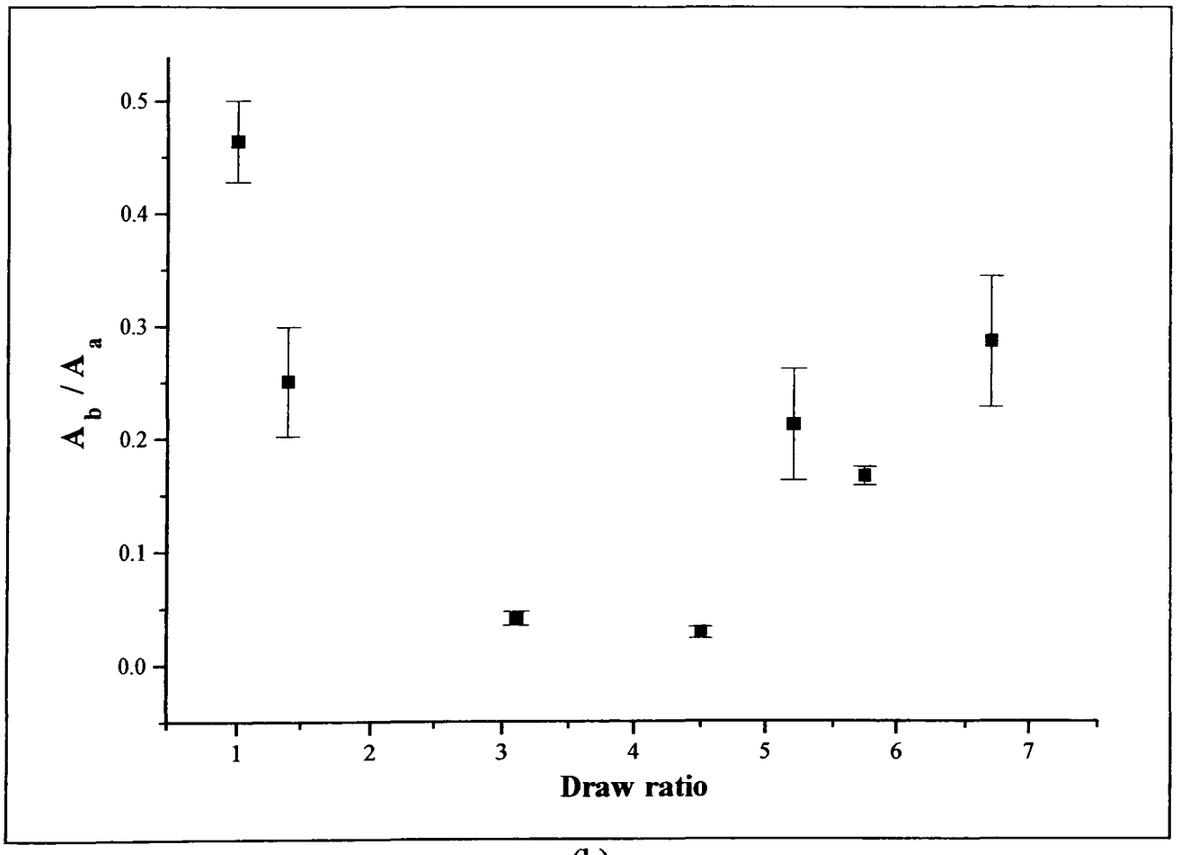

(b)

Figure VI. 9: *(a) Evolution of the normalised areas of the a- and b-polarised components and (b) evolution of the ratio, A_b/A_a, between the areas of the b- and a-polarised bands with draw ratio for sample LL/95/385.*

It should be noted that the analysis made in section VI.2.1 applies only to the crystals, and the behaviour of the amorphous polymer was not taken into account. But from the neutron scattering results, we know that initially the deformation is taking place in the amorphous region. Therefore, the behaviour observed in this first stage must be related to the deformation of the amorphous regions of the polymer. The study of the evolution of the area of the singlet component, presented in Figure VI. 10 along with the evolution of the total area of the doublet components (area of the a-polarised side of the profile added to the area of the b-polarised side), may give us some clues on the phenomenon occurring during the first stage of the deformation of sample LL/95/385.

Again, the two stages of the deformation are reflected in the evolution of the area of the singlet component which is presented in Figure VI. 10 along with the evolution of the total area of the doublet component (area of the a- plus area of b- component) of the CD_2 bending region. We can see from this figure that for a draw ratio of 4.5, the area of the singlet component reaches a minimum while the total area of the doublet component reaches a maximum. The second stage of Figure VI. 10, shows a very rapid increase of the absorbance of the singlet relative to the doublet component. This suggests the progressive break-up of groups of adjacent labelled stems.

The initial reduction in the area of the singlet component relative to the doublet suggests that the number of isolated stems within crystalline lamellae and/or the contribution of the amorphous polymer has been reduced. The most likely cause is a partial crystallisation of the amorphous polymer. If such a phenomenon of stress-induced crystallisation is occurring in this first stage of the deformation, this would result in an increase of the size of groups of adjacent labelled stems leading to an increase of the outermost infrared CD_2 bending splitting. This analysis will be carried out in the following section.

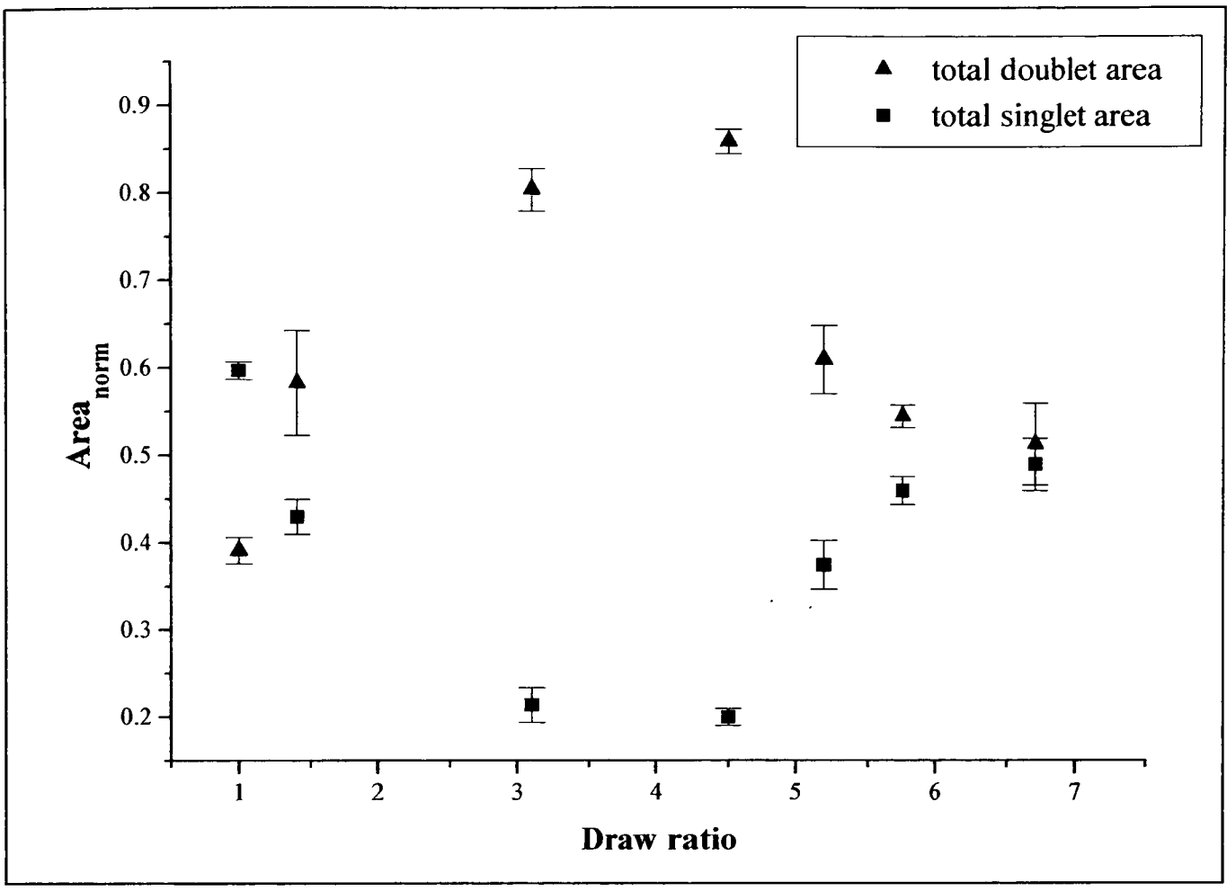

Figure VI. 10: *Evolution the area of the singlet and the total area of the doublet components of the CD_2 bending peak for sample LL/95/385.*

VI.2.2.1.2. Group size analysis.

In this section we will monitor the progressive destruction of the initial local stem arrangement using two different methods. First of all, the evolution of the doublet splitting, determined by the curve fitting of the CD_2 bending profile, will be presented in Figure VI. 11. Secondly, the evolution with deformation of the stem distribution within groups will be monitored (Figure VI. 12 and 13). This evolution was determined from calculated CD_2 bending doublet splittings , using the same process as was described in the previous chapter.

From Figure VI. 11, it can be noted that for the first drawn sample (lowest draw ratio larger than 1) the inner splitting (between approximately the 1089 cm^{-1} and 1086 cm^{-1} bands) has decreased whereas only a very small decrease is observed for the outermost splitting. The inner splitting has changed from 3.7 to 3.1 cm^{-1} which corresponds to a decrease of the group size from 4 to 3 adjacent stems in <110> directions. It appears that, on average, one of the stems contributing to the small groups has moved out from the <110> directions at the beginning of the deformation, maybe by slip or by a change in the lamellar thickness.

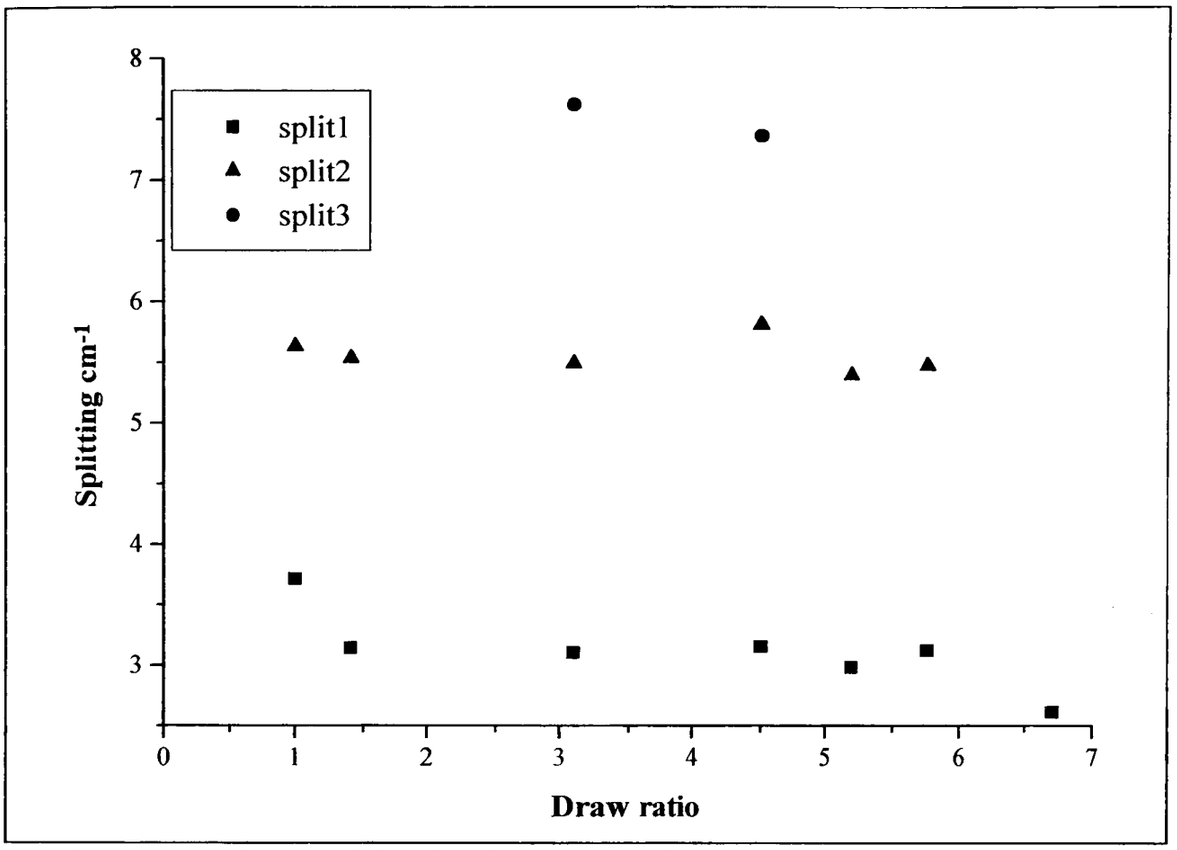

Figure VI. 11: *Evolution of the doublet splitting for sample LL/95/385 with draw ratio. Split 1 is the splitting between bands at approximately 1089 cm^{-1} and 1086 cm^{-1}. Split 2 is the splitting between bands at approximately 1091 cm^{-1} and 1086 cm^{-1}. Split 3 is the splitting between bands at approximately 1093 cm^{-1} and 1086cm^{-1}.*

After this decrease, the values of splittings 1 and 2 show no changes up to a DR of 5.8. Nevertheless, a new doublet was resolved for a draw ratio of 3.1. The splitting measured is of 7.6 cm^{-1}. This corresponds to groups of 3×3 adjacent stems in <110> directions (see Table III. 1 in chapter 3 section 4.2). However, the actual absorbance of the peak at around 1093 cm^{-1} is very low, meaning that only a very small number of stems contribute to these groups. Two possible reasons can be advanced for the emergence of these new groups. Two smaller groups may become adjacent during the deformation process and form one larger group, although this seems unlikely for the draw ratios considered here (although it may happen in forming fibres). At the same time, the deformation of the amorphous region may result in a stress-induced crystallisation, leading to the creation of new crystals. It is possible that within such newly formed crystals, stems may become adjacent to one or more labelled stems, leading to the formation of new groups. The degree of adjacency will presumably depend on prevailing conditions (e.g. temperature, stress...). This adds support to the suggestion made in the previous section that stress-induced crystallisation is occurring.

After a draw ratio of 4.5, the largest splitting has disappeared, and for a DR of 6.7, the second largest splitting has also disappeared. This reflects the fact that the outermost peaks at around 1091 and 1093 cm^{-1} were no longer resolved in the infrared CD_2 bending profile. This is consistent with the progressive destruction of the largest groups and the creation of smaller groups, as observed by Okoroafor and Spells for single crystals [24] (described in chapter one section 2.1). It is believed that the largest groups are breaking up into smaller groups which are then rotating so as to have the molecular axis aligned with the draw direction.

The above analysis was made using the positions of the peaks as determined by the curve fitting of deconvoluted data for sample LL/95/385. However, the solution given by the curve fitting technique only provides averaged values of group sizes, and also, only limited information on the evolution of the stem distribution with deformation can be obtained from this curve fitting analysis. As explained in the previous chapter, the splittings for various small groups of adjacent stems have been determined using a simple coupled oscillator theory (see chapter 3 section 4.2 and Table III. 1). Therefore, we can use this information for an alternative fitting process. The CD_2 bending profiles were simulated using a computer program by combining theoretical splittings in the same way as presented in Chapter 5 section 2.1.2. As mentioned in the preceding chapter, this process does not strictly constitute curve fitting, but probably provides the best estimates of the numbers of different groups present. Therefore, it becomes possible to monitor the evolution of the groups of adjacent stems with deformation and to observe the start of the destruction of the largest groups. Examples of simulated band profiles are presented in Figure VI. 12, along with the corresponding deconvoluted data. The stem distributions used for these simulations for sample LL/95/385 are presented in Figure VI. 13.

In contrast to the analysis made for the undeformed samples, here the contribution of the chains in the amorphous regions was not removed from the singlet component. This is because the evolution of the crystallinity of the sample with deformation was not known in detail. Crystallinity measurements made on LL/95/385 show an increase from 53% (undeformed sample) to 61% for a DR of 3.5. Similar measurements made on sample CL/378/385 also show an increase in the crystallinity from 50% for the undeformed sample to 63% for a sample deformed to a DR of 6. These experiments were performed with the DSC technique. The sample was firstly stretched and put in the clamping

system in order to obtain an infrared spectrum. After that, the sample was kept held in the clamps and placed between the DSC pan and its lid. The pan was then sealed. In this way, the sample was still stretched, clamped between the pan and its cover, for the DSC measurement. Because this process required the destruction of the sample, systematic DSC measurements for each draw ratio were not carried out. Therefore the detailed evolution of the crystallinity with deformation is not known, but it appears that upon drawing the sample crystallinity increases. Such stress-induced increase in crystallinity has been widely reported in the literature [25, 26, 27].

In order to make allowance for the orientation dependence in the calculation of the spectra, a coefficient, α, was introduced to scale the intensity of the low wavenumber side of the spectra (which corresponds to the b-polarised vibrations in the CD_2 bending mode). Therefore, the proportion of stems arising from each group, N, was determined from the proportion of stems, $N_{splitting}$ used in the calculation process of the CD_2 bending profile by the following expression:

$$N = \frac{\alpha_j}{\alpha_1} N_{splitting} \qquad \text{(VI 5)}$$

where α_j and α_1 are the scaling coefficients used to fit the low frequency profile respectively at a draw ratio j and for the undeformed sample.

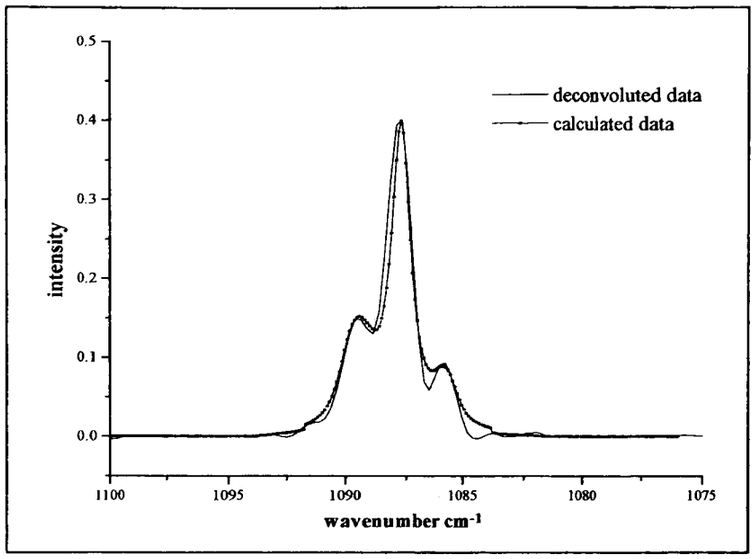

(a)

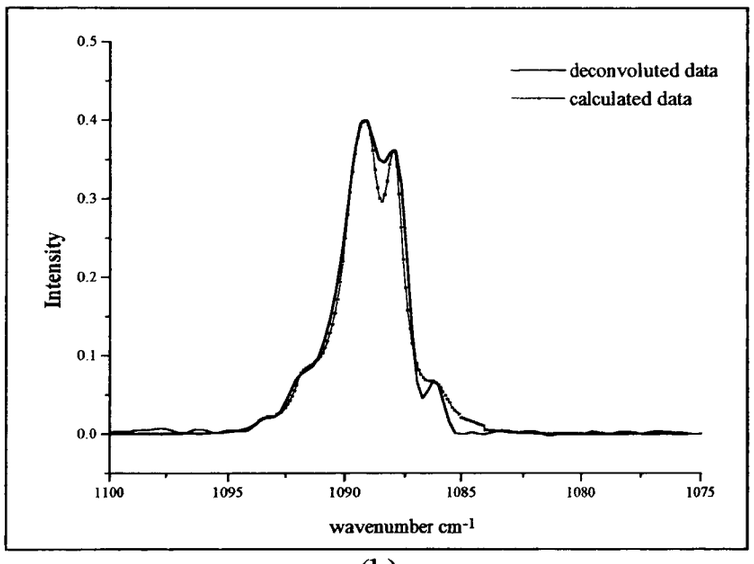

(b)

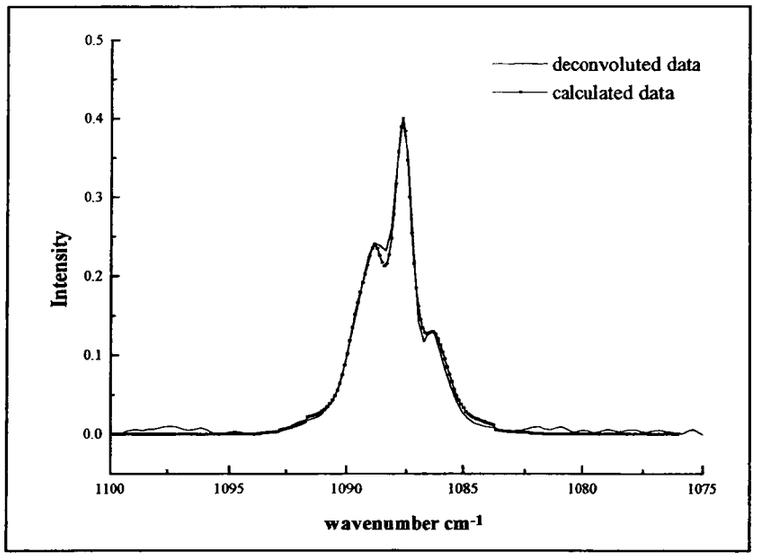

(c)

Figure VI. 12: *Example of the calculation of the CD_2 bending profiles by combining splittings calculated using a simple coupled oscillator theory together with deconvoluted experimental data for sample LL/95/385 (a) undeformed; (b) with a draw ratio, DR = 4.5; and (c) with a DR = 6.7. The calculations were made using Lorentzian shape functions.*

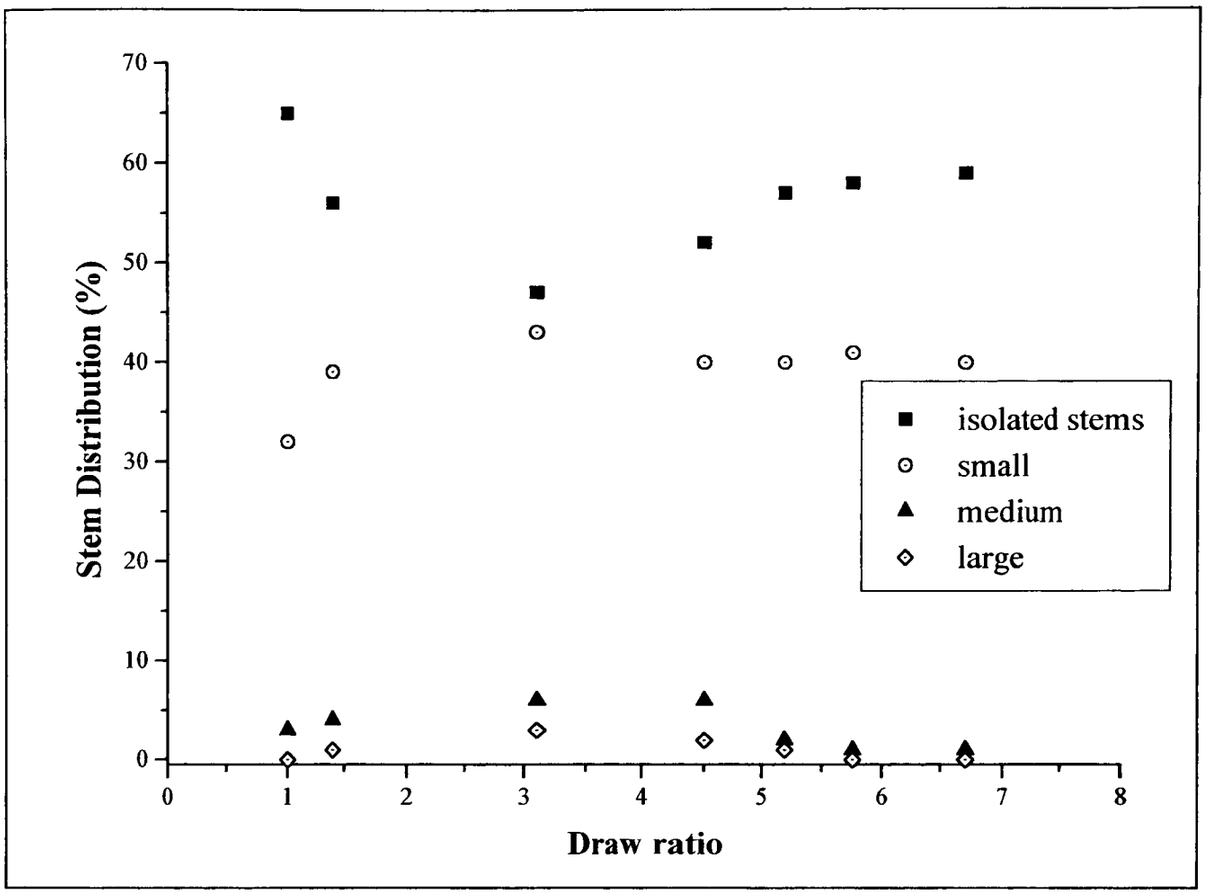

Figure VI. 13: *Evolution of the stem distributions with deformation for sample LL/95/385. The isolated stems are contributing to the singlet; the "small" groups are constituted of 2 to 4 stems in one plane (2×1, 3×1 and 4×1 corresponding to splittings between 2.6 and 3.9 cm^{-1}) and contribute to the inner doublets; the "medium" groups are constituted of 5 to 7 stems in one or two planes (5×1, 2×2 and 3×2 groups corresponding to splittings between 4.2 and 6.1 cm^{-1}) and contribute to the intermediate doublets; the "large" groups are constituted of 8 to 12 adjacent stems in 2 or 3 planes (4×2, 5×2, 3×3 and 4×3 groups corresponding to splittings between 6.4 and 8.1 cm^{-1}) and contribute to the outermost doublet.*

From Figure VI. 13, the group population evolves in two steps. Firstly, up to a draw ratio between 3.1 and 4.5, the number of isolated stems decreases from 65% to 50%. This decrease is linked to an increase in the number of stems distributed in groups: the number of stems in the small groups has simultaneously increased from 32 to 40%, from 3 to 6% in the medium size groups and from 0 to 4% in the largest groups. From this observation, it appears that, during the first stage of the deformation, 15% of the isolated stems are now included in groups. Also, the largest groups present are bigger than in the undeformed sample. This confirms the suggestion of crystallisation during deformation observed in the evolution of the CD_2 bending splitting (inferred from Figure VI. 11) and from our DSC results. The second stage of the deformation, from DR = 4.5 to the end of our data set, shows different behaviour. The number of isolated stems increases, while for the stems contributing to the doublets, two observations can be made. Firstly the

number of stems in medium groups decreases and the large groups disappear at a DR = 6.7. This is consistent with the observation made from the evolution of the splittings, where the outermost splitting had also disappeared at this draw ratio. At the same time, the number of stems in small groups increases slightly. These observations indicate that during deformation, groups of adjacent stems break up, with the proportion of isolated stems and smaller groups of adjacent stems increasing at the expense of the largest groups of adjacent stems.

VI.2.2.2. The CH_2 wagging region.

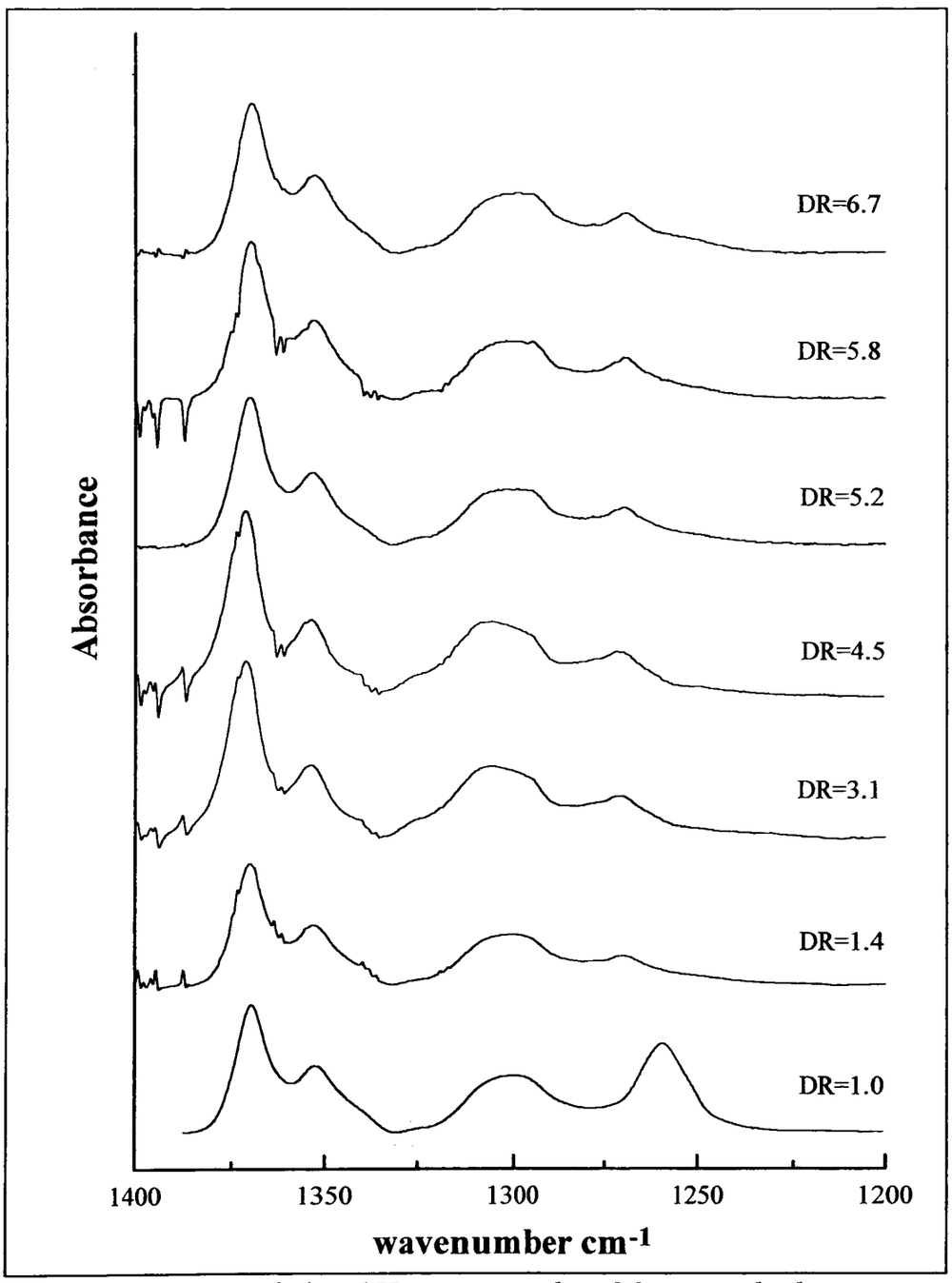

Figure VI. 14: *Variation of the CH_2 wagging bandshape with draw ratio, DR, for sample LL/95/385.*

Figure VI. 14 compares the CH_2 wagging region bandshapes for sample LL/95/385 at different draw ratios. This region includes three absorption bands associated with the departure from the all-trans polymer chain. As in the case of the undeformed samples, all the spectra presented were measured at -170°C. This results in the minimisation of the number of gauche conformations arising from thermal activation. Therefore, primarily structural gauche conformations are taken into account. For sample LL/95/385, three peaks can be seen, namely the gtg/gtg' peak at around 1368 cm^{-1}, the gg peak at around 1052cm^{-1} and the gtg/gtg' peak at around 1300 cm^{-1}. Also, a shoulder on the gg peak, at around 1341 cm^{-1} can be distinguished and corresponds to the end-gauche defect. As explained in the preceding chapter, a fourth band at around 1260 - 1270 cm^{-1} appears in all spectra. The assignment of this band is not known, but there is no reason to relate it to any wagging vibrations. It is supposed that this band is related to a vibration from the deuterated chains. Therefore this band will not be included in our analysis of the wagging modes.

At each draw ratio, it can be seen that the bandshapes are similar. No major changes have occurred during the deformation at the exception of the 1300 cm^{-1} band which shows some shape changes. Again, the process seems to be in two stages. The normalised intensity of each band is reported in Figure VI. 15 (as explained in Chapter 3, the normalisation of the intensity was done with respect to the whole area of the CD_2 bending region). In general, the trends in the evolution with deformation of the three non all-trans conformational bands are similar. Up to a draw ratio of 1.5, the number of non all-trans conformers decreases slightly. For DR values from 1.5 to 3.1, the number of non all-trans conformers increases and for the gtg/gtg' conformations seems to reach a plateau value for a DR between 3.1 and 4.5, after which their number falls.

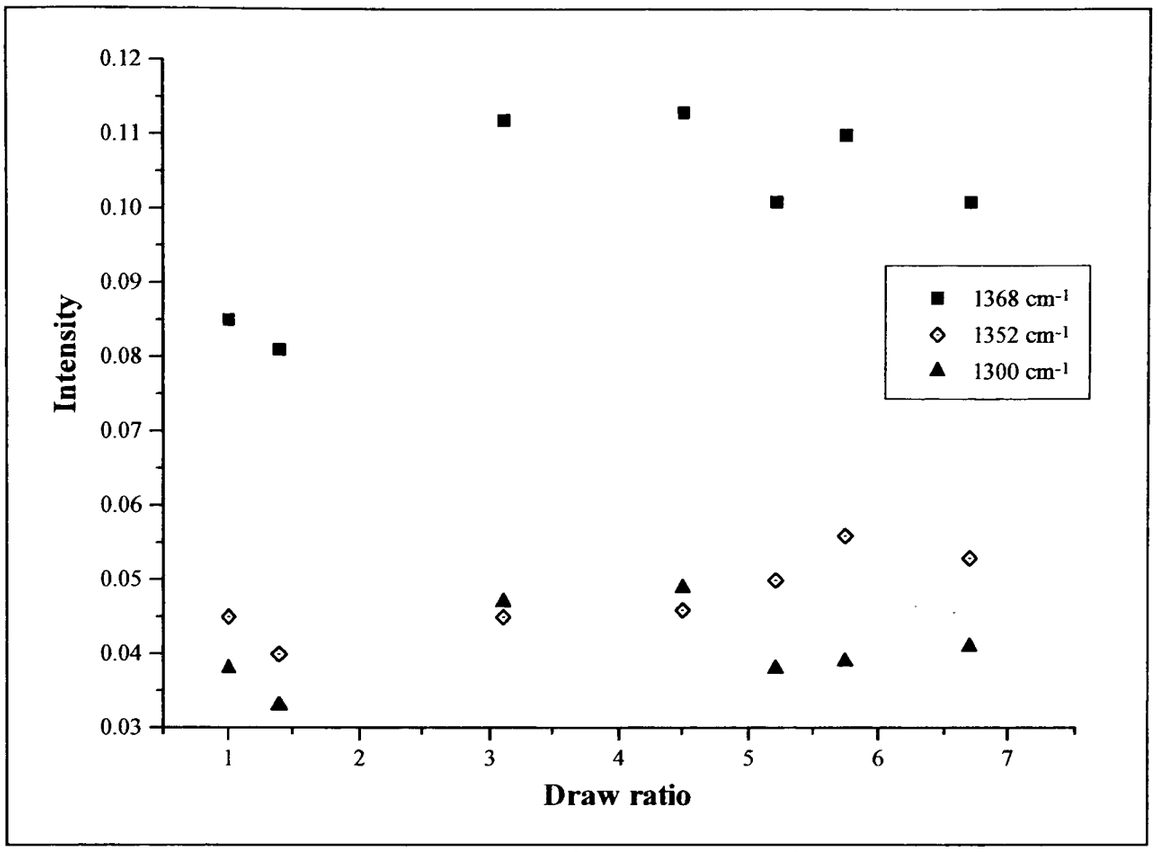

Figure VI. 15: *Evolution with draw ratio of the intensity of the gtg/gtg' band at around 1368 cm^{-1}, the gg band at around 1352 cm^{-1} and the gtg/gtg' band at around 1300 cm^{-1} for sample LL/95/385.*

In the previous section, we have seen that orientation and stress induced crystallisation of the amorphous polymer may occur up to a draw ratio of around 3. Ordering of the amorphous polymer will lead to a decrease in the number of non all-trans conformers. On the contrary, up to a draw ratio between 3 and 4, their number increases. Such an increase may result from an increase in the number of defects in the stressed crystalline regions.

From the neutron scattering results, we have seen that the crystalline regions start to be affected by the deformation after a draw ratio of 1.5. Before a draw ratio of 1.5, it is mainly the amorphous region which sustains the deformation. This results in the decrease in the number of non all-trans conformers observed at a draw ratio of 1.4 in Figure VI. 15. Therefore, it appears that for draw ratios between 1.5 and around 4, the effect of increasing numbers of defects in the crystals is larger than the effect of ordering of the amorphous polymer. In the second stage of the deformation, the number of non all-trans conformers decreases slightly. This may suggest that the disruption of the crystals is at its maximum and therefore, no more defect in the crystals can be created. On the others hand, there may be a compensating effect between the creation and the removal of the defects.

VI.2.1.4. Discussion.

From the different analyses made from the infrared data, we have determined that the deformation behaviour of sample LL/95/385 is in two stages. These two stages will now be discussed.

In the first stage, for draw ratios up to around 4, we have seen that the area of the singlet component decreases, indicating a reduction in the number of isolated stems. On the other hand, the outermost infrared splitting, the number of stems distributed in groups and the total area of the doublet components are increasing. All these results suggest that the number of isolated stems and the contribution of the amorphous polymer to the singlet component are reduced relative to the doublet components of the CD_2 bending region. Such effects on the CD_2 bending profile can only be attributable to stress-induced crystallisation of the amorphous regions. This is consistent with our neutron scattering results which suggest that, up to a draw ratio of around 1.5, the deformation is mainly taking place in the amorphous polymer. Therefore, in this first stage of the deformation, new crystals are created. How can we explain the initial increase of the area of the a-polarised side and the decrease in the area of the b-polarised side of the profile?

From the discussion made in section VI.2.1, we know that the process of final c-axis orientation in the spherulite crystalline lamellae involves a decrease of the absorbance of the a-polarised side of the spectrum. This is in contradiction with what was observed in the first stage of the deformation and thus, the behaviour observed does not reflect the re-orientation occurring in the crystalline lamellae of the spherulite. On the other hand, we know that new crystals are progressively created during the first stage of the deformation (the number of isolated stems decreases progressively up to a DR of around 4 while the number of stems in groups increases). The evolution of the a- and b-polarised components observed in this stage must, therefore, be related to these newly formed crystals. This suggests that these newly formed crystals are created with a preferential orientation. We have found that the behaviour observed is consistent with the a-axis being in the plane of the sample while the b-axis is normal to this plane, and since these new crystals are stress-induced, it is a reasonable to assume that the newly formed crystals have preferential orientation, with the c-axis more or less aligned with the draw direction. The identification of crystals with this orientation would be of interest here. This may be achievable by electron microscopy.

In the second stage of the deformation, for draw ratios larger than 4, we have seen that the area of the a-polarised side of the CD_2 bending profile is decreasing, while the area of the b-polarised side increases before reaching a plateau value. This behaviour is consistent with the re-orientation process of the spherulite crystalline lamellae described in section VI.2.1 and involves primarily the rotation of the unit cell around b so as to align the crystallographic c-axis in the draw direction while the a-axis becomes normal to the plane of the sample. As shown, this process results in the untwisting of the lamellae situated along the spherulite radii perpendicular to the draw direction. At the same time, the outermost splittings have disappeared, and the number of isolated stems is increasing at the expense of the number of stems distributed into groups. This suggests that the largest groups of adjacent labelled stems are breaking up into smaller groups. This is evidence that the crystalline lamellae are breaking up into blocks. The resulting blocks are rotating so as to have their c-axis parallel to the draw direction, corresponding to the start of fibre orientation. A quantitative analysis of the infrared results reveals that the average size of the crystallite is reduced to around 9 Å (corresponding to groups of two adjacent labelled stems in in [110] directions) at a draw ratio of 6.7. It is believed that the disruption of the lamellae may start at lower draw ratio than observed. This is simply because the effects of the break-up can only be seen when the block sizes are already reduced to the initial size (around 18 Å corresponding to groups of four adjacent labelled stems in [110] directions) of the largest groups of adjacent labelled stems (i.e. in undrawn samples). This may also explain the increase in the number of non all-trans conformers observed for draw ratios up to around 4. Indeed such an increase can only result from an increase of the number of defects in the crystalline lamellae.

Transformation from the orthorhombic to the monoclinic phase was detected from the appearance of an infrared absorption peak at 716 cm^{-1} in the CH_2 rocking vibration region. This transformation must only be partial since no sign of the WAXS reflections associated to the monoclinic phase (such as the (001) or $(\bar{2}01)$ monoclinic reflections [28] were observed, and at the largest draw ratio used in this study, a doublet is still observed in the CH_2 and CD_2 bending profiles. The fact that this doublet is still observed at the largest draw ratio confirms that the orthorhombic structure is kept through the deformation. Since the CH_2 wagging modes show a significant increase in some crystal defects, the orthorhombic structure must be highly disrupted. Similar

conclusions were drawn by Lagarón et al [1, 29] from the characterisation of uniaxially stretched HDPE and several branched polyethylene materials by Raman spectroscopy and other techniques. A decrease in the orthorhombic crystallinity, as determined by Raman spectroscopy, was observed and attributed to the creation of a highly disrupted and defective orthorhombic crystalline morphology, with some phase transformation to monoclinic phase and possibly some chain unfolding. These FTIR results cannot clarify this last result, although the increasing CD_2 bending singlet absorbance with draw ratio is consistent with it.

VI.2.3. Sample LL/413/385.

Before comparing the deformation behaviour of linear and branched polyethylene, it is important to have an idea of the effect of chain entanglement and tie-molecules on the deformation process. Because it is known that the number of tie-molecules and the degree of entanglement increases with increasing the molecular weight of the polymer, the deformation behaviour of sample LL/413/385 will give some clues to these effects, if the molecular weight is high enough.

VI.2.3.1. The CD_2 bending region.

The evolution of the CD_2 bending vibration region with uniaxial stretching is presented in Figure VI. 16. Representative values of the deconvolution parameter used are respectively around 1.5 cm^{-1} for the full width at maximum absorbance of the intrinsic lineshape, α and around 2 for the enhancement factor, K for the deformed samples.

First of all, in contrast to sample LL/95/385, the initial CD_2 bending profile and the profile for a DR = 7.4 are very different. For the undeformed sample, 4 peaks are clearly resolved by deconvolution. After deformation at a DR of 7.4, it becomes difficult to distinguish three peaks, even after deconvolution of the experimental data. However, the deconvoluted peak width suggests that these components are present, even if not resolved. Nevertheless, there is still not the degree of change that was previously observed for rolled polyethylene single crystals [24].

As in the case of LL/95/385, the a-polarised vibration of the CD_2 bending mode increases in absorbance with draw ratio. The second stage of the deformation, characterised by a decrease of the a-polarised absorbance, is not observed for sample LL/413/385: no reduction of the absorbance of the a-polarised peaks is observed, even at the largest draw ratio. In contrast to sample LL/95/385, a shift in the position of the singlet is observed after drawing the sample. Initially, the singlet position is at 1087.69 cm^{-1}, after deformation to a draw ratio of 1.8, it is at 1087.93cm^{-1} and appears to stay at a constant position up to the end of the deformation range studied. However, this shift is very small and is of the same order as the spectral resolution used and therefore may have no physical significance.

As for the analysis of the CD_2 bending profile of LL/95/385, results from the curve fitting and from the calculations of the CD_2 bending profiles will be discussed in the following sections.

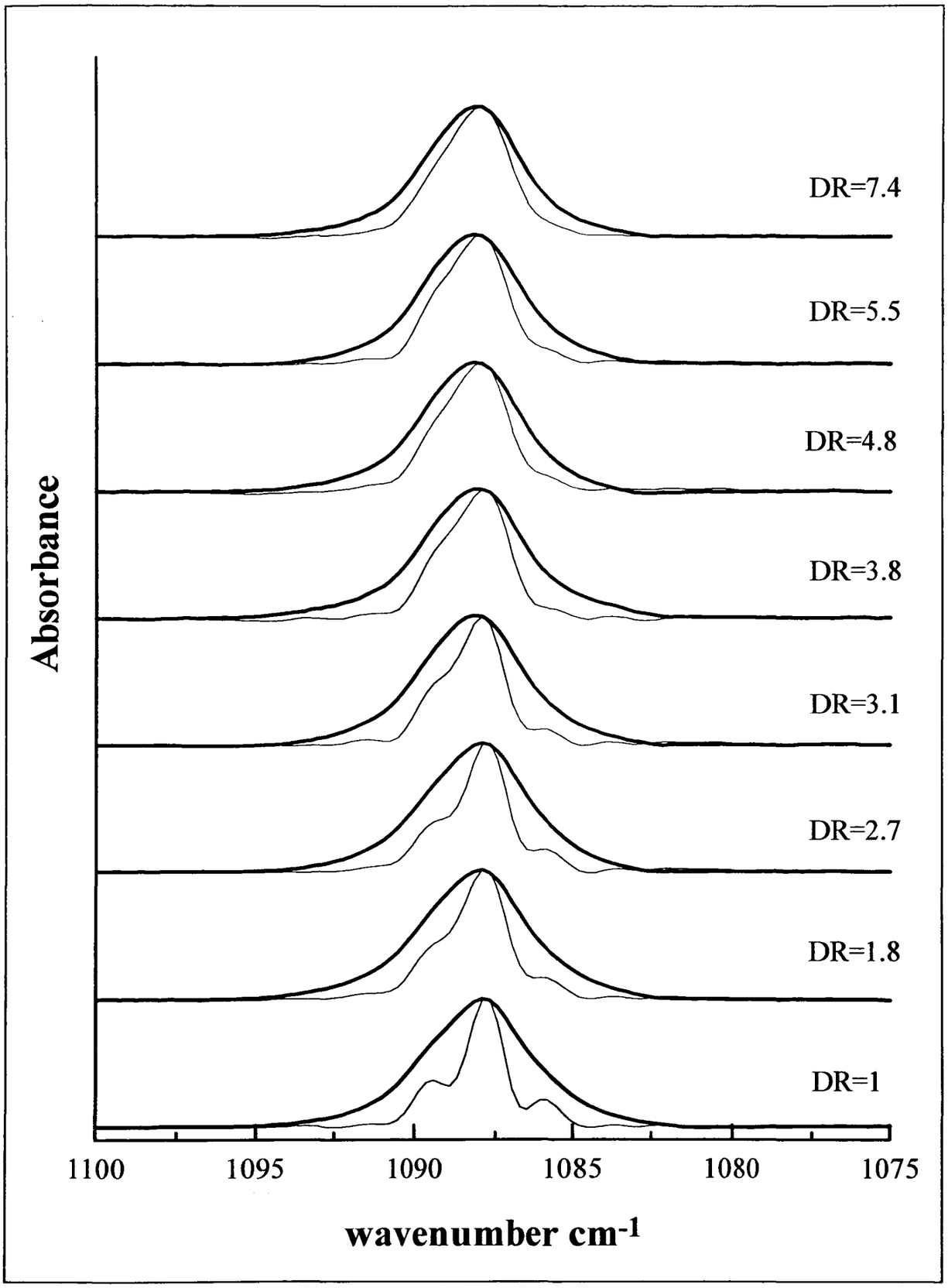

Figure VI. 16: *Evolution of the infrared CD_2 bending region for sample LL/413/385 with draw ratio. The different draw ratios are indicated. The thick line represents the raw data, the fine line the deconvoluted data.*

VI.2.3.1.1. Evolution of the a- and b-polarised components.

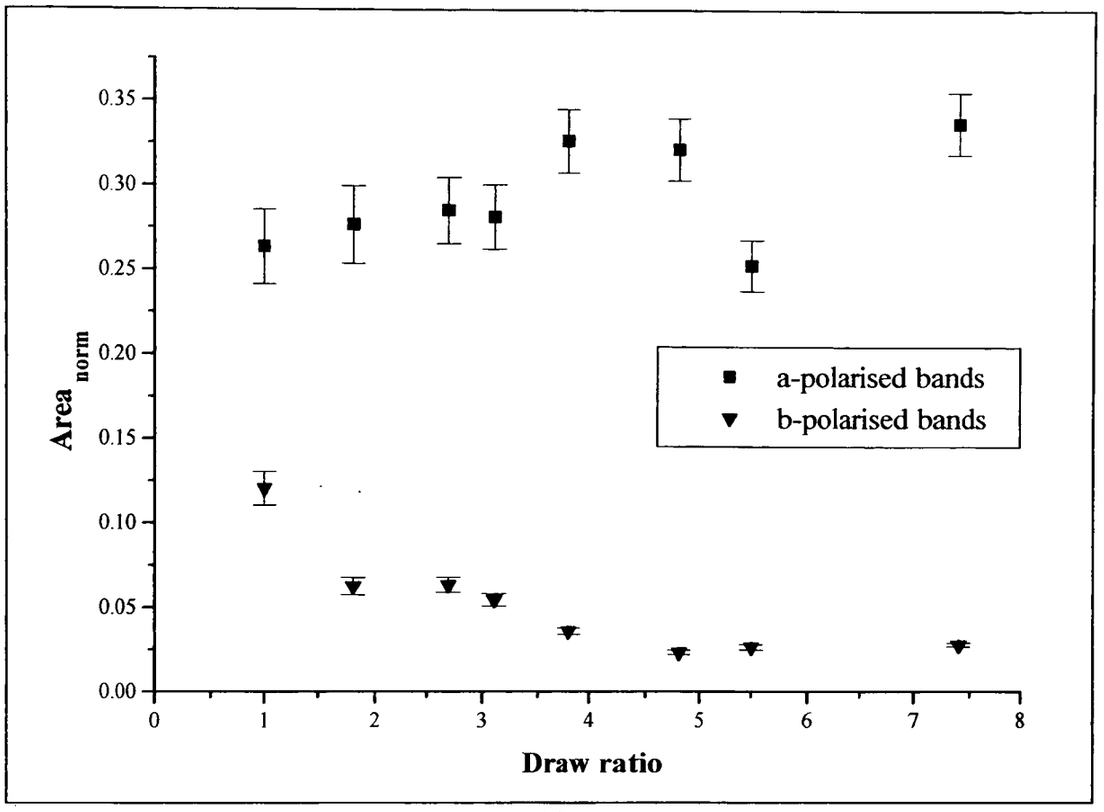

(a)

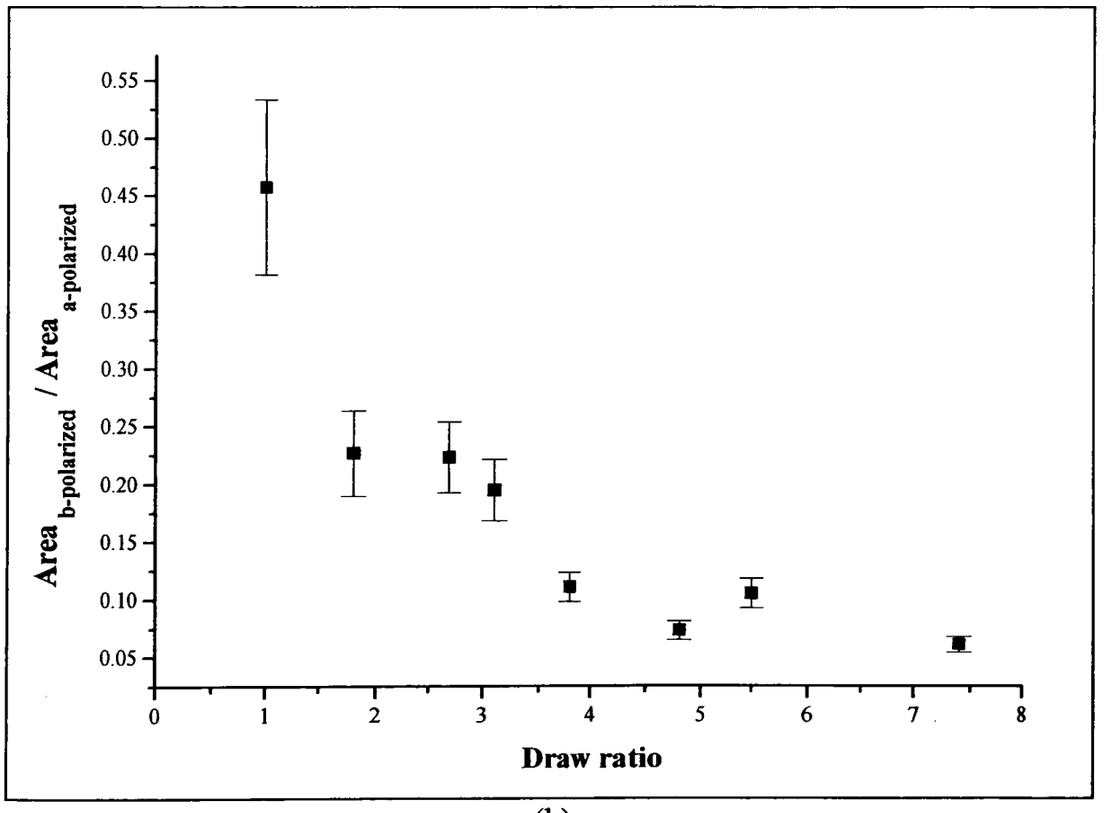

(b)

Figure VI. 17: *(a) Evolution of the normalised areas of the a- and b-polarised components; and (b) evolution of the ratio of the areas of the b- and a-polarised bands with draw ratio for sample LL/413/385. The areas were determined by curve fitting the deconvoluted data with 4 to 5 Voigt functions.*

As in the analysis made on the infrared data obtained from sample LL/95/385, in this section we will characterise the orientation development of the crystallographic axes with deformation. This is done by comparing the evolution of the areas, as determined by curve fitting, of the peaks resulting from a- and b-polarised CD_2 bending vibrations. The results are presented in Figure VI. 17.

From Figure VI. 17, it can be seen that the development of re-orientation through deformation is clearly different from the behaviour observed for sample LL/95/385. For sample LL/95/385, we have seen that the area of the a-polarised bands initially increases and then decreases with deformation, whereas the area of the b-polarised bands goes through a minimum. For sample LL/413/385, the area of the a-polarised components also increases with increasing deformation, and the area of the b-polarised bands decreases, but both types of behaviour extend over the whole deformation range. However, at the end of the deformation range studied, both areas seem to have reached a plateau value. Moreover, the increase in the area of the a-polarised part is very small in comparison to what was observed for sample LL/95/385 (around 30% of the initial value for LL/413/385 and around 210% for LL/95/385) while the decrease in the area of the b-polarised side of the profile is more or less the same in both cases (of around 80%).

For sample LL/95/385, the increase in the absorbance of the a-polarised component of the profile was attributed to the crystallisation and the orientation of amorphous polymer where the newly formed crystals have a preferential alignment with the c-axis aligned with the draw direction, the a-axis in the plane of the sample and b-axis normal to it. But in the case of sample LL/95/385, after a draw ratio of 4, the effect of the re-orientation of the crystallographic axes was compensating the effect of the amorphous crystallisation and orientation. For sample LL/413/385, the crystallisation and orientation of the amorphous region appears to develop more slowly (probably corresponding to a smaller change in crystallinity) and over a larger deformation range than for the low molecular weight linear sample. However, the evidence for crystallisation is quite minor here: the a-polarised area increases slightly, as does the outermost splitting (Figure VI. 19). On the other hand, the singlet area appears to increase slightly over the whole deformation range studied, while the total doublet area seems to decrease (presented in Figure VI. 18), suggesting that crystal break-up is

occurring over the whole deformation range. A clearer view of this phenomenon of break-up will be obtained in the following section.

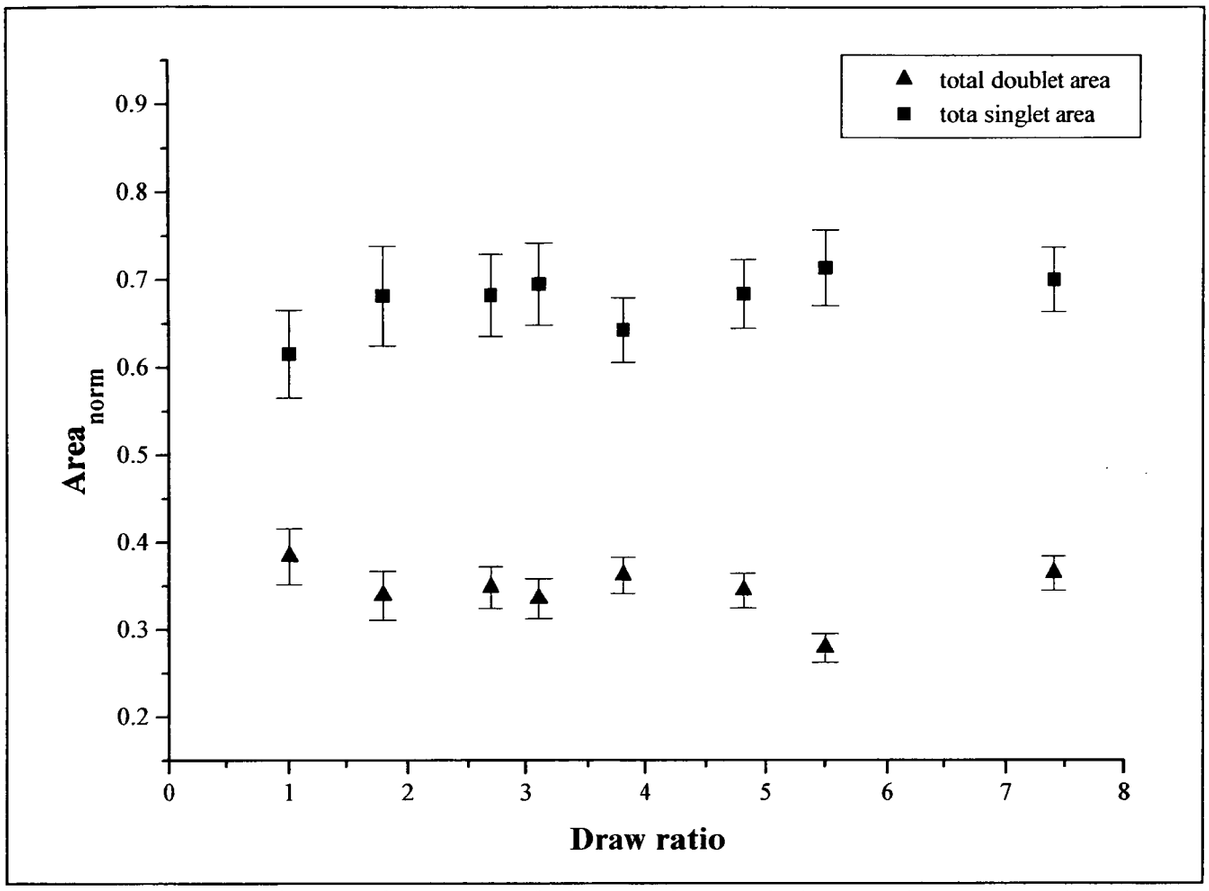

Figure VI. 18: *Evolution the area of the singlet and the total area of the doublet components of the CD_2 bending peak for sample LL/413/385.*

VI.2.3.1.2. Group size analysis.

As in the section devoted to sample LL/95/385, the progressive destruction of the initial local stem arrangement was monitored for sample LL/413/385 by characterising the evolution of the doublet splittings (determined from the curve fitting results and presented in Figure VI. 19) and the evolution of the stem distributions in terms of groups of adjacent stems (examples of calculated profiles are presented in Figure VI. 20, while the stem distributions obtained from the calculation of the CD_2 bending profiles are presented in Figure VI. 22).

Two doublets were initially resolved after the deconvolution of the experimental data as shown in Figure VI. 19. The inner splitting appears to have a constant value throughout the range of deformation studied, of around 3.5 cm^{-1}. This corresponds to groups of 3×1 or 4×1 adjacent labelled stems. Up to a DR = 3, the value of the outermost splitting has increased slightly, going from around 7.7 cm^{-1} to around 8.1 cm^{-1}, which correspond respectively to groups of 3×3 and 4×3 labelled stems.

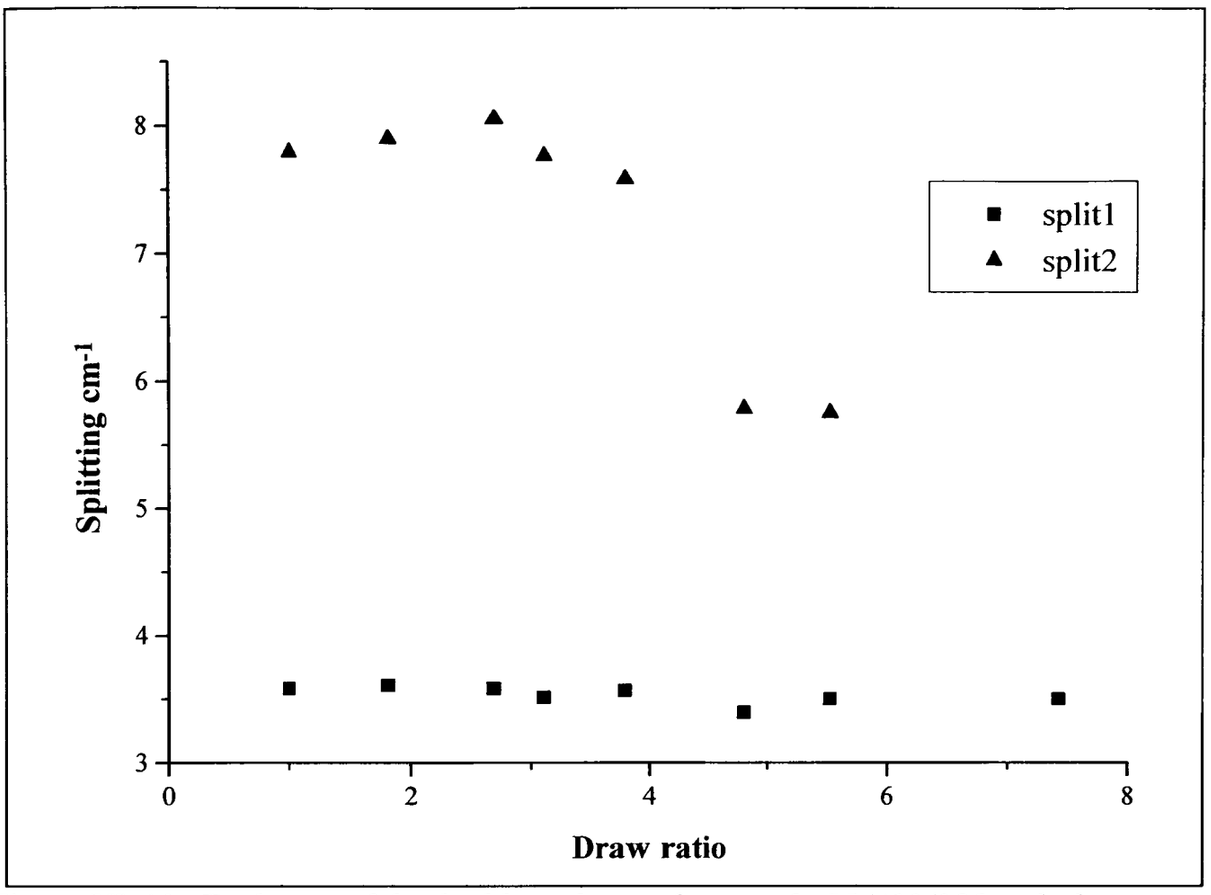

Figure VI. 19: *Evolution of the doublet splitting for sample LL/413/385 with draw ratio. Split 1 is the splitting between the 1089 cm^{-1} and the 1086 cm^{-1} bands; split 2 is the splitting between the 1091 cm^{-1} and 1083 cm^{-1} bands at low draw ration (DR < 4.5) and between 1091 cm^{-1} and 1086 cm^{-1} for DR > 4.5 (The frequencies quoted in this caption are approximate).*

As in the case of sample LL/95/385, crystallisation of the amorphous polymer has been inferred (previous section) on the drawing of the sample. This results in the creation of new crystals where, depending on initial conditions (such as stress, temperature..), new stems may become adjacent to each other or to an already existing group of adjacent stems, thus increasing the size of this group. Alternatively, this increase may result from the fact that two groups have become adjacent to each other in terms of [110] directions during the drawing. This later solution is certainly the less probable one since in melt quenched polyethylene the distance separating each group of adjacent labelled stems is believed to be very large in comparison to the size of the group (as explained in the subunit model proposed by Sadler and Harris [30]). It can be noted that this increase of the group size occurs progressively from the start of the sample drawing. For a DR > 3, the outermost splitting decreases as the deformation increases and finally disappears at a DR of 5.5. The splitting value decreases slowly from 8.1 cm^{-1} to 7.7 cm^{-1} and then rapidly from 7.7 to 5.8 cm^{-1}, corresponding to a change from 3×3 groups to 3×2 groups before disappearing at a DR = 5.5. The disappearance of the 5.8 cm^{-1} splitting is related

to the disappearance of the infrared band at around 1083 cm^{-1}. This is consistent with the progressive break-up of the largest groups as was the case for sample LL/95/385, although the effects here are more marked than in the case of low molecular weight linear sample. This is simply because groups of adjacent labelled stems are larger for sample LL/413/385 than for LL/95/385, so interrupting the lamellae on a particular length scale has more influence.

As in the case of the analysis made on sample LL/95/385, a quantitative analysis of the labelled stem distribution was made through the calculation of the CD_2 bending vibration profiles. The process used here is exactly the same as described in section VI.2.2.1.2 and in chapter 5 section 2.1.2. Examples of the simulation using Lorentzian shape functions to compare with the deconvoluted data are presented in Figure VI. 20, while the input data used to perform the calculation are presented in Figure VI. 22. As with the results for sample LL/95/385, here the contribution from the chains in the amorphous regions is not removed from the results.

It can be noted from Figures VI.20 that our simulations of the profiles do not provide good fits to the deconvoluted data, especially for the singlet component. The calculated singlet width is narrower than the deconvoluted one. As explained in Chapter 5, this is because a Lorentzian function was used to simulate the shape of the singlet peak, and better agreement can be obtained with a Voigt shape function (combination of Lorentzian and Gaussian shape functions). In addition, the disagreement between simulated and deconvoluted data appears to be greater after the drawing of the sample.

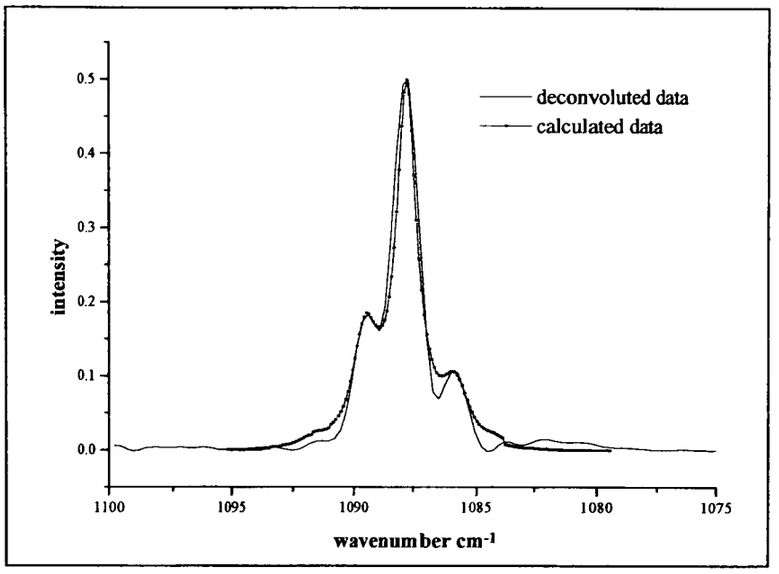

(a)

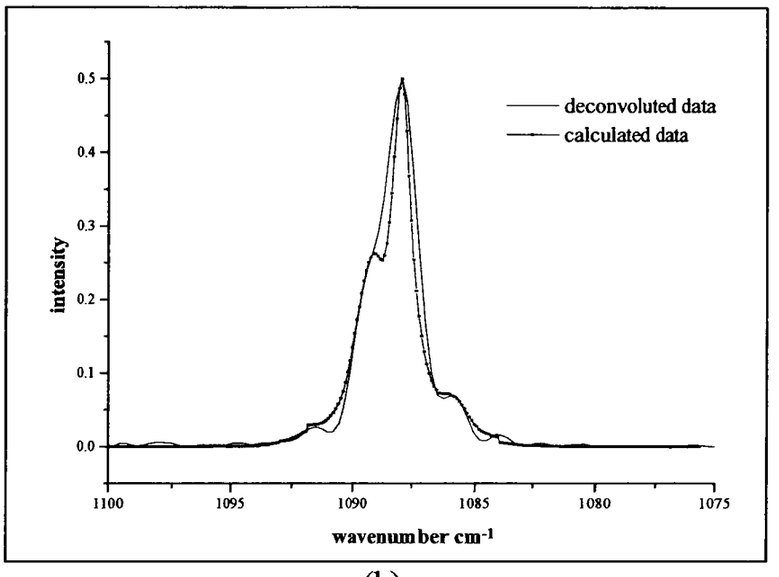

(b)

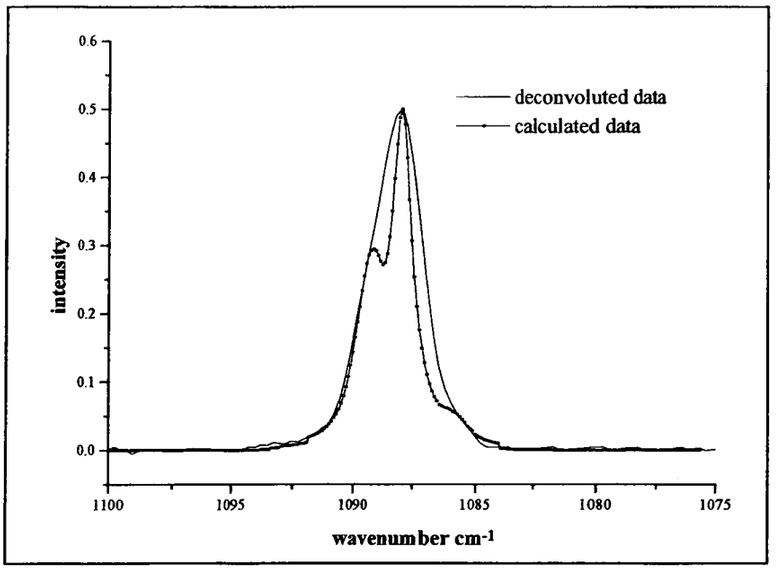

(c)

Figure VI. 20: *Calculated CD_2 bending profiles using Lorentzian shape functions and without singlet width increses for sample LL/413/385 along with deconvoluted experimental data. (a) undeformed; (b) with a DR = 3.1; and (c) with a DR = 7.4.*

When curve fitting of the deconvoluted data was carried out, the width of the singlet component was observed to increase with increasing draw ratio. This is illustrated in Figure VI. 21. Therefore, for our simulations of the deconvoluted data, the width of the Lorentzian function used to calculate the singlet component was increased. However, since this resulted in an even worse overall fit than before increasing the bandwidth (the tail of the Lorentzian function simulating the singlet peak is masking most of the doublet contributions), Figure VI. 20 shows the fits without the singlet width increases. When looking at the composition of the Voigt function (combination of Lorentzian and Gaussian) used to curvefit the singlet component, it was noted that the Lorentzian contribution to the Voigt function used was decreasing while the Gaussian contribution was increasing. This suggests that the shape of the singlet component has changed when the sample was drawn and may be related to the observed increase in width of the singlet. This suggests that using a Lorentzian function may not anymore be adequate to simulate the singlet component for the deformed sample. Such an effect was not observed in the case of sample LL/95/385 and may result, for example, from the appearance of a new infrared absorption band arising from the monoclinic phase.

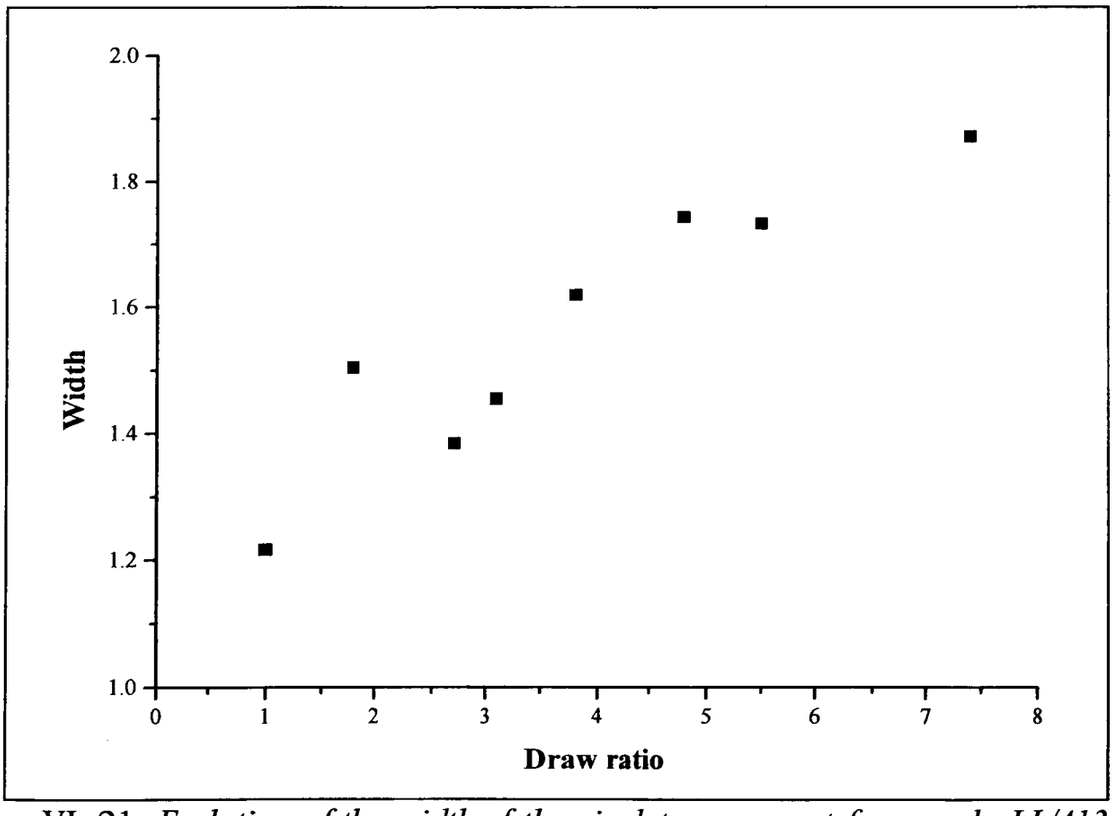

Figure VI. 21: *Evolution of the width of the singlet component for sample LL/413/385 obtain from the curve fitting analysis using a Voigt shape function to fit the single peak.*

From figure VI. 22, as in the case of LL/95/385, the number of stems in the largest groups is very small. Most of the stems are in the smaller groups. The number of

isolated stems increases with the deformation, going from 68% of the total number of stems before drawing to 79% at a DR = 7.4. As was mentioned for sample LL/95/385, the degree of crystallinity increases with increasing sample draw ratio. Therefore, the contribution of the chain segments in the amorphous region is reduced, which in itself would lead to a reduction of the number of isolated stems. The increase observed can only result from an increase of the number of isolated crystal stems. At the same time, the number of stems in the largest groups decreases and, ultimately, the number of groups larger than 4×1 adjacent stems reaches zero whereas the number of stems in the "small" groups first decreases and then for draw ratios larger than 4 stays constant up to the end of the drawing range studied. All these results are consistent with the progressive break up of the larger groups, while the smaller groups are first reduced in size up to a draw ratio of 4 and then remain more or less untouched and the number of isolated crystal stems increases (the increase in isolated percentage is related to the decrease in percentage of large groups). This confirms the results inferred from figure VI. 18, suggesting that crystal break-up is occurring over the whole deformation range.
In this particular analysis, no sign of a crystallisation process due to the drawing was observed, except maybe for the medium groups from draw ratio of 1 to 1.8, as was the case for the low molecular weight linear sample. However, slight signs of crystallisation were possibly observed in the evolution of the splitting with deformation, as determined by curve fitting (Figure VI. 19). The evolution of the area of the a- and b polarised bands suggests that orientation and crystallisation of the amorphous polymer is taking place. Therefore, a phenomenon of stress induced crystallisation is believed to occur for sample LL/413/385, but is not readily apparent in the stem distributions. This may be due to the fact that the effects of the crystallisation are masked by effect of the crystal break-up.

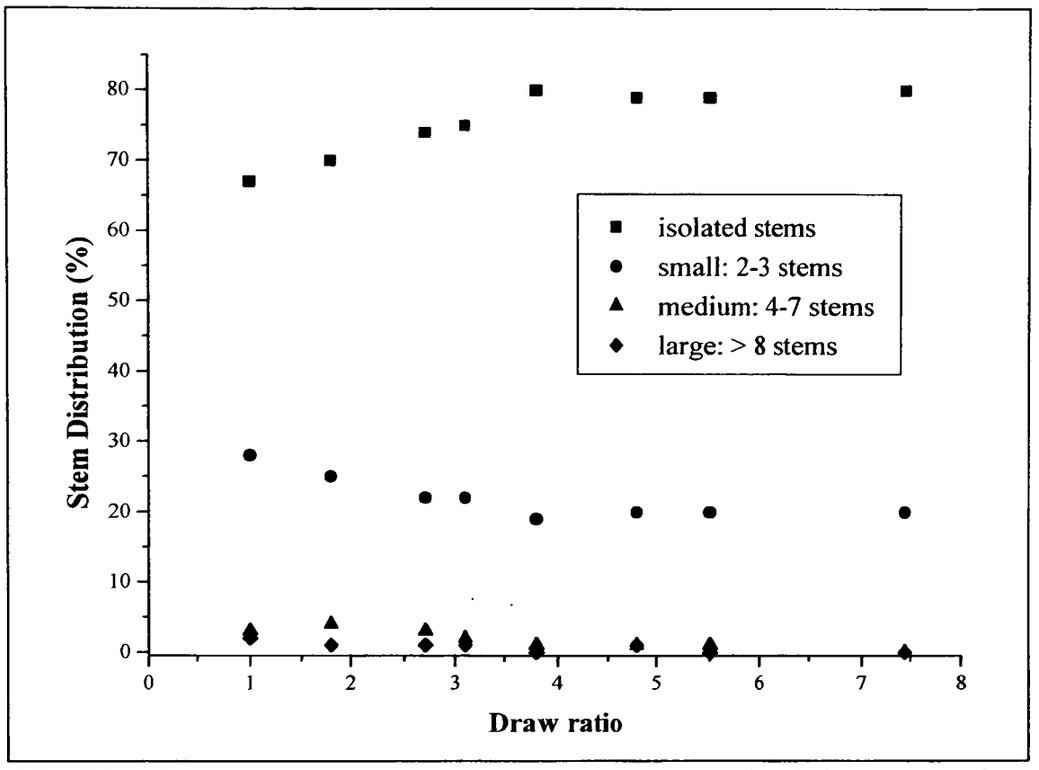

Figure VI. 22: *Evolution of the stem distributions with deformation for sample LL/413/385. The isolated stems are contributing to the singlet; the small groups are constituted of 2 to 4 stems in one plane (2×1, 3×1 and 4×1 corresponding to splittings between 2.6 and 3.9 cm^{-1}) and contribute to the inner doublets; the medium groups are constituted of 5 to 7 stems in one or two planes (5×1, 2×2 and 3×2 groups corresponding to splittings between 4.2 and 6.1 cm^{-1}) and contribute to the intermediate doublets; the large groups are constituted of 8 to 12 adjacent stems in 2 or 3 planes (4×2, 5×2, 3×3, 4×3 and larger groups corresponding to splittings larger than 6.4 cm^{-1}) and contribute to the outermost doublet.*

VI.2.3.2. The CH_2 wagging region.

As for sample LL/95/385, three absorption bands and a shoulder related to non all-trans conformations are observed. The end-gauche band also appears at 1341 cm^{-1} as a shoulder on the side of the gg peak. Because all the measurements made in this thesis were carried out at liquid nitrogen temperature, the number of gauche conformations arising from thermal activation is minimised. Therefore, the results emphasise those conformations which are structural in origin (e.g. folds).

The general shape of the CH_2 wagging region is not altered through the deformation range studied as shown in Figure VI. 23. Initially an increase of the normalised intensity of the three peaks can be distinguished. This is illustrated in Figure VI. 24.

Similarly to what was observed for sample LL/95/385, the trend of all three absorption bands is similar and two stages can be identified. Up to a DR = 4, the numbers of all types of non all-trans conformers increase and reach their maximum values. This

increase can only result from an augmentation of the number of defects in the crystalline lamellae. For DR larger than 4, a slight decrease in the number of non all-trans conformations is observed. As explained for sample LL/95/385, any reduction may be related to the ordering of the amorphous regions under deformation and to the reduction in the number of defects in the crystals themselves, due to the preferential alignment of the c-axis with the draw direction.

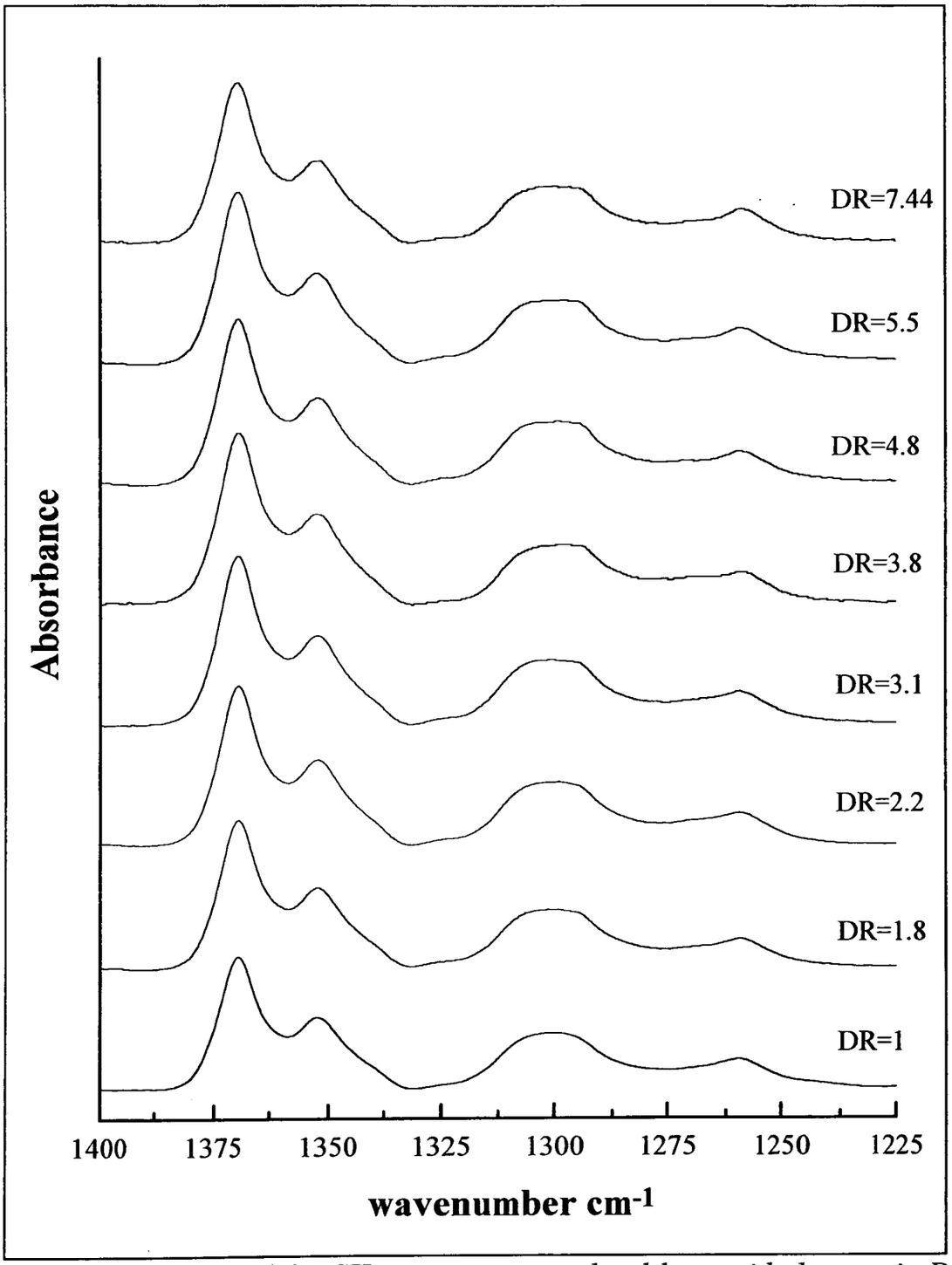

Figure VI. 23: *Variation of the CH_2 wagging region bandshape with draw ratio DR for sample LL/413/385.*

The fact that the number of non all trans-conformations is reaching a plateau value indicates either that no further crystalline defects are created or that crystals defects are created at the same rate as amorphous "defects" are removed. Since the crystal break-up continues, it is most likely that these is a compensating effect between the creation of defects and their removal.

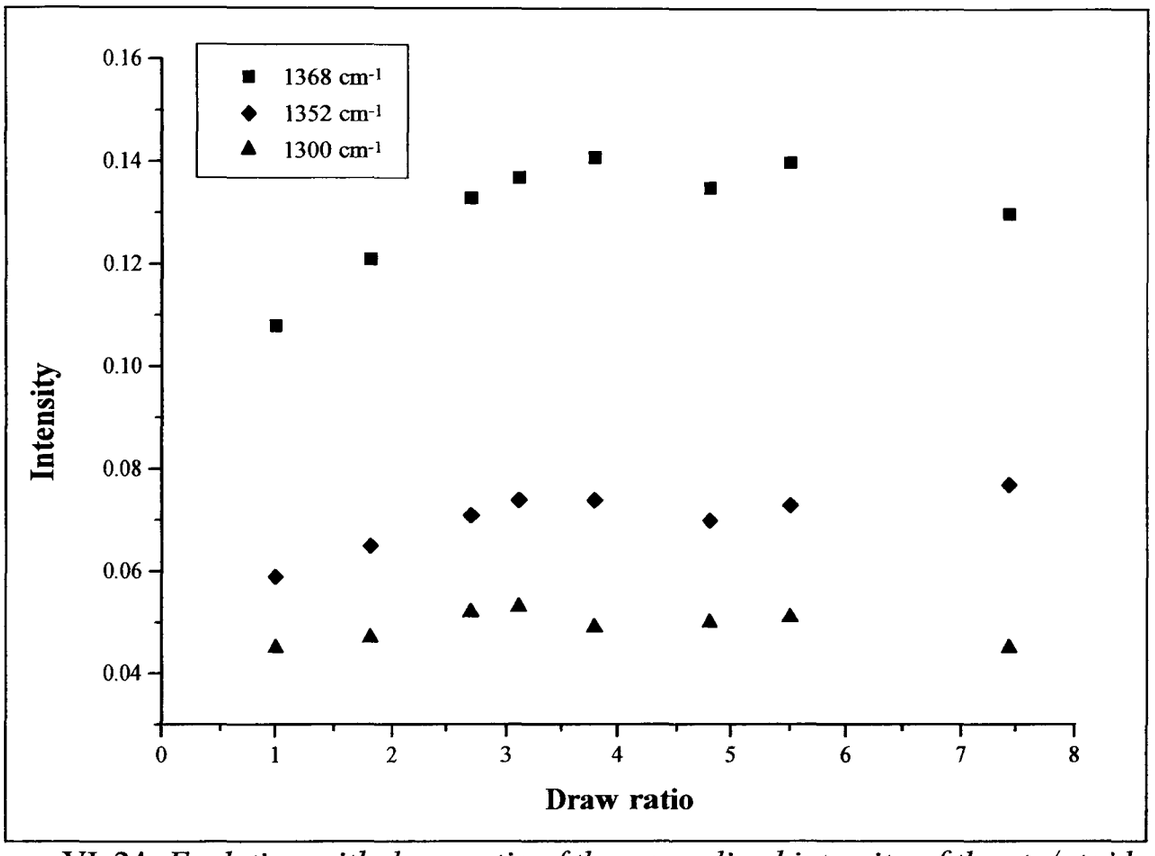

Figure VI. 24: *Evolution with draw ratio of the normalised intensity of the gtg/gtg' band at 1368 cm^{-1}, the gg band at 1352 cm^{-1} and the gtg/gtg' band at 1300 cm^{-1} for sample LL/413/385.*

VI.2.3.3. Discussion.

From the re-orientation analysis we have seen that the area of the a-polarised side of the CD_2 bending profile increases progressively, but only slightly, throughout the whole deformation range studied, while the area of the b-polarised side decreases up to a draw ratio of around 5 and seems to reach a plateau value for DR > 5. This is illustrated in the A_b/A_a ratio which first shows a large decrease up to a DR of around 5 and then decreases slightly and seems to reach a plateau value for DR > 5. Simultaneously, the outermost splitting is increasing up to a DR of around 3. We have seen in the case of sample LL/95/385 that such behaviour may be interpreted in terms of stress-induced crystallisation of the amorphous regions where the newly formed crystals have a preferential orientation with the c-axis parallel to the draw direction, the a-axis in the

plane of the sample and the b-axis normal to the plane of the sample. But, in contrast to sample LL/95/385, this phenomenon of crystallisation continues, albeit slowly, over the whole deformation range studied. In terms of draw ratio, the process is completed at much earlier stage for sample LL/95/385. However, this stress induced crystallisation phenomenon is not obviously reflected in the stem distribution study. The number of isolated stems is not decreasing, but first increases for DR up to 4 while the number of stems distributed in groups is decreasing progressively.

In the case of sample LL/95/385, at a draw ratio of around 4, the A_b/A_a ratio had reached a minimum value and for DR > 4 was increasing. This was understood as the start of untwisting of the crystalline ribbons close to the minor axis so as to ultimately achieve c-axis alignment in the draw direction. We have seen for sample LL/413/385 that at the end of our data set, for a draw ratio of 7.5, the A_b/A_a ratio seems to reach a plateau value. This may suggest that the crystallisation effects, characterised by an increase and a decrease of, respectively, the areas of the a- and b-polarised sides, start to be compensated by the effect of the re-orientation process of the crystalline lamellae. Indeed, in the discussion presented in section VI.2.1, we have seen that the ultimate alignment of the crystalline lamellae c-axis involves primarily the untwisting of the crystalline ribbons close to the minor axis of the deformed spherulite (this untwisting corresponds in fact to a rotation of the unit cell around the b-axis), and results in a decrease of the absorbance of the a-polarised side of the profile while the absorbance of the b-polarised side remains constant. Therefore, in the case of sample LL/413/385, clear signs of the untwisting are only observed, in this re-orientation analysis, at a draw ratio of around 7.5, suggesting that the onset of the re-orientation of the crystalline lamellae unit cell is only just starting. However, the singlet area increases while the doublet area decreases in the whole deformation range, and the splittings themselves decrease after a draw ratio of 2.5 indicating that crystal break-up is also occurring. How can this slow development of the crystallisation and orientation of the amorphous region and the resulting apparently delayed onset of the re-orientation of the crystalline lamellae be interpreted?

In the previous chapter, we have seen that, as expected, the radius of gyration of LL/413/385 is larger than the radius of LL/95/385 (532±9Å and 235±11Å, respectively), while the long spacings determined from X-rays (Chapter 4) are almost identical for both samples (254±13Å for LL/95/385 and 269±7Å for LL/413/385). Although the long

spacing and the radius of gyration cannot be directly compared for unoriented samples (if the lamellae were oriented and crystallinity was high, the X-ray long spacing and radius of gyration could be compared simply), these results suggest that the high molecular weight DPE linear chain may occupy several lamellae, while its low molecular weight counterpart may be limited to one lamella. This requires the presence of tie-molecules and probably also chain entanglements in LL/413/385. It is supposed that chain entanglements and tie-molecules are restricting the molecular movement, leading to slower development of the orientation and crystallisation of the amorphous polymer. Therefore, the slower change in the orientation of the amorphous polymer may be understood as the effect of the high the molecular weight of the deuterated molecules and therefore of chain entanglements and tie-molecules.

In the group size analysis, we have seen that up to draw ratio of around 4, the number of isolated stems is increasing while the number of stems distributed in small, medium and large groups are decreasing. For DR larger than 4, both the numbers of isolated stems and of stems distributed in small groups reach plateau values and stay more or less constant up to the end of the deformation range studied. In the same deformation range, the largest group size is first reduced to 7 stems at a DR of around 4, and at a DR of 5.5, the largest group size is further reduced to 3 stems. At a draw ratio of around 6 only the innermost doublet was resolved. Simultaneously, the number of non-all trans conformers is increasing, suggesting that the crystalline regions are increasingly defective. We have seen in the section devoted to the study of sample LL/95/385 that such behaviour is consistent with the progressive break-up of the spherulitic crystalline lamellae.

As mentioned above, clear signs of the untwisting of the crystalline ribbons were only observed for draw ratios larger than 7. However, because the break-up of the largest groups of adjacent labelled stems has already occurred at a DR of 3, the crystalline lamellae are clearly affected by the deformation before a draw ratio of 7.5. Nevertheless, the stress induced-crystallisation of the amorphous chains is the dominant effect and is masking the effect of the re-orientation of the lamellae in the evolution of the areas of a- and b-polarised components. Indeed, it appears that the two processes are occurring together over a wide range of draw ratios instead of being more or less separable as in sample LL/95/385.

From the group size analysis, it can be noted that the progressive break-up of the largest of the original groups of adjacent stems starts at lower draw ratio for the high molecular weight sample than for LL/95/385. This is attributable to the presence of larger original groups of adjacent stems in LL/413/385, which are easier to disrupt than smaller groups, and may also relate to tie-molecules being pulled through the lamellae, contributing to the crystal break-up. The broken blocks then rotate so as to align the c-axes with the deformation direction.

As in the case of LL/95/385, the absorption peak related to the monoclinic phase was observed in the CH_2 rocking mode (at 716 cm^{-1}) after deformation. But the transformation from orthorhombic to monoclinic must only be partial, since no sign of it was observed in the WAXS diffraction pattern.

To conclude, the re-crystallisation process in sample LL/413/385 appears to develop over a wider deformation range than in the case of sample LL/95/385 and is occurring together with the re-orientation of the crystalline lamellae (through crystal break-up and untwisting of the ribbons close to the minor axes of the spherulite). These differences appear to result from increasing the molecular weight of the DPE guest molecules and may be related to the effects of tie-molecules and chain entanglements in restricting the molecular movement.

VI.2.4. Sample CL/95/385.

In this section we will study the effect of branches on the deformation behaviour of polyethylene. For this, a copolymer DPE of molecular weight equal to 95000 was mixed with the high molecular weight linear matrix prior to crystallisation and its deformation behaviour was compared to LL/95/385. This should avoid effects on the deformation behaviour resulting from tie-molecules and chains entanglements due to molecular weight, as in the previous section.

VI.2.3.1. The CD_2 bending region.

The general evolution of the CD_2 bending profile of sample CL/95/385 is presented in Figure VI. 25. Firstly, little change in the profile was observed for a DR < 2.6. For a DR between 2.6 and 3.3, the intensity of the high wavenumber side of the spectrum, corresponding to a-polarised vibrations, increases. For DR larger than 3.7, the intensity of the a-polarised bands stays more or less constant.

In contrast to observations for the linear low molecular weight sample, the shape of the initial and final profiles are significantly different. But at the highest draw ratio measured, doublets can still be distinguished in the CD_2 and in the CH_2 bending profiles. A shoulder at around 716 cm^{-1} is also observed on the CH_2 rocking doublet, suggesting that some phase transformation from orthorhombic to monoclinic structure has occurred. The low absorbance and the fact that the monoclinic structure was not observed in the WAXS pattern suggest that this phase transformation is only a minor effect in the deformation process.

As for the analysis carried out for sample LL/95/385, the data were curve fitted using 4 to 5 Voigt functions. The results of the curve fitting are presented in the following section.

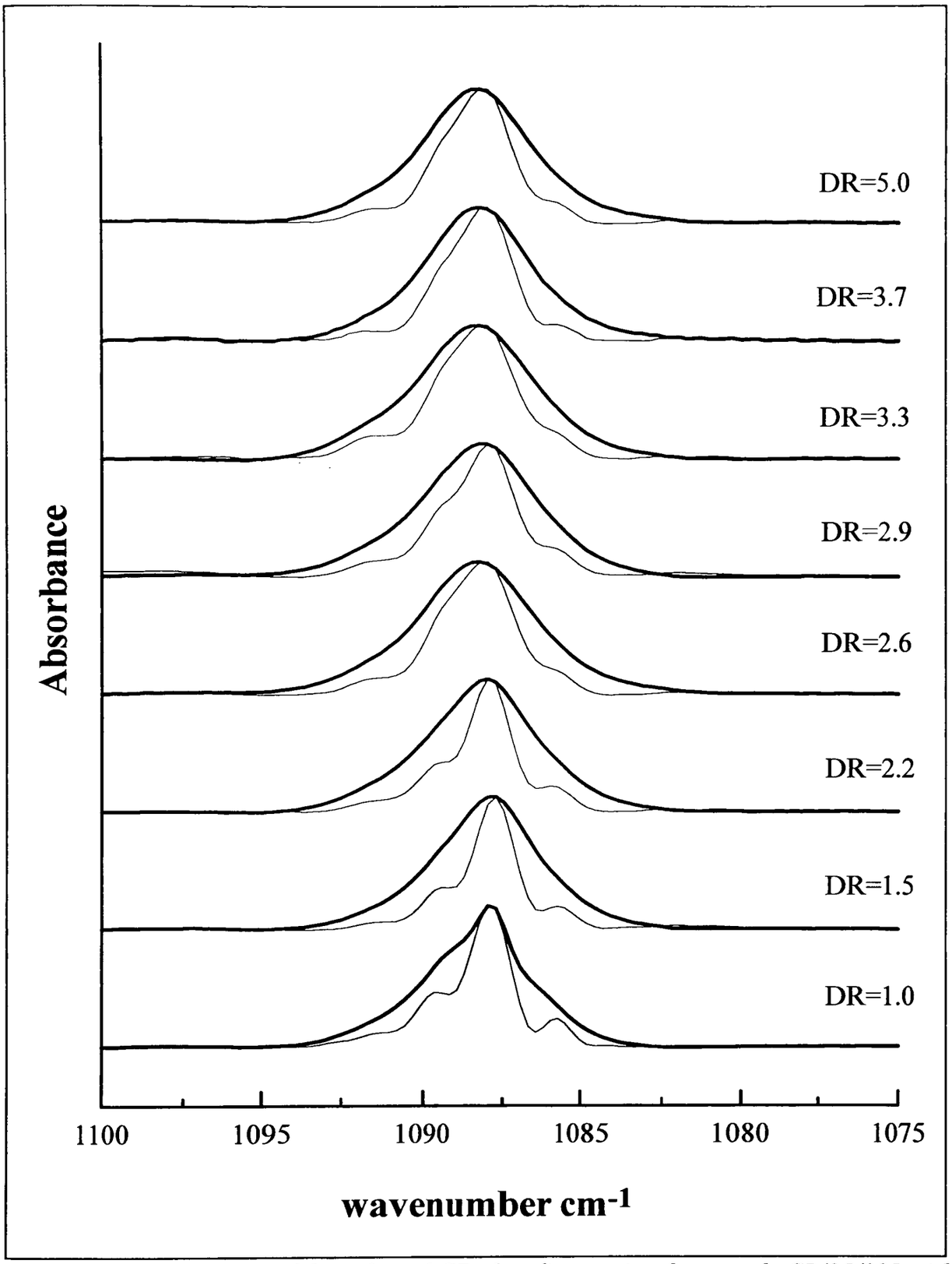

Figure VI. 25: *Evolution of the infrared CD_2 bending region for sample CL/95/385 with draw ratio. The different draw ratios are shown in the picture. The thick line represents the raw data, the fine line the deconvoluted data.*

VI.2.4.1.1. Evolution of the a- and b-polarised components.

In this section we will characterise the orientation development occurring with deformation in sample CL/95/385. As previously, this will be done by comparing the normalised areas of the low and high wavenumber sides of the profile (i.e. the b- and a-polarised parts of the spectrum) obtained from curvefitting the deconvoluted data. The results are shown in Figure VI. 26.

From this figure it can be seen that, apart from the region between a DR of 1 and 1.5, where the area of the a- polarised component decreases while the area of the b-polarised component increases, the evolution of the areas of the a- and b- polarised components is similar to the evolution observed for sample LL/413/385. For DR larger than 1.5, the area of the a- polarised side is increasing up to the end of the deformation range studied, while the area of the b- polarised side decreases through the deformation. As in the case of sample LL/413/385, the changes in both areas are relatively small and both seem to have reached plateau values by a draw ratio of around 4. As mentioned in the previous sections, the augmentation of the area of the a-polarised side of the profile results from the crystallographic a-axis tending towards the deformation axis, while the decrease in the area of the b-polarised side of the profile is attributed to the b-axes moving away from the plane of the sample. This was interpreted as resulting from the oriented-crystallisation of some amorphous chains, leading to the formation of new crystals. These new crystals have a preferential orientation with the c-axis aligned with the draw direction, the a-axis perpendicular to it and in the plane of the sample, while the b-axis becomes normal to the plane of the sample. After a draw ratio of 3.5, the areas of both the a- and b-polarised sides of the profile appear to have reached a plateau values. This may be understood as the first sign of the re-orientation of the spherulitic lamellae. Indeed, we have seen in the section VI.2.1 that a decrease in the a-polarised absorbance may result from the rotation of the crystals around the b-axis so as to align the c-axis with the draw direction, for crystals in the spherulite regions perpendicular to the draw direction. This was attributed to the untwisting of the crystalline ribbons close to the minor axis of the deformed spherulite. For a draw ratio larger than 3.5, the crystalline reorientation effects compensate the ordering effects of the amorphous chains, as was the case for sample LL/413/385.

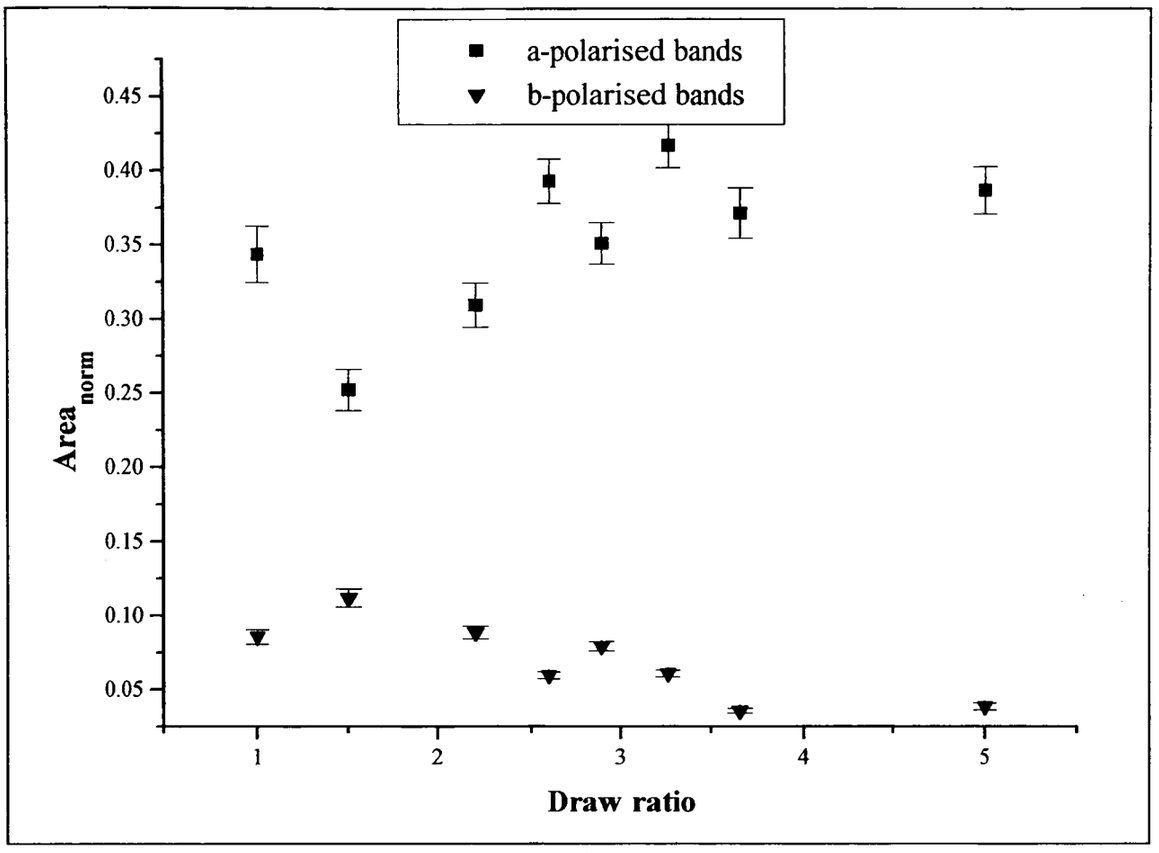

(a)

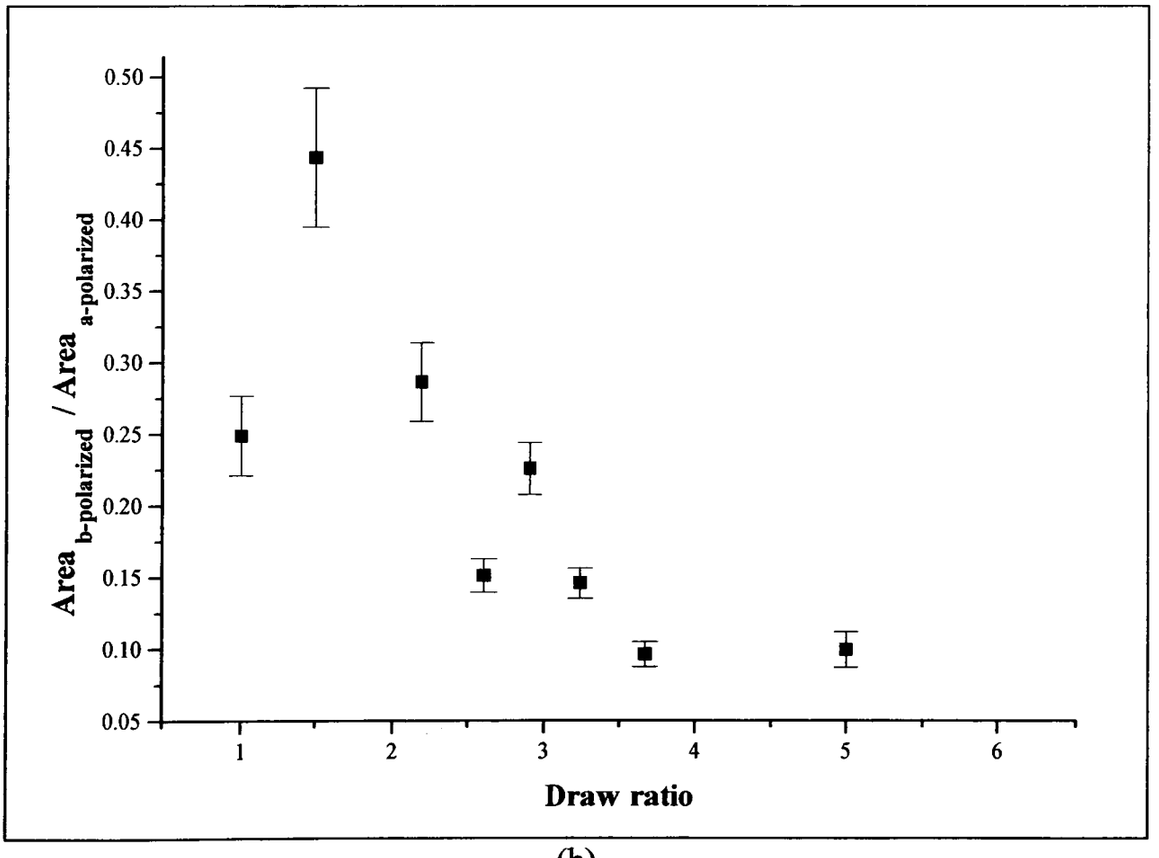

(b)

Figure VI. 26: *(a) Evolution of the normalised areas of the a- and b-polarised components; and (b) evolution of the ratio of the areas of the b- and a-polarised bands with draw ratio for sample CL/95/385. The areas were determined by curve fitting the deconvoluted data with 4 to 5 Voigt functions.*

VI.2.4.1.2. Group size analysis.

This section is devoted to the study of the evolution of the group sizes and stem distributions with deformation for sample CL/95/385 in a similar way as for the previous samples. First of all, we will study the evolution of the doublet splittings determined from curve fitting of the deconvoluted data (Figure VI. 27). This will give us the first information on the evolution of the local stem rearrangement. However, because the method of curve fitting can give only qualitative information, a second method, which consists in calculating the deconvoluted CD_2 bending profile using known doublet splittings for specific groups, will be applied in order to obtain information on the evolution of the stem distributions within groups.

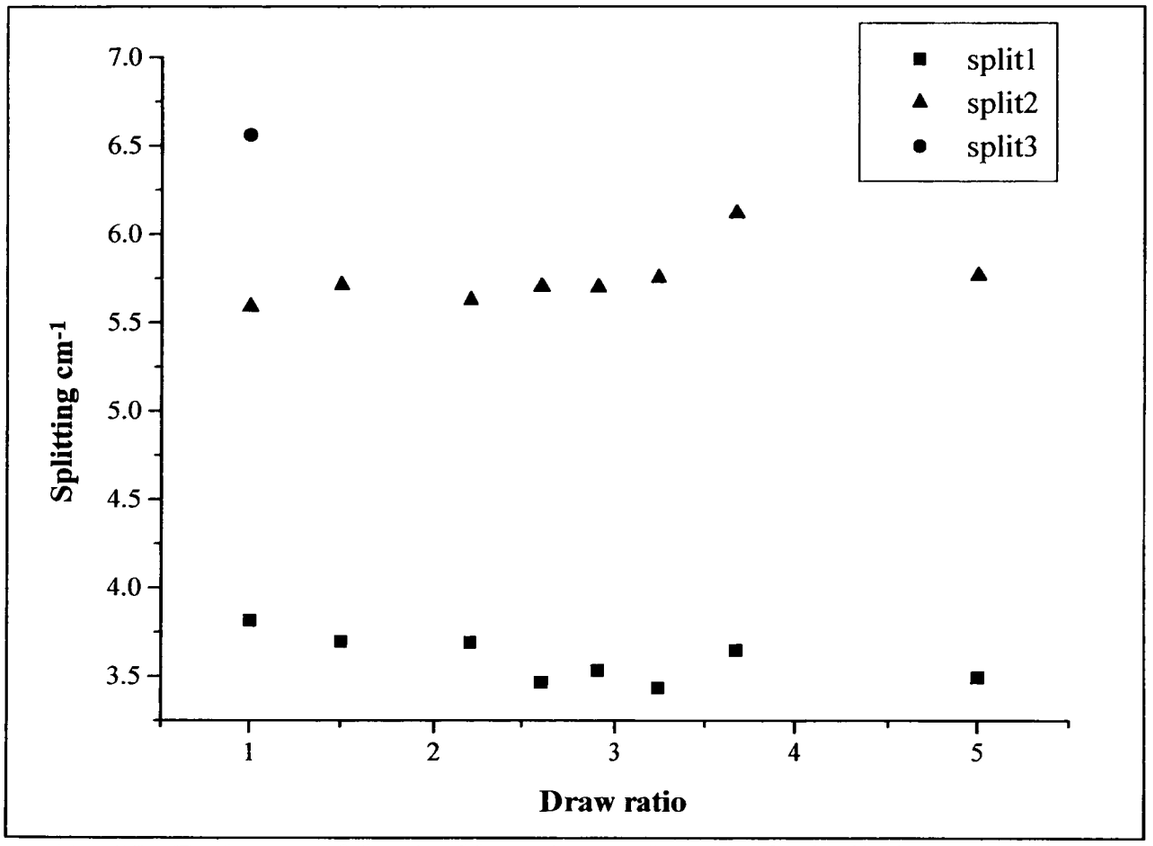

Figure VI. 27: *Evolution of the doublet splitting for sample CL/95/385 with draw ratio. Split 1 is the splitting between the bands at approximately 1089 cm^{-1} and 1086 cm^{-1}, split 2 is the splitting between the bands at approximately 1091 cm^{-1} and 1086 cm^{-1} and split 3 is the splitting between the bands at approximately 1092 cm^{-1} and 1086cm^{-1}.*

Three doublets were initial resolved after deconvolution of the experimental data. Both the inner splittings change very little throughout the deformation range. They have a constant value of around 3.5 cm^{-1} for the innermost splitting, which corresponds to groups of 3×1 adjacent labelled stems and between around 5.1 and 6.1 cm^{-1} for the second splitting, which corresponds to groups of between 2×2 and 3×2 of adjacent labelled stems. A splitting of around 6.5 cm^{-1} was observed for the undeformed sample, which corresponds to groups of 4×2 adjacent labelled stems. From the onset of deformation, this splitting disappeared. This may, therefore, result from the break-up of the largest groups. However, because the intensity of the outermost high wavenumber peak was very small in the undeformed sample, only a very small number of stems contribute to this band. More details of the local stem rearrangement upon deformation may be obtained from the results of our calculation of the CD_2 bending profiles, presented in figure VI. 28.

As was the case for sample LL/413/385, the simulations of the profiles do not provide good fits to the deconvoluted data, especially for the singlet component. The calculated singlet width is narrower than the deconvoluted one. This was explained by the fact that a Lorentzian function was used to simulate the shape of the singlet peak in Figure VI. 28, and better agreement can be obtained with a Voigt shape function (combination of Lorentzian and Gaussian shape functions). Also, the width of the singlet component appears to increase upon drawing. When looking at the composition of the Voigt function (combination of Lorentzian and Gaussian) used to curvefit the singlet component, it was noted that the Lorentzian contribution to the Voigt function used is reduced relative to the Gaussian contribution after deformation. This suggests that the shape of the singlet component has changed when the sample was drawn and that using a Lorentzian function may no longer be adequate to simulate the singlet component for the deformed sample.

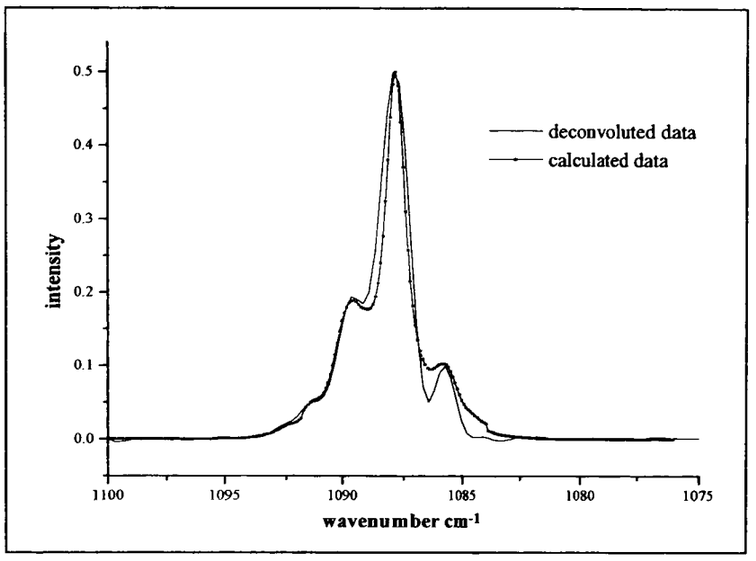

(a)

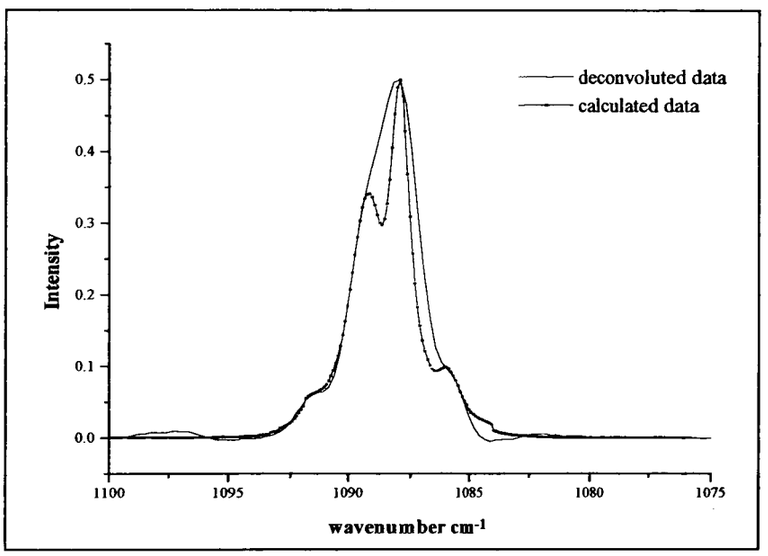

(b)

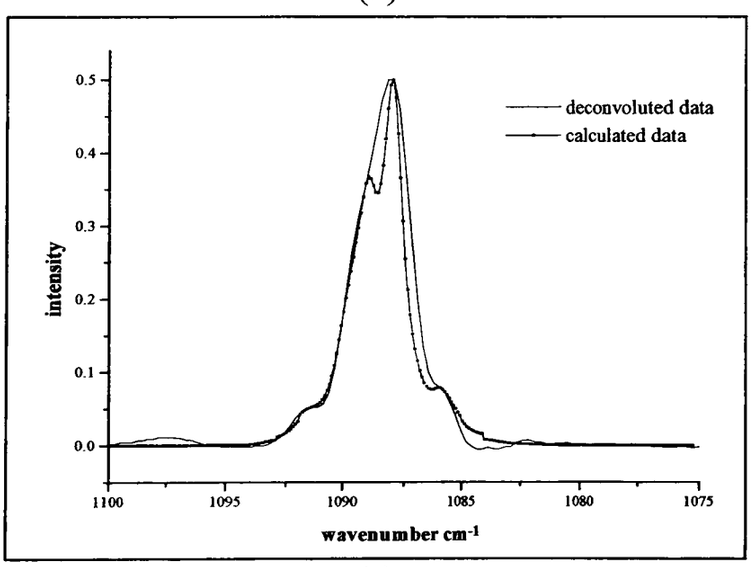

(c)

Figure VI. 28: *Example of calculated splitting using Lorentzian shape functions for sample CL/95/385, alongside the deconvoluted experimental data (dotted line). (a) undeformed; (b) at a DR = 2.6; and (c) at a DR = 5.0.*

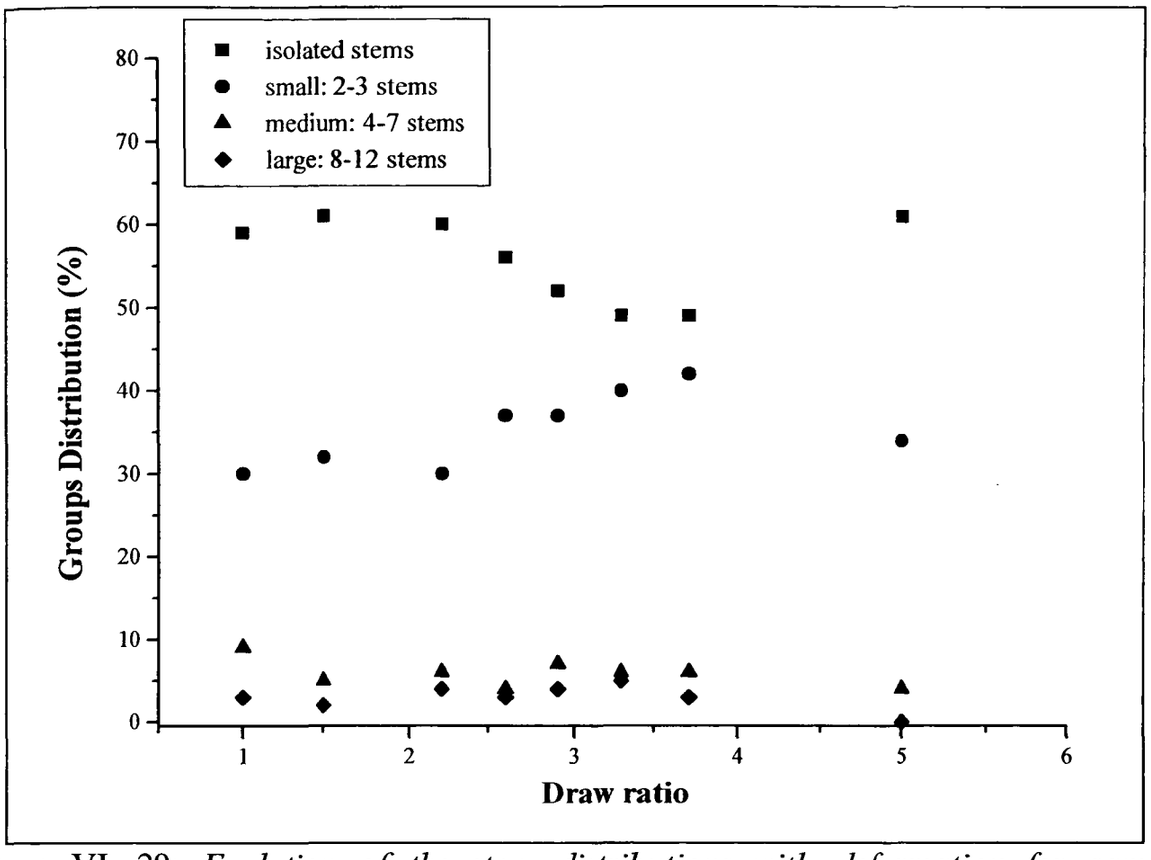

Figure VI. 29: *Evolution of the stem distributions with deformation for sample CL/95/385. The isolated stems are contributing to the singlet; the small groups are constituted of 2 to 4 stems in one plane (2×1, 3×1 and 4×1 corresponding to splittings between 2.6 and 3.9 cm^{-1}) and contribute to the inner doublets; the medium groups are constituted of 5 to 7 stems in one or two planes (5×1, 2×2 and 3×2 groups corresponding to splittings between 4.2 and 6.1 cm^{-1}) and contribute to the intermediate doublets; the large groups are constituted of 8 to 12 adjacent stems in 2 or 3 planes (4×2, 5×2, 3×3, 4×3 corresponding to splittings larger than 6.4 cm^{-1}) and contribute to the outermost doublet.*

From Figure VI. 29, the evolution of the stem distribution appears different to the previous behaviour observed for both sample LL/95/385 and LL/413/385.

The difference by comparison with the behaviour observed for sample LL/95/385 appears at low deformations (for a draw ratio up to 1.5). In the present case, both the numbers of isolated stems and those distributed into the small groups increases slightly (the first from 59% to 61%, the second from 30% to 32%), while the numbers of stems in the medium and large groups are diminishing respectively from 9% to 5% and from 3% to 2% after deformation of the sample to a draw ratio of 1.5. This is consistent with the break-up of the larger groups observed in Figure VI. 27 at a draw ratio of 1.5. For a draw ratio larger than 1.5, the number of isolated stems diminished progressively, from 61% to 49% at a DR of 3.3. At the same time, the number of stems in groups increases for all group sizes. This is consistent with a phenomenon of crystallisation induced by

deformation observed in the case of the baseline sample, LL/95/385. After a DR of 3.3, the behaviour changes. The number of isolated stems increases and reaches a value larger than in the undeformed sample (66%), while the number of stems distributed into groups decreases. This confirms that group break-up is occurring beyond draw ratios of 3.3. The resulting blocks are then rotated so as to have their c-axes aligned with the draw direction. It can be noted that the re-orientation of the crystalline lamellae, as observed in figure VI. 26, may occur at the same time as the crystal break-up. Finally, the behaviour observed here is generally more like sample LL/95/385, with the processes of crystallisation and block break-up more separable than with sample LL/413/385.

VI.2.3.2. The wagging region.

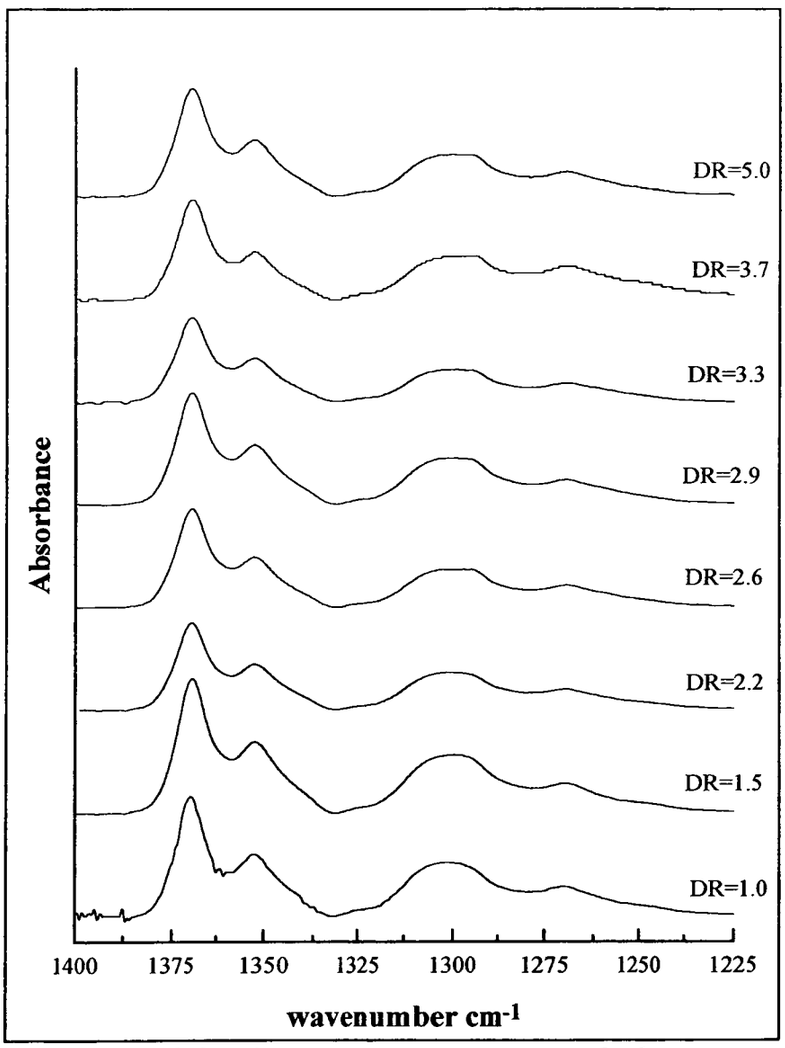

Figure VI. 30: *Variation of the CH_2 wagging region with draw ratio DR for sample CL/95/385. Three peaks are observed in the CH_2 wagging region, namely the gtg/gtg' peak at around 1368 cm^{-1}, the gg peak at around 1052cm^{-1} and the gtg/gtg' peak at around 1300 cm^{-1}. A shoulder at 1431 cm^{-1} corresponding to end-gauche defect can also be distinguished.*

As previously, in this section we will characterise the evolution of the number of non all-trans conformations with deformation for sample CL/95/385. The evolution with deformation of the CH_2 wagging profile for this sample is presented in Figure VI. 30.

It can be noted from Figure VI. 30 that the data are very scattered for all types of non all-trans conformers. Clearly, it is difficult to draw any firm conclusions from the wagging region for this sample, although, in general, all the intensities seem to decrease with deformation. For the previous sample, we have seen that two effects can be determined. One is associated with an increase in the number of gauche defects, resulting from an increase of the defects in the crystalline lamellae and the second one, associated with the removal of gauche conformers, resulting from the crystallisation of the amorphous region. Therefore, the decreasing intensities suggest that crystallisation has a larger effect than disruption / break-up of crystals in CL/95/385.

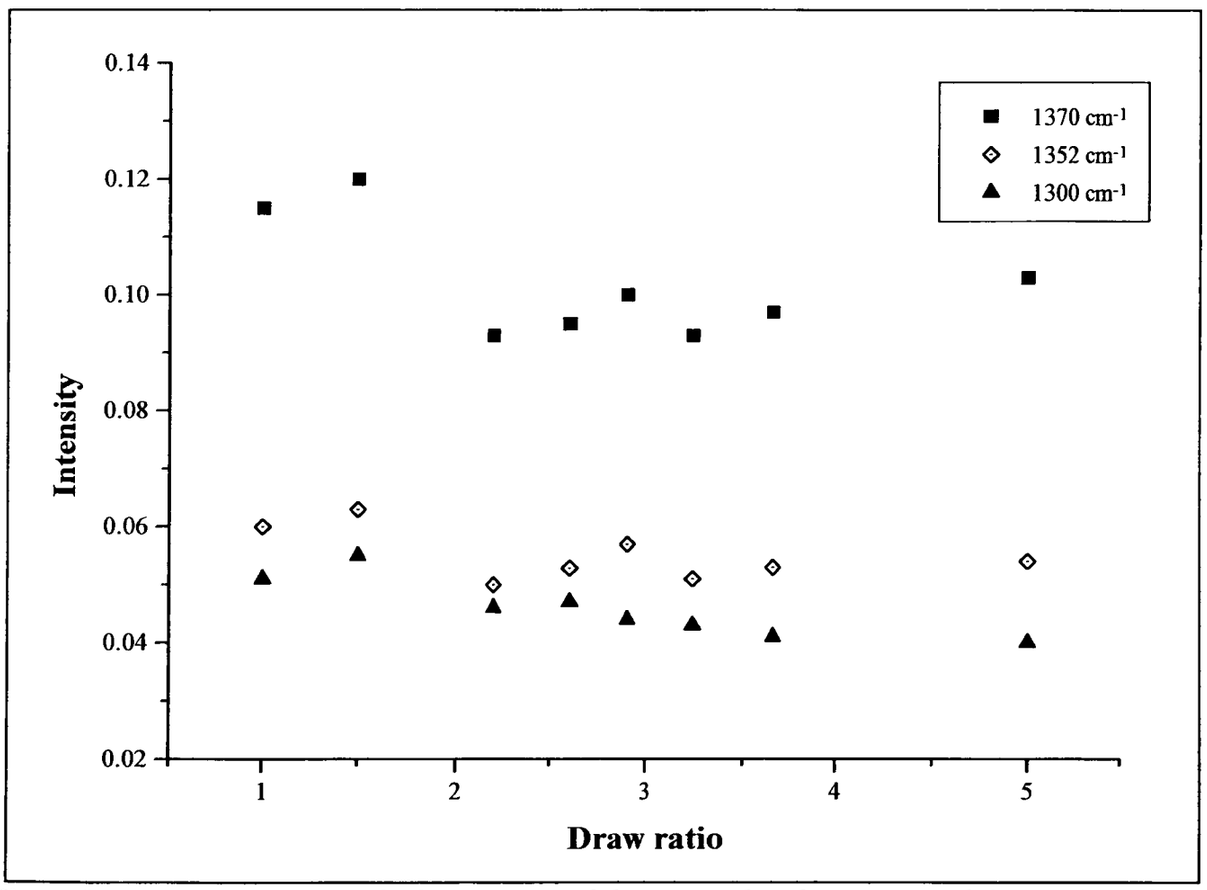

Figure VI. 31: *Evolution with draw ratio of the normalised intensity of the gtg/gtg' band at 1368 cm^{-1}, the gg band at 1352 cm^{-1} and the gtg/gtg' band at 1300 cm^{-1} for sample CL/95/385.*

VI.2.4.3. Discussion.

The first important point to be noted for sample CL/95/385 is that the outermost splitting disappeared at a draw ratio of 1.5. The numbers of stems in the medium and large groups are diminishing respectively from 9% to 5% and from 3% to 2% after the deformation of the sample at a draw ratio of 1.5. This corresponds to the break-up of the largest groups into smaller groups. At the same time, both the numbers of isolated stems and those distributed in the small groups stays more or less constant, the area of the a-polarised side of the spectrum is decreasing while the area of the b-polarised side is increasing. This suggest that the crystallographic b-axis is moving in the plane of the sample, while the a-axis is becoming normal to it. As seen in previous sections, such behaviour is not consistent with the progressive oriented crystallisation of the amorphous polymer. It is only for a draw ratio of around 2 that the oriented crystallisation of the amorphous regions occurs. Therefore, in contrast to samples LL/413/385 and LL/95/385, the onset of oriented crystallisation of amorphous regions appears to be delayed to larger draw ratios, certainly due to the presence of branches on the guest molecules, which may act as "anchors" restricting the molecular rearrangement.

After a DR of 1.5, from the re-orientation analysis we have seen that the evolution of the areas of the a- and b-polarised components is very similar to the behaviour observed for sample LL/413/385: the area of the a-polarised side of the CD_2 bending profile is increasing while the area of the b-polarised side is decreasing and at the end of the deformation range studied both areas seem to reach a plateau value. This behaviour is reflected in the evolution of the stem distribution: for draw ratios between 2 and around 4, the number of isolated stems is decreasing while the number of stems distributed in groups is increasing. In the discussion of the results of sample LL/413/385, we have seen that such behaviour is consistent with the progressive oriented crystallisation of the amorphous polymer where the newly formed crystals have a preferential orientation with the crystallographic c-axis aligned in the direction of the drawing, the a-axis been perpendicular to it and in the plane of the sample while the b-axis is normal to the sample plane.

As for sample LL/413/385, the development of the oriented crystallisation is taking place over a larger deformation range than in the case of LL/95/385. It is only at a draw

ratio of 5, where both a- and b-polarised areas seem to have reached plateau values, that the start of the untwisting of the spherulitic crystalline lamellae may be inferred. Indeed, we have seen that the crystallisation of amorphous polymer and the untwisting of the spherulitic ribbons have opposite effects on the infrared CD_2 bending profile. The crystallisation process is associated with an increase and a decrease in the respective areas of the a- and b-polarised components while the untwisting is associated with a decrease of the area of the a-polarised with the area of the b-polarised staying more or less constant. Hence, the plateau value observed in the evolution of the area of the a-polarised at a draw ratio of 5 may be understood as the untwisting (and crystal break-up at higher draw ratio) effects compensating presumably for the oriented crystallisation effect.

In the case of sample LL/413/385, it was suggested that the slow development of the crystallisation process may be a consequence of the presence of tie-molecules and chain entanglements restricting the molecular movement. But in the case of CL/95/385, both the radius of gyration and the X-ray long spacing (R_g = 209±9Å and L_{SAXS} = 259±14Å for CL/95/385) are very similar to sample LL/95/385 (R_g = 279±9Å and L_{SAXS} = 254±13Å), and suggest that each copolymer chain is restricted to only one lamella. Therefore, the guest molecules are unlikely to form tie-chains in sample CL/95/385. Chemically, the only difference with sample LL/95/385 is that the copolymer DPE molecules have 6.3 hexyl branches per thousand carbon atoms. It appears, then, that the branches are delaying the process of oriented crystallisation of amorphous polymer and the untwisting of spherulitic crystalline lamellae.

From the evolution of the stem distribution, we have seen that the number of stems distributed in the largest groups is progressively decreasing after a draw ratio of around 3.5 and finally reaches zero at a DR of 5. Also, the numbers of stems distributed in small and medium groups are decreasing after a draw ratio of around 4, while the number of isolated stems is increasing. This shows that the largest groups of adjacent labelled stems are breaking up into smaller groups, which is evidence that the crystalline lamellae are disrupted into blocks. The resulting blocks should ultimately rotate so as to have their c-axis parallel to the draw direction. A quantitative analysis of the infrared results reveals that the average size of the crystallite is reduced from around 22.5 Å initially to around 13.5 Å (using the dimensions of the largest remaining groups) at a draw ratio of 5.

VI.2.5. Sample CC/95/181.

In the previous section we have studied the behaviour of a copolymer DPE guest co-crystallised with a linear HPE matrix under deformation. We will now study the behaviour of a fully copolymer sample, i.e. a copolymer DPE guest co-crystallised with a copolymer HPE matrix. In chapter 5 it was observed from the neutron scattering and the infrared spectroscopy that the conformation of the undeformed CC samples is more 'compact' than for the other samples. Therefore, a different deformation behaviour may be expected.

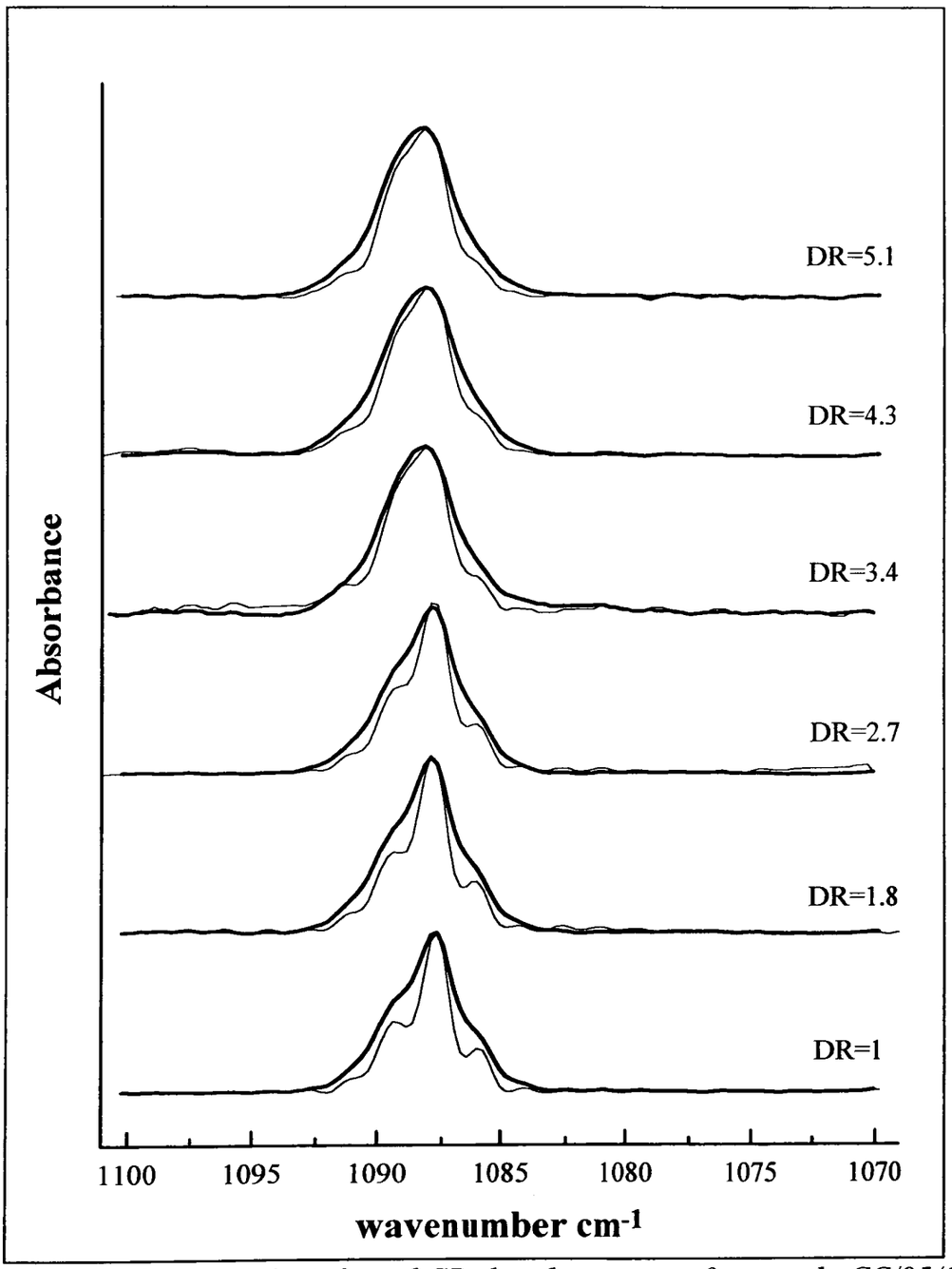

Figure VI. 32: *Evolution of the infrared CD_2 bending region for sample CC/95/181 with draw ratio. The different draw ratios are shown in the picture. The thick line represents the raw data, the fine line, the deconvoluted data.*

VI.2.4.1. The CD_2 bending region.

Two different analyses will be made from the evolution of the infrared CD_2 bending profile presented in Figure VI.32. The representative values of the deconvolution parameters used are respectively around 1.5 cm^{-1} for the full width at maximum absorbance of the intrinsic lineshape, α and around 2 for the enhancement factor, K for the deformed samples. These parameters are slightly smaller than for the undeformed sample. The reorientation under deformation of the crystallographic axes and the progressive disruption of the initial local stem arrangement will be characterised using the results obtained from (a) the curve fitting and (b) the calculation of the CD_2 bending profile from individual group splittings.

From figure VI. 32 it can be seen that, up to a DR of 2.7, the profile did not change much through the deformation. For a draw ratio between 2.7 and 5.1, the intensity of the a-polarised components appears to increase, while the absorbance of the b-polarised part is decreasing. In contrast to observations for the linear low molecular weight guest sample, the shapes of the initial and final profiles are significantly different. However, at the highest draw ratio measured, doublets can still be distinguished in the CD_2 and in the CH_2 bending profiles. A shoulder at around 716 cm^{-1} was also observed in the CH_2 rocking region, suggesting that some phase transformation from orthorhombic to monoclinic structure has occurred. The low absorbance and the fact that the monoclinic structure was again not observed in the WAXS pattern suggest that this phase transformation is only a minor effect in the deformation process.

VI.2.5.1.1 Evolution of the of the a- and b-polarised areas.

As for the other samples, information on the re-orientation of the crystallographic axes was obtained through the results of the curve fitting of the deconvoluted data. The evolution of the normalised areas of the a- and b-polarised components of the profile with deformation is presented in figure VI. 33.

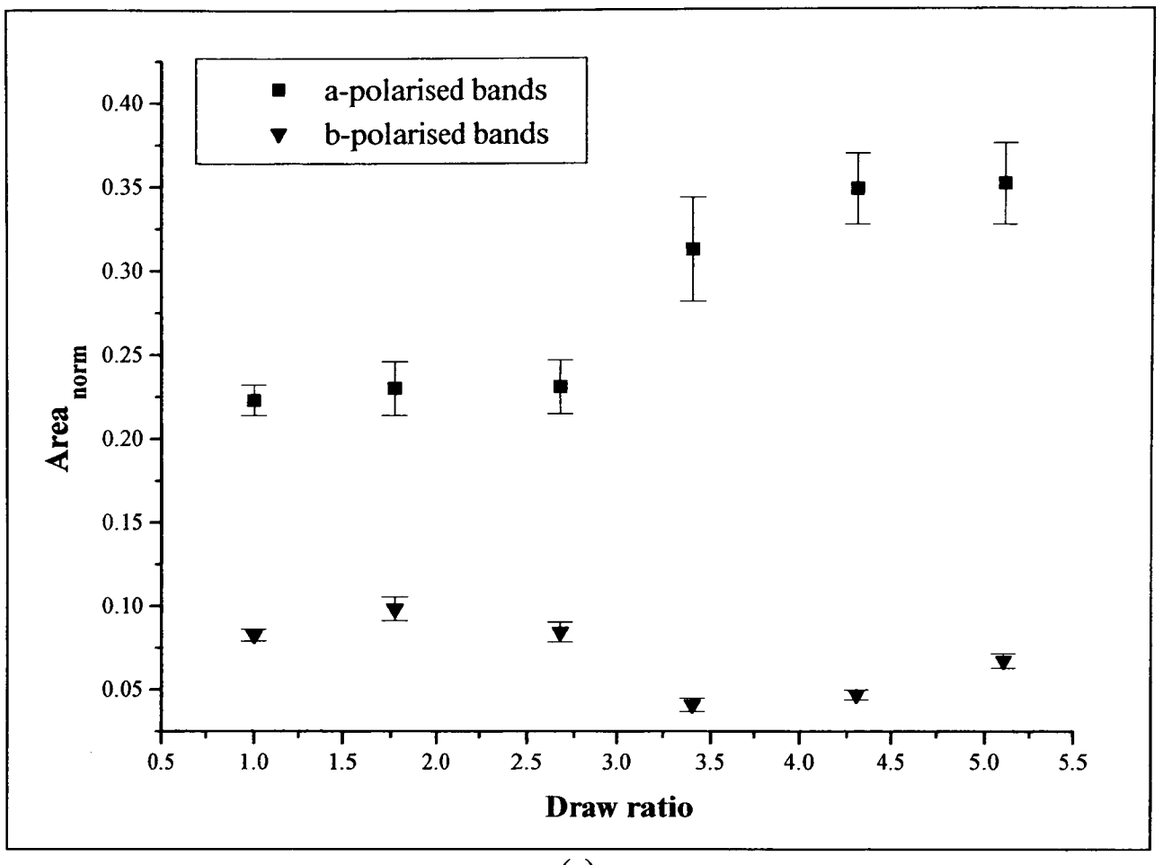

(a)

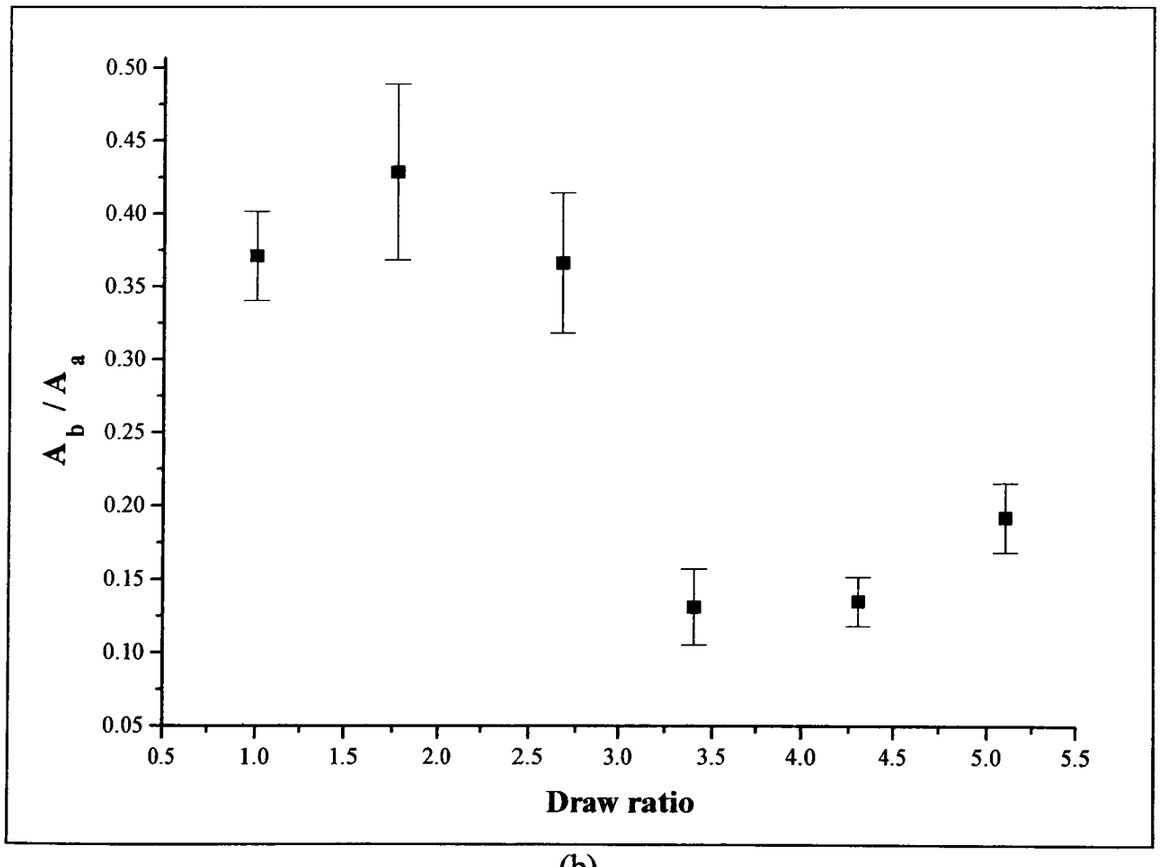

(b)

Figure VI. 33: *(a) Evolution of the normalised areas of the a- and b-polarised components; and (b) evolution of the ratio of the areas of the b- and a-polarised bands with draw ratio for sample CC/95/181.*

The shapes of these curves appear different from what was observed for the previous samples. Firstly, as was said above, up to a DR of 2.6, the areas of both the a- and b-polarised components are almost identical to the values observed for the undeformed sample. For draw ratios larger than 2.6, the a-polarised component area increases progressively up to the end of the deformation range studied, while the area of the b-polarised component first decreases and reaches a minimum between draw ratios of 2.6 and around 4.5. At a draw ratio of around 5, the b-polarised area is increasing while the a-polarised area seems to have reached a plateau value. This is reflected in the evolution of the A_b/A_a ratio, where the value of the ratio, after reaching a minimum between draw ratios of 3.5 and 4.5, is still increasing at a draw ratio of 5.

After the initial stage where almost no change was observed, the evolution of both the a- and b-polarised areas for a draw ratio greater than 2.6 appears to be similar to the behaviour observed for sample LL/413/385. In the case of sample LL/413/385, we have seen that the behaviour was consistent with the progressive oriented crystallisation of the amorphous polymer. This may suggest that such a phenomenon of oriented crystallisation is also occurring in the case of sample CC/95/181. Before studying the evolution of the group sizes in order to confirm our suspicion of stress-induced crystallisation of amorphous polymer, it can be noted that, in the case of sample CC/95/181, the onset of such a process appears to be delayed to larger draw ratios than in the case of sample LL/413/385.

VI.2.5.1.2. Group size analysis.

In this section, the progressive break-up of groups of adjacent stems will be monitored through the results obtained from both the curve fitting (presented in Figure VI. 34) and the calculation (presented in Figure VI. 35 and 36) of the CD_2 bending profiles.

Three doublets were initially resolved after the deconvolution of the experimental data. The evolution of the splittings of these doublets is represented in Figure VI. 34. First of all, the outermost splitting has an initial value of almost 8.5 cm^{-1}, which corresponds to groups of 3×4 adjacent labelled stems. This outermost splitting increases slightly until a DR of 2.7 with a maximum value of 8.7 cm^{-1}. This corresponds to groups of 8×3 adjacent stems, although only a very small number of stems are in the larger groups. For draw ratios larger than 2.7, this outermost splitting has disappeared. Initially the "medium" splitting has a value of 6.9 cm^{-1}, which corresponds to 4×2 adjacent stems.

Up to a DR of 2.7, the value of this splitting does not change much. Between DR values of 2. 7 and 3.4, it drops to only 5.4 cm^{-1}, which corresponds to groups of about 2×2 or 3×2 adjacent stems. Up to the end of the data set, the "medium" splitting value stays constant. This evolution is attributable to the break-up of the largest remaining groups as explained for sample LL/95/385. The inner splitting has an initial value of 3.5 cm^{-1}, which corresponds to groups of 3×1 adjacent stems. Through the deformation, the value of the inner splitting does not change significantly. This means that the small groups are not yet broken up, although they may be reduced in number. This will become clear in the following stem distribution analysis.

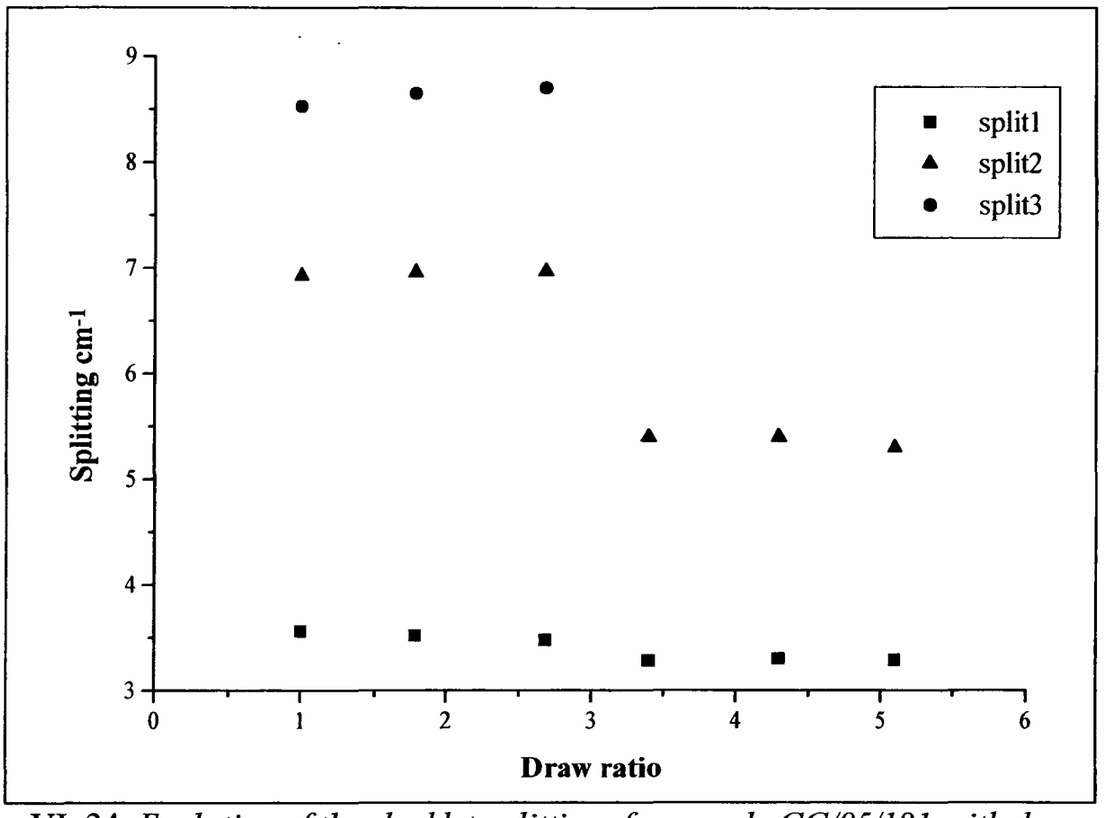

Figure VI. 34: *Evolution of the doublet splittings for sample CC/95/181 with draw ratio. Split 1 is the splitting between, approximately, the 1089 cm^{-1} and 1086 cm^{-1} bands, split 2 is the splitting between, approximately, the 1091 cm^{-1} and 1086 cm^{-1} bands and split 3 is the splitting between, approximately, the 1093 cm^{-1} and 1086cm^{-1} bands.*

As for the other samples, in order to validate the results obtained from the curve fitting, calculation of the infrared CD_2 bending profiles was carried out, and it becomes possible to monitor the evolution of the stem distribution with the degree of deformation of the sample. The results of the calculation are presented in Figure VI. 35, while the stem distributions are presented in Figure VI. 37.

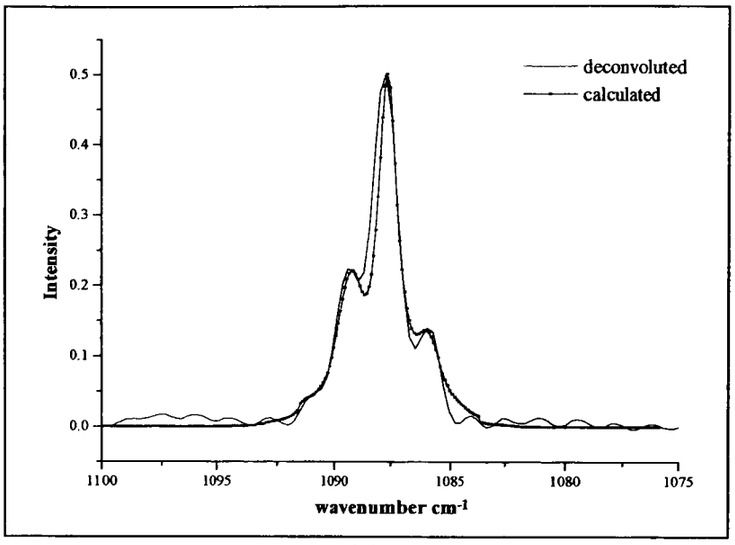

(a)

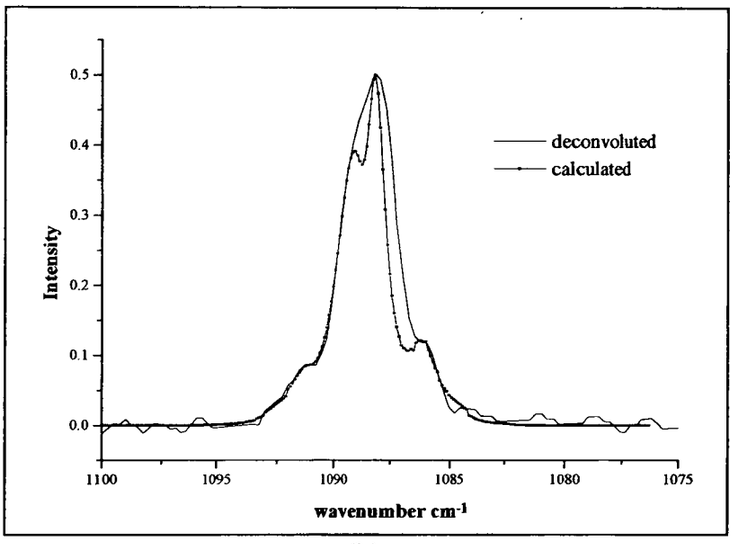

(b)

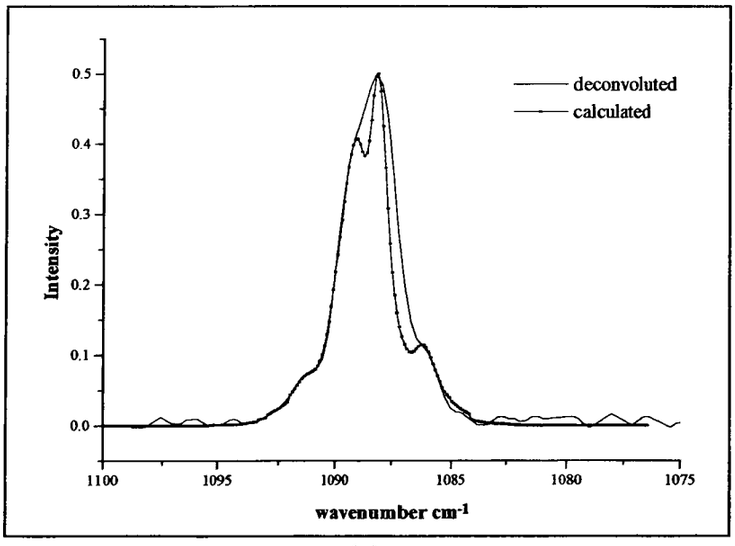

(c)

Figure VI. 35: *Examples of calculated CD_2 bending profiles using Lorentzian shape function without singlet width increases for sample CC/95/181, presented along with the corresponding deconvoluted experimental data. (a) undeformed sample: (b) at a DR = 2.7; at a DR = 5.1.*

As in the case of sample LL/413/385, the width of the singlet component appears to increase with increasing draw ratio, although here it appears to reach a plateau value at a draw ratio of around 3.5. This is illustrated in Figure VI. 36. Therefore, for our simulations of the deconvoluted data, the width of the Lorentzian function used to calculate the singlet component was increased. As in the case of sample LL/413/385, this gave no satisfactory fits, because the tail of the Lorentzian function simulating the singlet peak is masking most of the doublet contributions. The fits presented in figure VI. 35 are without singlet width increased. Similarly to samples LL/413/385 and CL/95/385, it was noted that the Lorentzian contribution to the Voigt function used was decreasing while the Gaussian contribution was increasing, suggesting that using a Lorentzian function may no longer be adequate to simulate the singlet component for the deformed sample and may explain the poor agreement between the deconvoluted and calculated profiles.

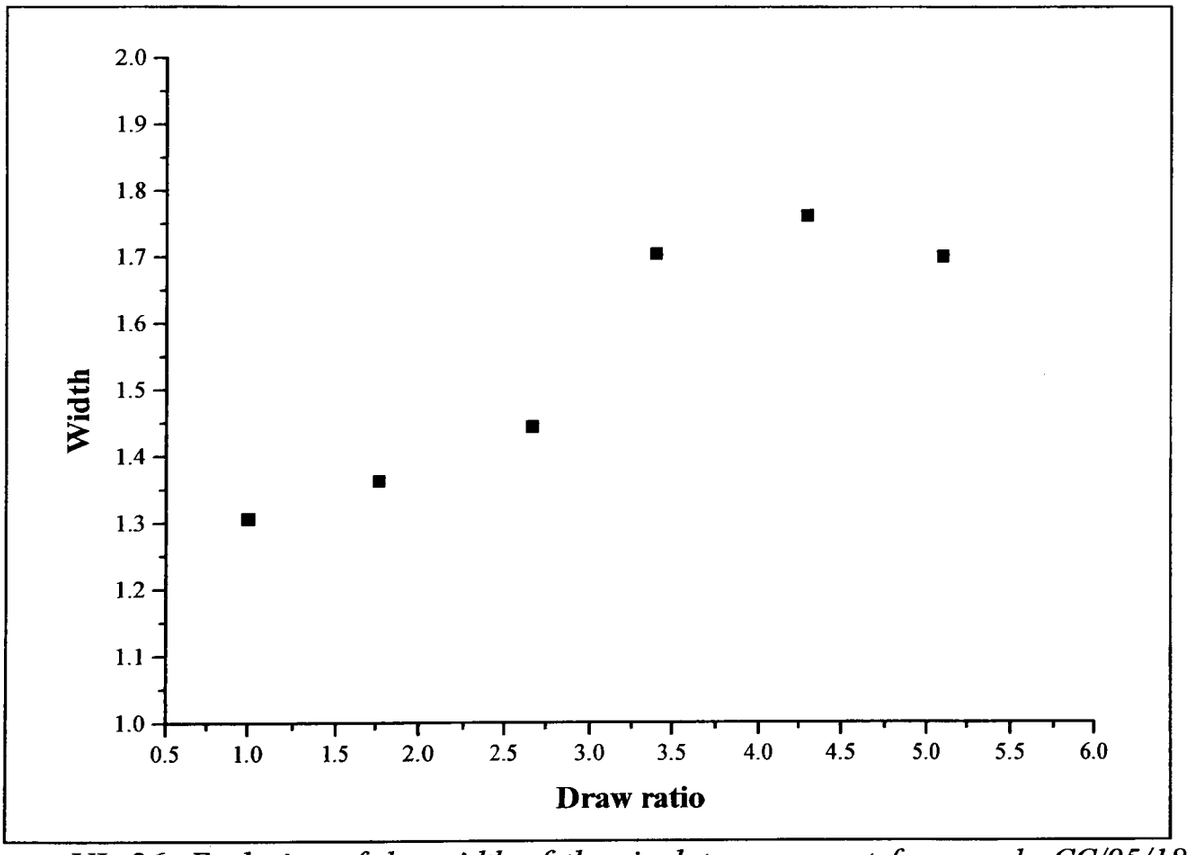

Figure VI. 36: *Evolution of the width of the singlet component for sample CC/95/181 obtained from the curve fitting analysis using a Voigt shape function to fit the singlet peak.*

It can be seen that for the undeformed sample most of the stems are isolated or in small groups of 2 to 4 adjacent stems. Only a very small number (2%) are actually in the largest groups. Up to a draw ratio of 3.4, the number of isolated stems decreases while the number of stems distributed within groups increases. This confirms that

crystallisation is occurring. Between a draw ratio of 2.7 and 3.4, the number of stems in the largest groups falls to zero. This corresponds to the break in the evolution of the outermost splitting shown in figure VI. 34. For draw ratios larger than 3.4, the number of isolated stems increases, while the numbers of stems in the "medium" and "small" groups decreases. This confirms the progressive break-up of the largest groups.

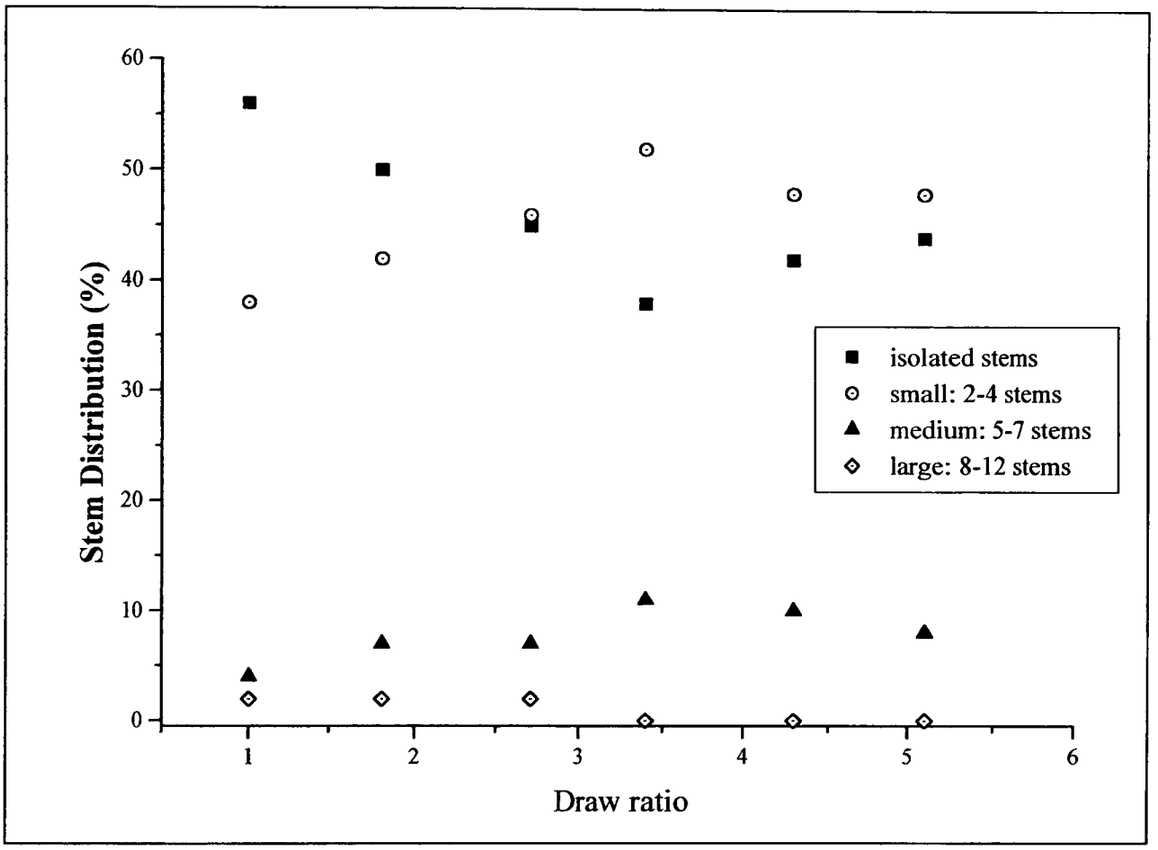

Figure VI. 37: *Evolution of the stem distributions with deformation for sample CC/95/181. The isolated stems are contributing to the singlet; the small groups are constituted of 2 to 4 stems in one plane (2×1, 3×1 and 4×1 corresponding to splittings between 2.6 and 3.9 cm^{-1}) and contribute to the inner doublets; the medium groups are constituted of 5 to 7 stems in one or two planes (5×1, 2×2 and 3×2 groups corresponding to splittings between 4.2 and 6.1 cm^{-1}) and contribute to the intermediate doublets; the large groups are constituted of 8 to 12 adjacent stems in 2 or 3 planes (4×2, 5×2, 3×3,4×3 corresponding to splittings between 6.4 and 8.3 cm^{-1}) and contribute to the outermost doublet.*

VI.2.5.2. The CH_2 wagging region.

In contrast to the samples with the linear matrix, a fifth peak can be seen in the CH_2 wagging region presented in Figure VI. 38. This peak appears as a shoulder to the gtg/gtg' band at 1368 cm^{-1}. This band at around 1378cm^{-1} corresponds to the CH_3 symmetric deformation. The methyl groups are situated only at the chain ends for the linear polyethylene, and consequently the number of methyl groups is generally very low in comparison to the number of CH_2 units. Hence this band does not appear in the

spectrum of the samples with the linear matrix. For the copolymer matrix, methyl groups are situated at each end of the main chain but also, in addition, at the end of each branch. Thus, the proportion of methyl groups is significantly larger in the copolymer matrix samples (for the copolymer matrix there are approximately ten methyl groups for one thousand CH_2 units while for the linear matrix there are around 0.1 methyl groups for a thousand carbon atoms). It is therefore expected that the CH_3 deformation will show a larger absorbance in the spectrum of sample CC/95/385.

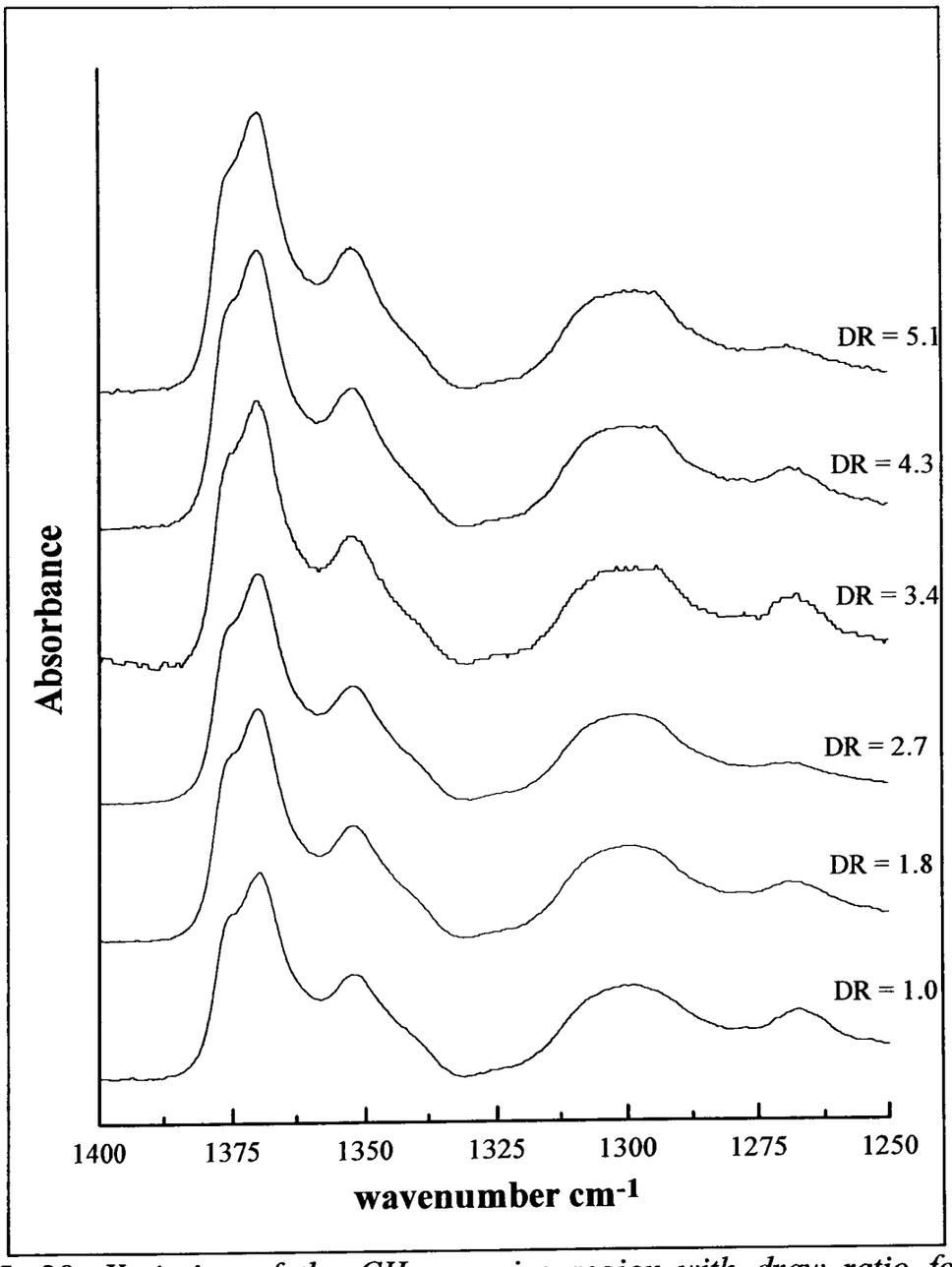

Figure VI. 38: *Variation of the CH_2 wagging region with draw ratio for sample CC/181/385. Four peaks are observed in the CH_2 wagging region, namely the methyl deformation at 1378 cm^{-1}, gtg/gtg' peak at around 1368 cm^{-1}, the gg peak at around 1052cm^{-1} and the gtg/gtg' peak at around 1300 cm^{-1}.*

As for the other samples, the general shape of the CH_2 wagging modes is not altered throughout the deformation. The evolution of the normalised intensities of the non all-

trans conformation bands is reported in Figure VI. 39. From this figure, all three absorption bands show a similar trend. The number of non all-trans conformations increases through the deformation range studied, and seems to reach a maximum value at the end of the data set. This augmentation of the number of non all-trans conformation can only result from an increase in the number of defects in the crystalline lamellae, related to the disruption of the crystals. This suggests that the crystals are becoming highly defective by a draw ratio of around 4. In the previous section we have seen that, in this deformation range, crystallisation of amorphous regions is occurring which must lead to a reduction in non all-trans conformations. Therefore, these increasing intensities suggest that existing crystals as well as new ones (created by crystallisation of amorphous regions) become progressively more disrupted, at least up to a certain draw ratio. The fact that the number of non all-trans conformers reaches a plateau value may suggest that the maximum degree of crystal disruption has been reached.

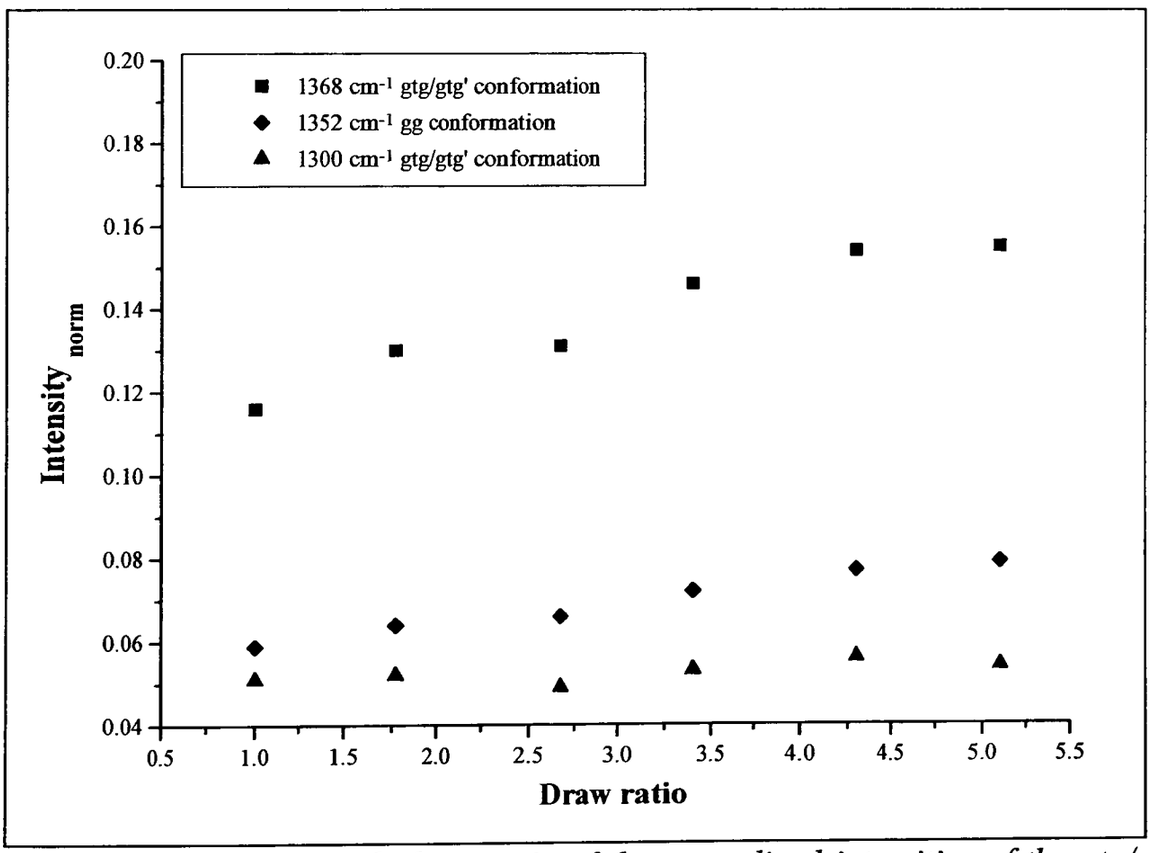

Figure VI. 39: *Evolution with draw ratio of the normalised intensities of the gtg/gtg' band at 1368 cm^{-1}, the gg band at 1352 cm^{-1} and the gtg/gtg' band at 1300 cm^{-1} for sample CC/95/181.*

VI.2.5.3. Discussion.

For sample CC/95/181, we have studied the molecular rearrangement upon deformation of the copolymer DPE guest mixed with a copolymer HPE matrix. Up to a draw ratio of around 3.5, the largest splitting is increasing slightly, the number of stems distributed in groups is increasing while the number of isolated stems decreases. This suggests that a phenomenon of crystallisation of amorphous regions is taking place. This is consistent with the neutron scattering results, which suggested that the deformation mainly takes place in the amorphous polymer, up to a draw ratio of around 3 in the case of CC/95/181. But in contrast to the other samples, the newly formed crystals do not exhibit the same preferential orientation, at least up to a draw ratio of 2.6, since both the a- and b-polarised areas stay more or less constant. Indeed, for the other samples, an increase of the a-polarised area relative to the b-polarised area was associated with the crystallisation phenomenon. This was understand as a preferential orientation of the newly formed crystals with the crystallographic c-axis aligned within the draw direction, the a-axis perpendicular to it and in the plane of the sample, while the b-axis is normal to the plane of the sample. In the case of sample CC/95/181, it is only between draw ratios of 2.6 and around 4 that the a-polarised area is increasing and the b-polarised area decreasing suggesting that the orientation process of the newly formed crystals is only just starting after a draw ratio of 2.6. It is believed that the newly formed crystals have, up to a draw ratio of almost 3, random orientations. In section VI.2.4, it was seen that the onset of the oriented crystallisation of CL/95/385 was also delayed to larger draw ratios. This may be related to the presence of branches which may act as "anchors" and therefore restrict the molecular rearrangement. But in the case of sample CC/95/181, the onset of the orientation of the newly formed crystals is delayed to even larger draw ratios than for CL/95/385. This may be related to the fact that both the matrix and host have now branches.

For draw ratios larger than 3.5, the number of isolated labelled stems increases while the number of stems in groups decreases and even reaches zero between draw ratios of 2.6 and 3.5 in the case of the stems contributing to the largest groups. This corresponds to the break-up of the largest groups of adjacent labelled stems, providing evidence that the crystalline lamellae are breaking up into blocks. The resulting blocks are ultimately expected to rotate so as to have their c-axes parallel to the draw direction, corresponding to fibre orientation.

At a draw ratio of 5, the A_b/A_a ratio is increasing slightly (figure VI. 33). This results from an increase of the b-polarised area while the a-polarised area seems to have reached a plateau value. This behaviour is consistent with start of the re-orientation process of some of the spherulitic crystalline lamellae, as described in section VI.2.1 and which primarily involves the rotation of the unit cell around b so as to align the crystallographic c-axis in the draw direction while the a-axis becomes normal to the plane of the sample. As shown earlier, this process results to the untwisting of the lamellae of the lamellae situated along the spherulite radii perpendicular to the draw direction. As in the case of samples CL/95/385 and LL/413/385, the onset of the untwisting process appears to be delayed to larger draw ratio than for sample LL/95/385. This is believed to be the effect of the branches which are acting as "anchors" and are restricting the molecular rearrangement introduced by drawing.

In the case of sample CC/95/181, not only does the oriented crystallisation process develop over a wider deformation range than for LL/95/385 but the orientation of the newly formed crystals is only starting at a draw ratio of around 3. It appears that the presence of branches in the guest, as well as in the host, has this additional influence on the deformation behaviour.

VI.3. Comparison of the deformation behaviour of the different samples.

In this section, we will now compare the results obtained from both the neutron scattering and the FTIR analysis for the different samples.

In the neutron scattering part of this chapter we have seen that, for both the linear and copolymer samples, the deformation behaviour of the radii measured parallel and perpendicular to the draw direction was affine in the first stages of the deformation. At larger deformations, departure from affine behaviour was observed. By suggesting that lamellae cannot be deformed affinely, it was concluded that the initial stage of the deformation involves mainly deformation of the amorphous polymer. Departure from affine behaviour was then understood as arising from lamellar deformation.

Differences between the linear and copolymer DPE guest samples were observed in the point of departure from affine behaviour. Departure has already occurred at a draw ratio of 1.5 for sample LL/95/385 while it was only observed from a draw ratio of 2.4 for CC/95/181. This delay could not be explained by the difference in crystallinity since for both LL/95/385 and LC/95/181 departure from affine behaviour was observed at almost the same draw ratio while their degrees of crystallinity are significantly different (50% for LL/95/385 and 38% for LC/95/181). Such effects were understood as resulting from the presence of branches on the guest molecules.

Information on the molecular processes involved in deformation was obtained from the different infrared analyses presented in this chapter. Three different phenomena were observed. The first one is related to the oriented crystallisation of amorphous regions, the second consists of the progressive development of the c-axis orientation and finally, the third one corresponds to the break-up of the crystalline lamellae.

When drawing the samples, oriented crystallisation of amorphous regions was shown to occur in all cases. This effect is very significant in the case of sample LL/95/385, but is less marked and occurs over a larger deformation range for the other samples. At larger draw ratios, the development of c-axis orientation starts and involves the progressive untwisting of the lamellae close to the minor axes of the deformed spherulites (perpendicular to the draw direction). Again, this was clearly observed for sample LL/95/385 and may just be starting at the end of the deformation range studied for the other samples. This is shown in Table VI.1, which includes the draw ratio at which the

infrared behaviour associated with the onset of developing c-axis orientation was observed.

In general, The processes are more clearly separable in sample LL/95/385: oriented crystallisation clearly dominates at low draw ratios and re-orientation of spherulite segments and crystal break-up dominates at higher draw ratios. Also, the oriented crystallisation is clearly more rapid in sample LL/95/385, and spherulite re-organisation starts earlier and develops more rapidly with draw ratio, but the block break-up is delayed in comparison with the other samples. This may be attributable to molecular weight fractionation, since the guest molecular weight is much less than that of the host. In this way, the guest molecules may crystallise with the lower molecular weight part of the matrix and form separate crystals. Hence the separate lamellae containing the shorter molecules may more readily undergo the development of the c-axis orientation. This relates to the observation, in chapter 5, of an excess in the SANS intensity for sample LL/95/385. However, as mentioned there, sample LL/95/385 is thought not to be isotopically fractionated on the basis of the relatively small excess in the SANS intensity and the relatively small splittings of the infrared CD_2 bending mode.

Sample	c-axis orientation (DR)	initial size (Å)	final size (Å)	starting point of break-up (DR)
LL/95/385	4.5	18	9	4.5
LL/413/385	7.4*	22.5	9	3
CL/95/385	5.1*	22.5	13.5 (DR= 1.5)	1.5
CC/95/181	5.1*	41.5	13.5	3

Table VI. 4: *Comparison of the start of development of c-axis orientation, the initial and final sizes of the largest groups of labelled stems and the starting point of crystal break-up for the different samples. * end of deformation range studied for these samples.*

The mixed crystal infrared technique applied to drawn samples of melt quenched polyethylene has provided information on the break-up of crystalline lamellae during drawing, via the observation of the break-up of groups of adjacent labelled stems within the crystalline lamellae. This was shown to occur for all samples, but to different extents and at different draw ratios as illustrated in Table VI. 4. From this table, it can be seen that the starting point of crystal break-up occurs at larger draw ratio in the case of sample LL/95/385, and that the extent of crystal break-up is the smaller. This may

simply be because the effects of the break-up can only be seen when the block sizes are already reduced to the initial size of the largest groups of adjacent labelled stems.

For sample CL/95/385, disruption of the crystalline lamellae has already started at a draw ratio of 1.5. The average size of the crystallite is reduced from 22.5 Å to 13.5 Å. After a draw ratio of 1.5, the outermost splitting appears to stay more or less constant throughout the deformation range studied. Therefore, after the initial break-up occurring at a draw ratio of 1.5, no more disruption of the lamellae is observed.

The effects are the largest for sample CC/95/181, which has also the largest initial groups. At a draw ratio of 5.1, the end of the deformation range studied for this sample, the average group size has been reduced from approximately 36 Å to 9Å. Extending the argument above, this large extent of disruption may be attributable to the initial presence of larger groups of adjacent stems in CC/95/181, which are easier to disrupt than smaller groups. It may also relate to branch molecules being pulled through the lamellae, contributing to the crystal break-up.

Finally, the disruption of the lamellae appears to be large in all the cases studied with the remaining blocks containing only up to two or three adjacent stems at the end of the deformation range studied. However, the disruptions observed here are not as large as in fibres, where the singlet is almost the only remaining component in the CD_2 bending vibration [31].

---

[1] D.M. Sadler, P.J. Barham, *Polymer*, **31**, 36 (1990).
[2] D.M. Sadler, P.J. Barham, *Polymer*, **31**, 43 (1990).
[3] D.M. Sadler, P.J. Barham, *Polymer*, **31**, 46 (1990).
[4] J. Lagarón, S. López-Quintana, J.C. Rodríguez-Cabello, J.C. Merino, J.M. Pastor, *Polymer*, **41**, 2999 (2000).
[5] W. Reed, *Personal communication.*
[6] R.G. Alamo, B.D. Viers, and L. Mandelkern, *Macromolecules*, **26**, 5740 (1993).
[7] C. France, P.J. Hendra, W.F. Maddams and H.A. Willis, *Polymer*, **28**, 710 (1987).
[8] J.P. Gorce, *PhD thesis*, Sheffield Hallam University, Sheffield, 2000.
[9] M. Doi, S.F. Edwards, *The theory of Polymer Dynamics*, Clarendon Press, Oxford, 1986.
[10] P.G. de Gennes, *J. Chem. Phys.*, **55**, 572 (1971).
[11] M. Doi, *Polymer J.*, **5**, 288 (1973).
[12] K. E. Ewans, S. F. Edwards, *J. Chem. Soc. Faraday Trans. 2*, **77**, 1891 (1981).
[13] J. Klein, *Nature (London)*, **271**, 143 (1978); *Phil. Mag.*, **A43**, 771 (1981).
[14] J. Klein, B.J. Briscoe, *Proc. R. Soc.*, **A365**, 53 (1979).
[15] K. Sasagury, S. Hoshino, R. S. Stein, *J. Appl. Phys.*, **35**, 47 (1964).
[16] K. Sasagury, R. Yamada, R.S. Stein, *J. Appl. Phys.*, **35**, 3188 (1964).
[17] S. Clough, J.J. Van Aartsen, R.S. Stein, *J. Appl. Phys.*, **36**, 10, 3072 (1965).

[18] J.J. Van Aartsen, R.S. Stein, *J. Polymer Sci.: A-2*, **9**, 295 (1971).
[19] T. Oda, S. Nomura, H. Hawai, *J. Polymer Sci: A*, **3**, 1993 (1965).
[20] S. Nomura, A. Asanuma, S. Suehiro, H. Kawai, *J. Polymer Sci: A-2*, **9**, 1991 (1971).
[21] M. Matsuo, C. Xu, *Polymer*, **38**,17, 4311 (1997).
[22] I.L. Hay and A. Keller, *Kolloid Z. Z. Polym.*, **204**, 43 (1965).
[23] R. Hiss, S. Hobeika, C. Lynn, G. Strobl, *Macromolecules*, **32**, 4390 (1999).
[24] E.U. Okoroafor and S.J. Spells, *Polymer*, **35**, 4578 (1994).
[25] R. Seguela, F. Rietsch, *Polymer*, **27**, 532 (1986).
[26] R.G. Matthews, A.P. Unwin, I. M. Ward,, G. Capaccio, *J. Macromol. Sci.-Phys.*, **B38** (1&2), 123 (1999).
[27] A.M.E. Baker, A.H. Windle, *Polymer*, **42**, 651 (2001).
[28] M.F. Butler, A.M. Donald and A.J. Ryan, *Polymer*, **39**, 1, 39 (1998).
[29] J. Lagarón, N.M. Dixon, W. Reed, J.M. Pastor, B.J. Kip, *Polymer*, **40**, 2569 (1999).
[30] D.M. Sadler, R. Harris, *J. Polym. Sci. Poly. Phys. Ed.*, **20**, 561 (1982).
[31] S.J. Spells, *Personal communication.*

Chapter seven:

Discussion and Future Work

This thesis has been devoted to the investigation of the molecular mechanism involved during the cold drawing of both linear and branched polyethylene. The overall aims were to establish any conformational differences between the homopolymer and copolymer in the melt quenched state prior to deformation and during cold drawing.

The motivation has been twofold. Despite the extensive study of the morphology of polymer fibre and the well documented macroscopic changes on deformation (such as slip and twinning), the detailed relationship between the initial and final molecular conformations is poorly understood. In addition, experiences with polyethylene suggest that the presence of some branched polymer has a significant influence on the chain morphology prior to deformation and on the drawing behaviour. Therefore, first we shall describe and discuss in the light of previous work the initial chain conformation before considering the molecular mechanisms involved during cold drawing and the effects of tie-molecules and branches on the deformation behaviour.

This study has been carried out using four different types of sample, namely a linear DPE guest mixed within a linear HPE matrix (LL samples), a combination of a linear guest and a copolymer host (LC), of a copolymer guest and linear host (CL) and finally a copolymer guest mixed within a copolymer matrix (CC).

VII.1. Chain conformation prior cold drawing.

Several techniques were combined in chapter 5 to determine the initial conformation and the results obtained show that in general isotopic fractionation has not occurred during the crystallisation process. Indeed, the outermost infrared splitting is in each case relatively small, only one melting peak was observed from all the DSC measurements and no large excess of neutron scattering intensity at small angles was detected using the Zimm plots presented in chapter 5. However, a small excess scattering was observed in the Zimm plot for the low molecular weight DPE guest and high molecular weight HPE matrix (sample LL/95/385), suggesting that a phenomenon of molecular weight fractionation has occurred to a limited extent in this case.

In addition to the problem of isotopic fractionation, co-crystallisation of linear and branched polyethylene may not be trivial, and this question has given rise to considerable investigation in the last 10 years. Hill et al [1, 2, 3] have studied the miscibility in the melt in blends of linear and branched polyethylene after rapidly quenching using differential scanning calorimetry and transmission electron microscopy (TEM). The regions of double morphology arising from liquid-liquid phase separation in the molten state have been mapped, and these studies have included metallocene-catalysed copolymer [4, 5]. In general, the authors observed a closed loop biphasic region when the linear polyethylene content is less than 50% and a similar loop was observed in blends of branched polyethylene. This was first believed to be related to the branch content. However, more recently, this conclusion was reviewed when Hill et al studied the phase behaviour of deuterated linear and branched hydrogenated polyethylene by micro-Raman imaging [6]. The authors concluded that the biphasic morphology observed in rapidly quenched blends of linear and branched polyethylene or blends of branched polyethylene does not result from the branch content as was initially believed, but rather from the different degrees of crystallinity in the linear and branched components.

Most of the experimental evidence for any phase separation come from indirect experiments in which rapidly quenched blend samples are studied in the solid state. However, small angle neutron scattering experiments, using blends of deuterated linear polyethylene with a branched polyethylene, provide a way to investigate phase separation directly in the melt. The use of excess SANS scattering intensity to detect

liquid-liquid phase separation directly in the melt has led to disagreement with the interpretation from TEM work [7]. For a range of molten blends of linear and branched polyethylene Alamo et al [8, 9, 10] showed that the mixtures were homogeneous for low branch contents (less than 4 branches per 100 Carbon atoms) and that phase separation occurred at branch contents greater than or equal to 8 branch per 100 Carbon atoms. Results based on TEM microstructures should, therefore, be viewed with some caution as a guide to morphologies expected for the blends studied in this thesis. Indeed, as already mentioned above, no sign of fractionation was observed in our samples (which have a branch content far smaller than those referred to above, namely less than 7 branches per thousand Carbon atoms and for blends of 5% of linear or branched deuterated polyethylene with a linear or branched matrix) which tends to justify this caution. Also, it must be noted that miscibility in the melt is not a prerequisite of fractionation. There may be fractionation on crystallisation of a homogeneous melt, although rapid quenching will minimise this.

Wide angle X-ray patterns showed that all the samples had an orthorhombic structure, without any sign of monoclinic structure, and that no preferred orientation existed prior to deformation. In addition, the characteristics such as crystallinity and long spacing determined from both DSC and small angle X-ray diffraction were similar to those found in literature [11, 12, 13, 14], taking into account that our samples are crystallised by quenching a melt (as shown in chapter 5). As expected a reduction in the crystallinity of polyethylene with increasing branch content is observed. However, it must be noted that the crystallinity values determined by DSC are larger than those measured by Raman spectroscopy [12]. Since the Raman technique is associated with the orthorhombic crystal structure, it has been proposed that a proportion of disrupted orthorhombic material is detected by the other methods, but not by Raman spectroscopy [12]. In addition, recent WAXS measurements on polyethylene materials with a range of branch contents indicate that the orthorhombic unit cell a and b dimensions both increase with increasing branch content [15]. This may be related to some incorporation of branches into the crystallites, which might, therefore, be expected in our case.

The evolution of the radius of gyration versus the molecular weight has been studied for the four different systems. The exponents α in the relationship $R_g \propto \overline{M}_W{}^{\alpha}$ found for the sample types LL, LC and CL agree, to within the errors, with published data [16, 17, 18, 19, 20, 21, 22] for blends of linear DPE guest and linear HPE matrix, as presented in Table VII.

1. All values of α are slightly smaller than the value of 0.5 expected for a purely random coil. This shows that the conformational changes during the crystallisation process involve very little movement of the polymer chain. Furthermore, the form of the Kratky plots presented in this thesis is consistent with the scattering from individual stems, as already observed by Sadler and Keller [23], rather than from sheets of stems as in the case of single crystals. These Kratky plots are roughly consistent with the subunit model developed by Sadler and Harris [24]. This subunit model requires a local rearrangement of the chain as it folds during the crystallisation, but the distribution of the subunits within the whole molecule is imposed by the pre-existing Gaussian chain of the melt. This suggests that adjacent re-entry is not the major type of folding here. This point is confirmed by our infrared results where most of the crystal stems contributing to the doublet components are in groups of only 3 to 4 adjacent labelled stems, as was observed by Jing and Krimm [25], and where the maximum size of groups of adjacent labelled stems appears more or less independent of the DPE guest molecular weight. But, contrary to the conclusion drawn by both Sadler and Harris [25] and by Jing and Krimm [26], that 60% to 70% of the crystals stems are [110] isolated or not associated with {110} adjacent folding, in our case 56% of the crystal stems contribute to the doublet components of the CD_2 bending region for LL/95/385, and even more in the case of copolymer guest species (62%).

	α
LL/X/385	0.48±0.04
CL/X/385	0.45±0.06
LC/X/181	0.48±0.03
ref. 16	0.47
ref. 17	0.47
ref. 18	0.44
ref. 19, and 20	0.46
ref. 21	0.47

Table VII. 1: *Results of least squares fits on the evolution of R_g as a function of the molecular weight of the DPE guest ($R_g \propto \overline{M}_W^{\alpha}$) obtained from references 16, 17, 18, 19, 20, 21 on melt quenched linear polyethylene.*

It is only for the CC sample types that the exponent of the relationship $R_g \propto \overline{M}_w^{\alpha}$ determined from the SANS data is different (α = 0.40), suggesting a more compact arrangement as the molecular weight of the DPE guest molecules increases. This was found consistent with the infrared results, where both curve fitting and the simulation of the infrared CD_2 bending profiles show that the number of small groups of adjacent labelled stems is significantly larger when the DPE guest is a copolymer molecule. From the neutron scattering results, it was shown that the copolymer DPE guests have a slightly smaller R_g than theirs linear counterparts when co-crystallised in the same matrix type (i.e. smaller R_g for LL than CL and for LC than CC). This suggests a more compact molecular conformation in the case of a copolymer guest molecule. The difference between the local stem arrangements determined by calculation and by curve fitting of the infrared CD_2 bending profiles of a copolymer and a linear DPE guest mixed with the same matrix is significant, even if this difference is small and is consistent with the neutron scattering results. More groups of adjacent labelled stems and a higher degree of adjacency are found in samples with the copolymer DPE guest than in samples with the linear guest, whatever the matrix type. Therefore, more and larger subunits are found when the guest molecule is a copolymer one. It appears that the copolymer DPE guest molecules undergo more adjacent folding than their linear counterparts. This is almost certainly due to the fact that branches are preferentially excluded from the crystalline lamellae [26, 27, 28], and that this is correlated with the reduction of crystal thickness. Finally, when the matrix is a copolymer, we observe that the degree of adjacency of the guest molecules and the number of groups of adjacent labelled stems are larger than for the linear matrix. This is believed to be related to the reduction of degree of crystallinity and thus, of lamellar thickness observed when crystallising the copolymer matrix samples. Indeed, when a guest molecule is incorporated in thinner lamellae, a larger number of groups of adjacent labelled stems is expected for the same probability of adjacent folding compared to the same molecule incorporated in thicker lamellae.

VII.2. Molecular mechanisms involved during cold drawing

It emerges from the results on the drawn samples presented in this thesis that the deformation behaviour of melt quenched spherulitic polyethylene is a structurally complex process. Our comparative studies on various types of polyethylene lead to the conclusion that their deformation behaviour under drawing has the same basis, with additional effects imputed to the presence of tie-molecules and branches. Three major processes were observed in this thesis. The changes produced by drawing imply (1) the crystallisation of some of the amorphous polymer, where the newly formed crystals have a preferred orientation, (2) the re-orientation of the crystalline ribbons and (3) the beginning of crystallite break-up. Similarly, Hiss et al [29] have shown that there exists a common general scheme for the deformation behaviour for various polyethylene types. The authors pointed out four characteristic points and they associated them with the onset of isolated slip processes, a change into a collective activity of the slips where blocks are sliding before separating in the beginning of crystallite fragmentation (which we see with the reduction in the CD_2 infrared splittings) and finally disentanglement resulting in a truly irreversible deformation. These processes involve mainly the deformation of crystals, whereas in our case both the crystalline and amorphous regions are taken into account. In addition, in this thesis, we have further demonstrated the role of the tie-molecules and branches on the deformation behaviour. This was done by combining the results obtained from infrared spectroscopy and neutron scattering techniques.

First we shall describe and discuss in the light of previous work the characteristic features of the deformation mechanism as determined from the study of the deformation behaviour of the baseline sample prior to considering the effects of increasing the molecular weight and adding branches on the DPE guest molecule.

VII.2.1. Basic deformation behaviour.

The basic deformation behaviour, as determined by the change in sample LL/95/385 with deformation, can be divided into three stages. In the first stage of the deformation, occurring at lowest elongations, both the evolution of the neutron scattering radii of gyration measured parallel and perpendicular to the draw direction and the evolution of the infrared CD_2 bending profile gave evidence of the crystallisation of the amorphous polymer where the newly formed crystals appear to have a preferential orientation with the a-axis is in the plane of the sample while the b-axis is normal to this plane, and it is believed that the c-axis is more or less aligned with the draw direction. Indeed, by showing that the evolution of the neutron scattering radii parallel and perpendicular has initially an affine behaviour, it was concluded that the deformation is initially taking place primarily in the amorphous regions. This is supported by the evolution of both the high and low frequency components of the infrared CD_2 bending profiles and the labelled stem distribution, both of which can be related to the orientation and crystallisation of the amorphous polymer. In addition, the DSC crystallinity is found to be increasing with increasing elongation of our samples. Thus, it was concluded that a phenomenon of stress-induced crystallisation of the amorphous polymer occurs. This phenomenon has been widely studied in the past. For example, Glenz and Peterlin [30] studied the changes in orientation and conformation of highly drawn linear polyethylene (for a draw ratio between 4 to 25, sample molecular weights of 80000 and 150000) by infrared spectroscopy using a dispersive instrument, and they showed that the crystallinity (determined from the absorbance of the 1894 cm^{-1} band, which corresponds to a combination of the Raman-active CH_2 rocking mode at 1170 cm^{-1} and IR-active CH_2 rocking mode at 725 cm^{-1} both arising from the crystalline regions) changes with draw ratio. Up to a draw ratio of around 7, the crystallinity remained constant and beyond this value it increased with gradually decreasing rate up to the highest draw ratios studied (between 20 and 25). In addition, their dichroic study on the bands in the wagging region (1400-1300 cm^{-1}) showed that chains in the amorphous parts become oriented, although to a much smaller extent than the orientation of the crystallites, reaching saturation between a draw ratio of 10 and 15. They concluded that the orientation of the chains in the amorphous regions and the increase in crystallinity are associated with the formation of tie-molecules by uncoiling the molecules in the

amorphous regions that bridge separated blocks resulting from the destruction of the original lamellae structure. This was found to be in good agreement with the model of plastic deformation of crystalline polymers developed by Peterlin [31]. The increase in crystallinity and in orientation of the chains in the amorphous regions was confirmed later by McRae et al [32] in their study of cold drawn high density polyethylene (slow cooled from the melt) by infrared spectroscopy and small and wide-angle X-ray diffraction. The authors added that, on the evidence of the infrared spectroscopy, these newly formed tie-molecules become increasingly closely packed and aligned with increasing draw ratio and thus form new oriented crystals. This correlates with the increase in the WAXS amorphous ring radius observed by Fisher et al [33] which indicates a reduction in the inter-chain distance. In our case, stress-induced crystallisation of parts of the amorphous regions was already observed for a draw ratio of 1.5, while the crystallinity only starts increasing at a draw ratio larger than 7 in the case of Glenz and Peterlin study and even later in the case of McRaye et al. This difference in the onset of stress-induced crystallisation is almost certainly due to the fact that both groups have drawn their samples at 60°C, while our experiments were preformed at room temperature and therefore the deformation effects were enhanced. The initial crystallinity of the samples used by both groups were also higher than in our case. Seguela and Rietsh [34] carried out a similar study on LLDPE slow cooled from the melt and cold-drawn at 80°C and observed a similar trend for the crystallinity as observed by Glentz and Peterlin. More recently Baker and Windle [35], in their study of the effects of branching and fibre drawing on the crystal structure of polyethylene, also observed an increase in the sample crystallinity after uniaxially drawing the sample to form a fibre at a temperature between 75 and 90°C. The authors interpreted this as resulting from stress induced crystallisation of some of the chains in the amorphous regions. In addition to this increase of crystallinity, we have observed from our infrared study that the newly formed crystals appear to have a preferential orientation, with the crystallographic c-axes aligned in the draw direction, the a-axes in the plane of the sample and the b-axes normal to this plane. This correlates with the infrared evidence shown by McRaye et al, which suggests that the tie molecules, which are initially part of the amorphous phase, become increasingly closed packed and aligned with the draw direction as the draw ratio increases, certainly resulting from shear of the lamellar crystals parallel to each other [48]. This observation was recently confirmed in the study

of evolution of the content of extended chain segments in uniaxially stretched polyethylene by Raman spectroscopy carried out by Lagarón et al [36]. This showed that the proportion of extended chain segments outside the crystalline regions rises when the samples are stretched. Also, in this region of the load extension curve, corresponding to low draw ratio, Butler et al [37] have shown that martensitic transformation from orthorhombic into monoclinic crystal structures is occurring. However, this transformation must be only partial and some orthorhombic material certainly remains. When the stress becomes sufficiently large (when the stress is in the plateau region after the yield point and before the stress hardening region of the load-extension curve), the crystallites themselves are affected by the deformation. This is confirmed by the departure from affine behaviour observed in the evolution of the neutron scattering radii of gyration parallel and perpendicular to the draw direction and by the radical changes observed in the evolution of the CD_2 bending profiles. In the discussion in Chapter 6, it was shown that the reorientation process of the crystallographic axes depends on the locality of the unit cell within the spherulite. Indeed, for ribbons parallel to the draw direction, the reorientation process implies rotation of the unit cell around the a-axis for all crystals. For ribbons perpendicular to the draw direction, alignment of the c-axis in the draw direction involves rotation of the unit cell around the b-axis. This rotation of the unit cell around the b-axis requires the untwisting of the crystalline ribbons perpendicular to the draw direction [38, 39, 40, 41, 42, 43, 44]. Since only rotation around the b-axis was inferred from our infrared analysis, we concluded that the ribbons parallel are more resistant to deformation than ribbons perpendicular. This was already proposed by Hay and Keller [45] in their study of the deformation of polyethylene spherulites, where they have observed evidence of rotation of the unit cell about the b-axis to begin with (up to a draw ratio of 7), while signs of rotation about the a-axis were only found at the largest draw ratio studied (draw ratios of 10 and above). They suggested that radii parallel to the draw direction appear more resistant to deformation to begin with and they concluded that rotation of the crystal axes about b occurs more readily than about a. More recently, wide angle X-ray patterns obtained by Hiss et al [29] on different types of polyethylene stretched up to a draw ratio of around 5 suggest also that the reorientation of the chain axis about the b-axis occurs more readily than about the a-axis. As mentioned by both authors, this may be due to crystallographic factors such as an easier chain slip of the (100) planes in the direction of the [001] molecular axis (namely a

[001](100) slip) than [100](010) slip within the lamellae and/or [001] lamellar slip occurring most readily on {h0l} lamellar interfaces. Indeed, Galeski et al [46] in their study of the morphological alterations during compression of high density polyethylene have correlated the crystal rotation about the b-axis with the activation of [001](100) slip systems. Also, the preference for (100) as the intralamellar slip plane has been repeatedly pointed out in the literature [47, 48, 49] and the lamellar interfaces are known to be predominantly {101} or {201} [29, 50].

In the same deformation range as for the crystal re-orientation process, groups of adjacent labelled stems are breaking up. This was shown by a decrease in both the outermost infrared splitting and in the number of the largest groups of adjacent stems (the latter quantity even reaching zero). This is believed to result from chain segments being pulled through the crystals as suggested by Okoroafor and Spells [51]. The remaining blocks then rotate under deformation so as to have their crystallographic c-axes ultimately aligned in the draw direction. We have therefore identified the start of fibre orientation, as described by Peterlin's model [19]. The model developed by Peterlin is based on a three stage process, with the stages identified as the plastic deformation of the original spherulitic structure, the discontinuous transformation of the spherulites into a fibre structure by micronecking, where blocks from the original lamellae are incorporated in microfibrils, and finally the plastic deformation of the fibre structure. In our case, for our highest draw ratios we would not have completed the second stage determined by Peterlin, since break-up of the crystallites and the rotation of the remaining blocks is still occurring and the transformation of the blocks into "microfibrils" is presumably starting. However, our infrared data support the fact that blocks from the original lamellae are incorporated into the forming microfibrils, since it is difficult to imagine a dynamic destruction and reforming of blocks of the same size. Although the model proposed by Peterlin has been widely acknowledged, criticism has come from several directions, notably in relation to transformation of the lamellae into microfibrils [52], and from the fact that the block thickness (along the chain direction) in the fibrillar state generally differs from the original crystal thickness [29]. Finally, it is believed that the initial orthorhombic structure is becoming more and more fractured and ill-defined upon cold drawing, as shown by Lagaròn et al [36].

A quantitative analysis of the infrared results reveals that the average crystallite size decreases from around 18 Å to around 9 Å (corresponding to 2 adjacent stems) for a

draw ratio of 6.7 in the case of our baseline sample. This information is uniquely available from mixed crystal infrared spectroscopy, and demonstrates the extent of disruption within the crystals.

A summary of the general structural changes observed in the deformation behaviour of all samples types studied in this thesis is presented in Table VII. 2.

First step: (starting at the lowest draw ratio studied, DR ≤ 2.5)	• stress-induced crystallisation of part of the amorphous chains • c-axis orientation of the newly formed crystals • activation of interlamellar slip process • transformation of spherulites from spherical to ellipsoidal	• IR doublet splitting, R_g and Ref. 11, 53, 54 • IR doublet dichroism and Ref. 30, 32 • Ref. 29 • Ref. 45
Second step:	• re-orientation of the crystallographic axes by rotation around the b-axis and by intralamellar slip • start of the lamellar break-up	• IR doublet dichroism and Ref. 29 and 45 • IR doublet splitting
Third step: (only starting at the highest draw ratio studied, DR > 6)	• lamellae break-up caused by molecules being pulled through the crystals • chain unfolding • destruction of the spherulite • development of the fibre orientation	• IR doublet splitting and Ref. 51 • Ref. 31 and 51 • Ref. 45 • IR doublet dichroism, R_g

Table VII. 2: *Summary of the structural changes observed in general in the deformation behaviour of all samples types studied in this thesis. It must be added that for each step, the molecular anisotropy, R_{Par}/R_{Per} increases. Refernces to IR doublet splitting, dichroism and R_g correspond to our results.*

VII.2.2. Effect of increasing the molecular weight of the DPE guest molecule.

When increasing the molecular weight of the DPE guest molecules from 95000 to 413000, we have seen that the sample X-ray long spacing becomes smaller than the radius of gyration of the guest molecules. This suggests that the labelled molecules may occupy more than one lamella. Therefore, tie-molecules are certainly present in the highest molecular weight linear sample. Despite the presence of tie-molecules, the infrared CD_2 bending profile is very similar to the profile observed for sample LL/95/385, though some slightly larger groups of adjacent stems are found in the case of LL/413/385. This is an expected result: in melt crystallised polyethylene adjacent folding is not the main mode of chain folding, so that the size of groups should be more or less independent of the molecular weight of the guest molecules. This result taken together with the shape of our intermediate angle neutron scattering Kratky plots broadly confirms that the initial chain conformation exhibits a subunit structure [24]. In the subunit model, the polyethylene molecule is composed of groups of small number of adjacent labelled stems (the subunits) separated by a distance which is large in comparison to the stem separation within the subunit.

As repeatedly pointed out in the literature, tie-molecules drastically improve the deformability of the sample. Thus, the deformation behaviour of sample LL/413/385 should be affected by the presence of these tie-molecules. Indeed, although the three different stages of deformation, as determined in sample LL/95/385, were also observed in sample LL/413/385, differences were demonstrated from our infrared analysis. Firstly, the processes of stress-induced crystallisation of the amorphous regions and the re-orientation of the lamellae occurred together over a wide range of draw ratios instead of being more or less separable as in the case of sample LL/95/385. Also, the stress-induced crystallisation of some of the amorphous polymer appears to be not such a major effect as was observed for sample LL/95/385. In addition, the progressive crystal break-up appears to be more accentuated in the case of high molecular weight sample. All these points were directly related to the tie-molecules which initially are restricting the molecular movement induced by drawing in the amorphous regions. When the stress is large enough, these are pulled through the lamellae, accelerating the crystal break-up. Glenz and Peterlin [30] studied the changes in orientation and conformation of two highly drawn linear polyethylenes, one with a molecular weight of 80000 and the second with a

molecular weight of 150000 and showed that both polymers have identical behaviour with first the crystallinity remaining constant and then increasing. However, the onset in the increase of crystallinity is at lower draw ratio for the high molecular weight sample (around 7) than for the low molecular weight sample (around 10). The authors attribute this to the initial difference of crystallinity between the two samples. At a draw ratio of around 12, both crystallinities start to follow the same trend.

VII.2.3. Effect of branching.

The effect of the branches on deformation behaviour has been probed by replacing in the baseline sample the linear guest molecules by a copolymer guest of the same molecular weight (sample CL/95/385).

Since the branches are preferentially excluded from the crystalline lamellae [26, 27, 28], it is expected that the initial chain conformation would be different for a copolymer DPE guest sample. Indeed, from our infrared analysis, it appears that the local labelled stem arrangement is different for the copolymer sample: a somewhat larger number of labelled stems is distributed into small groups as compared with isolated stems. This is understood as the branches forcing the chain to undergo more folding than in the case of the linear sample. On the other hand, our baseline sample and the copolymer samples of similar molecular weight (CL/95/385 and CC/95/181) have very similar neutron scattering radii of gyration, although slightly smaller when the guest molecule is a copolymer. Therefore, despite of the presence of branches, the average size of the copolymer chain is similar to the linear one, for the low molecular weight samples. However, the evolution of the radii of gyration with increasing molecular weight was found to differ between the linear and copolymer samples. The exponent of the evolution of the radius of gyration as a function of the molecular weight of the copolymer guest molecule is smaller than for its linear counterpart. It was concluded that the copolymer guest molecules tend to have a more compact structure as the molecular weight of the guest molecules is increased.

Differences were also observed in the deformation behaviour from both the neutron scattering and infrared analysis. Although the basic general behaviour is still observed, in contrast to samples LL/95/385 and LL/413/385, the onset of oriented crystallisation of amorphous regions appears to be delayed to larger draw ratios. This is confirmed from the evolution of the radii of gyration parallel and perpendicular to the draw

direction which follow the theoretical prediction of the affine model up to a larger draw ratio than was observed for sample LL/95/385, suggesting that deformation of crystalline regions is delayed in this case. In addition, after a draw ratio of 2, as in the case of sample LL/413/385, the development of the oriented crystallisation takes place over a larger deformation range and is less marked than in the case of sample LL/95/385. The onset of the untwisting of the lamellae is also delayed to larger draw ratios. All these phenomena were related to the presence of branches in the guest molecules, and it was concluded that the branches are acting as anchors. They are restricting the molecular rearrangement of the amorphous polymer and are delaying the oriented crystallisation and the re-orientation of the lamellae. Similarly, Butler et al [53] concluded that the crystalline deformation mechanisms are activated at higher degrees of deformation in the case of the branched polyethylene from their comparative study of the deformation behaviour of linear and branched polyethylene by synchrotron X-ray scattering. This is because the importance of the non-crystalline component in the deformation process is increased when the branch content is increased. Furthermore, when the copolymer DPE guest is mixed with the copolymer matrix (sample CC/95/181) our infrared doublet splitting study shows that, up to a draw ratio of around 3, the newly formed crystals have random orientations. It is only for draw ratios larger than 3 that these new crystallites rotate so as to have their c-axes aligned with the draw direction. On the other hand, the break-up of the crystalline lamellae appears to occurs at a lower draw ratio than was observed for the linear samples. This is expected as branches would be more disruptive when passing through the crystals. To summarise, the effects of the branches are enhanced in the case of CC/95/181, almost certainly due to the fact that both guest and host are copolymer molecules.

VII.3. Time dependent behaviour of clamped samples.

Because some of the neutron scattering experiments took several hours, it was important to determine whether stress relaxation occurs as a function of time in stretched and clamped samples. Therefore, a scattering pattern was collected for each 30 minute interval during the whole experiment. Preliminary results were obtained using the LOQ instrument at ISIS and different behaviour was observed for the linear and copolymer samples studied. For the linear sample (LL/95/385 drawn at a DR of 1.5), the LOQ results appear to be consistent with a development of the molecular deformation within the sample with time. In the case of a copolymer sample (sample CL/95/385), the values of the radii stay constant to within experimental errors during the whole run. However, the small samples involved and short data acquisition times led to large experimental errors, possibly obscuring any significant trends. Repeating the measurements on D11, for samples stretched and then left clamped for the duration of the experiment, showed negligible variation of R_{Par} or R_{Per} as a function of time, with the possible exception, at least in some cases, of the shortest times after stretching. This tends to confirm that the ISIS results should be viewed with caution. In view of the ILL results, both R_{Par} and R_{Per} can be considered constant during the whole time of the experiments, and therefore it is possible to calculate a weighted average of these values for each draw ratio.

VII.4. Time dependent behaviour on the relaxing samples.

Evolution of the radii of gyration parallel and perpendicular with elapsed time after unclamping the samples have been studied in this thesis. From the results presented in chapter VI.1.2, it was observed that the relaxation time seems to vary with the sample type. Copolymer samples appear to have the longest relaxation time constant, while the linear one has the shortest one. Also, it appears from these results that increasing the molecular weight of the guest molecule increases the relaxation time. A similar trend is observed for the amount of recoverable deformation. The copolymer guest samples appear to be more 'elastic' than their linear counterparts. All the results presented in this section appears to be in qualitative agreement with the reptation predictions, although

the observed relaxation time does not appear to increase as the cube of the molecular weight.

Unfortunately, due to the way the experiments were carried out, most of the rapid early stages of relaxation could not be assessed. Also because short data collection times and small samples were used, the uncertainties in the time constants are very large. This make it difficult to draw any firm conclusion from these results. The experiment is clearly on the limit of practicality with current SANS instrumentation.

VII.5. Concluding remarks.

Neutron scattering and infrared data were combined to provide information on molecular conformation for various type of metallocene-catalysed polyethylene, both in the melt quenched state and after uniaxial cold drawing. Both the neutron scattering and infrared results support the fact that adjacent chain folding is not the main mode of chain folding in melt quenched polyethylene, and that the initial general chain conformation exhibits a subunit structure. The initial conformation was found to be different for the copolymer and linear systems. The neutron results imply a slight lack of randomness in the chain conformation in CC samples, increasing with increasing molecular weight. This conclusion is reinforced by FTIR measurements, which show that a significantly smaller proportion of the deuterated crystal stems are isolated with respect to {110} nearest neighbours in CC. There is a corresponding increase in the number of stems involved in groups of 2 to 4 {110} nearest neighbour stems.

The same general deformation mechanisms involving the orientation and stress-induced crystallisation of the amorphous polymer, the untwisting of the crystalline lamellae close to the minor axis, the progressive disruption of the orthorhombic structure and the progressive break-up of groups of adjacent labelled stems were observed in both the linear and copolymer low and high molecular weight systems (as summarised in Table VII.2). Similar conclusions have already been reached by Butler et al [54] and Hiss et al [29] in their comparative work on the deformation of different types of polyethylene. However, additional effects were observed for the high molecular weight linear sample and the copolymer sample and were attributed, respectively, to the presence of tie-molecules and of branches. It was concluded that both the tie-molecules and the branches are restricting the molecular movement during deformation, and that the

branches may be acting as anchors. In addition, we observed that the effects of the branches are enhanced in the fully copolymer sample (CC/95/181).

VII.6. Future work.

In this thesis the mixed crystal infrared technique was applied for the first time to the deformation of melt quenched polyethylene. We did not use any statistical model of the molecular conformation to provide the input to our calculations of the CD_2 bending profile: we simply presented and discussed the basis of such a model in chapter 3. To complete this work, more investigations concerning the folding probabilities to be used in such a model are needed. For example, the Levy distribution may be relevant to model the labelled stem separations of melt quenched polyethylene.

Also, we have presented in Chapter 6 the evolution of the neutron scattering radii parallel and perpendicular with elapsed time after releasing the sample clamps. Unfortunately, due to the experimental set-up, the first neutron measurement could only be made after 15 minutes, and therefore most of the initial relaxation was missed. Because of the short data collection time and the small amount of sample used, the uncertainty in the relaxation time measured is very large. Therefore any conclusions drawn from these relaxation measurements are tentative. Despite all these problems, the trend found for the relaxation time constant is as expected from current theories. This is a promising result and clearly shows that more work on the stress relaxation experiment is needed. Such experiments could be achieved by doing "in situ " stretching, where the sample would be drawn directly inside the sample holder. When the desired draw ratio is reached, the stress would be removed (using a clamp releasing device or by reversing the tensile testing machine). Subsequent neutron scattering runs would start with increasing acquisition time (beginning with runs of 1 min for the first fifteen minutes or so and then progressively increasing the acquisition time). In order to achieve reasonable statistics it is necessary to use the highest neutron flux at the sample. Therefore, using the instrument D11 at ILL would be preferred to the instrument LOQ at ISIS simply because the count rate will be higher on D11. Also, such neutron scattering experiments on relaxing polyethylene could be correlated with simultaneous small and wide angle X-ray scattering measurements at the Synchrotron Radiation Source at Daresbury.

In order to obtain a complete picture of the structure evolution with increasing the degree of deformation, the evolution with deformation of the spherulite size and crystallite long spacing would be interesting to investigate. Measurement of the average spherulite size could be achieved by light scattering measurements. Upon stretching, the four-leaved pattern changes to a pattern which is extended perpendicular to the stretching direction, indicating that the greatest dimension of the deformed spherulite is in the stretching direction. This will enable the onset of the spherulite deformation to be determined and similarly the final spherulite destruction can be observed. As mentioned in the literature survey presented in chapter one, such small light angle scattering experiments have already been performed on linear polyethylene [23-29], but the study of the evolution of the diffraction pattern as a function of draw ratio was limited to a draw ratio of only 1.5 and to linear samples. On the other hand, measurement of the crystallite long spacing could be combined with measurement of the evolution and re-orientation of the unit cell structure by carrying simultaneous small and wide angle X-ray scattering measurements at the Synchrotron Radiation Source at Daresbury. Such work on synchrotron X-ray measurements has already been carried out by Butler et al [11, 53, 56] on purely linear and purely branched polyethylene (for a range of 6.3 to more than 20 butyl groups per 1000 carbons atoms). However a draw ratio of only around 2.25 was reached and the authors used relatively thick samples (almost 1 mm), which may have an effect on the deformation behaviour of the bulk [55].

Finally, since our results and previous ones [11, 53, 54] have shown that the percentage of crystallinity is of great importance in determining the tensile deformation behaviour, systematic study of the evolution of the crystallinity by DSC or by using other techniques, such as X-ray scattering and Raman spectroscopy, would be necessary to complete the picture of the deformation behaviour of the different types of polyethylene studied in this thesis. Indeed, the evolution of the crystallinity appears different depending on the crystallisation conditions and more complex than a simple increase with increasing draw ratio [30, 32]. Raman spectroscopy has been shown to give valuable information on the content of extended chain segments in the amorphous region [12], which may be directly related to the formation of tie-molecules as suggested, for example, in the Peterlin model.

[1] M.J. Hill, P.J. Barham, A. Keller, C.C.A. Rosney, *Polymer*, **32**, 8, 1384 (1991).
[2] M.J. Hill, P.J. Barham, A. Keller, *Polymer*, **33**, 12, 2530 (1992).
[3] C.C. Puig, J.A. Odell, M.J. Hill, P.J. Barham, M.J. Folkes, *Polymer*, **35**, 11, 2452 (1994).
[4] M.J. Hill and P.J. Barham, *Polymer*, **38**, 5595 (1997).
[5] M.J. Hill and P.J. Barham, *Polymer Commun.*, **41**, 1621 (2000).
[6] R.L. Morgan, M.J. Hill, P.J. Barham, A. van der Pol, B.J. Kip, R. Ottjes, J. van Ruiten, *Polymer*, **42**, 2121 (2001).
[7] B. Crist, *Polymer*, **38**, 3145 (1997).
[8] R.G. Alamo, J.D. Londono, L. Mandelkern, F.C. Stehling, G.D. Wignall, *Macromolecules*, **27**, 411 (1994).
[9] G.D. Wignall, J.D. Londono, J.S. Lin, R.G. Alamo, M.J. Galante, L. Mandelkern, *Macromolecules*, **28**, 3156 (1995).
[10] R.G. Alamo, W.W. Graessley, R. Krishnamoorti, D.J. Lohse, J.D. Londono, L. Mandelkern, F.C. Stehling and G.D. Wignall, *Macromolecules*, **30**, 561 (1997).
[11] M.F. Butler, A.M. Donald, and A.J. Ryan, *Polymer*, **38**, 5521 (1997).
[12] J.M. Lagarón, S. López-Quintana, J.C. Rodriguez-Cabello, J.C. Merino and J.M. Pastor, *Polymer*, **41**, 2999 (2000).
[13] R. G. Matthews, I.M. Ward and G. Cappacio, *J. Mat. Sci.*, **34**, 2781 (1999).
[14] R. G. Matthews, A.P. Unwin, I.M. Ward and G. Cappacio, *J. Macromol. Sci. Phys.*, **B38**(1&2), 123 (1999).
[15] A.M.E. Baker, A.H. Windle, *Polymer*, **42**, 651 (2001).
[16] D.G.H. Ballard, G.W. Longman, T.L. Crowley, A. Cunningham and J. Shelten, *Polymer*, **20**, 399 (1979).
[17] D.M. Sadler, P.J. Barham, *J. Polym. Sci. Poly. Phys. Ed.*, **21**, 309 (1983).
[18] G.G. Summerfield, J.S. King, *J. Appl. Cryst.*, **11**, 548 (1975).
[19] J. Shelten, D.G.H. Ballard, G.D. Wignall, G. Longman and W. Schmatz, *Polymer*, **17**, 751 (1976).
[20] J. Shelten, G.D. Wignall, D.G.H. Ballard, G. Longman, *Polymer*, **18**, 1111 (1977).
[21] D.M. Sadler, A. Keller, *Science*, **203**, 263 (1979).
[22] D.G.H. Ballard, A.N. Burgess, A. Nevin, P. Cheshire and G.W. Longman, *Macromolecules*, **13**, 667 (1980).
[23] D.M. Sadler, A. Keller, *Macromolecules*, **10**, 5, 1128 (1977).
[24] D.M. Sadler, R. Harris, *J. Polym. Sci. Poly. Phys. Ed.*, **20**, 561 (1982).
[25] X. Jing, S. Krimm, *J. Polym. Sci. Poly. Phys. Ed.*, **21**, 123 (1983).
[26] C. France, P.J. Hendra, W.F. Maddams and H.A. Willis, *Polymer*, **28**, 710 (1987).
[27] R.G. Alamo, B.D. Viers, and L. Mandelkern, *Macromolecules*, **26**, 5740 (1993).
[28] J.P. Gorce, *PhD thesis*, Sheffield Hallam University, Sheffield, 2000.
[29] R. Hiss, S. Hobeika, C. Lynn, G. Strobl, *Macromolecules*, **32**, 4390 (1999).
[30] W. Glenz and A. Peterlin, *Plastic Deformation of polymers*, Ed. A. Peterlin, Marcel Dekker, New York, 13 (1971).
[31] A. Peterlin, *J. Mat. Sci.*, **6**, 409 (1971).
[32] M.A. McRae, W.F. Maddams, J.E. Freddy, *J. Mat. Sci.*, **11**, 2036 (1976).
[33] E.W. Fisher, H. Goddar and G.F. Schmidt, *J. Polymer Sci: A2*, **7**, 37 (1969).
[34] R. Seguela, F. Rietsch, *Polymer*, **27**, 532 (1986).
[35] A.M.E. Baker, A.H. Windle, *Polymer*, **42**, 651 (2001).

[36] J.C. Rodriguez-Cabello, L. Martìn-Monge, J.M. Lagarón, J.M. Pastor, *Macromol. Chem. Phys.*, **199**, 2767 (1998).
[37]
[38] K. Sasagury, S. Hoshino, R. S. Stein, *J. Appl. Phys.*, **35**, 47 (1964).
[39] K. Sasagury, R. Yamada, R.S. Stein, *J. Appl. Phys.*, **35**, 3188 (1964).
[40] S. Clough, J.J. Van Aartsen, R.S. Stein, *J. Appl. Phys.*, **36**, 10, 3072 (1965).
[41] T. Oda, S. Nomura, H. Hawai, *J. Polymer Sci: A*, **3**, 1993 (1965).
[42] J.J. Van Aartsen, R.S. Stein, *J. Polymer Sci.: A-2*, **9**, 295 (1971).
[43] S. Nomura, A. Asanuma, S. Suehiro, H. Kawai, *J. Polymer Sci: A-2*, **9**, 1991 (1971).
[44] M. Matsuo, C. Xu, *Polymer*, **38**,17, 4311 (1997).
[45] I.L. Hay, and A. Keller, *Kolloid Z. Z. Polym.*, **204**, 44 (1965).
[46] A. Galeski, Z. Bartczak, A.S. Argon, R.E. Cohen, *Macromolecules*, **25**, 5705 (1992).
[47] F.C. Frank, A. Keller, A. O'Connor, *Phil. Mag.*, **4**, 200 (1959)
[48] P.B. Bowden, R.J. Young, *J. Mat. Sci.*, **9**, 2034 (1974).
[49] A. Keller, D. Pope, *J. Mat. Sci.*, **6**, 453 (1971).
[50] A. Keller, S. Sawada, *Makromol. Chem.*, **74**, 190 (1964).
[51] E.U. Okoroafor and S.J. Spells, *Polymer*, **35**, 4578 (1994).
[52] G. Kamig, *J. Cryst. Growth*, **48**, 303 (1980).
[53] M.F. Butler, A.M. Donald, and A.J. Ryan, *Macromolecules*, **28**, 19, 6383 (1995).
[54] M.F. Butler, A.M. Donald, and A.J. Ryan, *Polymer*, **39**, 39 (1998).
[55] W. Reed an M. Vickers, *Private communications*.